

MODELING, SYSTEM IDENTIFICATION, AND PARAMETER ESTIMATION FOR ELECTRIFIED AIRCRAFT SYSTEMS AND HYDROELECTRIC POWER PLANTS

Meaghan Hughes Podlaski

Submitted in Partial Fulfillment of the Requirements
for the Degree of

DOCTOR OF PHILOSOPHY

Approved by:
Luigi Vanfretti, Chair
Xavier Bombois, Co-Chair
Joe H. Chow
Farhan Gandhi
A. Agung Julius



Department of Electrical, Computer, and Systems Engineering
Rensselaer Polytechnic Institute
Troy, New York

[December 2022]
Submitted September 2022

© Copyright 2022
by
Meaghan Hughes Podlaski
All Rights Reserved

CONTENTS

LIST OF TABLES	ix
LIST OF FIGURES	x
NOMENCLATURE	xix
ACKNOWLEDGMENT	xx
ABSTRACT	xxii
1. INTRODUCTION	1
1.1 Background	1
1.1.1 Hydroelectric Power Systems	2
1.1.2 Electrified Aircraft Systems	3
1.2 Scope and Goals	5
1.2.1 Power Plant Modeling and Identification	6
1.2.2 eVTOL Modeling and Identification	9
1.2.3 Electrified Aircraft Modeling	11
1.3 Thesis Overview and Summary of Contributions	14
1.3.1 Part 1: Hydroelectric Power Plant Modeling and Identification	14
1.3.1.1 Chapter 2 Overview	14
1.3.1.2 Chapter 2 Contributions	14
1.3.1.3 Chapter 3 Overview	15
1.3.1.4 Chapter 3 Contributions	15
1.3.2 Part 2: eVTOL Systems	16
1.3.2.1 Chapter 4 Overview	16
1.3.2.2 Chapter 4 Contributions	16
1.3.2.3 Chapter 5 Overview	17
1.3.2.4 Chapter 5 Contributions	17
1.3.3 Part 3: Electrified Aircraft	18
1.3.3.1 Chapter 6 Overview	18
1.3.3.2 Chapter 6 Contributions	18
1.3.3.3 Chapter 7 Overview	18
1.3.3.4 Chapter 7 Contributions	19

2.	PARAMETER ESTIMATION AND CALIBRATION OF STANDARD AND USER-DEFINED MODELS WITH APPLICATION TO THE ITAIPÚ HYDROELECTRIC PLANT	20
2.1	Introduction	20
2.1.1	Motivation	20
2.1.2	Related Works	21
2.1.3	Chapter Contribution	22
2.1.4	Chapter Organization	22
2.2	Proposed Power System Models	23
2.2.1	Re-Implementation of Models from Other Tools	25
2.2.2	Using PMU Data with Modelica	28
2.3	Parameter Estimation Process	28
2.3.1	Sequential Component Calibration	28
2.3.2	Parameter Estimation Methodology	32
2.4	Fault Data Case Study and Results	33
2.4.1	Results - Case 1: September 22, 2015	33
2.4.2	Results - Case 2: November 2, 2016	35
2.4.3	Errors with the User-Defined Turbine-Governor Model	38
2.5	Itaipú Case Study Discussion	40
2.6	Conclusions	41
3.	VALIDATION OF POWER PLANT MODELS USING FIELD DATA WITH APPLICATION TO THE MOSTAR HYDROELECTRIC PLANT	43
3.1	Introduction	43
3.1.1	Motivation	43
3.1.2	Related Works	44
3.1.3	Chapter Contributions	46
3.1.4	Chapter Organization	46
3.2	Components of the Power Plant	46
3.2.1	AVR and Exciter Model	47
3.2.2	PSS Model	48
3.2.3	Generator Model	48
3.2.4	Governor Model	49
3.3	Validation Methodology	49
3.3.1	Validating Component Models	49
3.3.2	Case of Invalid Models	52

3.4	Mostar Power Plant Case Study	53
3.4.1	Introduction	53
3.4.2	AVR and Excitation System Model	53
3.4.3	PSS model	55
3.4.4	Generator model	56
3.5	Mostar Power Plant Validation	57
3.5.1	AVR and Excitation System Model Validation	58
3.5.2	Generator Model Validation	58
3.5.3	PSS Model Validation	59
3.6	Validation Based on Simulation Data	60
3.7	Conclusion and Future Works	62
4.	UAV DYNAMICS AND ELECTRIC POWER SYSTEM MODELING AND VISUALIZATION USING MODELICA	66
4.1	Introduction	66
4.1.1	Motivation	66
4.1.2	Related Works	67
4.1.3	Chapter Contributions	68
4.1.4	Chapter Organization	68
4.2	Modelica Drone Library	68
4.2.1	Blocks	69
4.2.2	Sensors	70
4.2.3	Electrical	70
4.2.3.1	Sources	71
4.2.3.2	Machines	74
4.2.3.3	Power Electronics	75
4.2.4	Controllers	77
4.2.5	Mechanical	79
4.2.5.1	Blades	79
4.2.5.2	Propeller	81
4.2.5.3	Chassis	82
4.2.5.4	Rotor	82
4.2.5.5	Motor	83
4.2.6	Examples and Test Systems	84
4.3	Drone Visualization and Animation	85
4.4	Studies	85

4.4.1	Ideal Flight Path Reference Tracking	87
4.4.1.1	Ideal Power System, Ideal Motor	88
4.4.1.2	Ideal Power System, Permanent Magnet DC Machine with Losses	88
4.4.1.3	Non-ideal Power System, Permanent Magnet DC Machine with Losses	89
4.4.1.4	Non-ideal Power System, Permanent Magnet DC Machine with Losses, and DC/DC Converter	90
4.4.2	Power System Impact on Closed Loop Dynamics	93
4.4.3	Payload Variation	96
4.5	Discussion: Model Variance, Power Consumption, and Dynamic Performance	97
4.6	Conclusions	99
5.	MULTI-DOMAIN ELECTRIC DRIVETRAIN MODELING FOR UAM-SCALE eVTOL AIRCRAFT	101
5.1	Introduction	101
5.1.1	Motivation	101
5.1.2	Related Works	101
5.1.3	Chapter Contributions	103
5.1.4	Chapter Organization	103
5.2	Modeling	104
5.2.1	Platform Description	104
5.2.2	Motor Models	106
5.2.2.1	Simple DC Motor without Inductance	106
5.2.2.2	Simple DC Motor with Inductance	106
5.2.2.3	Brushless DC Motor with Averaged EMF	107
5.2.2.4	Brushless DC Motor with Trapezoidal EMF	107
5.2.3	Battery Models	109
5.3	Multi-Domain Model Coupling in Simulink	110
5.3.1	Speed Control Architecture	111
5.4	Results	112
5.4.1	Isolated Rotor	112
5.5	Multi-rotor System	114
5.5.1	Centralized Battery Architecture	114
5.5.2	Distributed Battery Architecture	117
5.6	Conclusion	122

6.	POWER SYSTEM ARCHITECTURE DEVELOPMENT AND MULTI-DOMAIN MODELING FOR FULLY-ELECTRIC AIRCRAFT	126
6.1	Introduction	126
6.1.1	Motivation	126
6.1.2	Related Works	127
6.1.3	Chapter Contribution	128
6.1.4	Chapter Organization	128
6.2	CHEETA Electrical System Architecture	129
6.2.1	Multi-Domain Modeling Approach	129
6.2.2	Power System Architecture Overview	129
6.3	Power System Models	133
6.3.1	Fuel Cell	134
6.3.2	Battery	137
6.3.3	Electrified Drivetrain	140
6.3.3.1	Controller	141
6.3.3.2	Modulation Method for Inverter Control	142
6.3.3.3	Inverter	143
6.3.3.4	Machine	145
6.3.4	HTS Transmission Line and Bus Bars	147
6.3.4.1	High Temperature Superconductor Component Validation Results	150
6.3.5	Fan Load	151
6.4	Preliminary Results	154
6.5	Conclusions	155
7.	MULTI-DOMAIN MODELING AND SIMULATION OF HIGH TEMPERATURE SUPERCONDUCTING TRANSMISSION LINES UNDER SHORT CIRCUIT FAULT CONDITIONS	158
7.1	Introduction	158
7.1.1	Motivation	158
7.1.2	Related Works	159
7.1.3	Chapter Contributions	160
7.1.4	Chapter Organization	161
7.2	HTS Model	161
7.2.1	Modelica and Multi-Domain Modeling Overview	161
7.2.2	CHEETA Electrical System One-Line Diagram	162

7.2.3	Model Overview: Liquid Cooled Transmission Line	163
7.2.4	Model Overview: Gas Cooled Transmission Line	166
7.3	Component Model Analysis	167
7.4	Fault Analysis	169
7.4.1	Fault Model Overview	169
7.4.1.1	PEM Fuel Cell Model	172
7.4.1.2	Inverter Model	173
7.4.2	Fault Studies	174
7.4.2.1	Liquid Hydrogen Cooling	174
7.4.2.2	Liquid Nitrogen Cooling	176
7.4.2.3	Hydrogen Gas Cooling	177
7.5	Conclusion	179
8.	CONCLUSION	182
8.1	Hydroelectric Power Plants	182
8.2	eVTOL Systems	184
8.3	Fully-electric Aircraft Systems	188
	REFERENCES	192
	APPENDICES	203
A.	SUPPLEMENTAL FILES	203
A.1	Permissions for Chapter 2	203
A.2	Permissions for Chapter 6	203
A.3	Permissions for Chapter 7	203
B.	PUBLICATIONS	205
C.	ITAIPÚ PARAMETER DEFINITIONS AND GENERATOR EQUATIONS	208
C.1	GENSAE Generator	208
C.2	SEXS AVR	208
C.3	STAB3 PSS	209
C.4	IEEE HYGOV Turbine Governor	210
C.5	Itaipù Component Variables and Parameters	212
D.	MOSTAR HYDROELECTRIC PLANT PARAMETER DEFINITIONS AND GEN- ERATOR EQUATIONS	213
D.1	IEEE Standard Model Equations	213
E.	CHEETA SUBSYSTEM PARAMETER DEFINITIONS	217

LIST OF TABLES

1.1	Inputs and outputs for the validation methods used in Chapters 2 and 3. . . .	8
2.1	$\ \mathbf{x}\ $ fitness of results per model for September 22, 2015 and November 2, 2016 events.	38
3.1	Generator parameters for re-identified model due to 10% increase on X_d	63
4.1	Energy metrics for the ideal flight path tests.	99
4.2	Tracking response for the ideal flight path tests.	99
5.1	Aircraft parameters.	104
6.1	Fuel cell parameters.	137
6.2	Battery parameters.	141
6.3	CHEETA machine parameters.	147
6.4	CHEETA HTS line parameters.	150
C.1	SEXS AVR parameters.	209
C.2	STAB3 PSS parameters.	210
C.3	HYGOV TG parameters.	211
C.4	Itaipù component variables and parameters.	212
D.1	GENSAL generator parameter definitions.	214
D.2	Generator variables used in estimation - IEEE GENSAL Model.	214
D.3	ST5B AVR parameters.	215
D.4	PSS2A PSS parameters.	216
E.1	HTS line parameters.	217

LIST OF FIGURES

1.1	Overview of the objectives for the three systems studied.	6
1.2	Objectives of hydroelectric power system studies.	9
1.3	Objectives of eVTOL system studies.	11
1.4	Objectives of electrified aircraft studies.	13
2.1	Modelica model of the generator, TG, AVR, and PSS in Dymola, which is compared to an SMIB one line diagram.	24
2.2	Block diagram showing the relationship between each system component, their inputs, and their outputs.	25
2.3	Itaipú user-defined AVR model in CduEdit software.	26
2.4	SMIB system model implemented in Dymola. An equivalent system is also modeled in Anatem.	27
2.5	OpenIPSL vs Anatem voltages at bus B1 for software validation.	27
2.6	OpenIPSL vs Anatem rotor angle at bus B1 for software validation.	28
2.7	Itaipú system in Simulink using the FMI Toolbox for use in RaPIId.	29
2.8	Process for calibrating components in the Itaipú system.	30
2.9	Calibration results for the user-defined AVR/PSS calibration (Phase C - red), user-defined AVR/PSS/TG (Phase D - green), and IEEE standard AVR/PSS/TG (Phase D - purple) for the September 22, 2015 event.	34
2.10	Comparison of all user-defined model estimation phases for the September 22, 2015 event.	35
2.11	Calibration results for the user-defined AVR/PSS calibration (Phase C - red), AVR/PSS/TG (Phase D - green), and IEEE standard AVR/PSS/TG (Phase D - purple) for the November 2, 2016 event.	36
2.12	Comparison of all user-defined model estimation phases for the November 2, 2016 event.	37
2.13	Response of the system consisting of generator, AVR, and PSS during the event on November 2, 2016.	37
2.14	Final calibration phases for user-defined AVR and PSS models with both a user-defined and IEEE standard TG model compared for the September 22, 2015 data set.	39

2.15	Final calibration phases for user-defined AVR and PSS models with both a user-defined and IEEE standard TG model compared for the November 2, 2016 data set.	40
2.16	20 Hz oscillation observed during fault at Itaipú plant.	42
3.1	Block diagram of the power plant showing the relationships between each component and their inputs and outputs.	47
3.2	AVR inputs and outputs for static exciter example.	48
3.3	PSS inputs and outputs.	48
3.4	Generator block diagram.	50
3.5	Governor inputs and outputs.	50
3.6	Real system S_i and model M_i comparison.	51
3.7	Block diagram of the power plant showing the relationships between each component and their inputs and outputs for the Mostar plant.	54
3.8	AVR ST5B block diagram.	55
3.9	PSS2B block diagram.	56
3.10	Generator direct axis block diagram.	57
3.11	Generator quadrature axis block diagram.	57
3.12	AVR validation data and results, where (a) Inputs to AVR. (b) AVR field voltage response comparison.	58
3.13	Generator validation data and results, where (a) Inputs to generator. (b) Generator output response comparison.	59
3.14	PSS validation data and results, where (a) Inputs to PSS. (b) AVR field voltage response comparison.	60
3.15	Block diagram of the power plant showing the relationships between each component and their inputs and outputs for the Mostar plant.	61
3.16	Inputs to generator in case of changed parameters.	62
3.17	Generator validation results for when X_d is increased by 10%, where (a) Invalidated generator model response. (b) Validated generator model response with re-identified models.	63
3.18	Controller validation when there is a change in generator parameters, where (a) AVR validation. (b) PSS validation.	64

3.19	PSS validation with only step excitation, where (a) PSS with halved time constants for T_{w1}, T_{w2}, T_6 . (b) PSS with doubled time constants for T_{w1}, T_{w2}, T_6	64
3.20	PSS validation with both step and white noise excitations, where (a) PSS with halved time constants for T_{w1}, T_{w2}, T_6 . (b) PSS with doubled time constants for T_{w1}, T_{w2}, T_6	65
4.1	Drone library file structure: (a) Library package hierarchy. (b) Electrical package hierarchy.	69
4.2	Complete drone model consisting of propellers, motor, controller, and chassis with battery power system. Inputs come from x, y, and z coordinate location commanded by the user.	71
4.3	Otus Quadcopter power system block diagram.	72
4.4	Battery from Modelon Library Suite.	73
4.5	Modelica Standard Library permanent magnet DC machine model.	75
4.6	Model for the motor in the propeller system. The red box contains the components used to calculate the thrust.	76
4.7	Buck converter model in Dymola.	77
4.8	Drone controller model in Dymola.	78
4.9	Speed controller model in Dymola.	79
4.10	Mechanical package setup.	79
4.11	Blade model in Dymola.	80
4.12	Chassis model in Dymola.	80
4.13	Model for the propeller system containing mechanically linked motor, rotor, and blades (a) without; (b) with power connections.	81
4.14	Rotor model in Dymola. The aerodynamic forces applied to the rotor are located in the red box.	83
4.15	Complete drone model consisting of propellers, motor, controller, and chassis with ideal power system.	84
4.16	Drone model configured for 1 m/s 5 second ramp input in the Z-direction test.	85
4.17	Drone animation at time = 0 seconds.	86
4.18	Drone animation at time (a) 1 seconds at 1 m (b) 1.5 seconds at 1.5 m (c) 2 seconds at 2 m for an ideal motor and ideal power system.	86

4.19	Drone animation with the path of the propeller shown as a trace for the flight path in Figure 4.16.	87
4.20	Drone with an ideal motor and ideal power system XYZ position under a ramp signal input.	89
4.21	Drone with DCPM motor and ideal power system XYZ position under a ramp signal input.	90
4.22	Thrust from one motor in the Z direction compared for the ideal motor and DC motor with losses.	91
4.23	Drone with DCPM electrical motor and battery power system XYZ position under a ramp signal input.	91
4.24	Battery (a) state of charge (b) voltage discharge response under a ramp signal input.	92
4.25	Drone with DC permanent magnet electrical motor, battery power system, and DC to DC converter XYZ position under a ramp signal input.	93
4.26	Battery voltage with a DC/DC converter included in the power system architecture with (a) Battery voltage over 10 second testing period. (b) Battery voltage inset from 0 seconds to 0.01 seconds. (c) Battery voltage inset from 9.99 seconds to 10 seconds.	94
4.27	Position signal compared to motor output when converter is connected to the power system and supplies voltage ripple.	95
4.28	Battery voltage and state of charge over 13 minutes at 5m hovering.	96
4.29	Drone XYZ position during test where the battery is discharged and the quadcopter remains in hover at 5m until failure.	97
4.30	Drone position with a payload of 3kg applied to airframe. (a) Drone position. (b) Rotor thrust.	98
5.1	Electric powertrain schematic.	105
5.2	Circuit diagram of DC motor without inductance.	105
5.3	Circuit diagram of DC motor with inductance.	105
5.4	Circuit diagram of the averaged brushless motor.	107
5.5	Back EMF of trapezoidal brushless machine with a duty cycle of 0.33.	108
5.6	Switched three-phase converter with averaged input voltage.	108
5.7	Battery schematic.	109

5.8	Integration of the drivetrain model with RMAC rotor model.	110
5.9	Forward path of explicit-model-following controller.	111
5.10	Second order speed command response with (a) First 500ms of the response. (b) First 50ms of the response.	112
5.11	Motor current when a second order speed command is applied with (a) First 500ms of the response. (b) First 50ms of the response.	113
5.12	Motor torque when a second order speed command is applied with (a) First 500ms of the response. (b) First 50ms of the response.	113
5.13	Multi-rotor aircraft model with centralized battery.	114
5.14	Heave command and vehicle response.	115
5.15	Speed response of the multi-rotor system to a heave command.	115
5.16	Current response of the multi-rotor system to a heave command.	115
5.17	Voltage response of the multi-rotor system to a heave command.	116
5.18	Pitch command and vehicle response.	117
5.19	Speed response of the multi-rotor system to a pitch command.	118
5.20	Current response of front and rear motors of the multi-rotor system to a pitch command.	118
5.21	Current response of the multi-rotor system battery to a pitch command.	119
5.22	Voltage response of the multi-rotor system when pitch command is applied.	119
5.23	Multi-rotor aircraft model with individual batteries connected to each motor, creating a distributed architecture.	120
5.24	Speed response of the multi-rotor system with individual batteries to a heave command.	120
5.25	Current response of the multi-rotor system with individual batteries to a heave command.	121
5.26	Voltage response of multi-rotor system with individual batteries to heave com- mand.	121
5.27	Speed response of the multi-rotor system with individual batteries to a pitch command.	122
5.28	Current response of the multi-rotor system with individual batteries to a pitch command.	123

5.29	Voltage response of the multi-rotor system with individual batteries to pitch command.	123
5.30	Speed response of the multi-rotor system to a heave command with unbalanced batteries with (a) Speed response of the multi-rotor system to a heave command with imbalanced batteries. (b) Inset from 6 to 6.5 seconds.	124
5.31	Current response of the multi-rotor system to heave command with unbalanced batteries.	124
5.32	Voltage response of the multi-rotor system to heave command with unbalanced batteries.	125
6.1	Power system architecture layout inside of proposed CHEETA aircraft in terms of sub-systems and sub-domains to demonstrate the physical placement of components.	130
6.2	The CHEETA electric aircraft architecture configured to show the electrical wiring scheme for the system. This representation only shows the go portion of the circuit, the return lines will also have the same structure.	131
6.3	Cooling system concept for one branch of the power system.	132
6.4	Cooling system flow chart for the power system with losses and operating temperatures for each component in the aircraft.	133
6.5	Single branch of power system modeled, highlighting the interaction between the domains in the CHEETA power system.	134
6.6	Power system with fuel cell operations and functionalities shown in detail.	135
6.7	Electrical schematic of the PEM fuel cell.	136
6.8	Electrical losses in fuel cell.	136
6.9	Multi-domain schematic for the battery.	138
6.10	Circuit for the battery subsystem in Modelica using Dymola.	139
6.11	Cylindrical scaled battery pack model from Dassault Battery Library.	140
6.12	PI speed controller used in electric speed drive.	142
6.13	No modulation method for electric powertrain controller from EPTL.	143
6.14	Averaged inverter model from EPTL in Dymola.	144
6.15	Simplified electrical circuit model for the machine.	145
6.16	Synchronous machine model in Dymola.	146

6.17	HTS pi-line model schematic.	148
6.18	Circuit consisting of HTS line and current source.	152
6.19	Heat transfer characteristics as a function of change in temperature for the line submerged in a liquid hydrogen cooling bath.	152
6.20	Heat transfer characteristics as a function of change in temperature for the line submerged in a liquid nitrogen cooling bath.	153
6.21	Comparison between the difference in temperature of the surface of the transmission line and cooling both media, where liquid hydrogen (blue) and liquid nitrogen (red), as a function of line current.	153
6.22	The multi-domain fan model in Modelica.	154
6.23	Machine during half hour flight path. It is split into three parts: part 1 is when the aircraft is taking off, part 2 is steady state flight, and part 3 is landing. . .	155
6.24	Change in HTS line temperature during the 30 minute flight path. Any difference in temperature between the cryogenic media and line less than 2K ensures that the line will operate in the cryogenic region.	156
6.25	Fan model animation at (a) 5 seconds (b) 5.6 seconds (c) 5.8 seconds (d) 5.9 seconds with motor moving at a constant speed of 7000 RPM.	156
7.1	The CHEETA electric aircraft architecture configured to show the electrical wiring scheme for the system. This schematic focuses on the electrical components; all cooling and thermal components are omitted. This representation only shows the go portion of the circuit, the return lines will also have the same structure.	164
7.2	HTS pi-line model schematic.	165
7.3	Heat transfer characteristics as a function of temperature for the line submerged in a liquid hydrogen cooling bath.	168
7.4	Heat transfer characteristics as a function of temperature for the line submerged in a liquid nitrogen cooling bath.	169
7.5	Gas cooling ΔT_z vs I_{op} , where ΔT_z is the difference in temperature between the hydrogen gas and the cable at a distance (x) from the gas cooling inlet.	170
7.6	Multi-domain aircraft electrical power system modeled using Modelica with each component used labeled.	171
7.7	PEM fuel cell electrical circuit diagram.	172
7.8	The Thévenin equivalent electrical model for common-mode operation of an inverter.	172

7.9	Difference between in HTS line and cryogen temperature (ΔT_ρ) and fraction of operational current (I_{op}) as a function of fuel cell impedance prior to applying the short circuit fault in liquid hydrogen cooling media.	175
7.10	Difference between in HTS line and cryogen temperature (ΔT_ρ) and fraction of operational current (I_{op}) as a function of fuel cell impedance after to applying the short circuit fault in liquid hydrogen cooling media.	176
7.11	Difference between in HTS line and cryogen (ΔT_ρ) and fraction of operational current (I_{op}) as a function of fuel cell impedance prior to applying the short circuit fault in liquid nitrogen cooling media.	177
7.12	Difference between in HTS line and cryogen (ΔT_ρ) and fraction of operational current (I_{op}) as a function of fuel cell impedance after applying the short circuit fault in liquid nitrogen cooling media.	178
7.13	Difference between in HTS line and cryogen (ΔT_z) at different locations and fraction of operational current (I_{op}) as a function of fuel cell impedance prior to applying the short circuit fault in hydrogen gas cooling media.	179
7.14	Difference between in HTS line and cryogen (ΔT_z) at different locations and fraction of operational current (I_{op}) as a function of fuel cell impedance after applying the short circuit fault in hydrogen gas cooling media.	180
8.1	Comparison of IEEE standard and user-defined turbine-governor models for the Itaipú plant.	183
8.2	PSS validation with only step excitation, where (a) PSS with halved time constants for T_{w1}, T_{w2}, T_6 . (b) PSS with doubled time constants for T_{w1}, T_{w2}, T_6	184
8.3	PSS validation with both step and white noise excitations, where (a) PSS with halved time constants for T_{w1}, T_{w2}, T_6 . (b) PSS with doubled time constants for T_{w1}, T_{w2}, T_6	185
8.4	Relationship between the quadcopter modeled in Chapter 4 and the drivetrain studied in Chapter 5. (a) Overview of quadcopter model developed in Chapter 4. (b) Overview of electric drivetrain model studied in Chapter 5.	187
8.5	DC motor with trapezoidal back EMF ripple current behavior, where (a) First 500ms of the response. (b) First 50ms of the response.	188
8.6	DC motor with trapezoidal back EMF ripple torque behavior, where (a) First 500ms of the response. (b) First 50ms of the response.	188
8.7	The CHEETA electric aircraft architecture configured to show the electrical wiring scheme for the system.	190
C.1	Control diagram for SEXS AVR.	209

C.2	Control diagram for STAB3 PSS.	210
C.3	Control diagram for IEEE HYG0V TG.	210
D.1	Control diagram for ST5B AVR.	215
D.2	Control diagram for PSS2A PSS.	215

NOMENCLATURE

Hydroelectric Power Systems: Chapters 2 and 3

AVR	Automatic voltage regulator
dq-axis	Direct-quadrature axis
GENSAE	Salient pole generator with exponential saturation
PSO	Particle swarm optimization
PSS	Power system stabilizer
SMIB	Single machine infinite bus
TG	Turbine governor

eVTOL Systems: Chapters 4 and 5

EMF	Electromotive force
OCV	Open circuit voltage
PWM	Pulse width modulation
RMAC	Rensselaer Multicopter Analysis Code
SoC	State of charge

Electrified Aircraft Systems: Chapters 6 and 7

BMS	Battery management system
CHEETA	Cryogenic High-Efficiency Electrical Technologies for Aircraft
EMS	Energy management system
FMI	Functional mock-up interface
FMU	Functional mock-up unit
HTS	High temperature super-conducting transmission line/cable
MSL	Modelica Standard Library
PEMFC	Proton-exchange membrane fuel cell
PWM	Pulse-width modulation
SoC	State of charge
SOFC	Solid oxide fuel cell
VSD	Variable speed drive

ACKNOWLEDGMENT

First of all, I would like to thank my advisors, Dr. Luigi Vanfretti and Dr. Xavier Bombois. This work would not have been possible without your guys support, patience, and guidance. Back when we first met in fall 2017, Luigi was the first person to encourage me to pursue a PhD, so thank you for seeing something that I did not see in myself and getting me started with this adventure. Xavier, thank you for being so patient with conducting research with me with an ocean and a six hour time difference separating us for many, many months and for being a wonderful mentor.

In addition to Dr. Vanfretti and Dr. Bombois, I also would like to thank Dr. Chow, Dr. Gandhi, and Dr. Julius for serving on my doctoral committee. Your time, support, and encouragement to improving my research means so much to me. I would also like to thank the administrative staff of the ECSE department, Priscilla Magilligan and Kelley Kritz, for their patience and help with all of the logistics with my degree.

I'd like to thank my research group members (and friends) - Sergio Dorado Rojas, Abhijit Khare, Protay Adhikari, Miguel Aguilera, Eric Segerstrom, Marcelo de Castro Fernandes, Giuseppe Laera, Fernando Fachini; and friends - Katie Clark, Mara Giga, Sofia Perez Guzman, and Chris Aquino for their help, friendship, and continuous support.

I'd like to thank my parents, Linda and Tony, for their love and support. I am so lucky to have two educators as parents, absolutely none of this would have been possible without you setting the example to prioritize my education and making sacrifices in order to make it happen. It makes me feel so loved that you have taken genuine interest in navigating this process with me, between watching all of my presentations the second they are uploaded on Youtube and planning celebrations to make each milestone in the PhD feel special.

I'd like to thank my human sister Lindsey and pug sister Andi. Lindsey is the best friend you could ever ask for, the absolute best personal cheerleader. You have the best skills in knowing exactly which jokes will make me forget why I was upset, and you match everyone's excitement for their special interests to make them feel important and valued. Andi, thanks for tolerating my existence.

Finally, a very special thanks to my partner, Duncan Leathrum, for the love, patience, encouragement, and support. Thanks for putting up with me through the most stressful times.

This work was supported in whole or in part by the National Science Foundation Graduate Research Fellowship Program under Grant No. DGE 1744655 and the Chateaubriand Fellowship of the Office for Science & Technology of the Embassy of France in the United States. Additional support from the National Aeronautics and Space Administration under award number 80NSSC19M0125 as part of the Center for High-Efficiency Electrical Technologies for Aircraft (CHEETA) is gratefully acknowledged.

ABSTRACT

In recent years, there has been a push to electrify everyday technologies to help meet emissions reduction and promote more sustainable energy consumption practices. Three systems that consider the different aspects of electrification development are modeled, identified, and analyzed in this work. The methods applied for modeling, identification and analysis aim to help in making the electrification more sustainable through their entire engineering life cycle. This work considers a model-based systems engineering framework, where the systems are represented by physics-based models to analyze with system identification methods and for various trade studies.

Hydroelectric power plants are first considered as a well-established system that has been in operation for decades, where field measurement data collected from the electric power grid is used to validate and identify power plant models. These models have been defined in a standardized and custom manner, allowing us to apply our methodology to a system with models that have been in use for a long time. The parameters of the models are estimated using field data, showing the value in model maintenance and standardization. This work also introduces a methodology for validating the individual components of a power plant, making it necessary to re-identify and re-validate only the affected components. This methodology is incredibly valuable when performing re-validation, as considering only the invalid component reduces the complexity of the optimization problem.

Next, we model and study an electric vertical take-off and landing (eVTOL) aircraft. These systems are in an earlier stage of development than Hydroelectric power plants, where physical prototypes and products exist for some eVTOL systems, but have been limited in wide-scale application and therefore operational measurement data is not readily available (e.g. hobbyist drones). Many existing eVTOL systems are small, so this work shows how we can expand on the existing modeling technology and study multi-domain dependencies when eVTOL are scaled to provide human-scale transport. The modeling approach enables the development of a library to model quadcopters using physics-based components through a flexible modeling framework. It is then used to study an eVTOL drivetrain to determine the effects of battery configuration and motor modeling fidelity on dynamic response, showing necessary considerations needed for eVTOL design.

The third system discussed is an electrified aircraft system that is still in the early

phases of design and development. It is necessary to expand upon existing research to develop sub-domain components for the aircraft as there is no cohesive physical prototype of the specific aircraft or its subsystems available to validate the models. A novel system architecture was developed for the fully-electric aircraft concept, showing the different considerations needed to design the electrical and thermal systems as well as each of the individual subsystems. This also required the development of novel cryogenic component models, which were then studied in the aircraft configuration under fault conditions. This fault study shows how the sizing of other components in a novel aircraft system can be utilized to mitigate the impact of faults.

CHAPTER 1

INTRODUCTION

1.1 Background

As our societies commit to transforming our infrastructure and systems to reduce our Greenhouse Gas emissions, cyber-physical systems and technologies will be instrumental in the electrification of these systems. In recent years, the growth cyber-physical systems have strictly coupled physical systems with computational technologies [1]. These technologies, also known as part of the Fourth Industrial Revolution, are increasing connectivity, monitoring, and automation of systems [2].

Cyber-physical systems have been of particular interest in recent years for application in both existing technologies, such as hydroelectric power systems, and in the development in new systems like fully-electrified aircraft. Simulation-based studies are extremely valuable in determining which technologies have the most benefit, saving time and money in testing concepts prior to building a physical prototype. In bulk electric power systems, testing opportunities are limited as the physical system is costly and time consuming to develop. It is nearly impossible to create an exact physical prototype of the electric grid for testing, and testing can only be conducted on the physical system when it is offline. Power plants only receive compensation for the power they generate, so shutting down the plant to do testing not during planned maintenance periods is not possible. The plants may also provide electrical stability to the grid, limiting testing opportunities. In the case of electric aircraft, it is impossible to test a system where most of the technology does not exist in the capacity needed to build the entire physical prototype of the aircraft. Instead, models of individual subsystems can be developed in parallel with ongoing research and development to perform simulation studies of the completed aircraft.

In addition to assisting in the development of new technologies to reduce emissions, cyber-physical systems and technologies provide an opportunity to create more resilient and reliable systems. As the electrical and transportation infrastructure is updated to accommodate for climate change, the extent and influence of system failure can be mitigated through cyber-physical systems. Environmental disasters are becoming increasingly more common, with extreme weather events such as hurricanes, tornadoes, and wildfires affecting every community. As we prepare for these events to become increasingly more common,

cyber-physical systems can aid in developing inclusive disaster response to ensure that the most basic services remain available to vulnerable communities. The failure of critical infrastructure such as the bulk electric grid disproportionately affects the most vulnerable populations: disabled people, low-income communities, and communities in which their infrastructure heavily depends on the local environment. The absence of electrical resources increases burden on the community, affecting food, medical, and other supply levels. The development of cyber-physical systems can be used to improve system resiliency and aid in disaster response. By creating well-defined cyber-physical models of power plants and other grid infrastructure, we have a better understanding on how to approach system planning and operations. This can help engineers and system operators plan for a more resilient grid as well as take effective operation measures during emergency operations. Electrified systems such as electrified aircraft can serve as a vital resource in disaster response, in which they can operate when standard petroleum fuel supplies are not available.

1.1.1 Hydroelectric Power Systems

A modernized electrical grid is necessary as the United States re-imagines and rebuilds its infrastructure for a carbon-neutral future to combat climate change. Through the passing of the Infrastructure Investment and Jobs Act (H.R. 3684), the United States has committed to investing in renewable generation, system monitoring, and control systems to lead to a more resilient, flexible grid that is environmentally, economically, and operationally sustainable [3], [4]. As other industries such as the automotive industry seek to decrease their Greenhouse Gas emissions through electrification, electricity consumption would increase up to 55% in states like Maine [5], driving the demand for a more resilient and flexible grid.

Large portions of the American electrical grids are aging, making it necessary to have an accurate representation of the existing system as the current infrastructure is being upgraded to accommodate for increased power consumption from electrification. One particular area of interest is to ensure accurate dynamic models of existing power plants, especially as the grid shifts from synchronous generators to inverter-based resources. Inverter-based resources, such as wind turbines and solar panels, have a significant impact on power system stability characteristics and performance under disturbances. These resources are subject to numerous dynamic simulation studies while in the planning phase of the project to understand how they will interact with the existing system under various operating conditions. The infrastructure

supporting these plants is aging, which causes the electrical and mechanical dynamics of the power plants to change over time. Maintenance and wear of these existing plants may cause the system model parameters to differ from those that can characterize the actual physical system, which causes an inherent uncertainty in the model [6]. This ultimately leads to erroneous simulation results and more conservative grid operations.

Accurate representations of these dynamic models have been proven useful in the planning and operation of the grid. For example, the Independent System Operator-New England used PMU data from a ground fault that occurred 16 miles away from a large nuclear power plant to validate the model [7]. This produced a model that can reproduce the voltage and real output for the specific disturbance for two nuclear units and HVDC lines connecting the plant to the rest of the system. As a result of these tests, the system operator now has a model that reproduces real system behavior to determine actions during other disturbances and determine how proposed infrastructure would interact with the plant.

In February 2021, the Texas electric grid was placed under extreme operational constraints following large-scale generation failure from unexpected weather conditions. Due to the significant loss in generation and increased demand due to unusually cold temperatures, the system frequency dropped so low that the grid would suffer from frequency collapse in four minutes and 37 seconds and require black start operation [8]. Events like this highlight the importance of accurate, reliable dynamic models so that these entities can study and prepare for unusual and extreme system conditions as unseasonable weather patterns become more common as a result of climate change.

1.1.2 Electrified Aircraft Systems

Electrified aircraft has recently seen advancements as a result of demand for increased sustainability in both fixed-wing and electric vertical take-off and landing (eVTOL) systems. The global aviation industry produced 2% of all human-induced carbon dioxide (CO₂) emissions and 12% of total CO₂ emissions from transportation sources in 2019 [9]. The aviation industry has also committed to reducing net aviation CO₂ emissions by 50% (compared to 2005 emissions levels), making the electrification of aircraft necessary to help reach these goals [9].

The commitment to the electrification of the aviation sector has enabled the development of an array of new concept vehicles and programs such as NASA's Advanced Air

Mobility (AAM) initiative [10], Uber Elevate [11], NASA ULI Center for High-Efficiency Electrical Technologies for Aircraft (CHEETA) [12], and More Open Electrical Technologies (MOET) [13]. Many of these projects and initiatives are on-going work early in technological development, so physical prototypes are either non-existent or extremely limited in capability. As the technologies and designs for the aircraft mature, accurate, physics-based models can aid in early-phase integrated system design and trade-off studies. These studies allow for testing of novel aircraft configurations and to understand how novel aircraft subsystems interact with one another, improving system design.

These electrified aircraft systems will diversify transportation methods, decreasing travel time and making travel methods more accessible. Projects such as Uber Elevate would introduce eVTOL ride share to various American markets, decreasing travel time on commutes in cities congested with automotive traffic [11]. In cities with existing and robust public transportation infrastructure, urban air mobility (UAM) eVTOL would diversify public transportation methods. This would improve the resiliency of the transportation network, providing alternative options for transit when other methods such as buses are out of operation or unavailable. Uber expects that UAM systems will first serve heavily congested urban and suburban areas with long commutes as these communities may be already under-served by the existing transportation infrastructure. These systems would be targeted at decreasing commute time, traffic congestion, and emissions. Since these systems are designed to have zero-emissions during operation, air pollution in cities would decrease and air quality would improve.

Electrified fixed-wing aircraft has similar goals and benefits to UAM eVTOL systems, where aircraft projects such as CHEETA would be targeted to serve short distance commercial flight operations [12]. These systems could initially operate routes that shuttle passengers from regional airports to larger hubs, as these flights normally only travel a few hundred miles with very few passengers. Since these systems are designed to operate using liquid hydrogen, the fueling infrastructure will be initially sparse. Aircraft would have to take multiple short range trips departing from hubs to airports less than 250 nautical miles away [14]. Eventually, if demand warrants it, hydrogen could be produced on site at airports to eliminate distribution costs for the fuel. This would make electric air travel a more cost-efficient way to travel.

Many aircraft electrification projects currently focus on bridging the gap between ex-

isting internal combustion engine powered aircraft and fully-electric aircraft projects like CHEETA. This includes projects like MOET [15], which focused on scaling up electric systems for aircraft and improving the system flexibility to include electric resources. Activities from the project provide a foundation for developing electrified aircraft models using Mod-elica [13]. Other programs such as CFM’s Revolutionary Innovation for Sustainable Engines (RISE) [16] focus on improving the efficiency of aircraft engines, which then requires detailed simulation studies to understand how the new technologies change the behavior of the system for different domains.

1.2 Scope and Goals

This section includes a summary of the scopes and limitations of the three systems presented in this document. The systems modeled and studied are complex and difficult to implement in a laboratory setting, as well as some of the systems are constrained by the limitations of ongoing research due to the novelty of the components used. Three systems are studied in this work: **hydroelectric power plants, electric vertical take-off and landing (eVTOL) aircraft, and electrified cryogenically cooled aircraft.**

Each of these systems are under various stages of development and operation, allowing us to explore how to accurately model, validate, and study them. Hydroelectric power plants are well-established systems that have been in operation for decades and the processes for modeling components are standardized within the industry. The scope is focused on validating and improving models for a system that has changed over time due to aging and degradation where many measurements tracking grid events are available. Physical prototypes and measurements are available for some eVTOL systems, but are limited. The scope for eVTOL systems focuses on modeling multi-domain dynamic behavior for an aircraft where the systems are in earlier phases on development than the hydroelectric power systems. The final system discussed in this work is an electric aircraft, which is in the early stages of development. The models in these system rely on previous experiments and research conducted on similar systems to validate the behavior and concept of the individual components used in the aircraft as physical prototypes of any of the components used in the aircraft do not exist yet.

The scope for the thesis is summarized in Figure 1.1. The objectives for modeling and analyzing each system is defined while comparing the models and data available to study


	Objective	Models and data available	
Hydroelectric power plants	Model, simulate, and validate from measurement data obtained during multiple operating conditions.	<ul style="list-style-type: none"> • Represent system by standard and user-defined transfer function models. • Data from various operational states at different points in the plant's life cycle. 	<p style="text-align: center;">More established</p>  <p style="text-align: center;">Novel and conceptual</p>
eVTOL systems	Develop multi-domain models at varying levels of detail to perform a broad range of trade studies.	<ul style="list-style-type: none"> • Create physics-based models for multiple levels of fidelity. • Less operational data available. 	
Electrified fixed-wing aircraft systems	Develop a system with multi-domain models for a novel power delivery system concept.	<ul style="list-style-type: none"> • The physical system does not exist yet, no measurements are available. • Depend on pre-existing research to create multi-domain, physics-based models to integrate with each other. 	

Figure 1.1: Overview of the objectives for the three systems studied.

the system.

1.2.1 Power Plant Modeling and Identification

Power plants models that are a valid representation of the physical system are necessary for planning and operation of electric grids. With grid infrastructure aging and the integration of renewable resources, it is necessary to have accurate and well-defined models of all components to understand and predict grid behavior under dynamic conditions. Advancements in cyber-physical systems have improved our ability to monitor these systems and maintain accurate models.

Mathematical models were developed to represent the behavior of generators and their control systems using models implemented in popular power system analysis tools such as PSS/e and described by IEEE control standards for excitation systems [17]. Custom, user-defined models of plant controllers are also simulated and studied when available. These models are validated using field data collected from various stages of a plant's life-cycle and operation, including fault data and commissioning test data.

This results in two sets of simulation studies run on the systems:

1. Model validation and parameter estimation of hydroelectric generator and control sys-

tem using PMU data from disturbances and faults.

2. Model validation, and if necessary re-identification, of hydroelectric generator and control system using PMU data from commissioning tests.

Model validation and calibration for power system components previously have used PMU data, such as with [18], [19]. In [18], PMU data is collected at the point of connection between the grid and plant during disturbances and is then used to validate and calibrate the model parameters. When there is a large mismatch between the plant model and the PMU data, the parameters of the plant are calibrated using an extended Kalman filter technique. Ref. [19] introduces a tool to validate power plant models without taking them offline using PMU data collected at the terminal bus of the plant. If the model is invalid, the tool recalibrates the parameters. NASPI recommends using PMU data collected from frequency excursion events, voltage excursion events, device trips, remedial action scheme activation, and probing signals to validate the plant model because these events offer a significant excitation in the system that can be useful for validation [6]. It is best to use data collected at a PMU that is electrically close to the desired component; however, this may result in the PMU possibly collecting data on the combined performance of multiple generators and other electrical equipment. The analyst must model the rest of the components that would be included in this PMU data, which will introduce more errors into the model as each component has parameters that must be calibrated as well. By studying commissioning test or maintenance data to validate the plant model, the complexity of the plant can be reduced as the measurements would be collected at the machine terminal and possibly between each component in the generator.

Classical methods for validating and calibrating plant models follow the approach shown in works such as [18]-[20]. These works use a limited set of signals from PMU data to validate models that were collected only at the plant's point of connection to the grid. Both works inject the terminal voltage and angle measurements into the model with the goal of validating the plant's active and reactive power response. All components of the plant (generator, automatic voltage regulator, power system stabilizer, etc.) must be validated together as a result, as no intermediate measurements are available. Conventional power systems analysis software such as PSS/e are configured to support this validation problem, as they contain blocks that load and play back time-series voltage magnitude and angle data.

This approach is used in Chapter 2, where the generator and controller models for a hydroelectric power plant are validated using PMU data recorded during grid disturbances. After evaluating the fitness of the models shown in Chapter 2, we formulate a new approach for plant model validation in Chapter 3 that utilizes measurements recorded between the generator and all plant controllers, allowing for each component to be validated and re-identified if necessary. The methodology in Chapter 3 also uses the plant’s active and reactive power as an input to excite the generator model to validate the voltage magnitude, speed, and field current. By changing the inputs and outputs of the validation problem from what has been used in conventional studies, a better fit is achieved for the models. The inputs and outputs used in the two validation problems in Chapters 2 and 3 are shown in Table 1.1 to highlight the difference between them.

Table 1.1: Inputs and outputs for the validation methods used in Chapters 2 and 3.

	Inputs	Outputs
Conventional validation methods (Chapter 2)	Terminal voltage and angle	Active and reactive power
New validation method (Chapter 3)	Active and reactive power, field voltage	Voltage magnitude, machine field current, machine speed

The validation and calibration methodology proposed herein uses data collected during disturbances and commissioning tests applied to two different hydroelectric plants with the main objectives of the study summarized in Figure 1.2. First, we consider the case with fault data collected from a large hydroelectric plant to validate and calibrate both user-defined and standardized models. The plant owner created user-defined models representative of the system dynamics that were re-implemented for the study. The model parameters were then calibrated using the fault data by validating each component in succession with one another. This is considered “Case 1” in Figure 1.2. Next, a smaller hydroelectric plant is validated and when necessary re-identified using commissioning test data. A validation methodology is proposed in which each component in the plant (e.g. controllers, generator) are individually validated, which is considered “Case 2” in Figure 1.2. When the component is no longer a valid representation of the system, the component is re-identified using RaPIId, a MATLAB toolbox for model parameter estimation [21]. This is the final objective investigated in this work, denoted as “Case 3”. The model may become invalid when the physical component is

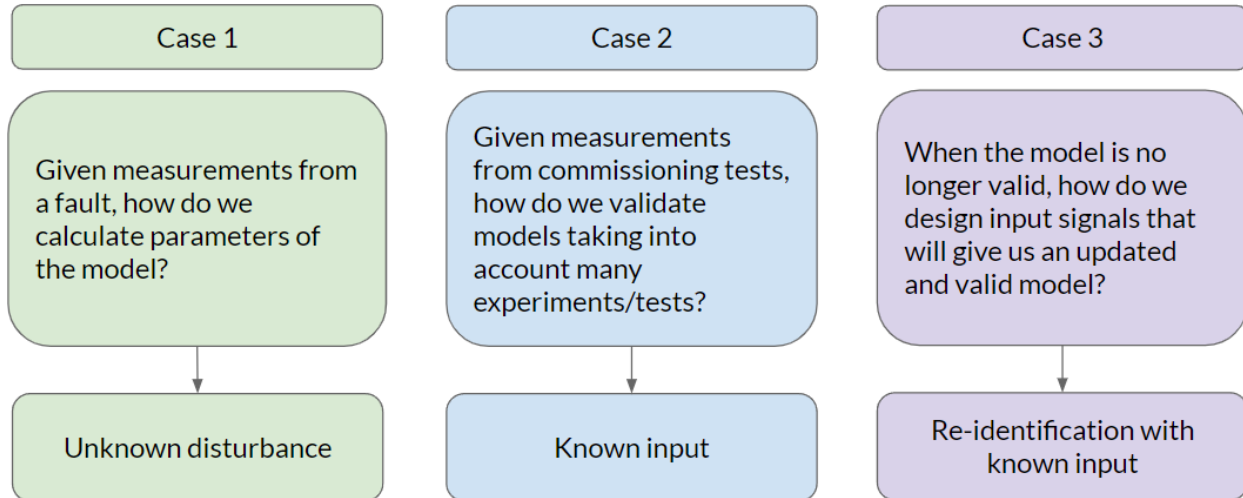


Figure 1.2: Objectives of hydroelectric power system studies.

subject to aging or maintenance, making these tests necessary.

Limitations: This research is limited to using the measurement data received from the power plant operators for the identification and parameter estimation of the power plants described in Chapter 2 and 3. The design, testing, and identification of the experimental power plant model in Chapter 3 is limited to simulation data only given constraints on hardware.

It is assumed that all plant components that are not user-defined have the structure defined by the industry standards in [17]. As a result, all identified models are under constraint of a pre-defined structure.

1.2.2 eVTOL Modeling and Identification

Modeling and simulation focused on a cyber-physical system framework enables multi-domain studies for eVTOL systems, especially with system design and dynamic response for next generation vertical lift systems. Multi-domain models were developed to represent a quadcopter and its drivetrain at various levels of modeling fidelity. This allows us to observe the effects of modeling detail on the system itself, addressing where these models are effective in representing the physical system depending on the analysis desired for the model. The modeling and analysis of the eVTOL system is divided into two parts:

1. Development of a quadcopter model with components representing the electrical, mechanical, and control domains. These models were compiled into an open source Mod-

elica library to aid in the development of quadcopter models, which can then be used for trade studies, animation, and virtual reality applications.

2. Modeling and analysis of an electric drivetrain considering how the modeling details impact the electrical and mechanical dynamic response of the drivetrain. The drivetrain model was developed using Modelica and was studied for various maneuvers produced by a more detailed aerodynamic model in Simulink.

The development of a modeling library consisting of multi-domain, physics-based representations of the eVTOL system components is discussed in Chapter 4 [22]. The models were developed using the object-oriented modeling language, Modelica [23]. Physics-based modeling has previously been used to model eVTOL systems, such as [24] where the quadcopter is modeled using MATLAB. The approach in [24] limits the application and flexibility of the models: the model structure does not allow for integration with other tools, visualization, or re-configuration at varying levels of modeling fidelity. By creating a library of eVTOL component models using Modelica as done in Chapter 4 and [22], the models can be easily interfaced with other software and tools via the Functional Mock-up Interface (FMI) standard [25]. Other multi-rotor aerial vehicle (MAV) systems have been developed using Modelica such as with [26]. It focuses on the modeling of the aerodynamics of the system while assuming an ideal power system; the system described in Chapter 4 expands on this through modeling an eVTOL system with non-ideal behaviors such as losses in the electrical and mechanical systems.

The Modelica drone library provides a foundation for more detailed analysis on multi-domain electric drivetrain modeling. Chapter 5 expands on the modeling framework in Chapter 4, focusing on the development of an electric drivetrain with components modeled at various levels of fidelity. These drivetrain models were interfaced with the RMAC tool in MATLAB [27] via FMI standard so the system could be interfaced with a detailed aerodynamic model for simulation. Various dynamic studies were performed on the drivetrain system to understand how the modeling details of the motor, power electronics, and battery affected system performance. Previous works such as [28],[29] explore the impact motor dynamics have on handling qualities of single-passenger vehicles, but do not further investigate the effects the power system has on the performance. They utilize an idealized motor model, using a simplified DC motor representation to capture the dynamics. This simplified model

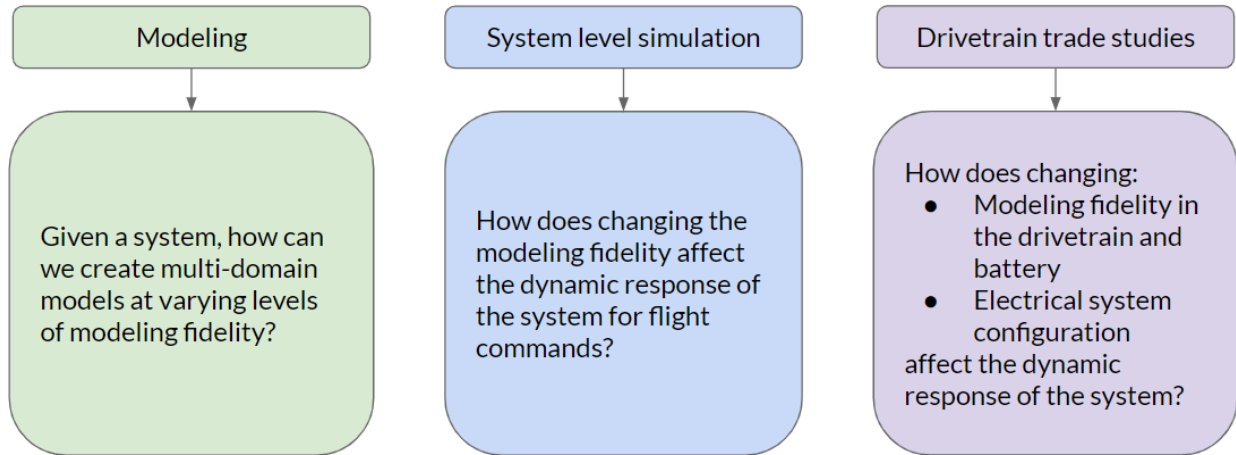


Figure 1.3: Objectives of eVTOL system studies.

also neglects the effects from the electronic speed controller as described in [30].

The tasks carried out on the eVTOL system are summarized in Figure 1.3. In both Chapters 4 and 5, the eVTOL system is modeled using varying levels of fidelity to represent the components in the system. Multiple engineering domains are represented in the models, so the differences in dynamic response are studied. In Chapter 4, a simple, 5 second long flight command is applied to the multi-domain drone model to compare how modeling fidelity affects dynamic response and estimated power consumption. In Chapter 5, the drivetrain is integrated with a detailed aerodynamic model to simulate and analyze the effects of drivetrain modeling fidelity and electrical architecture configuration on the dynamic response of the system. The drivetrain in Chapter 5 is simulated using more detailed maneuvers than those simulated for the drone model in Chapter 4.

Limitations: These studies focus solely on using simulation data due to limitations on the availability of hardware to use for appropriate testing. The thermal models of the motors and batteries were not studied in detail for this work due to the modeling scope. Each of the components (e.g. motors and batteries) were parameterized using data from previous research and information provided from data sheets supplied by the manufacturers.

1.2.3 Electrified Aircraft Modeling

Emission reduction goals have led to investment in developing and investigating fully-electric aircraft technologies. In the electric aircraft developed through the Center for High-Efficiency Electrical Technologies for Aircraft (CHEETA), the power system is cryogenically

cooled using liquid hydrogen and many novel components. Fully-electric aircraft concepts are being developed for deployment by 2050, so simulation studies are necessary to understand system design and concepts in such early phases of the project. Since the technologies that will be eventually used in the CHEETA aircraft are in early stages of development, this work shows how to develop and integrate multi-domain models using previous research and pre-existing solutions as a baseline for development.

Two main tasks from the development of the CHEETA system are presented in this thesis:

1. Modeling and development of the electrical system architecture and components. This consists of defining the specific components used, initial parameters, and the layout within the aircraft.
2. Trade studies conducted on the high temperature superconducting (HTS) transmission lines. This is a novel component in the aircraft's power system, so it was necessary to understand how to mitigate fault behavior for different cryogenic cooling media.

Multiple aircraft power system architectures were taken into consideration in Chapter 6 to determine the best system layout according to reliability and total system weight. Chapter 6 also discusses each of the subsystems in the aircraft in detail, providing preliminary mathematical models for the power generation, power delivery, and load components.

Since the aircraft is subject to liquid hydrogen cooling, the power delivery components have unique loss characteristics. It is necessary to conduct failure analysis studies to understand how these novel components interact with the rest of the system and to improve system reliability. Chapter 7 introduces a multi-domain high temperature superconducting transmission line that will be studied under short circuit fault conditions in a single branch of the electrical system presented in Chapter 6. Multiple cryogenic cooling media for the aircraft are considered to justify the use of liquid hydrogen in this aircraft application. This study also shows the value of integrated system models at early stages of development, as the parameter sizing of the individual components in the power system affect the system's ability to remain thermally stable during and following a fault. This effectively identifies gaps in the concepts and technologies early in system development, improving the system design and encouraging multi-disciplinary teams to consider the broader impact of their subsystem design on the integrated aircraft system.

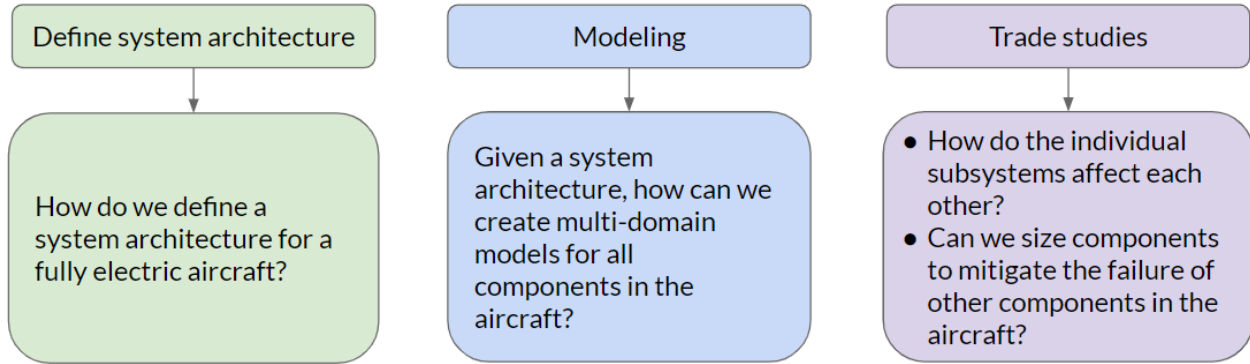


Figure 1.4: Objectives of electrified aircraft studies.

Fully-electric aircraft is currently being investigated through many other programs; however, they do not utilize cryogenic cooling and corresponding components in the system design. The aviation systems in [13],[31] utilize the same first-principles, multi-domain modeling techniques used to develop the CHEETA aircraft concept, but the high temperature superconducting (HTS) components and cryogenic cooling behavior has not been previously modeled or studied in aircraft in detail. Each of the components in the system have been independently modeled, tested, and studied outside of aviation applications.

The objectives of the electric aircraft system studies are shown in Figure 1.4. Since the aircraft system is entirely novel, an electrical system architecture must be defined considering reliability, power requirements, and other subsystem requirements. Preliminary models for the system must be defined as well, using previous research and development as a foundation for the individual subsystems. This is discussed in Chapter 6 and [12]. Once initial subsystem models have been defined, they can be integrated to conduct trade studies and determine component sizing. This is discussed in Chapter 7, where the electrical system is subject to fault tests to aid in the sizing of various subsystems to improve reliability and resiliency.

Limitations: This work depended on developments from other research groups in the CHEETA project. To date, there is no experimental data available. The technology for many of the components modeled does not exist yet, so validation of the specific components are not possible. This happens for the cryogenically cooled components, high-temperature superconducting components, and fuel sources. Instead, these components have been validated against data from similar experiments for specific behaviors. Similar to the eVTOL system, some components are parameterized using scaled values from published research and information provided from data sheets from manufacturers as the systems do not exist in

the capacity needed to definitively parameterize the model.

1.3 Thesis Overview and Summary of Contributions

The remainder of this document contains three main sections covering the development and analysis of three different cyber-physical systems: (1) **hydroelectric power plants**, (2) **eVTOL systems**, and (3) **cryogenically cooled electrified aircraft**.

1.3.1 Part 1: Hydroelectric Power Plant Modeling and Identification

1.3.1.1 Chapter 2 Overview

Chapter 2 focuses on model development and parameter estimation for the Itaipù hydroelectric power plant and its control system using fault data. Data recorded from two different fault events were used to estimate the parameters of both user-defined and IEEE standard models [17]. The user-defined models were provided by the plant’s engineers. By studying the parameter estimation of both types of models, we gain insight on the value of model maintenance. The shortcomings of this parameter validation methodology are also discussed in this chapter.

1.3.1.2 Chapter 2 Contributions

The work presented in Chapter 2 contributes the following:

- The parameter estimation and calibration of a hydroelectric power plant using field measurements collected during grid disturbances. This procedure is done using both standard and user-defined models.
- Two calibration methods are introduced and compared to determine the most effective method for model calibration.
 - Both a classical gradient optimization method and a particle swarm optimization method are utilized in model calibration.
 - This method uses model exchange, allowing us to use functionalities of different software and tools to simulate and analyze the model.

First, the user-defined and standard models were implemented using Modelica into Dymola, a Modelica development environment. Both sets of models were validated against

other power systems modeling and analysis software to ensure they produced the same result, ensuring that these models were accurately implemented using Modelica. Both sets of models were simulated using the field data as inputs to compare and calibrate the model's dynamic response with the physical system. Two different calibration methods are studied in this chapter to determine the most effective process.

Since these models are implemented using the Modelica programming language, the Functional Mock-Up Interface (FMI) standard can be used to communicate models between software. This enables us to use the same model in multiple software programs to utilize each program's specific functionalities to simulate and analyze the models. In Chapter 2, the models were developed in Dymola and exported to Simulink via FMI to use MATLAB's optimization routines to estimate the model's parameters. This approach to modeling shows how the benefits of having flexible models, as we only have to maintain one model that can be used in a variety of tools.

1.3.1.3 Chapter 3 Overview

Chapter 3 introduces a validation methodology for a hydroelectric power plant using commissioning test data. Prior to putting the plant onto the bulk electric system, the equipment was subject to various tests to ensure all of the functionalities worked properly. The methodology is applied to validate the machine and controller models for a hydroelectric power plant. A methodology for re-identifying the component models when they are no longer an accurate representation of the power system is also included in this chapter.

1.3.1.4 Chapter 3 Contributions

This work expands upon the parameter estimation and model calibration for hydroelectric power plants discussed in Chapter 2. The work presented in Chapter 3 explores using field data to validate the individual components in the plant, and contributes the following:

- A validation methodology for a hydroelectric power plant's control system and generator using field measurement data.
- A methodology to update plant models when they are no longer an accurate representation of the power system.

In this chapter, only standardized models are used in the validation process; these models were already validated as part of the OpenIPSL library [32]. Since measurements

were available for the signals between components in the plant, we developed a method to validate components individually and if necessary, re-identify them when the component was invalid. Similar to the process in Chapter 2, these models were developed using Modelica and then exported to Simulink using the FMI Standard to complete the validation process.

1.3.2 Part 2: eVTOL Systems

1.3.2.1 Chapter 4 Overview

Chapter 4 covers the development of the multi-domain models for a quadcopter eVTOL aircraft. This chapter includes the modeling development of all of the eVTOL system components, studying the electrical, mechanical, and control domains. The quadcopter component models are configured to study the system at various levels of modeling fidelity, in which the power consumption of the system for different amounts of modeling detail are compared. This chapter also introduces non-ideal behavior seen in the eVTOL system that can affect its dynamic response, which is continued in further depth in Chapter 5.

1.3.2.2 Chapter 4 Contributions

This chapter introduces a library of flexible, replaceable multi-domain models for a quadcopter. These models are developed as a result of previous development of single domain, physics-based models for quadcopters. The main contributions of this chapter are:

- Proposal of an open-source Modelica library consisting of multi-domain components to model a quadcopter at varying levels of modeling fidelity.
- Discuss the details and mathematical models for each component in the quadcopter; show the simulation and animation of these models.
- Perform studies to highlight importance and impact of modeling the quadcopter power system with adequate modeling detail.
- Illustrate the importance of multi-domain modeling for closed-loop system performance.

First, physics-based, multi-domain models were developed to represent all sub-systems in the quadcopter. These models were all developed in Dymola using the Modelica language. In this chapter, we focus primarily modeling the mechanical and electrical domains as well as

the quadcopter controls. The quadcopter models are then simulated in various configurations to study the effects of modeling fidelity of the closed-loop response.

1.3.2.3 Chapter 5 Overview

Chapter 5 shows the results of a study conducted on an eVTOL drivetrain. The eVTOL drivetrain is studied with varying levels of modeling detail for the battery and the motor and is interfaced with an open-source MATLAB tool that provides the aerodynamics of the vehicle. This study shows the value of the modeling methods used to develop the drivetrain, as it can easily be interfaced to work with other researchers' work. The drivetrain is subject to multiple maneuvers to provide an understanding on how the complexity of the drivetrain and power source systems affect the system performance.

1.3.2.4 Chapter 5 Contributions

This study expands on the modeling and analysis of the quadcopter models introduced in Chapter 4; the model is coupled to a MATLAB toolbox to understand how detailed aerodynamic behavior affects the quadcopter. The objectives of the study presented in this chapter are:

- Application of multi-engineering domain (mechanical-electrical) models for an electric drivetrain with varying degrees of complexity, including detailed battery, machine, and power electronic converter models.
- Modeling drivetrain response for power source models, including an ideal power source, fully charged battery, and battery at 30% charge.
- Comparing drivetrain response for different machine configurations under various speed commands, namely quadcopters with fully-distributed batteries (where each motor has a dedicated power source) and a fully-centralized battery (where all rotors share a single power source).

Chapter 4 focuses on studying the entire quadcopter, while Chapter 5 focuses on modeling the drivetrain and power system in further detail. The drivetrain is modeled at varying levels of fidelity using the Dassault Electrified Powertrains Library (EPTL) [33] and coupled to the Rensselaer Multicopter Analysis Code (RMAC) [27] in Simulink using FMI. The

system is studied for multiple drivetrain and power system configurations to compare the system's dynamic response under various speed commands.

1.3.3 Part 3: Electrified Aircraft

1.3.3.1 Chapter 6 Overview

Chapter 6 focuses on the design and development of the CHEETA electric aircraft system. The development of the power system architecture for the aircraft is discussed as well as the design of the liquid hydrogen cooling loops. This chapter also includes the selection of fuel cell chemistry, developing models for the cryogenically cooled transmission lines, and determining parameters for all of the components according to system parameters and operating conditions.

1.3.3.2 Chapter 6 Contributions

The main contributions of this chapter are as follows:

- The multi-domain modeling and development of the components in the CHEETA power system. The thermal and electrical domains are modeled; this allows for trade-off studies for different operating power capacities and cooling mediums.
- The thermal and electrical domains are interfaced at the equation-level, allowing to compute the thermal performance under different electrical configurations and cooling media.

The aircraft configuration and component models were identified through collaboration with the other research groups participating in the CHEETA program. With their insight, we developed and parameterized multi-domain models according to their specifications. These models were developed using Modelica, allowing us to create models that couple the thermal, electrical, mechanical, and control behaviors of the models to then complete system level studies.

1.3.3.3 Chapter 7 Overview

In Chapter 7, we study one of the high temperature superconducting (HTS) transmission lines under fault conditions in the CHEETA system. The models for the HTS lines are discussed, as well as the models for all of the components used to represent the CHEETA

system. Three different cooling mediums are compared for the scenario where the system is subject to a fault, enabling the comparison between each medium's ability to keep the system cryogenically cooled following system failure. The fuel cell resistance is manipulated to determine how the fuel cell can be utilized to improve system resiliency during faults.

1.3.3.4 Chapter 7 Contributions

This chapter presents reusable, open-source models of HTS transmission lines, which presents the opportunity for reuse and reproduction for future research. The main contributions of this work are:

- A multi-domain (thermo-electrical) model for an HTS transmission line where the thermal behaviors have been verified against experimental stability studies.
- Fault analysis for an electrified aircraft power system architecture that uses the proposed HTS line.

This line is studies using various cryogenic cooling media to justify the use of liquid hydrogen cooling in aircraft applications. These trade-off studies show how the sizing of other components in the system can be advantageous to the system design.

CHAPTER 2

PARAMETER ESTIMATION AND CALIBRATION OF STANDARD AND USER-DEFINED MODELS WITH APPLICATION TO THE ITAIPÚ HYDROELECTRIC PLANT

2.1 Introduction

2.1.1 Motivation

Advancements in renewable power generation and control transform the grid to reduce emissions, improve resiliency, and limit the negative impact on the environment. As these new technologies are incorporated into the grid, simulation-based studies are helpful to determine the benefit of proposed projects and potential impact of integrating a resource with the existing bulk electric grid. Highly accurate dynamic power system models of the existing system are necessary as a result, as an accurate representation of the system is crucial in understanding projects in which testing using a physical prototype is not possible. Many power plants and their control systems utilize user-defined models in their simulations, creating the burden of maintaining multiple custom models for system operators. It is necessary to determine the accuracy of these models and investigate if these models can be replaced by a generic, standardized model. It is also necessary to determine the accuracy of the model parameters, as low confidence in the parameters of these models leads to more conservative and possible erroneous assessments by the system operator of their responses to an event. There is also inherent uncertainty due to changes in the system parameters due to wear and aging of system components. Limited opportunities exist to test the physical power system because the existing system cannot be compromised for experimentation; building a new system for testing is not be a viable option, as it would be too costly [34].

Real-world measurement data from phasor measurement units (PMU) can be used to improve power system models; faults and disturbances provide valuable insight in tracking the changes in system parameters as power plants age since testing opportunities are lim-

Portions of this chapter previously appeared as: M. Podlaski, L. Vanfretti, J. Pesente and P. H. Galassi, “Automated parameter identification and calibration for the Itaipú power generation system using Modelica, FMI, and RaPID,” in *7th Work. Modeling and Simulation Cyber-Physical Energy Sys. (MSCPES)*, Apr. 2019, pp. 1–6, doi: 10.1109/MSCPES.2019.8738793. Reprinted with permission of IEEE. © 2019 IEEE.

Portions of this chapter previously appeared as: M. Podlaski, L. Vanfretti, M. de Castro Fernandes, and J. Pesente, “Parameter estimation of user-defined control system models for Itaipú power plant using Modelica and OpenIPSL,” in *Proc. American Modelica Conf.*, Sep. 2020, pp. 139–148, doi: 10.3384/ECP20169139.

ited. Faults and disturbances evoke the faster dynamics of a plant, providing a situation where the model parameters corresponding to fast time constants and sub-transient behavior could be estimated. By implementing these models with Modelica and interfacing with other software tools using FMI, the parameters can be calibrated for various power system components. Using a set of measurements obtained from PMUs attached at the terminal bus of Itaipú Binacional, the world's second-largest renewable hydro-electric dam, the parameters of different components of the power generation can be calibrated. This particular generator studied in this work produces 700 megawatts [35], an amount of power capable of supplying a city of 1.5 million people.

2.1.2 Related Works

Previous studies for power system model calibration using PMU measurements focus on using different solver methods and standardized models. PMU measurements have been used for dynamic model validation and calibration using various methods such as extended Kalman filter techniques [18]. Existing conventional and renewable plants are calibrated in [36] using PMU data to help determine the cause of faults within the system. The dynamic parameter identification uses a combination of particle swarm optimization (PSO) and sensitivity analysis for a system consisting of a wind turbine, its reactive power support, and step up and step down transformers. The parameter identification in [36] produces good results for an undamped oscillation under weak grid conditions. The calibrated models helped operators find problems with the AVR of the plant for the fault studied, allowing for improved operations under weak grid conditions in the future. This is especially important for a plant like Itaipú, which provides such a large amount of power.

The estimation problem used in this study uses the same approach as in [18]-[20]. Since there few signals quantities measured by the PMUs, all of the plant components (machine, controls) must be validated together. All of these studies use the same inputs and outputs to formulate the estimation problem for their respective plants. Voltage magnitude and angle measured at the terminal point of the system is used as an input, while the active and reactive power generated by the plant is used as an output. This serves as the basis for the selection of inputs and outputs used to validate the Itaipú system.

Modelica and the FMI standard have also been used extensively in power system model calibration. In [37], a multi-domain model for a wind turbine is calibrated using synthetic

and real-life measurement data. The model calibration follows a sequential approach in calibrating system components similar to the one outlined in this chapter. The identification process outlined in [37] utilizes the optimization features in the Modelica Design Library in Dymola rather than exporting the models as FMUs to utilize optimization routines in other software, such as MATLAB as shown in this chapter. The OpenIPSL library [32] was used to develop the Itaipù system model. OpenIPSL is an open-source Modelica library for power systems models, where the models have been validated against other power system software results. This approach to modeling enables integration between software tools to simulate and analyze results.

2.1.3 Chapter Contribution

This chapter contributes the following:

- Parameter estimation and calibration of a hydroelectric power plant and control system using PMU data from fault disturbances. The system is represented using both standardized models and user-defined models.
- Two calibration methods are introduced and compared to determine the most effective method for model calibration. Both a classical gradient optimization method and a particle swarm optimization method is utilized in model calibration.

2.1.4 Chapter Organization

This chapter focuses on the validation and estimation of parameters of both user-defined and standard models representing the Itaipù system. Section 2 introduces both the user-defined and standard generator and control models used to represent the plant. The parameter estimation methodology is discussed in Section 3, which shows how each plant component will be identified and the optimization algorithm used for updating plant parameters. The parameter estimation methodology is then applied to the system in Section 4, where both sets of model parameters are estimated using PMU data collected from faults. This allows us to compare the simulated model response to the physical system and update the parameters accordingly.

2.2 Proposed Power System Models

The Itaipú system model was created using the Modelica language with the Dymola software. The specific component models are developed from the OpenIPSL Library [32], which is an open-source library of power system component models written in the Modelica language. The models in OpenIPSL have been validated against other power systems tools like PSS/E, enabling the development of power systems models to conduct dynamic studies using Modelica. The engineers at Itaipú have also provided the models for their user-defined representation of the plant from an industry-specific power systems analysis software commonly used in Brazil. As a result, these models were implemented into Dymola using functionalities from the Modelica Standard Library (MSL) [38] and validated against the original software's simulation results.

The power system model was developed using the Modelica language and Dassault's Dymola software as shown in Figure 2.1. The model in Dymola is compared to the one-line diagram of the system, where the plant models are denoted by the magenta box, the interface to inject data is denoted by the green box, and the measurement data used to excite the system is denoted by the orange box. The components are labeled as follows:

- (A) Tables containing the PMU data for the active and reactive power measurements.
- (B) System data contains frequency and base power for the system. The `machineData` block contains parameter data stored in a record, which is propagated to all system components. A record exists with the results of every parameter calibration test run.
- (C) Turbine governor model (Itaipú user-defined and IEEE HYG0V).
- (D) GENSAE generator model.
- (E) AVR model (Itaipú user-defined and IEEE SEXS).
- (F) PSS model (Itaipú user-defined and IEEE PSS2A).
- (G) Active and reactive power outputs to be used in the FMU.
- (H) Controllable voltage source component.
- (I) Tables containing real and imaginary voltage components from the PMU measurements.

The Itaipú generators are salient pole generators with exponential saturation as derived in [39], so a standard model is used for both the user-defined and standard model controller cases. This is the GENSAE model used in PSS/e and other popular power system analysis

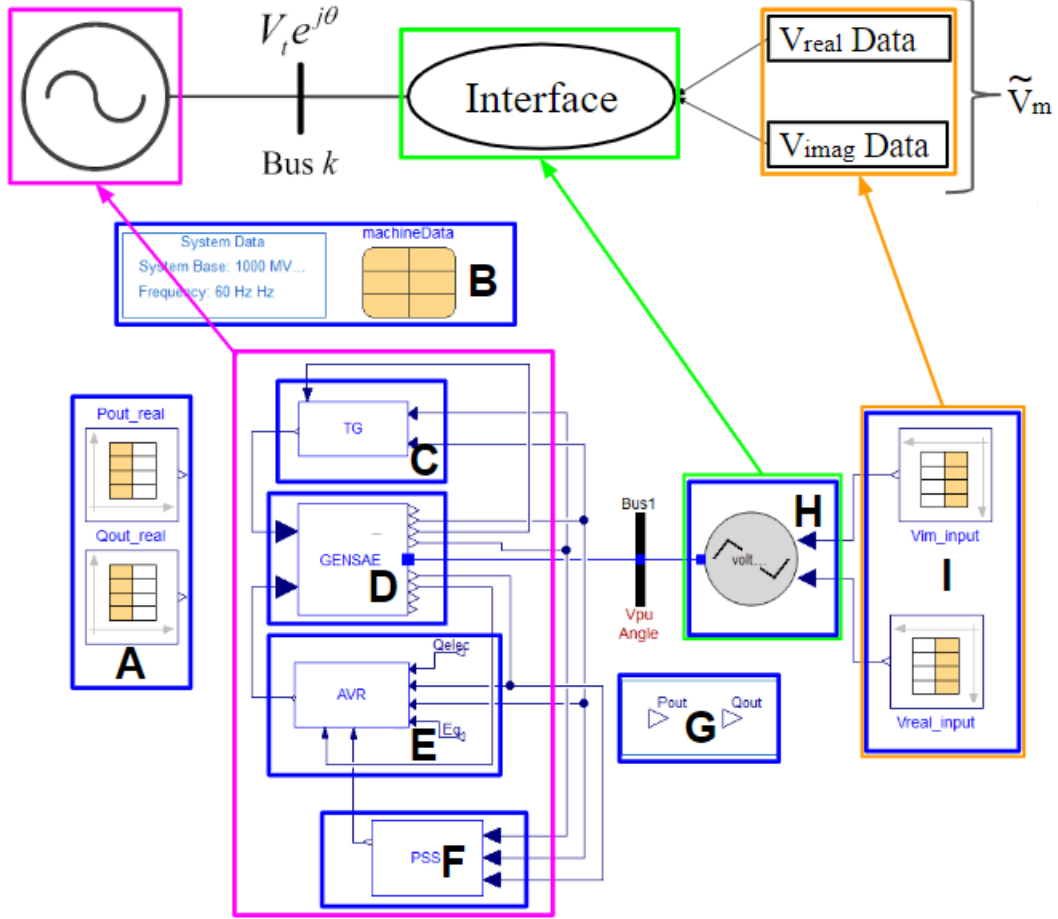


Figure 2.1: Modelica model of the generator, TG, AVR, and PSS in Dymola, which is compared to an SMIB one line diagram.

tools [39], [40]. The turbine-governor (TG), automatic voltage regulator (AVR), and power system stabilizer (PSS) models are user-defined models that were originally implemented in ANATEM, the simulation software Itaipú uses for their plant. When considering the case of standard models, the turbine-governor is represented by the IEEE HYG0V model, the AVR is represented as IEEE SEXS, and the PSS is represented as the IEEE PSS2A model. The voltage measurements from the PMU are injected into the system at the terminal bus to calibrate the generator, TG, AVR, and PSS. The definitions of the parameters and the control diagrams for each of the IEEE components representing the system are listed in Appendix A.

Figure 2.2 shows the relationships between the components shown in Modelica model in Figure 2.1. The generator outputs an active (P_{elec}) and reactive (Q) power, as well as speed derivation ($\Delta\omega$), mechanical power (P_{mech}). The PSS uses P_{elec} as an input to obtain an additional tracking signal (V_{PSS}) for the AVR's input. The AVR is initialized by the

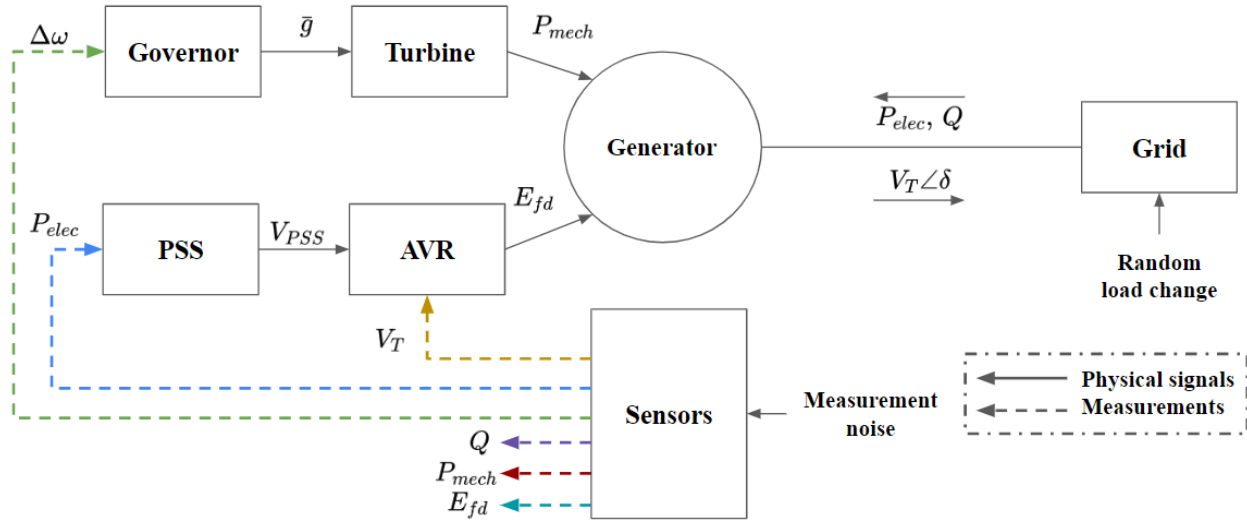


Figure 2.2: Block diagram showing the relationship between each system component, their inputs, and their outputs.

generator's initial exciter field voltage (E_{fd0}) and controlled by the terminal machine voltage (V_t) to determine what adjustments need to be made to E_{fd} . The governor, which is a speed controller for the generation unit, utilizes $\Delta\omega$ and the reference mechanical power (P_{mech0}) to control the turbine behavior in terms of speed and mechanical power. The turbine will then provide a mechanical power signal P_{mech} to the generator. These components are also mapped to a one line diagram of an SMIB system to provide understanding of where these components would be in a power system.

2.2.1 Re-Implementation of Models from Other Tools

Two different sets of models are considered in the study, and it is necessary to ensure that the models are valid when implemented using Modelica. The IEEE standard models are validated as part of OpenIPSL. These models have been software-to-software validated against PSSE to ensure the model was re-implemented correctly, as shown in [32].

The engineers at Itaipu used industry-specific software to implement their models, which required them to be re-implemented in Dymola to integrate with the rest of the power system models. The software CduEdit [41], which is pictured in Figure 2.3, is used to create control system diagrams for components. It is proprietary software used in Brazil in the utility sector for engineers to maintain a database of user-defined controller models for power systems [41]. It is a graphical interfaces used to create and edit user defined controls (CDUs). The CDUs can be simulated in ANATEM [42], which is an industry-specific tool

used for electromechanical transient analysis. These softwares also interact with ANAREDE [43], which is a program that assists in the analysis of power system networks, such as power flow, network equivalents, and contingency analysis. These tools are limited in analysis capability nor do they support the FMI standard to share the models between softwares, so the CDUs of the Itaipù plant components must be re-implemented in Dymola for parameter calibration.

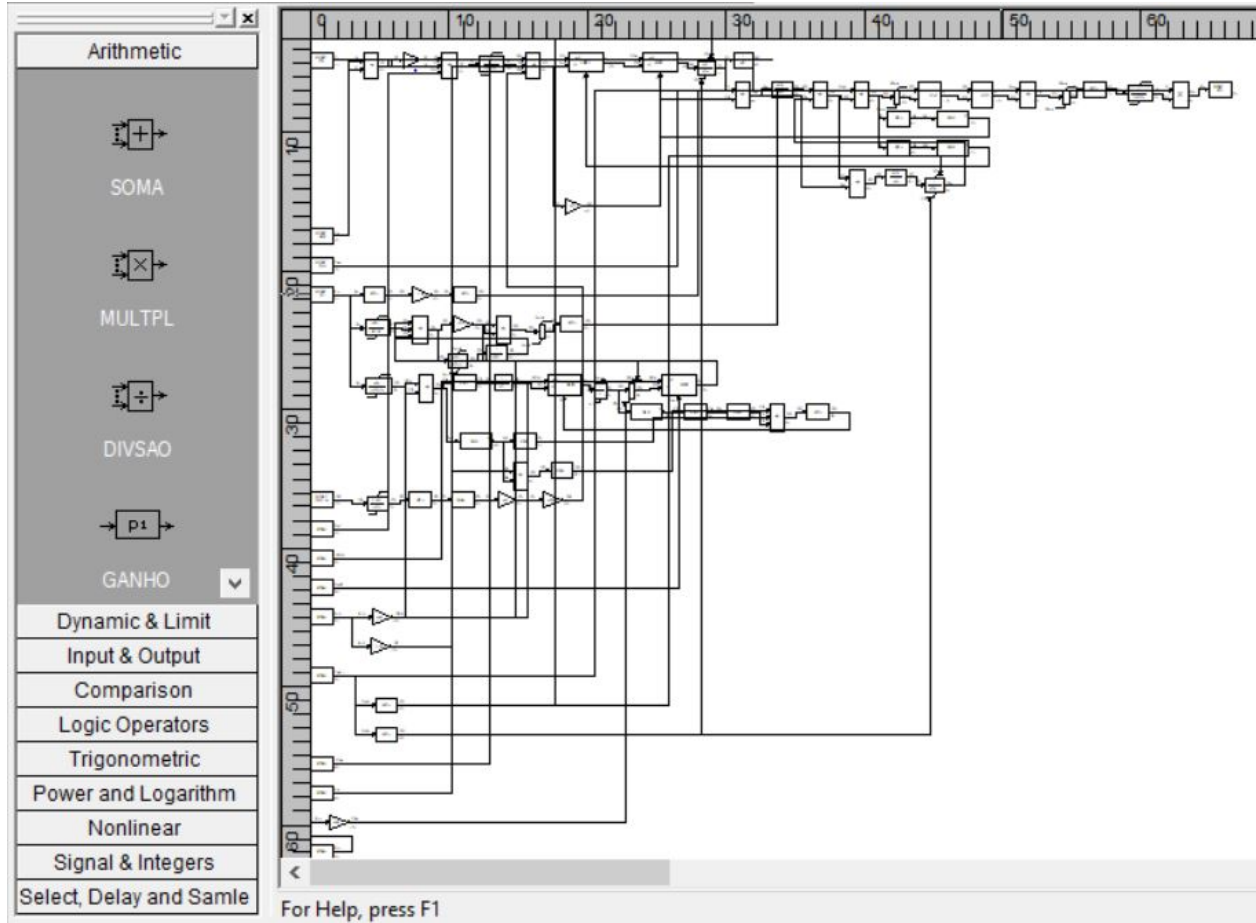


Figure 2.3: Itaipù user-defined AVR model in CduEdit software.

The verification will be carried out by simulating the same system in both software packages (ANATEM and Dymola) and comparing the obtained results, with the goal of showing that the models are equivalent in both software programs. This is necessary because it is challenging to prove to the users of domain-specific tools that they can obtain the same results as those tools in Modelica as long as the models are correctly re-implemented. This brings confidence to the models in Modelica that the results are going to be just as good as, if not better than, the domain-specific tool.

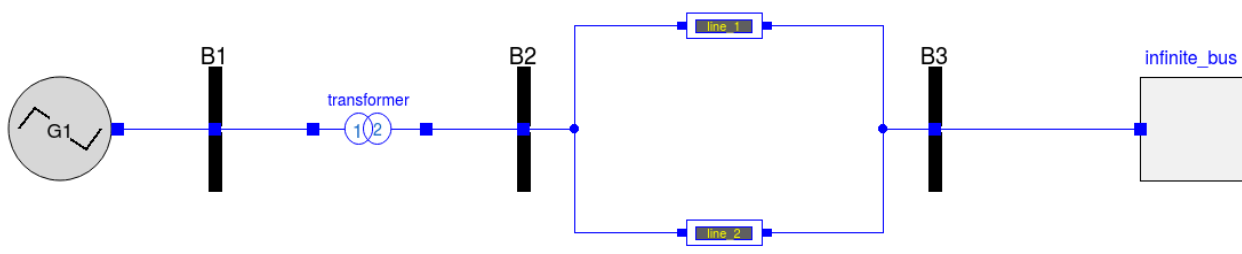


Figure 2.4: SMIB system model implemented in Dymola. An equivalent system is also modeled in Anatem.

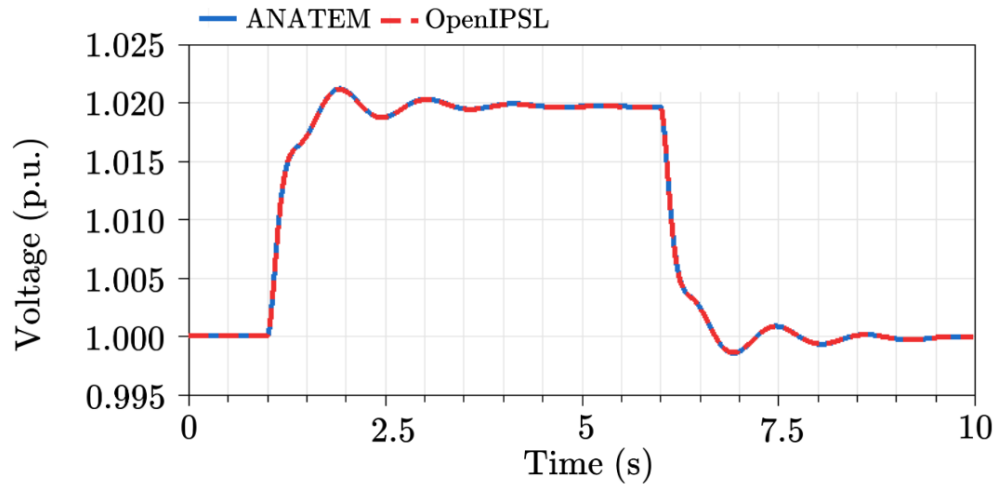


Figure 2.5: OpenIPSL vs Anatem voltages at bus B1 for software validation.

The system chosen to be implemented is the single-machine infinite-bus (SMIB) system, due to its simplicity. The SMIB system implemented using OpenIPSL is shown in the Figure 2.4. It is important to mention that some parameter conversion need to be carried out. For example, the saturation curves need to be converted from an exponential representation to a polynomial one. In addition, exciter and power system stabilizers were adapted. The per unit parameters from the circuit were converted to ANAREDE in the Anatem software for the power-flow calculation, resulting in the adequate initial guess values to the system.

The event tested is a step change in the terminal voltage reference for the exciter system. The reference voltage increases by 0.02 p.u. at time $t=1s$. At 6 seconds, the voltage reference decreases as a step back to the original value. The resultant voltage at bus B1 given by both software packages is displayed in Figure 2.5, where the curves from ANATEM and OpenIPSL overlap throughout the entire simulation. The rotor angle behavior given by both software packages is shown in Figure 2.6, where the two models match perfectly.

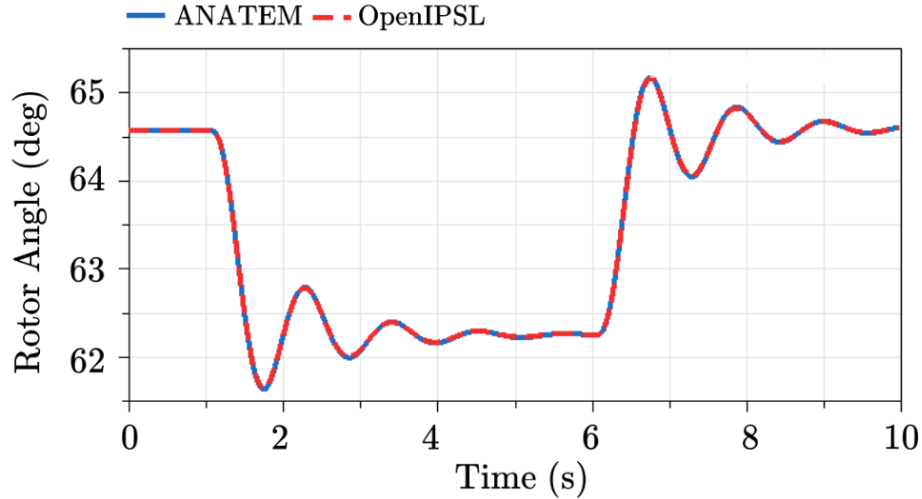


Figure 2.6: OpenIPSL vs Anatem rotor angle at bus B1 for software validation.

2.2.2 Using PMU Data with Modelica

The voltage data obtained from the PMUs is injected into the system at the site of the infinite bus, shown in Box I in Figure 2.1. Inside of the `combiTimeTable` blocks in Block I, the real and imaginary components of the voltage are listed in tables over the period of the system event. Those voltage signals are then converted to flow variables (real and imaginary currents) to be injected at the machine’s point of interconnection. Those flow variables then control the generator power output according to the voltage input.

Block A in Figure 2.1 contains the tables of data for the active and reactive power. The purpose for including these measurements in the model is to observe the fit of the simulation to the measurements in the plotting window.

2.3 Parameter Estimation Process

2.3.1 Sequential Component Calibration

All models were optimized using RaPIId [21], which is a MATLAB toolbox used for parameter validation, calibration, and optimization that uses models exported using FMI standard for Model Exchange, called Functional Mock-up Units (FMUs). RaPIId uses both Simulink and MATLAB functions from the FMI Toolbox for MATLAB [44] to simulate and perform the computations with the model. The FMUs need to be loaded and configured in a Simulink block from the FMI Toolbox library via model exchange. A MATLAB script is used to specify measurements, define an optimization problem, and to provide an initial

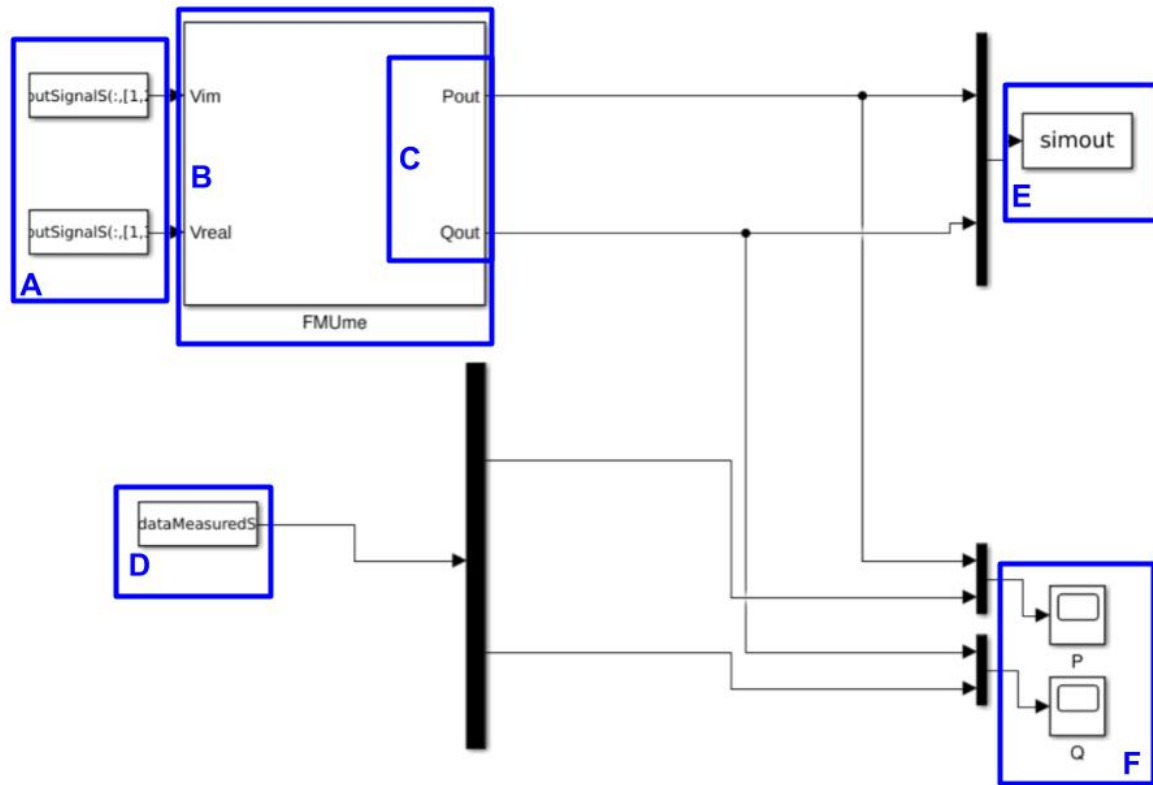


Figure 2.7: Itaipú system in Simulink using the FMI Toolbox for use in RaPIId.

guess of the desired parameters. The complete system used for all experiments discussed in this chapter is configured in Simulink is shown in Figure 2.7, labeled as follows:

- (A) Input voltage measurements split into a real and imaginary component. Measurements are from PMUs.
- (B) FMU containing the Modelica model.
- (C) Output of the FMU (created from system in Figure 2.1); simulated P_{elec} and Q .
- (D) Measurements of P_{elec} and Q for graphical comparison, used in software for validation.
- (E) Output P_{elec} and Q results to the work space. This is updated every iteration.
- (F) Scopes to monitor the simulated response against the measurements during each simulation run.

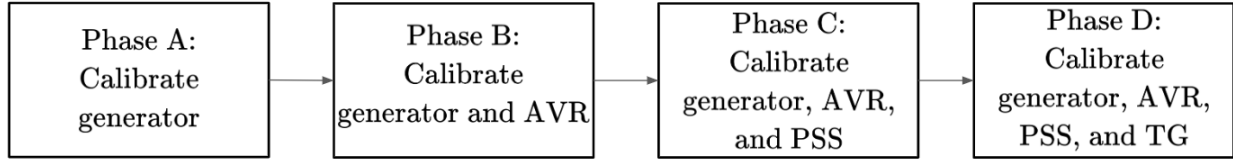


Figure 2.8: Process for calibrating components in the Itaipú system.

The parameter estimation relies on both `fmincon` and particle swarm optimization (PSO) solvers to determine the parameters of the IEEE standard and user-defined models. First, the PSO solver is used to find an estimate of the parameter vector near the global minimum for each component in the system. After the PSO solver finds an approximate solution for all of the parameters in the model, `fmincon` is used to optimize the local solution by tuning each parameter sequentially. In other words, all of the parameters for a specific component are first estimated using the PSO solver. The result from the PSO run is then used as an initial guess to calibrate the individual parameters sequentially when using the `fmincon` solver.

The steps to calibrate the individual components in the plant is shown in Figure 2.8. The components included in the plant model were verified by the plant’s engineers. Since there were limited signals available from the field data that were only collected at the terminal connection of the plant, it was necessary to validate and calibrate the components together. First the generator parameters are calibrated without any of the control system included in the model. All of these parameters are calibrated simultaneously using PSO. The results from the PSO are then used as the initial guess to calibrate the parameters sequentially. After all of the parameters in the generator are calibrated, the controllers are added to the model and their parameters are updated according to Figure 2.8.

The model shown in Figure 2.1 was exported from Dymola as a Functional Mock-up Unit (FMU) [25] using model exchange to simulate in Simulink. The models’ parameters were calibrated using MATLAB’s optimization solver, `fmincon` [45] and a particle swarm optimization (PSO) solver. The `fmincon` optimization runs were executed for up to 5000 iterations using an error tolerance of 1×10^{-5} . The PSO optimization runs were executed for up to 200 iterations with an error tolerance of 1×10^{-3} . The parameter values were changed each iteration with the goal of providing the best optimization fit to the reference measurements using RaPIId [21], a MATLAB toolbox for rapid parameter identification.

The sequential parameter estimation process used to calibrate the plant follows the

method shown in Algorithm 1. All parameters in a component are estimated together first using the heuristic (PSO) solver, and the result is then used as an initial guess to calibrate each parameter individually. For example, the generator has 12 parameters, so all parameters will be calibrated during the PSO run. The first generator parameter will then be calibrated using `fmincon` with the PSO result as an initial guess. Next, the first and second generator parameters would be calibrated using the previous `fmincon` result as an initial guess for the first parameter and the PSO result as an initial guess for the second parameter. This process is repeated until all 12 parameters are calibrated. For the PSO optimization stage, the initial guess for the user-defined model parameters were provided by Itaipu's engineers using their current model parameters. In the IEEE standard models, the model is initially parameterized with the suggested operating values from the standard in [17] for the PSO stage.

Algorithm 1 Sequential parameter calibration using heuristic solver for initial guess for whole component, then gradient solver to tune individual parameters.

Use PSO algorithm:

θ = list of all parameters in all components to be calibrated

θ_{min} = list of lower limit of all parameters in all components that will be calibrated

θ_{max} = list of upper limit of all parameters in all components that will be calibrated

$\theta = \min f(x)$ such that $\theta_{min} \leq \theta \leq \theta_{max}$

Use fmincon solver:

p = empty vector

p_{min} = empty vector

p_{max} = empty vector

For parameter in θ :

$p = p.append(\theta)$ % Add a new parameter, use results of PSO as initial guess θ

$p_{min} = p_{min}.append(\theta_{min})$

$p_{max} = p_{max}.append(\theta_{max})$

$\min f(x)$ such that $p_{min} \leq p \leq p_{max}$

This method follows the sequence defined in Figure 2.8. After calibrating the generator parameters, the final solution of the generator `fmincon` optimization is used as the initial guess of generator parameters for calibrating the AVR. Similarly to the calibration of the generator model, Algorithm 1 is used to calibrate the parameters of the generator and AVR model. A PSO routine is run for all of the parameters in the generator and AVR, then its solution is used as the initial guess for the calibration of the individual AVR parameters with the `fmincon` solver. This process is then repeated again for the PSS and TG, adding them

into the system sequentially.

2.3.2 Parameter Estimation Methodology

To estimate the parameters of the system components, we must define the model's inputs, outputs, and parameters. We had measurements for the voltage (V), voltage angle (θ_V), active power (P_{elec}), and reactive power (Q) recorded at the connection between the bulk electric grid and the terminal bus of the plant. The voltage and voltage angle measurements were transformed into real and imaginary voltage components, V_r and V_i , determined as follows:

$$V_r = V \cos \theta_V \quad (2.1)$$

$$V_i = V \sin \theta_V \quad (2.2)$$

The Itaipú system is simulated with inputs $u = [V_r, V_i]$ and outputs $y = [P_{elec}, Q]$. All parameters in the system that we wish to estimate are defined in a vector θ . The system is simulated in Simulink such that:

$$y_{sim}(t) = G(s, \theta)u(t) \quad (2.3)$$

where $G(s, \theta)$ is the Itaipú plant model for a parameter set θ , $u(t)$ is the input voltage data, and $y_{sim}(t)$ is the simulation result of the active and reactive power of the plant model.

This data is then compared to the measurement data collected from the physical system, $y_{meas}(t)$. The absolute difference between the simulation and measurements is calculated at each time step, as follows:

$$\epsilon(t) = y_{meas}(t) - y_{sim}(t) = \begin{bmatrix} P_{elec}^{simulated}(t) - P_{elec}^{reference}(t) \\ Q^{simulated}(t) - Q^{reference}(t) \end{bmatrix}^T \quad (2.4)$$

where $P_{elec}^{simulated}(t)$ is the output from the simulation of the FMU for the active power, $P_{elec}^{reference}(t)$ is the active power measurement from the PMU data; $Q(t)$ is the reactive power and follows the same process.

The objective function is then determined by computing the Euclidean norm from the mismatch $\epsilon(t)$ between the simulation and field measurements for active and reactive

power produced by the plant. The sum of mismatches is calculated from the norms of the measurement/simulation pair at each time step, returning the fitness of the simulated model to the measurements:

$$f(x) = \sum_{i=1}^m \sum_{t=1}^n \epsilon_i(t) \cdot \epsilon_i(t) \quad (2.5)$$

For the system presented here, $m = 2$ as two outputs are being studied (P_{elec} and Q) with $n = 950$ as the data recorded at a rate of 200 Hz for a 5 second period.

The minimization criterion (i.e. objective function) $f(x)$ was set as the sum of the Euclidean distances between the simulated model's response and the reference PMU data at each time step. The objective function defined in Equation 2.6 is constrained by the minimum and maximum limits for all parameters, θ_{min} and θ_{max} .

$$\bar{\theta} = \min f(x) \quad \text{s.t.} \quad \{\theta_{min} \leq x \leq \theta_{max}\}. \quad (2.6)$$

The tool then returns a vector of the optimal parameters after reaching the error tolerance or maximum number of iterations. This calibration process is repeated for all parameters in all components in the system with the goal of iteratively calibrating each block according to Figure 2.8. The parameters of each block are listed in Appendix A.

2.4 Fault Data Case Study and Results

Data from two different fault events occurring at or near a generator at Itaipú were used for this model validation and calibration process. The faults triggered the PMUs to record the generator's terminal voltage, angle, active power, and reactive power. The models with calibrated parameters were simulated in Dymola with a variable time step solver, `Dassl` with a tolerance of 10^{-3} . The model is calibrated using both user-defined components and IEEE generic components for the AVR, PSS, and TG models.

2.4.1 Results - Case 1: September 22, 2015

The system in Figure 2.1 is configured to be compared to PMU data corresponding to a fault occurring on September 22, 2015. The system components are calibrated using the process described in the previous section. Figure 2.9 shows the results of the AVR and PSS calibration for this data set using both the user-defined and IEEE generic models. This corresponds to Phases C and D for the user-defined models and Phase D for the generic

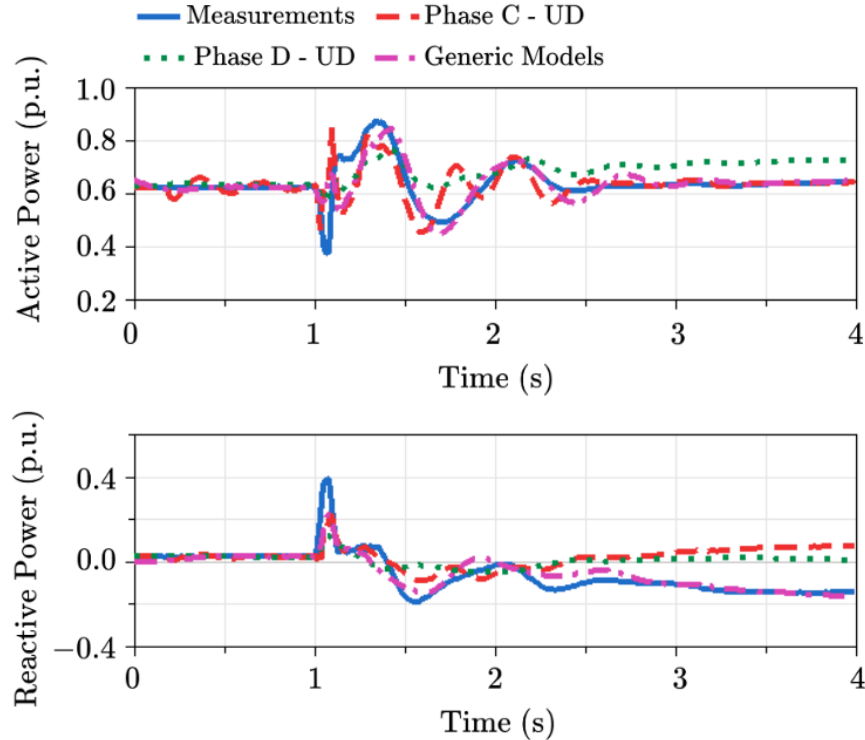


Figure 2.9: Calibration results for the user-defined AVR/PSS calibration (Phase C - red), user-defined AVR/PSS/TG (Phase D - green), and IEEE standard AVR/PSS/TG (Phase D - purple) for the September 22, 2015 event.

models as per Figure 2.8. The generic models show graphically that they perform better at modeling the fault response than the user-defined models. The Euclidean norm of the user-defined models is 1.2; the IEEE generic models have a Euclidean norm of 1.1017. After completing the calibration process, the IEEE generic models have a slightly better fit than the user-defined models. The results for all of the calibration steps are shown in Table 2.1.

The AVR/PSS calibration shows a better fit than the AVR only calibration according to Figure 2.10. The accuracy of the model decreases when the turbine-governor is added to the system, causing distrust in that model. The turbine-governor model significantly damps the active power output from the generator and provides too much reactive support. The reference signals, such as reference voltages, were not calibrated in the turbine-governor and may need to be adjusted in the future to develop a more accurate model.

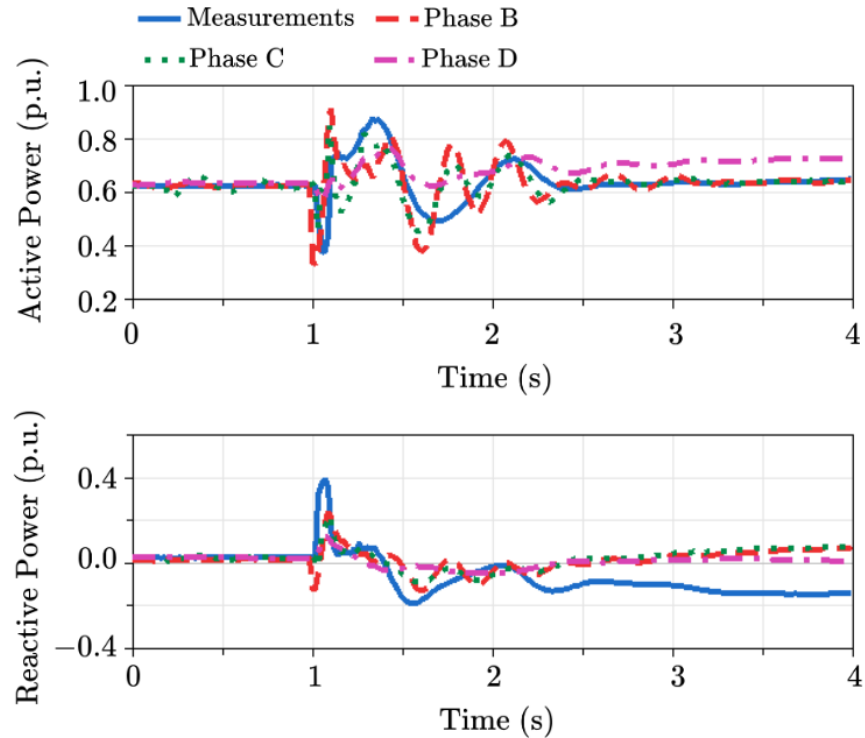


Figure 2.10: Comparison of all user-defined model estimation phases for the September 22, 2015 event.

2.4.2 Results - Case 2: November 2, 2016

The system in Figure 2.1 is configured to be compared to PMU data corresponding to a fault occurring on November 2, 2016. The system components are calibrated using the process described in the previous section. Figure 2.11 shows the results of the AVR and PSS calibration (Phases C and D) for the data set using the generic and Phase D of the user-defined control system models. The user-defined models have a better fit with the measurements than the generic models as seen with the previous case.

Figure 2.12 shows the results of the calibration of the user-defined models at each phase. When the user-defined turbine-governor is added to the model, the simulation creates a poor fit to the measurements. The turbine-governor damps the power output from the generator and causes a large dip in reactive power when the system returns to steady state around 1.5 seconds. The model for the user-defined turbine-governor is evidently incorrect, making it necessary to consider a standard turbine-governor model in the system instead.

The user-defined turbine-governor model has an issue similar to the results of the previous data set where the power from the generator is significantly damped. The addition

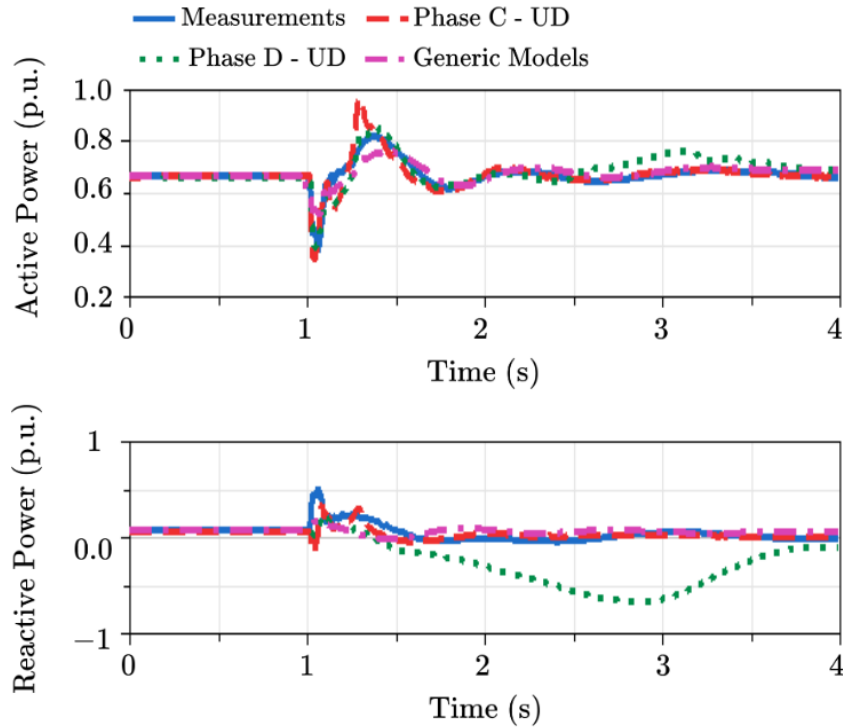


Figure 2.11: Calibration results for the user-defined AVR/PSS calibration (Phase C - red), AVR/PSS/TG (Phase D - green), and IEEE standard AVR/PSS/TG (Phase D - purple) for the November 2, 2016 event.

of the turbine-governor in the model causes an over correction of reactive power after the fault, as shown in Figure 2.12. After the fault, the turbine-governor does not let the system return to a steady state; there is a slow oscillation most evidently seen in the reactive power response of the model. When the mechanical power of the generator is used to control the input (shown in Figure 2.1 with block C removed), the system recovers to near steady state within 1-2 seconds after the fault, as shown in Figure 2.13. The mechanical turbine power P_{mech} is held constant due to the absence of the turbine-governor.

The fitness of the model calibration to the measurements are shown in Table 2.1. The fitness of the AVR/PSS user-defined model and the generic model are comparable, but the fitness significantly decreases when the turbine-governor is included in the model. Based off of these results, it is evident that the turbine-governor model is erroneous and has not been maintained over the lifetime of the plant. By utilizing a standard model, a more accurate simulation result can be achieved while minimizing the model maintenance requirements for the plant owner and system operator.

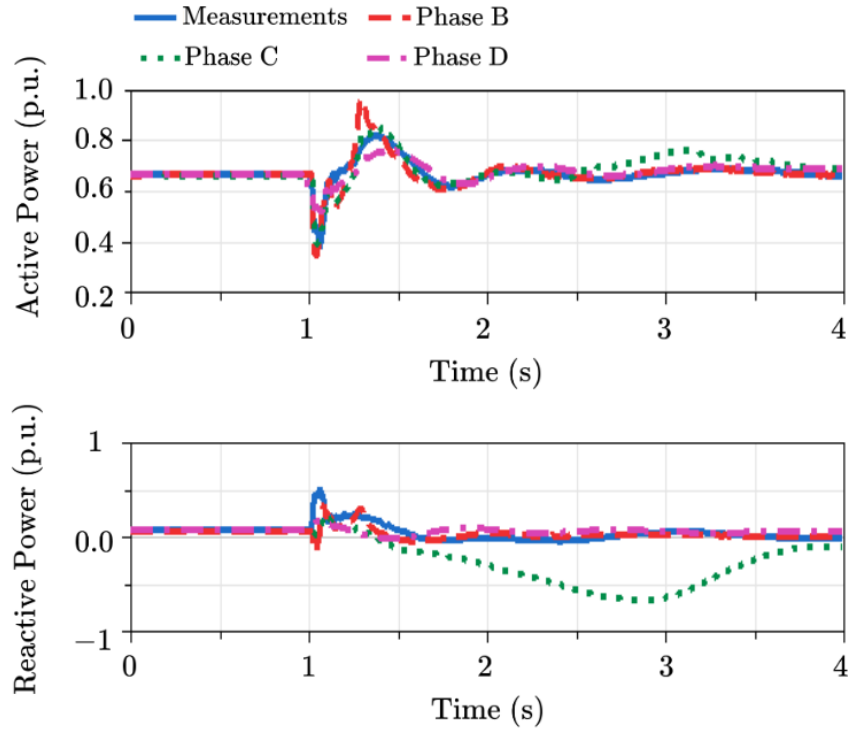


Figure 2.12: Comparison of all user-defined model estimation phases for the November 2, 2016 event.

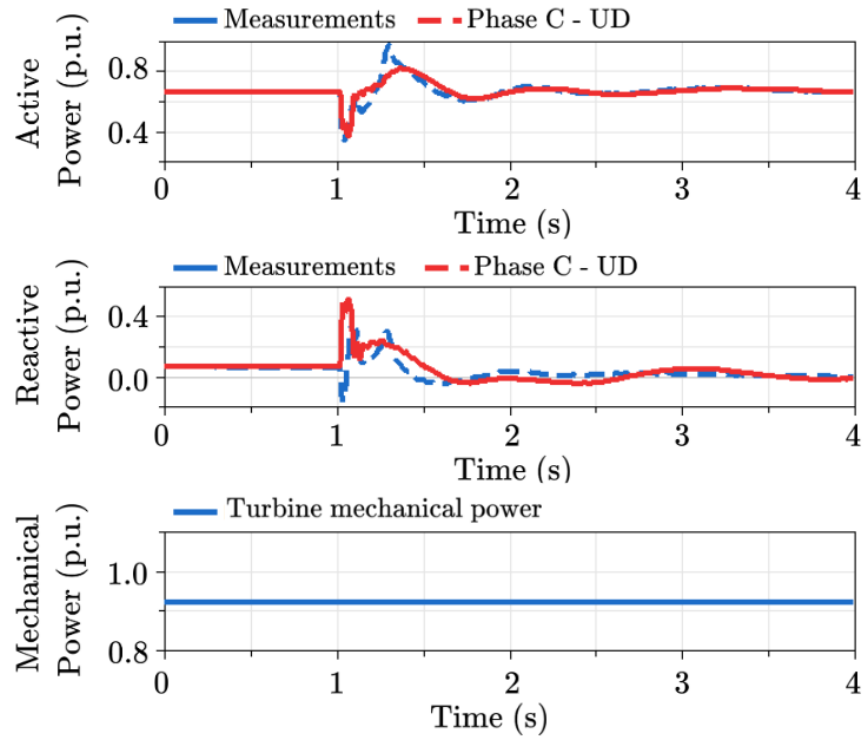


Figure 2.13: Response of the system consisting of generator, AVR, and PSS during the event on November 2, 2016.

Table 2.1: $\|x\|$ fitness of results per model for September 22, 2015 and November 2, 2016 events.

Model Setup/Date	9/22/2015	11/2/2016
GENSAE generator	1.9548	1.0884
Standard AVR	1.5767	2.2833
Standard AVR/PSS	1.1017	1.1017
Standard AVR/PSS/TG	1.3192	1.3288
UD AVR	2.2875	2.2827
UD AVR/PSS	1.2	1.1055
UD AVR/PSS/TG	2.0944	5.6683

2.4.3 Errors with the User-Defined Turbine-Governor Model

Based off of the results from both calibration cases, the user-defined turbine-governor is an inaccurate representation of the physical Itaipù system. As a result, it is necessary to simulate the user-defined AVR and PSS components with both the user-defined and an IEEE standard turbine-governor model to understand how it affects the simulation. Figures 2.14 and 2.15 shows the results for the power system containing models of the re-implemented user-defined AVR and PSS. The turbine-governor was varied between a calibrated model for the user-defined turbine-governor and the IEEE HYG0V turbine-governor model. The components were parameterized with their initial values provided by Itaipù's engineers as this analysis focuses on the modeling error, not the calibration of the plant's parameters.

The system is simulated using the fault data for the first case in Figure 2.14. Both the user-defined and standard turbine-governor models produce a similar response with respect to the reactive power output. The user-defined turbine-governor produces a more damped active power response than the IEEE standard model, and is ultimately over-damped compared to the physical system response. There is an error in the user-defined turbine governor model that results in the mechanical power output P_{mech} damping the active power output under certain operating conditions.

The system is simulated using the fault data for the second case in Figure 2.15, which shows a drastic change between the user-defined Itaipù turbine-governor and the IEEE HYG0V turbine-governor response with respect to the reactive power output. The IEEE standard model is again more accurate than the user-defined model, showing that the user-defined turbine-governor model also has some error that causes the machine to absorb large amounts of reactive power. There seems to be an error in the transfer function of the user-defined

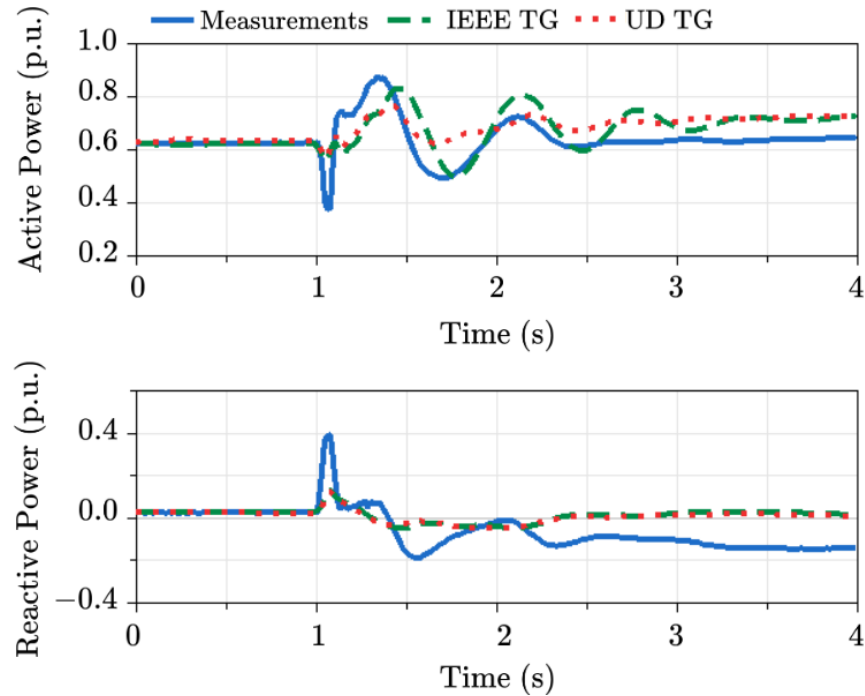


Figure 2.14: Final calibration phases for user-defined AVR and PSS models with both a user-defined and IEEE standard TG model compared for the September 22, 2015 data set.

turbine-governor that causes the machine to consume a large amount of reactive power under certain conditions instead of going back to steady-state like the actual system response.

Based off of the simulation results, it is evident that the user-defined turbine-governor model is not an accurate representation of the system and that it cannot be updated to an accurate one through parameter estimation. The cause for the errors in the model are unclear without further analysis on the turbine-governor itself, but we do not have access to more data nor any other user-defined models than the ones provided to us by Itaipu's engineers. If more data were available, further analysis of the turbine-governor model could be conducted by focusing on tuning the model response to inputs and outputs measured at the turbine-governor itself rather than the terminal connection of the machine to the grid. This would follow a similar validation process that will be outlined and discussed in Chapter 3.

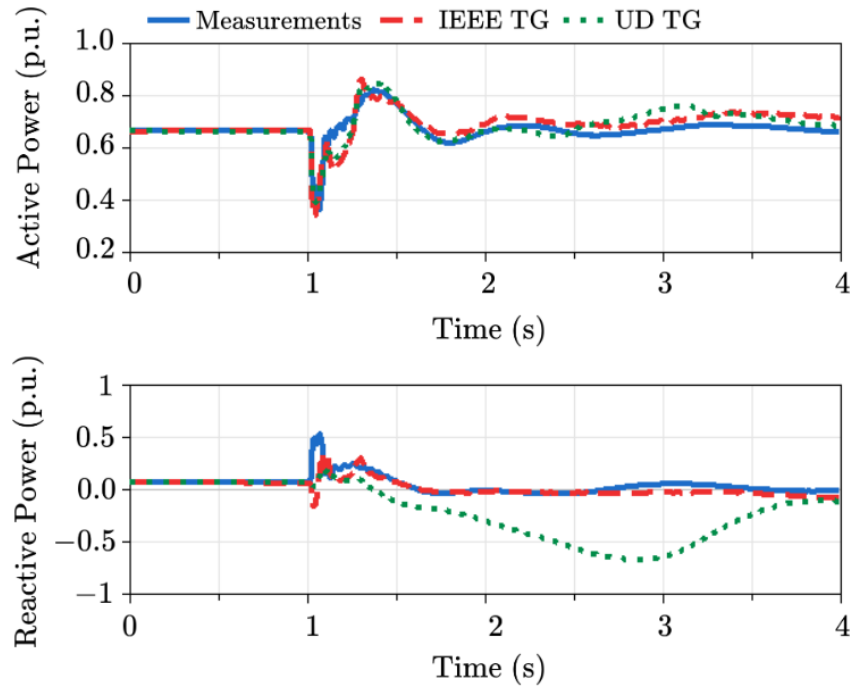


Figure 2.15: Final calibration phases for user-defined AVR and PSS models with both a user-defined and IEEE standard TG model compared for the November 2, 2016 data set.

2.5 Itaipú Case Study Discussion

While carrying out this work, it was expected that the user-defined model description would produce a more accurate result than the generic models. It initially seemed logical that models made custom to match a the plant’s response would be more accurate than a standard model that is a more generalized representation of system components. The model of the Itaipú plant was most likely originally described in the 1980s or 1990s shortly after when the plant was commissioned. There have been changes in the system since, but they likely have not updated to be reflected in the model. The user-defined models were created back before the IEEE standard models were originally defined, which is why the plant uses detailed models that are specific only to Itaipú for dynamic studies rather than the generic standard models commonly used to represent power plants components today. Although the IEEE standard models are simplified, they have a broader application scope and are able to capture the actual system response and dynamics with better accuracy.

These observations raise the importance of model maintenance and model validation for power system components. Thanks to the availability of PMU measurements, this is

becoming more possible. The parameter estimation process shows that the models must be validated and maintained regularly, as the models have become inaccurate over time. This may be caused by aging, component degradation, and hardware upgrades that have not been reflected in the model over time.

2.6 Conclusions

The case studies in this chapter show that a sequential optimization of the plant parameters help improve the accuracy of the final parameter set. The proposed approach suggests that engineering know-how can help in developing the different stages of the optimization problem, and help understanding the influence of each of the model parameters in the governing dynamics in the measured data. Due to the availability of signals, the validation and optimization problems are not well defined.

The user-defined models did not perform as well as the generic models for the control system of the plant after calibrating the parameters for the two faults analyzed. Although the fitness of the two modeling methods are comparable when the AVR and PSS are included in the system, the generic models are consistently more accurate than the user-defined models. In both cases studied, the fitness of the model increases when the user-defined AVR is added to the system from the basic generator only model; however, in the generic case, the models show an improvement in fitness to the PMU measurements after each parameter is calibrated. In the future, the models used for the Itaipú power plant need to be corrected to better to fit the actual response of the plant to the simulation.

These results show that the models currently used for power systems cannot be blindly trusted without the type of analysis shown in this chapter. The approximations of the models do not capture all of the behaviors in the physical system, causing distrust in the models. For example, there is a 20 Hz oscillation seen in the measurements (shown in Figure 2.16) that the models cannot replicate. This implies for both the user-defined and generic models that more detailed representations of certain components need to be developed. This implies that the models need to be revisited to be able to capture the behavior, but also the traditional modeling approach may be insufficient. There is also a chance that there are electrical components affecting the system that are reflected in the PMU data but are not included in the system model. Using this set of measurements, it may not be possible to effectively separate the generator system from the rest of the grid. Instead, data collected

from commissioning and maintenance tests can be used to validate the generator components as shown in the next chapter.

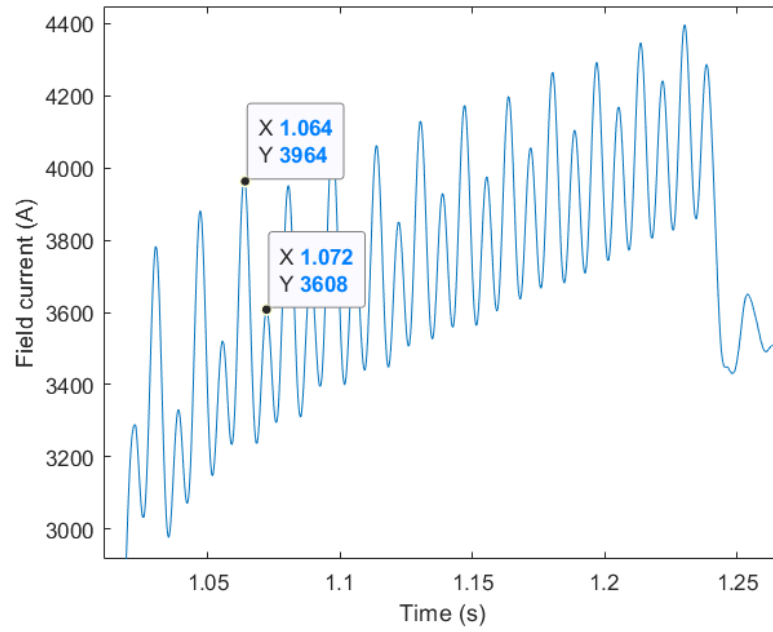


Figure 2.16: 20 Hz oscillation observed during fault at Itaipú plant.

CHAPTER 3

VALIDATION OF POWER PLANT MODELS USING FIELD DATA WITH APPLICATION TO THE MOSTAR HYDROELECTRIC PLANT

3.1 Introduction

3.1.1 Motivation

Simulation-based studies are indispensable in determining the best practices for power system planning and operation. They give insight on how components will interact dynamically with one another in various operational states. The existing grid infrastructure is aging globally, increasing the likelihood that plant characteristics have changed over time due to maintenance, electrical overload, and other physical degradation. It is important to ensure that the models representing existing infrastructure, specifically power plants, are valid for performing these studies. Having accurate dynamic models is crucial to understand how planned electrical infrastructure, such as inverter-based resources, e.g. wind and solar generation, interact with the existing system. These inverter-based resources have a significant impact on power system stability characteristics and performance under disturbances, so accurate representation of existing infrastructure is necessary to study the system to the best of our ability for these cases. It is also necessary to maintain accurate models as low confidence in the parameters of individual components in a system leads to more conservative or erroneous assessments and operation.

Highly accurate dynamic power system models are necessary to perform simulation-based studies. While it is assumed that the plant model is accurate at commissioning time, this situation can change over time. The dynamics of the generator can change due to wear, electrical overload, and maintenance, as replacement of degraded components in the system can result in altered dynamics. The power electronics dynamics present in the AVR have the same behavior and can change over time. Even though it is less likely, the controller parameters of the PSS, AVR and governor can also have been modified without general knowledge, changing their input-output behavior.

This chapter previously appeared as: M. Podlaski, X. Bombois, and L. Vanfretti, "Validation of power plant models using field data with application to the Mostar hydroelectric plant," *Int. J. Elect. Power Energy Syst.*, vol. 142, no. B, pp. 1-13, Jun. 2022.

This chapter presents a methodology based on field data that allows us to verify if the current model of the power system is (likely to be) still valid at any time. The proposed methodology enables us to make this diagnosis independently for each of the power plant components (i.e., the generator, the AVR, the PSS and the governor). In order to do this for an arbitrary component, measurements of the output vector of this component are compared to the output vector predicted by the current model of the component. This predicted output vector is computed by "filtering" the (measured) input vector of a given component by the current model of the component.

The data used in the above mentioned validation procedure can be normal operation data (where the system is basically excited by random load changes). It is to be noted that normal operation data may not be able to detect any dynamics change due to a lack of informativity. Consequently, data obtained during major disturbances could also be used to detect those changes invisible with normal operation data. The system can also be excited with (small) probing tests in order to enhance the detection ability of the proposed validation procedure. A major maintenance could be the ideal moment to gather such informative data (so-called commissioning tests). In particular, the methodology proposed in this chapter is here validated based on a set of real measurements obtained during commissioning tests measured at the terminal bus of Mostarsko Blato hydroelectric plant in Bosnia, which produces 30 megawatts [46].

3.1.2 Related Works

This work builds off of the work in [47] and [48], which focuses on parameter estimation for the Itaipù hydroelectric plant. Itaipù is about 20 times larger than Mostarsko, using phasor measurement unit (PMU) data from various faults and system disturbances. These studies have shown the shortcomings in the user-defined models and the necessity of model maintenance in aging power plants. This study also highlights how plants characteristics change over time.

Most of the previous studies have focused on monitoring the plant online or from disturbance data for the purpose of validation. Ref [49] focuses on the validation and calibration of a 20 MVA hydroelectric plant, which is comparable in size to the Mostarsko plant. The study focuses on testing the plant before, during, and after a generator upgrade project. Six test series were applied to the system, including loss of excitation and load rejection tests.

The voltage regulator and machine models calibrated in the study are the most simplified models available, so the parameter estimation is limited.

Ref [50] shows the validation of a power plant using both commissioning tests and fault data. In [50], a fault affects a plant consisting of three thermal generating units. The excitation system/AVR and generator are validated together in these tests; the main benefit of this approach is to be able to validate the model using data collected from actual events that are overlooked in system planning studies. The data is collected at the plant's terminal, so the measurements allow for the plant to be isolated from the rest of the grid; however, the validation method may lead to an erroneous model since all components are lumped together for the validation.

Previous studies for power system model validation using field measurements focus on using disturbance data only. The methods in [36] uses PMU data to determine the cause of faults within the system and calibrate both conventional and renewable plants. The parameter identification uses a combination of particle swarm optimization (PSO) and sensitivity analysis for a localized portion of the system consisting of a wind turbine and its corresponding reactive power support, step-up and step-down transformers. The calibrated models helped operators find problems with the AVR of the plant for the fault studied, allowing for improved operations under weak grid conditions in the future. This is especially important for a plant like Mostarsko Blato, which provides voltage support and a large local inertia for dynamic stability under fault conditions. As per [51], the location of the Mostarsko plant has significant impact on the local grid's dynamic stability.

Process monitoring studies have also motivated this work such as [52], which propose methods to monitor the models in closed-loop operation. In this study, a model-based approach is introduced to be exploited for change detection and isolation when the performance of the system degrades. Other process monitoring methods, such as [53], describes how controllers can be altered to optimize system efficiency for controllers developed separately from one another. This is useful for the methodology outlined for the power plant, as it proposes that the components are validated apart from the rest of the system with the goal of re-identifying the components when necessary.

Methods that perform joint estimation of states and parameters have been reported in the literature [54]-[55] and have been applied for model validation [56]. However, these methods require continuous excitation to guarantee unbiased estimates. In contrast, our

approach can be used when the system is excited or (though with less accuracy) under normal operating conditions.

3.1.3 Chapter Contributions

This chapter contributes the following:

- A new methodology for validation of the (current) model of the control system and generator of a power plant using field data. The purpose is to determine if these models are still an accurate representation of the elements of the power system. Four elements are validated: the AVR, the PSS, the turbine-governor, and the generator. The methodology is illustrated using data from a hydro-electric power plant obtained during commissioning tests.
- A methodology to update the models when they are no longer an accurate representation of the power system.

3.1.4 Chapter Organization

The chapter is organized as follows: the general power plant model and the components are shown in Section 3.2. The proposed validation methodology is described in Section 3.3. Section 3.4 outlines the case study for the Mostar plant, including the introduction of the specific models for the system and data collection method. The validation of the AVR, PSS, and generator using the Mostar data are shown in Section 3.5.

3.2 Components of the Power Plant

The representative structure of a hydro-electric power plant consists at a minimum of four components: a generator, an automatic voltage regulator (AVR), a power system stabilizer (PSS), and a turbine-governor (TG) as shown in Figure 3.1. In this section, we describe these elements in more details with a special attention to their respective inputs and outputs. We suppose that a model of these components is available i.e., a software artifact that allows to compute/predict the output vector of a given components based on the knowledge of its input vector. As mentioned in the introduction, we can suppose that these models are accurate at commissioning time; however, the model accuracy can be altered over time. The generator has physical characteristics that can change over time; this can be

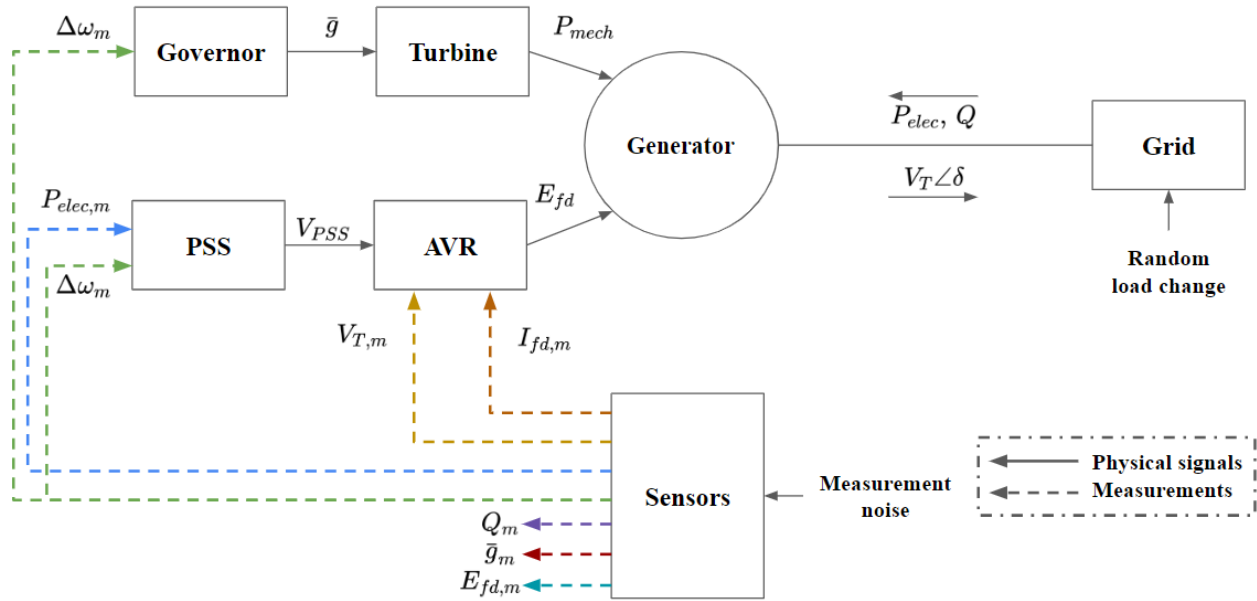


Figure 3.1: Block diagram of the power plant showing the relationships between each component and their inputs and outputs.

caused by current overloading on the generator and aging of the plant components. While it is less likely to happen, the controllers have time constants that can be changed in the plants without updating the model accordingly due to human error. The power plant is connected to the electrical grid, which has an influence on the signals that will be measured at the power plant. An appropriate choice of the inputs and outputs of the generator will be necessary to validate the generator models. The electrical power ($P_{elec} + jQ$) measured at the terminal will have to be considered as an input of the generator to effectively separate the grid behavior from the generator.

3.2.1 AVR and Exciter Model

The automatic voltage regulator, or AVR, is a controller that regulates the voltage of a generator subject to the error between the plant's operating voltage and a reference voltage as well as the field current produced by the generator. It is important to note that, as per common practice, we define the AVR as the combination of a controller and an exciter [17], [57]. The exciter is the power electronics of the excitation system of the power plant that creates the field voltage (E_{fd}) based on the controller portion of the AVR. The controller part of the AVR takes as inputs the control signal (V_{PSS}) generated by the PSS and a measurement ($V_{T,m}$) of the field voltage (V_T). In some configurations, a measurement of the

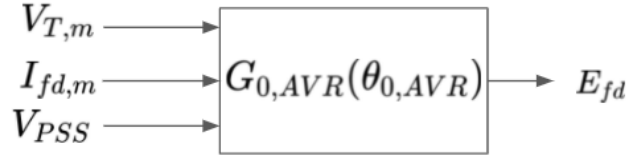


Figure 3.2: AVR inputs and outputs for static exciter example.

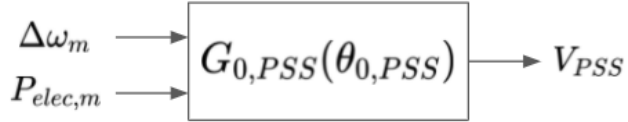


Figure 3.3: PSS inputs and outputs.

field current (I_{fd}) is also used as an input. As shown in Figure 3, the AVR determines E_{fd} (the output of the AVR) as a function of V_{PSS} , $I_{fd,m}$ and $V_{T,m}$ (the inputs of the AVR). The physical signal E_{fd} is not available, but measurements $E_{fd,m}$ of that physical signal are available. In the AVR, the dynamics of the power electronics are most likely to change over time due to degradation from heat, voltage or current overload, and other stresses on the system.

3.2.2 PSS Model

The power system stabilizer, or PSS, is a controller that adds an additional signal (V_{PSS}) to the AVR with the purpose of controlling the damping of oscillations in the system. The main task of the PSS is to adjust the phase compensation by compensating for phase lags through the generator, excitation system, and power system. The PSS provides torque changes in phase with speed changes to provide damping [57], [58]. The inputs and outputs are further visualized for the PSS in Figure 3.3. The PSS output is the signal V_{PSS} and the input of the PSS is generally a measurement $\Delta\omega$, which is the deviation of the rotational speed of the rotor shaft with respect to its nominal value. In some cases, the PSS has a second input which is a measurement $P_{elec,m}$ of the electrical power. Consequently, the PSS can be seen as an operator that computes V_{PSS} as a function of $\Delta\omega_m$ and $P_{elec,m}$.

3.2.3 Generator Model

As shown in Figure 3.4, the generator consists of two parts representing the mechanical and electrical behavior in the system. The mechanical part is the physical phenomenon that allows to derive the speed deviation $\Delta\omega$ of the rotor shaft based on the difference between the mechanical power P_{mech} created by the turbine and the (active) electrical power P_{elec}

that is sent to the grid at the terminal voltage. This part of the dynamics of the generator is generally described by the swing equation in generator's model. It is to be noted that P_{mech} is created by the turbine using the output \bar{g} of the governor, which is the gate opening of the governor.

The electrical dynamics of the generator are influenced by the field voltage (E_{fd}) and the value of ω . The field current is produced by the electrical portion; the terminal voltage (V_T) is determined based on the complex power ($P_{elec} + jQ$) transmitted to the grid at the terminal voltage. The generator is an operator with inputs P_{mech} , P_{elec} , Q and E_{fd} and outputs ω , V_T and I_{fd} . This means in fact that we can find equations that can compute these outputs based on solely these inputs. It should be noted that only measurements of P_{elec} , Q , E_{fd} , ω , V_T and I_{fd} are available, the exact values of these quantities are not available. It is to be noted that P_{mech} cannot be measured in practice, but can be computed using a model of the turbine and the gate opening \bar{g} (the output of the governor; see next subsection). In this way, we integrate the model of the turbine in the generator model.

3.2.4 Governor Model

The governor is the main controller in a hydraulic turbine system. The governor controls the speed of the generator by varying the water flow through the turbine [59]. Modern turbine control systems include the primary function of the governor, i.e. to maintain and adjust the unit's speed for synchronization with the grid, and have other functions such as to adjust output of the unit in response to operator commands and perform shutdown of the plant.

The governor system $G_{0,governor}$ is described in details in [57]. The input of the governor is the measurement of the speed deviation $\Delta\omega$. The output of the governor is the gate opening, \bar{g} . The governor is a controller that computes \bar{g} based on $\Delta\omega_m$. It can thus be seen as an operator with as input $\Delta\omega_m$ and with as output \bar{g} .

3.3 Validation Methodology

3.3.1 Validating Component Models

The system in Figure 3.1 can be divided into four components to be validated due to the availability of all input/output measurements from the recorded field data: the generator, the AVR, the governor, and the PSS. As described in the previous section, each component

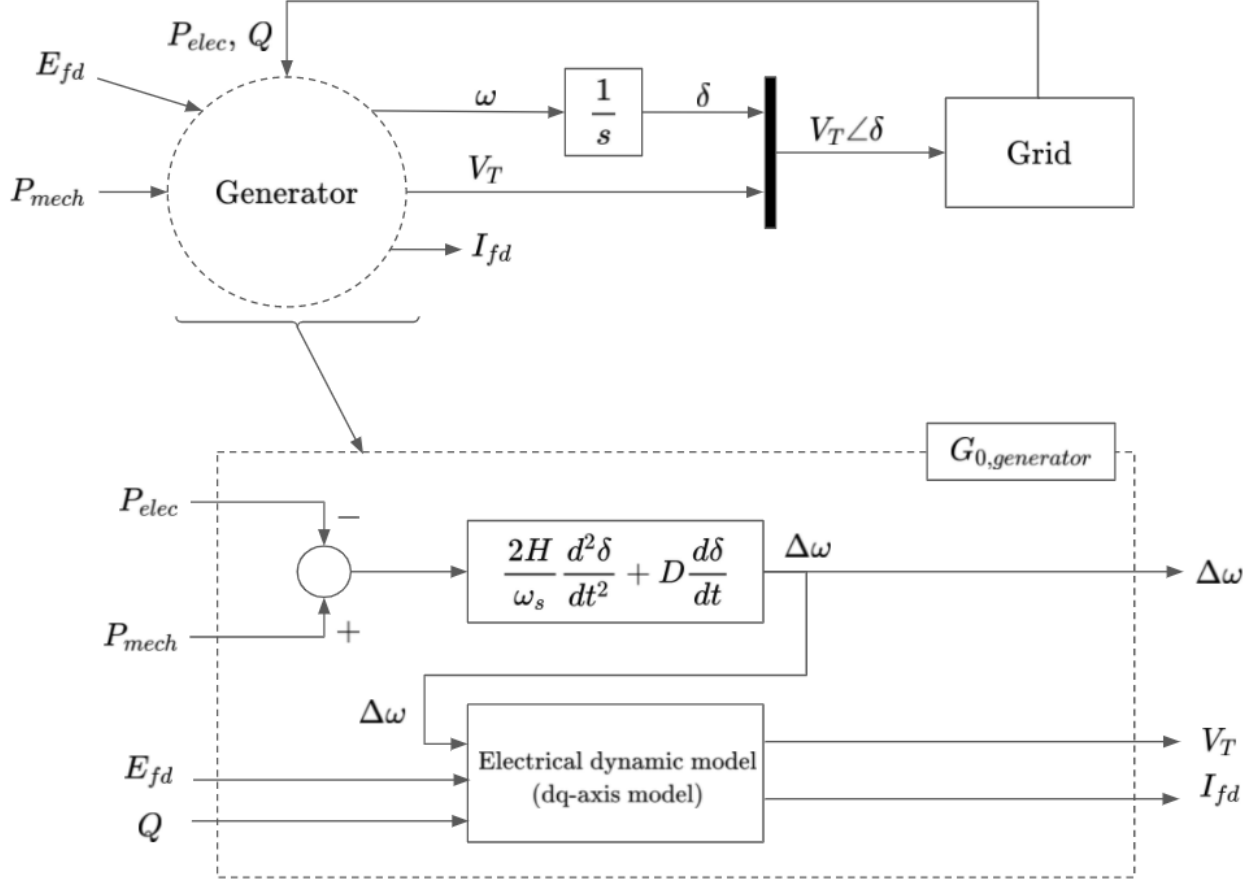


Figure 3.4: Generator block diagram.

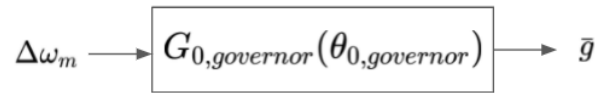


Figure 3.5: Governor inputs and outputs.

of the power plant can be seen as an operator relating inputs and outputs. Let us write these different operators as follows:

$$y_i = G_{0,i} u_i \quad (3.1)$$

where $i = \{AVR, PSS, generator, governor\}$ and u_i (resp. y_i) is a vector containing the corresponding inputs (resp. outputs). For example, when $i = AVR$, $u_{AVR} = (V_{T,m}, I_{fd,m}, V_{PSS})^T$, $y_{AVR} = E_{fd}$, and $G_{0,AVR}$ represents the dynamical operator relating these inputs and outputs.

At commissioning time, accurate models M_i ($i = \{AVR, PSS, generator, governor\}$) of these different operators $G_{0,i}$ have been determined. We assume that these models M_i

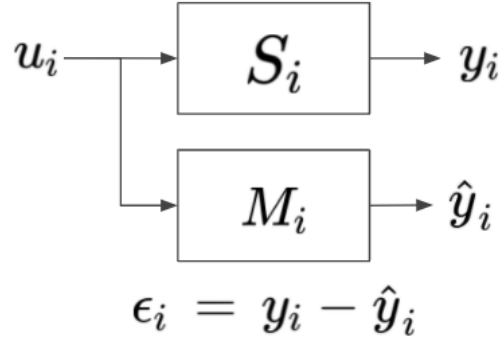


Figure 3.6: Real system S_i and model M_i comparison.

were at that time very accurate representations of $G_{0,i}$. Due to the reasons presented in the previous section, the operators $G_{0,i}$ can however change with time and we need to be able to verify whether the models M_i are still good representations of $G_{0,i}$.

When such a validation step is necessary, we collect the input and output vectors u_i and y_i for each component i on the power system (replacing the unknown physical quantities by their measurements when necessary). These data (u_i, y_i) can be collected in normal operations (with the sole excitation of random load changes) or by adding some excitation signals to make the data richer.

Once these data u_i and y_i are collected for all i , we compute the predicted output vector of each model as follows:

$$\hat{y}_i = M_i u_i \quad (3.2)$$

and we verify whether \hat{y}_i is still a good representation of the true output y_i . This can e.g. be done based on the so-called FIT. Let us denote by y_{ij} (resp. \hat{y}_{ij}) the j^{th} entry of y_i (resp. \hat{y}_i). We define FIT_{ij} as:

$$FIT_{ij} = 100\% \left(1 - \frac{\|y_{ij} - \hat{y}_{ij}\|_2}{\|y_{ij}\|_2} \right) \quad (3.3)$$

where for any signal $x(t)$ ($t = 1, \dots, N$), the Euclidean norm $\|x\|_2$ of $x(t)$ is defined as Equation 3.4.

$$\|x\|_2 = \sqrt{\frac{1}{N} \sum_{t=1}^N x^2(t)} \quad (3.4)$$

For each component i , we thus have n_i FITs where n_i is the dimension of y_i .

The model M_i will be deemed validated if all FIT $_{ij}$ ($j=1,\dots,n_i$) yield a value close to the one observed at commissioning. If it is observed for a given component that a FIT $_{ij}$ with a value that has significantly decreased, then the model M_i is no longer a good representation of the dynamic $G_{0,i}$ of component i . In the next section, we show how to update such a model M_i that has become inaccurate.

3.3.2 Case of Invalid Models

In the case where the FIT of the component has significantly decreased with respect to the FIT observed at commissioning time, the component model is considered invalid. For each invalid model M_i where $i = \{AVR, PSS, governor, generator\}$, the input/output data (u_i, y_i) will be used to re-identify a new model for that component of the system. Since the components can be validated individually, only the invalid component needs to be re-identified. For this re-identification, the model M_i is parameterized by a number of parameters gathered in a parameter vector θ_i . For each value of θ_i , the model has different dynamics $G_i(\theta_i)$. In particular, the invalidated model M_i was described by $G_i(\theta_{i,init})$ for some value $\theta_{i,init}$ of the parameter vector θ_i .

The new value of the parameter vector will be the one that minimizes the Euclidean norm of $y_i - G_i(\theta_i)u_i$, where (y_i, u_i) is the collected data. The solution of that optimization problem is denoted by $\theta_{i,new}$. This produces a new model $M_{i,new}$ equal to $G_i(\theta_{i,new})$. The quality of this new model can be assessed by computing the FIT corresponding to $M_{i,new}$.

To perform the identification, we will here use RaPId, a MATLAB toolbox for parameter estimation [21]. It should be noted that in [60], the data (u_i, y_i) should be sufficiently rich to ensure the consistency of the re-identified model. This entails in general that the data should have been generated with a sufficient number of excitation signals (see [60] for more details). Details about computational aspects of RaPId and the algorithms used can be found in [21] and [61], respectively.

Remark. If the re-identified model is still not validated (its FIT is still too low), this could be a sign that the chosen model structure does not correspond to the structure of the true system and should be modified. In other words, the order/complexity of the model should be increased, e.g. in the case of the generator model, instead of using the GENCLS model, we could use a GENSAL model, which is more complex [40].

3.4 Mostar Power Plant Case Study

3.4.1 Introduction

In order to validate the proposed approach, the model validation methodology presented previously is applied to the Mostar hydroelectric power plant, using real data to validate the models. The data has been collected after significant maintenance had been performed on the plant, where a large step perturbation V_{step} had been added to the terminal voltage measurement ($V_{T,m}$) with the goal of exciting various functions in the system. The plant consists of the components described in Section III, with the exception of the turbine-governor system for which no measurements were available. Each of the components is validated independently using field data collected during commissioning tests, as there is enough data available to validate the components with their inputs and outputs. This specific excitation is depicted in Figure 3.7 where the first AVR input becomes $V_{AVR} = V_{step} + V_{T,m}$.

This excitation V_{step} allows to gather data for the validation of the models M_i of the different components of the Mostar power plant, models that have been provided to us by the engineers at this power plant. These models have all the IEEE standard form [17]. In particular, M_{PSS} is a PSS2B model, with the control block diagram shown in Figure 3.9. The model M_{AVR} for the AVR is an ST5B model, with the control block diagram in Figure 3.8. The model $M_{generator}$ of the generator is the salient pole with linear saturation (GENSAL) model with the equations listed in Appendix D. All of the parameters definitions are listed in Appendix D sorted by component type.

Since these commissioning tests focus on testing the functionalities of the electrical controllers, the measurements of the turbine and governor are unavailable. As a result, the models for these components are not included in the model in Figure 3.7. It is assumed that the mechanical power (P_{mech}) is a constant value that is derived during the initialization of the model as a result of the power flow.

3.4.2 AVR and Excitation System Model

The AVR and excitation system is represented by the IEEE ST5B standard model [17], [62], with the complete transfer function model shown in Figure 3.8. The unit has a static potential-source excitation system, meaning the voltage is transformed to an appropriate level using a controlled-rectifier. Controlled-rectifiers provide the necessary direct current for the generator field.

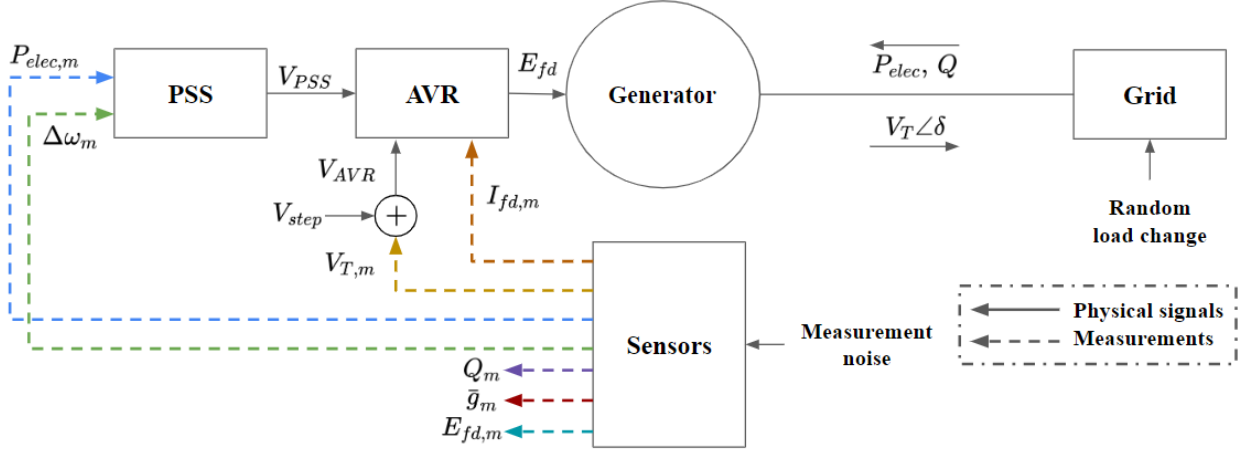


Figure 3.7: Block diagram of the power plant showing the relationships between each component and their inputs and outputs for the Mostar plant.

The input AVR voltage is the sum of the machine voltage and step excitation ($V_{AVR} = V_{T,m} + V_{step}$), which is passed through a transducer delay lag:

$$\frac{1}{1 + sT_R} \quad (3.5)$$

where the output is used to calculate the error between the reference voltage (V_{ref}) and PSS voltage (V_{PSS}). This transfer function is used to account for the time delay created by the sensors measurements. The reference voltage (V_{ref}) is a pre-defined set point value for the controller, not an input. The definition of each parameter is listed in Appendix D.

In this configuration, we assume a continuous time controller, so the main regulator transfer function consists of two anti-windup lead-lag blocks and a gain:

$$K_R \frac{1 + sT_{C1}}{1 + sT_{B1}} \frac{1 + sT_{C2}}{1 + sT_{B2}} \quad (3.6)$$

The difference between the regulator transfer function and the field current (I_{fd}) scaled by the rectifier regulation factor (K_C) is then applied to the transfer function for the power electronics:

$$\frac{1}{1 + sT_1} \quad (3.7)$$

Since the commissioning tests do not excite the system such that the controller would experience a fast perturbation, the rectifier function has little effect on the system. If the

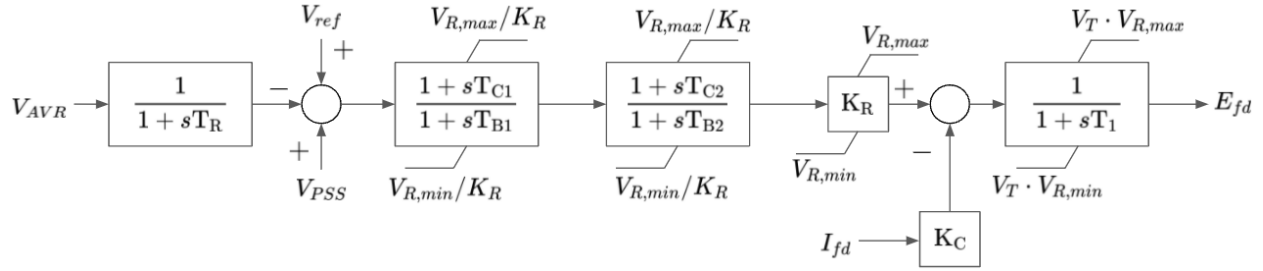


Figure 3.8: AVR ST5B block diagram.

system were subject to a fault, the rectifier function will have an impact on the AVR model response. The most crucial functions in the controller are represented by the main regulator transfer functions.

3.4.3 PSS model

The power system stabilizer, or PSS, is a controller that adds an additional signal to the AVR with the purpose of controlling the damping of oscillations in the system. The Mostar plant uses the IEEE PSS2B model to represent the PSS controller [17], [58]. The inputs and outputs of the PSS are shown in Figure 3.9, where the inputs of the generator speed deviation ($\Delta\omega$) and electric power (P_{elec}). The output of the PSS is the PSS voltage (V_{PSS}), which is subsequently used as an input to the AVR. The description of all of the time constants, gains, and other variables used in the PSS in Figure 3.9 are listed in Appendix D. The AVR model is compatible with the PSS2B PSS model [17].

The PSS is a dual-input controller that uses the machine speed and electrical power to calculate the integral of the accelerating power to make the calculated stabilizer signal insensitive to mechanical power change. Each input has two washouts ($T_{w1}, T_{w2}, T_{w3}, T_{w4}$) represented as well as transducer time constants (T_6, T_7). To determine the integral of accelerating power of the PSS, the gain K_{S2} would be:

$$K_{S2} = \frac{T_7}{2H} \quad (3.8)$$

where H is the total shaft inertia of all mechanically connected rotating components of the unit. In the case of Mostar, the unit is represented as one machine, so H is the shaft inertia of the generator. The exponents M and N allow for a “ramp-tracking” characteristic to be represented in the controller; phase compensation is provided by the three lag-lead blocks

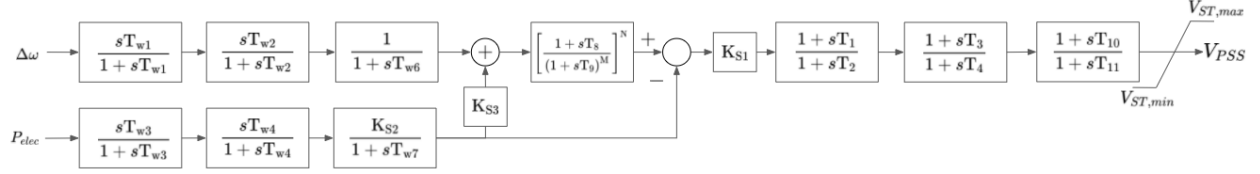


Figure 3.9: PSS2B block diagram.

with time constants $T_1, T_2, T_3, T_4, T_{10}, T_{11}$. The output of the controller is limited by the minimum and maximum setpoints, $V_{ST,min}$ and $V_{ST,max}$.

3.4.4 Generator model

The Mostar plant uses a salient pole generator with linear saturation, for which all equations are shown in Appendix D [63]. The generator is represented in a direct-quadrature axis equivalent structure. In geometric terms, the d and q axes are per-phase representations of the flux contributed by the three separate sinusoidal phase quantities at the same frequency. The flux produced by the field winding is located on the d-axis; the q-axis is the axis where the torque is produced. The block diagram for the direct axis is shown in Figure 3.10, where E_{fd} is the field voltage signal produced by the AVR. The model also uses the direct-axis current I_d as an input. The output I_{fd} directly feeds back to the AVR, and Ψ_d'' is the sub-transient flux which is further used to calculate the terminal voltage of the machine. The d-axis component of the terminal voltage is shown in Equations 3.9 and 3.10. Equation 3.9 calculates the total flux through the d-axis Ψ_d , where I_d is the current through the d-axis, X_d'' is the sub-transient d-axis reactance, and Ψ_d'' is the sub-transient flux shown as the output of the generator in Figure 3.10.

$$\Psi_d = \Psi_d'' - X_d'' * I_d \quad (3.9)$$

$$u_d = (-\Psi_q) - R_a * I_d \quad (3.10)$$

The block diagram of the quadrature axis is shown in Figure 3.11, where the quadrature current I_q is the input to the system and q-axis sub-transient Ψ_q'' flux is the output. These are based on the equations in Appendix D. The q-axis component of the terminal voltage is shown in Equations 3.9 and 3.10. Equation 3.9 calculates the total flux through the q-axis Ψ_q , where I_q is the current through the q-axis, X_q'' is the sub-transient d-axis reactance, and

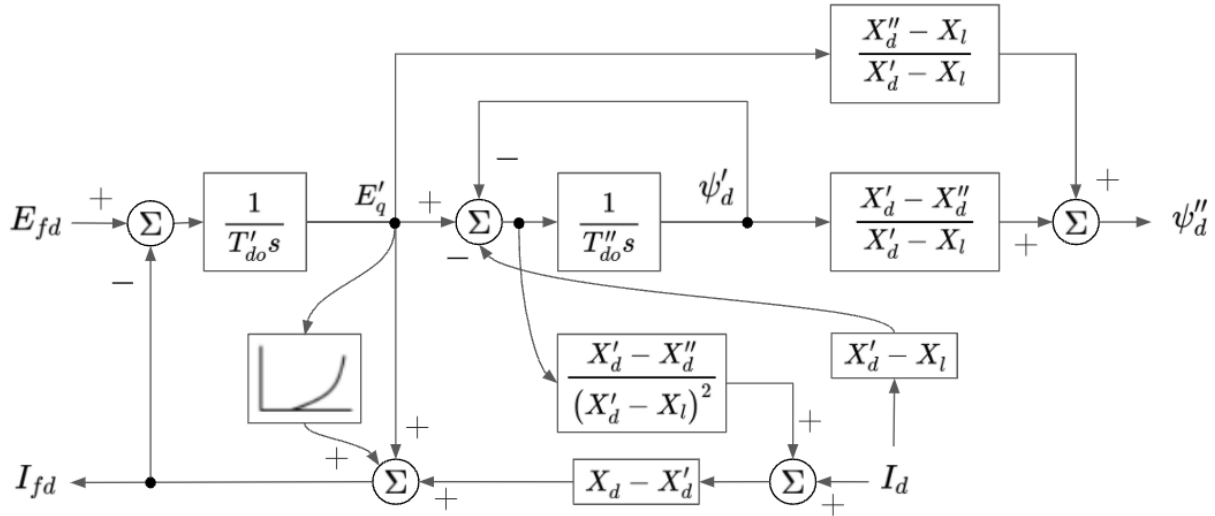


Figure 3.10: Generator direct axis block diagram.

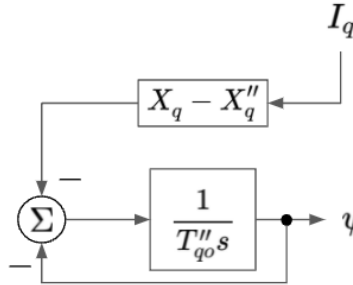


Figure 3.11: Generator quadrature axis block diagram.

Ψ''_q is the sub-transient flux shown as the output of the generator in Figure 3.11.

$$\Psi_q = \Psi''_q - X''_q * I_q \quad (3.11)$$

$$u_q = \Psi_d - R_a * I_q \quad (3.12)$$

3.5 Mostar Power Plant Validation

Each of the specific models outlined in Section 3.4 is validated using the methodology from Section 3.3. The inputs and outputs of the components are selected based on the relationships shown in the system block diagram in Figure 3.7 using the data available. The data are collected using a sampling rate of 5ms.

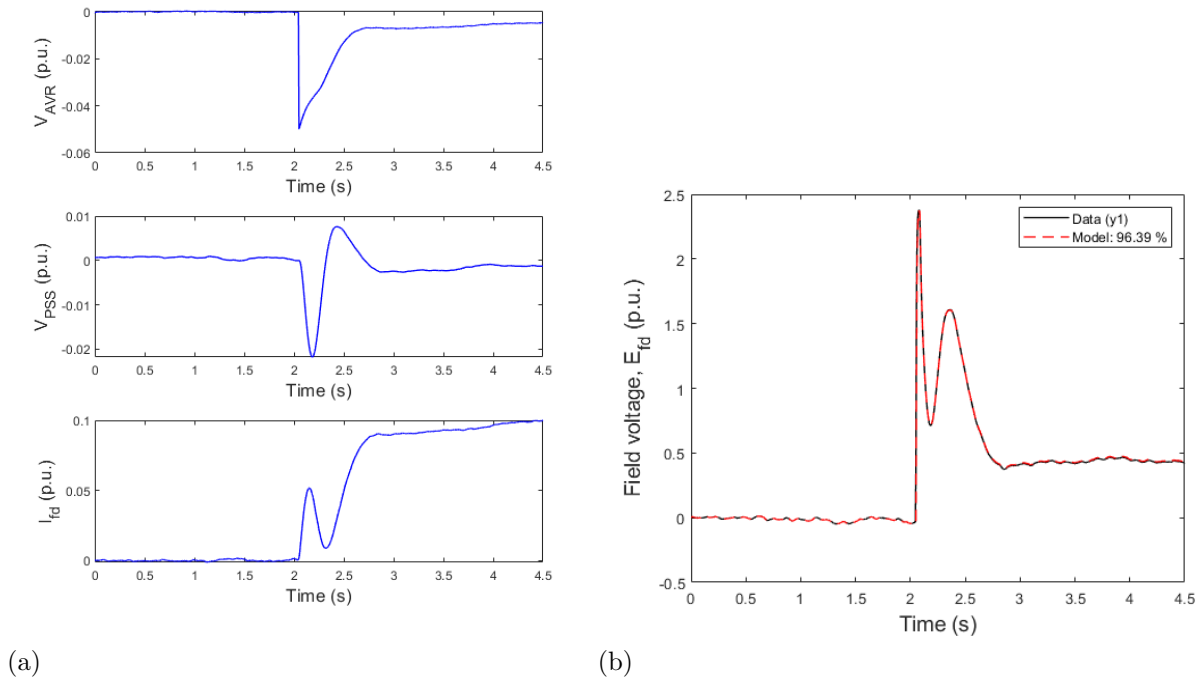


Figure 3.12: AVR validation data and results, where (a) Inputs to AVR. (b) AVR field voltage response comparison.

3.5.1 AVR and Excitation System Model Validation

As explained in Section 3.4, the AVR input vector is $u_{AVR} = [V_{AVR}, V_{PSS}, I_{fd,m}]^T$ and its output $y_{AVR} = E_{fd}$, which will be approximated by $\hat{y}_{AVR} = E_{fd,m}$. The response of the model is $\hat{y}_{AVR} = M_{AVR}u_{AVR}$, where M_{AVR} has the structure given in Figure 3.8. In Figure 3.12a, the different inputs in u_{AVR} are represented while y_{AVR} and \hat{y}_{AVR} are compared in Figure 3.12b. In this last figure, we observe that \hat{y}_{AVR} is almost equal to the actual output y_{AVR} ($FIT_{AVR} = 96.39\%$). The model M_{AVR} can be thus deemed validated.

3.5.2 Generator Model Validation

Let us now consider the next component: the generator. Recall that we do not have turbine governor measurements, so P_{mech} will therefore be assumed constant and computed from the plant's dispatch of P_{elec} . Consequently, the generator input vector is $u_{generator} = (E_{fd}, P_{elec}, Q)$ and its output $y_{gen} = (\Delta\omega, V_T, I_{fd})$. As previously stated, the physical quantities will be replaced by their measurements in $u_{generator}$ and $y_{generator}$.

The measurement of $\Delta\omega$ was not collected during the commissioning tests, so this output will not be considered in the validation. The output vector therefore reduces to

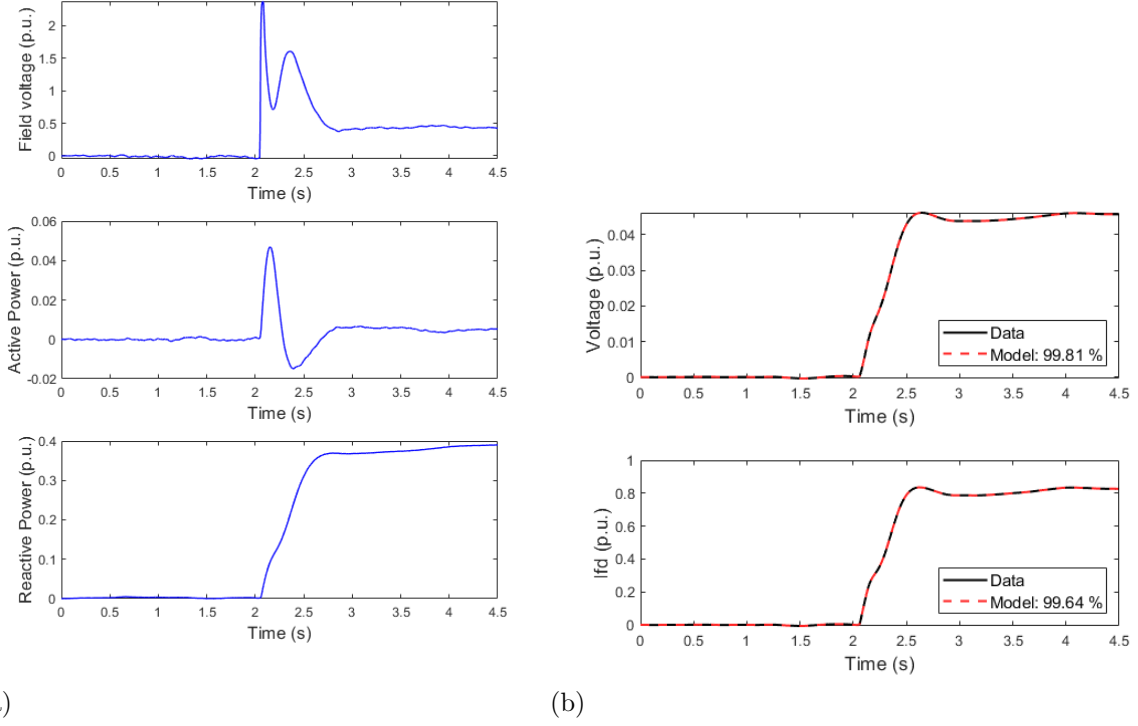


Figure 3.13: Generator validation data and results, where (a) Inputs to generator. (b) Generator output response comparison.

$$y_{generator} = (V_T, I_{fd}).$$

Using $M_{generator}$, We then compute $\hat{y}_{generator} = M_{generator}u_{generator}$. In Figure 3.13a, the different inputs in $u_{generator}$ are represented while $y_{generator}$ and $\hat{y}_{generator}$ are compared in Figure 3.13b. In Figure 3.13b, we here also observe that both entries of $\hat{y}_{generator}$ are almost equal to the entries of the actual output vector $y_{generator}$ ($FIT_{generator} = 99\%$ for both entries). The model $M_{generator}$ can be thus deemed validated.

3.5.3 PSS Model Validation

As explained in Section 3.4, the PSS input vector is $u_{PSS} = [\Delta\omega_m, P_{e,m}]^T$ and its output $y_{PSS} = V_{PSS}$. We compute $\hat{y}_{PSS} = M_{PSS}u_{PSS}$. Since the measurement for $\Delta\omega$ was not collected from the commissioning test, input data for $\Delta\omega_m$ comes from the simulation of the validated generator model. In Figure 3.14a, the different inputs in u_{PSS} are represented while y_{PSS} and \hat{y}_{PSS} are compared in Figure 3.14b. In Figure 3.14b, we observe that \hat{y}_{PSS} is here also almost equal to the actual output y_{PSS} ($FIT_{PSS} = 97.32\%$). The model M_{PSS} can be thus deemed validated.

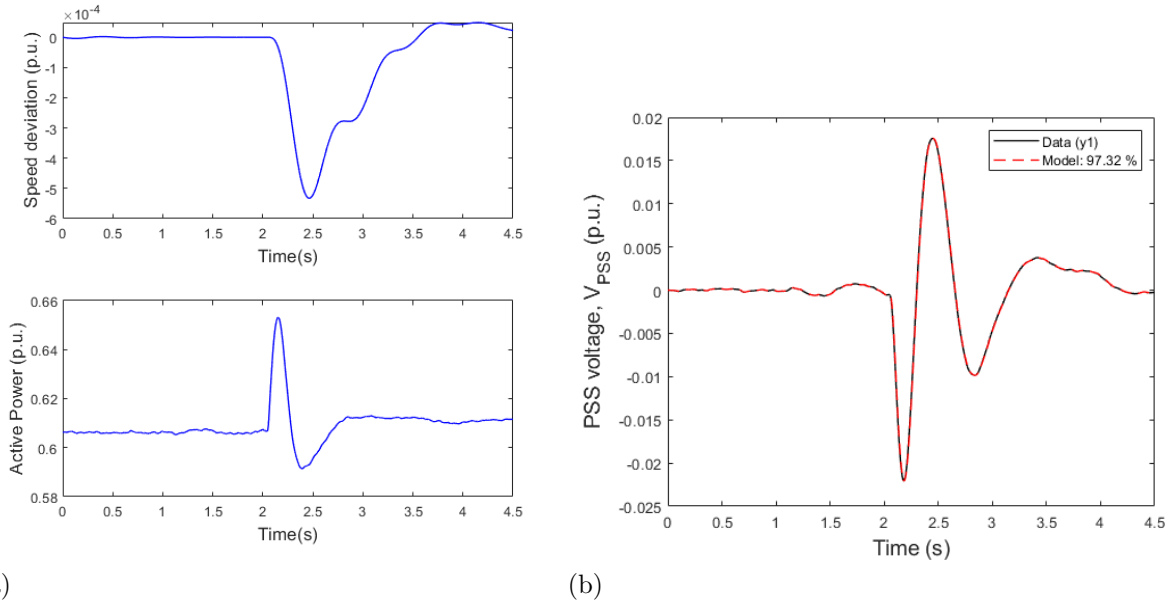


Figure 3.14: PSS validation data and results, where (a) Inputs to PSS. (b) AVR field voltage response comparison.

3.6 Validation Based on Simulation Data

Using Mostar’s measurement data, the commissioning models M_i remain validated. Now we consider a simulation study to show that the method presented in Section 3.3 can detect a change on the system’s dynamics. In this simulation study, the Mostar power plant (with no governor) is represented by the models M_i of the different components validated in the previous section. Some of the parameters of the original models will be modified in the simulator to show that the original models will not longer be validated by the model validation procedure.

As a first example, we increase the value of the generator parameter X_d by 10%. In the simulator of the power plant, the value of X_d is equal to 1.3013 p.u. while, in $M_{generator}$, $X_d = 1.183$ p.u. We collect data on the simulator of the power system by applying, in addition to the step excitation V_{step} , three (small) white noise excitation signals r_k ($k = 1, 2, 3$) at different locations (see Figure 3.15). Using [60], it is clear that these data will be sufficiently rich to re-identify the system if it is necessary.

Since $G_{0,AVR} = M_{AVR}$ and $G_{0,PSS} = M_{PSS}$ in the simulator, we expect that M_{AVR} and M_{PSS} will be deemed validated using the simulation data and that is indeed the case (see Figures 3.18a and 3.18b). As far as the generator is concerned, the results are depicted in Figure 3.16 (representing the input vector $u_{generator}$) and Figure 3.17a representing $y_{generator}$

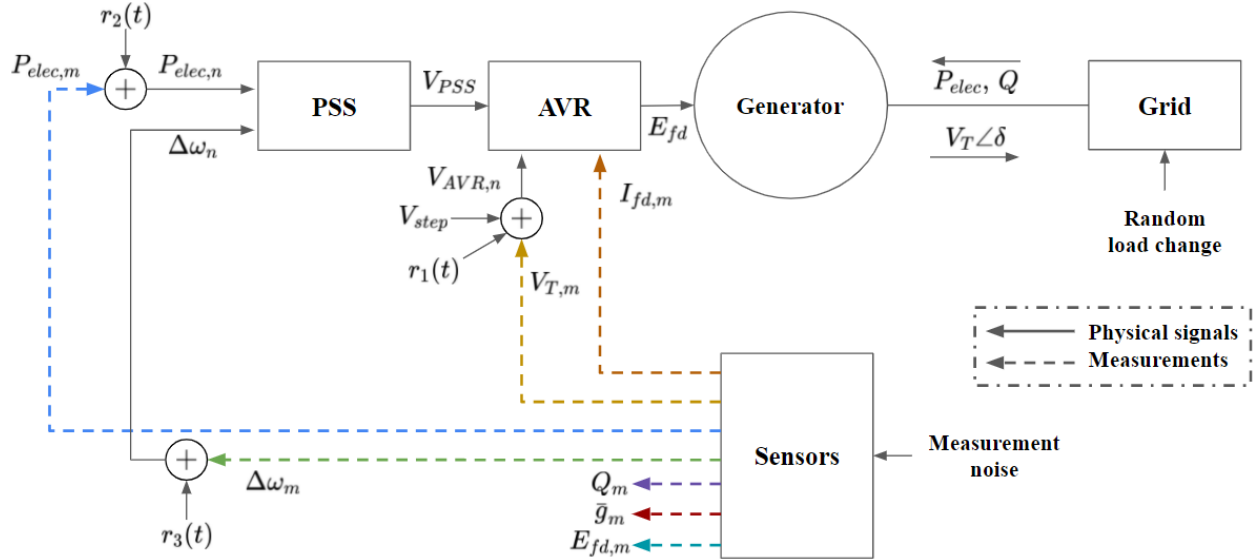


Figure 3.15: Block diagram of the power plant showing the relationships between each component and their inputs and outputs for the Mostar plant.

and $\hat{y}_{generator} = M_{generator}u_{generator}$ where we observe a significant difference between the predicted terminal voltage and the observed terminal voltage. The generator model $M_{generator}$ is thus invalidated and the identification procedure described in Section 3.3.2 is launched to update the parameters of the model. In Table 3.1, the identified parameter vector $\theta_{generator,new}$ is compared to the true value of this parameter vector (the one used in the simulator) and we see that the identification procedure allows to obtain sufficiently close estimates of all parameters. This is confirmed by comparing $y_{generator}$ to $\hat{y}_{generator,new} = M_{generator,new}u_{generator}$ (where $M_{generator,new}$ is the model of the generator with the parameter vector $\theta_{generator,new}$). This comparison is done in Figure 3.17b where we can see that predicted outputs and actual outputs are very close ($M_{generator,new}$ can thus be deemed validated).

Let us finally consider another case that stresses the importance of rich data for the validation step. We now consider a simulator where $G_{0,generator} = M_{generator}$ and $G_{0,AVR} = M_{AVR}$ and where the washout constants of the PSS (see Figure 3.9) are modified with respect to M_{PSS} . We consider here the case where these constants are all doubled and the case where they are all halved. If the excitation is only a step added at the measurement of V_T , the model M_{PSS} remains validated even though $G_{0,PSS} \neq M_{PSS}$, as shown in Figure 3.19a and 3.19b. This is due to the fact that the step on $V_{T,m}$ does not have a strong influence $\Delta\omega_m$, the signal driving the part of the PSS containing these washout constants.

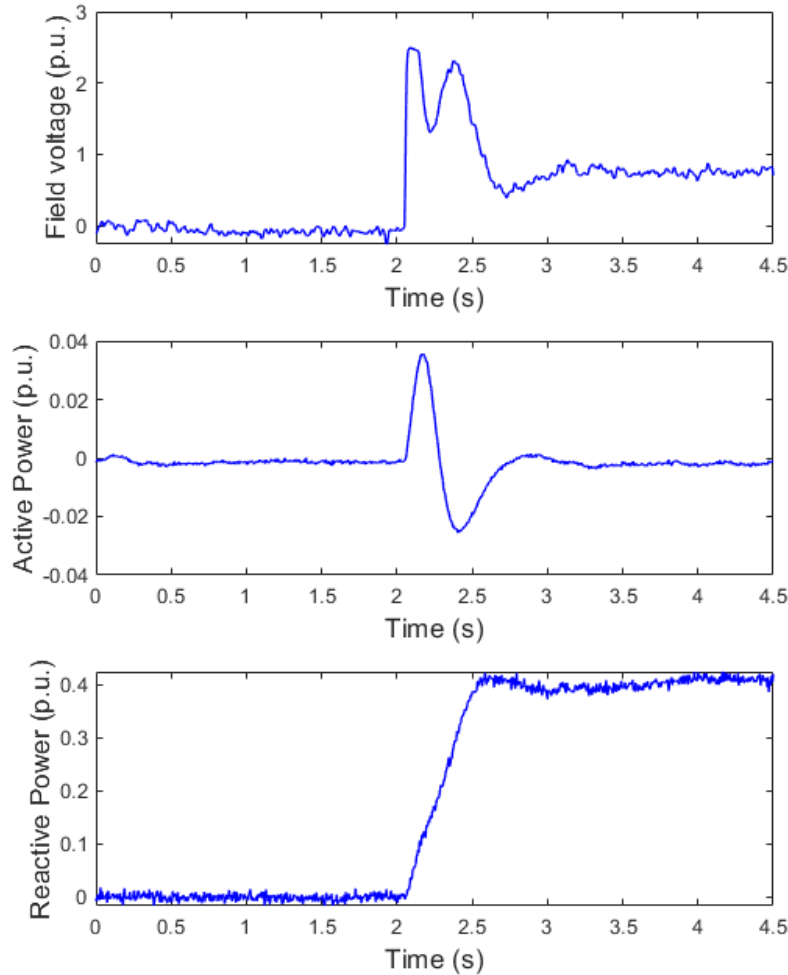


Figure 3.16: Inputs to generator in case of changed parameters.

If we now consider the multiple excitation signals shown in Figure 3.15 (where the excitation r_2 is added to $\Delta\omega_m$), the validation procedure succeeds in detecting the change in the PSS as shown in Figures 3.20a and 3.20b where y_{PSS} is compared with $\hat{y}_{PSS} = M_{PSS}u_{PSS}$ for both halved and doubled time constants respectively.

3.7 Conclusion and Future Works

In this chapter, a methodology for component validation for power plants has been proposed and effectively tested using both real-world and simulation data. The controllers and the generators can be separately validated from each other by having sufficiently informative data for each selected input/output of the system. In the case of invalidated models, a

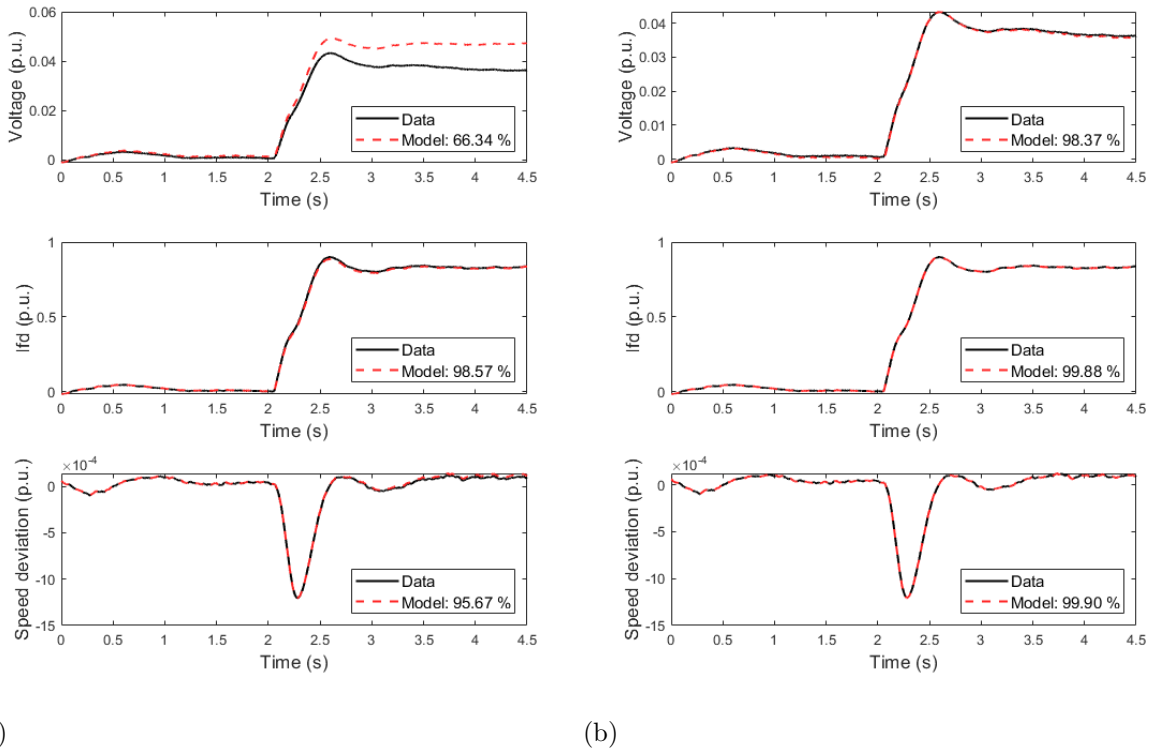


Figure 3.17: Generator validation results for when X_d is increased by 10%, where (a) Invalidated generator model response. (b) Validated generator model response with re-identified models.

Table 3.1: Generator parameters for re-identified model due to 10% increase on X_d .

	X_d	R_a	H	D
True generator parameters	1.3013	0.004799	2.137	0
Identified generator parameters	1.318	0.00471	2.148	0
Relative error (%)	1.28	1.85	0.51	0
	X'_d	X_q	X''_d	X''_q
True generator parameters	0.371	0.62	0.215	0.241
Identified generator parameters	0.367	0.63	0.2166	0.239
Relative error (%)	1.08	1.61	0.74	0.83
	X_l	T'_{d0}	T''_{d0}	T'''_{q0}
True generator parameters	0.1	3.77	0.0552	0.0823
Identified generator parameters	0.1001	3.775	0.0601	0.0775
Relative error (%)	0.1	0.13	8.8	5.83

method to re-validate and re-identify the component model is introduced. This methodology is applied using measurements collected from the Mostar hydroelectric plant.

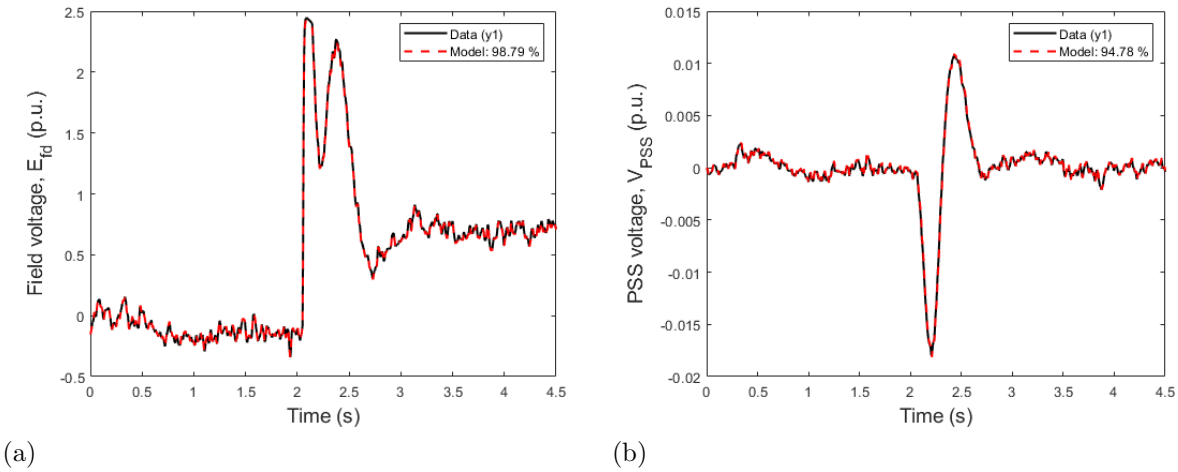


Figure 3.18: Controller validation when there is a change in generator parameters, where (a) AVR validation. (b) PSS validation.

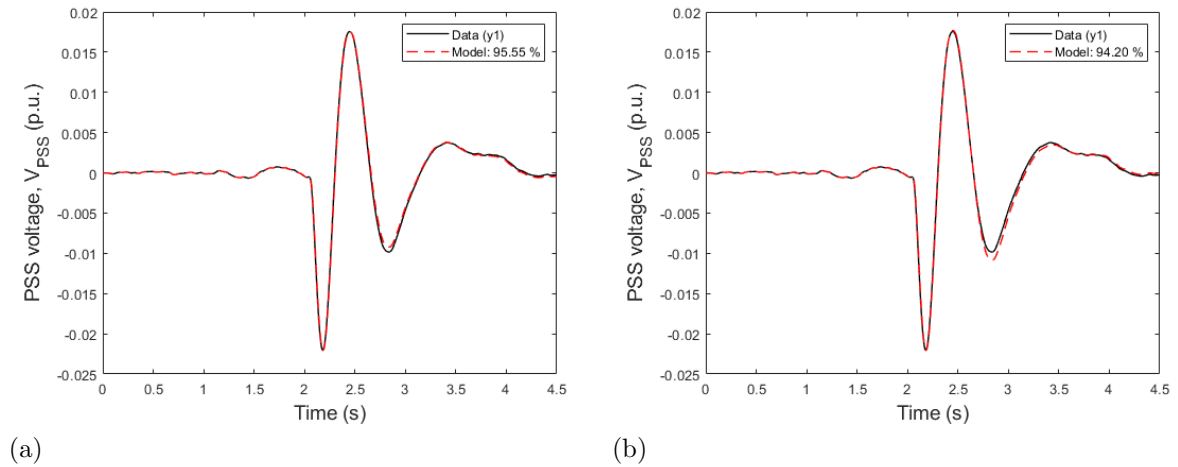


Figure 3.19: PSS validation with only step excitation, where (a) PSS with halved time constants for T_{w1}, T_{w2}, T_6 . (b) PSS with doubled time constants for T_{w1}, T_{w2}, T_6 .

Using test data from the Mostar plant, we can distinguish inputs and outputs to validate each of the three elements in the plant. A good validation of the three elements can be obtained based on the results presented in Sections 3.4 to 3.6. The AVR and PSS have inputs and outputs that can be intuitively chosen to validate the model; however, the inputs and outputs of the generator must be selected to separate the generator from the rest of the grid. When the conventional inputs and outputs are chosen to validate the generator, the dynamic behavior is influenced by the grid. By following the equations of the model instead,

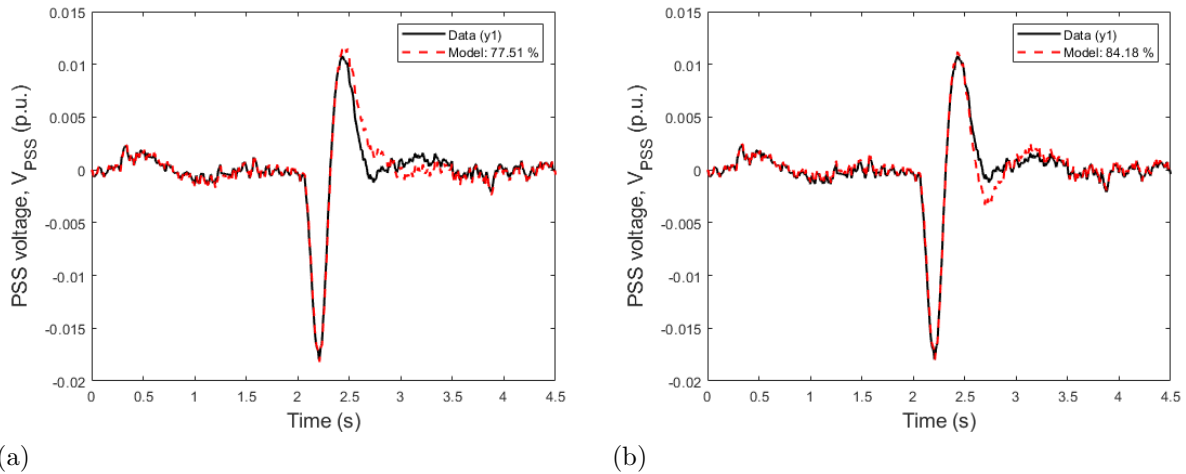


Figure 3.20: PSS validation with both step and white noise excitations, where (a) PSS with halved time constants for T_{w1}, T_{w2}, T_6 . (b) PSS with doubled time constants for T_{w1}, T_{w2}, T_6 .

like shown in Figure 3.4, the component can be effectively isolated. Once the correct inputs and outputs were selected for each component, they each had a high FIT to the data and are considered valid.

The major concern of these systems is that the properties of the generator can change over time [63]. After re-identifying the model, the parameters of the new model are close to the actual system. Since the components can be separately validated, it is only necessary to re-identify and re-validate the affected component. This is incredibly valuable when re-validating the plant using optimization methods to solve the objective function of the problem, as the optimization problem is focused on fewer parameters. This reduces the chance of the solution of the parameter estimation arriving at a local minimum and decreases the time needed to re-identify the model.

Additional cases of the generator parameter changes will be studied in the future when appropriate real-world data is available, analyzing changes to both the excitation system and mechanical system, which will result in changed behavior in the swing equations.

CHAPTER 4

UAV DYNAMICS AND ELECTRIC POWER SYSTEM MODELING AND VISUALIZATION USING MODELICA

4.1 Introduction

4.1.1 Motivation

The increased demand for high-speed mobility and sustainability has led to advancements in aviation technologies, including the research and exploration of intelligent autonomous flying machines, specifically multi-domain Unmanned Aerial Vehicle (UAV) drone modeling. Simulation-based studies are valuable in determining which concepts and methods for eVTOL systems best meet requirements and specifications. Creating physical prototypes for these complex multi-engineering systems early in development can be costly, time consuming, and difficult. Opportunities for testing the existing physical prototypes can be limited, especially in terms of which physical qualities of device are recorded. As a result, well-defined, reliable models are essential for the development of new UAV drone systems and technologies.

This multi-domain model-based systems engineering method is implemented herein for a drone, which has been created using the object oriented modeling language, Modelica [23]. Multi-domain models were created to represent each aspect of the drone, specifically focusing on the mechanical, electrical, and control domains. The primary focus of this chapter is to outline the development of a Modelica library for drone modeling. It shows these models at varying levels of detail under different operating conditions, and discusses the importance of multi-domain models for the design of the electrified propulsion power system. These component models are developed in a manner to easily replace them for different simulation applications, creating replaceable models that are easy to maintain with a broad application scope.

Portions of this chapter previously appeared as: M. Podlaski, L. Vanfretti, H. Nademi and H. Chang, "UAV dynamic system modeling and visualization using Modelica and FMI," in *VFS 76th Annu. Forum & Tech. Display*, Oct. 2020, pp. 1058-1072, doi: 10.4050/F-0076-2020-16289.

4.1.2 Related Works

In recent years, the development of physics-based quadrotor models has been of interest to study with cyber-physical models. These models have primarily been developed using software programs such as MATLAB such as [64]. The MATLAB model in [64] only covers a quadrotor case without option for model visualization with limited flexibility for implementing components with higher modeling fidelity. The application scope of this model is limited; however, it serves as a foundation for the drone model presented in this chapter. It presents a preliminary model for a quadcopter with simplified physics-based models for components such as the motors, which is further explored in this work by including more detailed models to consider non-ideal and other dynamic behaviors.

The quadcopter presented in this chapter was developed using the Modelica modeling language, which has previously been used to develop system level quadcopter models such as in [26]. The system discussed in [26] mainly focuses on multirotor aerial vehicle (MAV) dynamics modeling, while assuming ideal power consumption and operation. All of the dynamics are reduced to one domain to a linear, mathematical model. In this chapter, the drone model is expanded to consider a multi-domain model with a non-ideal power system and switching power electronic components rather than only the MAV dynamics.

A drone PID controller developed using Modelica is introduced in [24]. The drone model presented in [24] assumes that the body is rigid and symmetrical, the center of mass and body fixed frame origin, and the force of each propeller of the aircraft is proportional to the square of the speed of the propeller. The model presented in this chapter does not make these ideal assumptions and accommodates for the non-ideal behavior and different airframe structures, as the mechanical domain is modeled to have flexible parameters for the airframe.

Quadcopter modeling and simulation has been investigated and analyzed using MATLAB and Simulink as per [65], [66]. Both of these studies primarily focus on the analysis of the dynamical model of the quadrotor in the mechanical domain; the dynamic behavior of the electrical system is simplified or entirely omitted from system analysis. The analysis in [66] provides the most complete work regarding multirotor aerial vehicles (MAVs), where the dynamics, advanced state estimation, control and motion planning algorithms for the MAV are derived. This model strictly focuses on the linear dynamic mathematical models, while the models presented in this chapter focus on more detailed dynamic models of the

drone’s power system, including motor models considering electrical effects and the effects of a non-ideal power source on the system.

4.1.3 Chapter Contributions

This work expands on previous physics-based modeling of quadcopter systems focusing on the development of flexible, replaceable models in the electrical domain. The main contributions of this chapter are:

- Proposal of an open-source Modelica library consisting of multi-domain components with varying modeling fidelity used to represent a drone.
- To show the details and mathematical models for each component used as well as results of simulation and animation of these models.
- To perform studies highlighting the importance and impact of adequately modeling the power system of the drone.
- To illustrate the importance of multi-domain modeling for closed-loop system performance.

4.1.4 Chapter Organization

This chapter utilizes the Modelica modeling language to develop the multi-domain model of a drone and all of its respective control components. The chapter is organized as follows. First, the models and components used to create the drone are discussed in detail, showing the mathematical modeling for each component in the drone. Next the animation and simulation of the drone model is discussed. The model is then studied for reference tracking for an ideal flight path focusing on the time specification responses and energy metrics. The impact of the power system modeling level of detail on closed loop dynamics is discussed, as well as models including a payload and the effect of a varying payload on the model.

4.2 Modelica Drone Library

The Modelica Drone Library was developed using Modelica in the Dymola software environment. The library is open-source and can be found at [67]. The functionalities of the

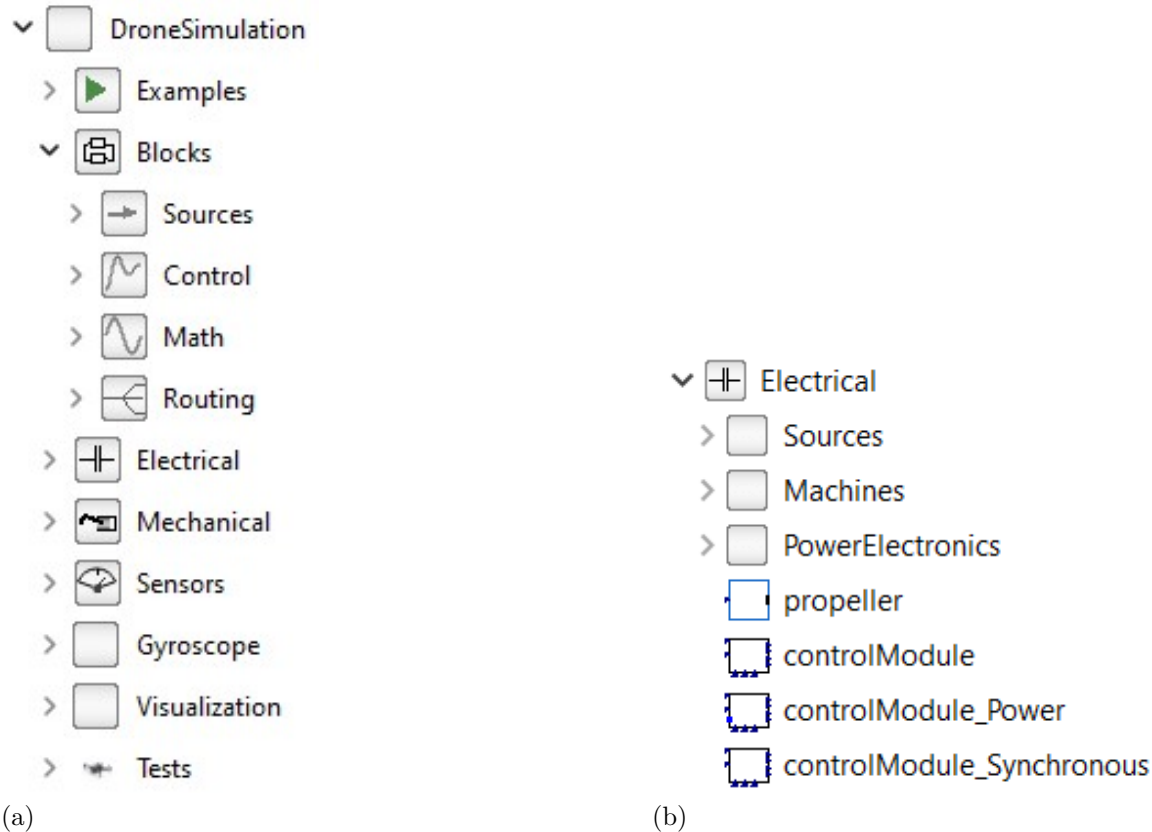


Figure 4.1: Drone library file structure: (a) Library package hierarchy. (b) Electrical package hierarchy.

library are divided into different packages, or sub-directories, consisting of blocks, sensors, electrical components, mechanical components, and examples as shown in Figure 4.1a. Each of these packages contain the component models and functions of the components needed to build the drone model. The library is dependent on the Modelica Synchronous Library [68], Modelon Base Library [69], and Modelica Standard Library [38] to run certain model variants and configurations. The Modelica Standard Library (MSL) is a library consisting of standardized models maintained by the Modelica Association [38]. The drone model used in the examples is based on the Otus Quadcopter [70]. The model’s main limitations arise from assuming that the drag and power of the quadrotor is not affected by the altitude of flight.

4.2.1 Blocks

The `Blocks` package contains signal sources, control models, math functions, and routing functions. The `Sources` are the customized signal blocks that can be used to create

flight paths for the drone, which includes a circular and straight line flight path. In addition to using these pre-existing flight paths to control the drone, data obtained from a physical system experiments can be defined in a table consisting of time and physical (XYZ) position. The **Control** sub-package contains models for a discrete PID controller used to control the drone. These models utilize the Modelica Synchronous Library [68] to precisely define and synchronize the sampled data components with different sampling speeds in the controller and to improve simulation speed. The **Math** sub-package has the customized math functions used in the controller, and the **Routing** sub-package features functions for expanding the data from sensors to be used in the three dimensional plane.

4.2.2 Sensors

Custom sensor functions for the drone that track the position and acceleration of the drone are in the **Sensors** sub-package. These sensors are shown in Figure 4.2 as the **GPS** and **Accelerometer** components, which connect the drone chassis to the main controller. These components are multi-domain, where they measure the acceleration and relative position coordinates of the drone in the mechanical domain and then output those values as a **real** signal to interface with the controller.

The **GPS** model uses a relative position sensor to tracks the position of the drone with respect to the ground. It couples to the mechanical domain in and uses that information to change the flight path in the controller block, MCU. The **Accelerometer** component uses a relative angle sensor to track the pitch, yaw, and roll of the drone’s airframe. The sensor links the mechanical domain to a **real** signal that will be used to control the drone via the MCU.

4.2.3 Electrical

The **Electrical** package contains models for the DC machines and power system used in the drone model, split into sub-packages as shown in Figure 4.1b. The **Sources** sub-package contains models for the batteries used in the non-ideal power system, **Machines** sub-package has models for the motors driving the propellers, and **Power Electronics** includes converter and switch models for the drone power system. These models are implemented in a manner where they can be easily replaced to consider different levels of dynamics and losses without having to restructure the model.

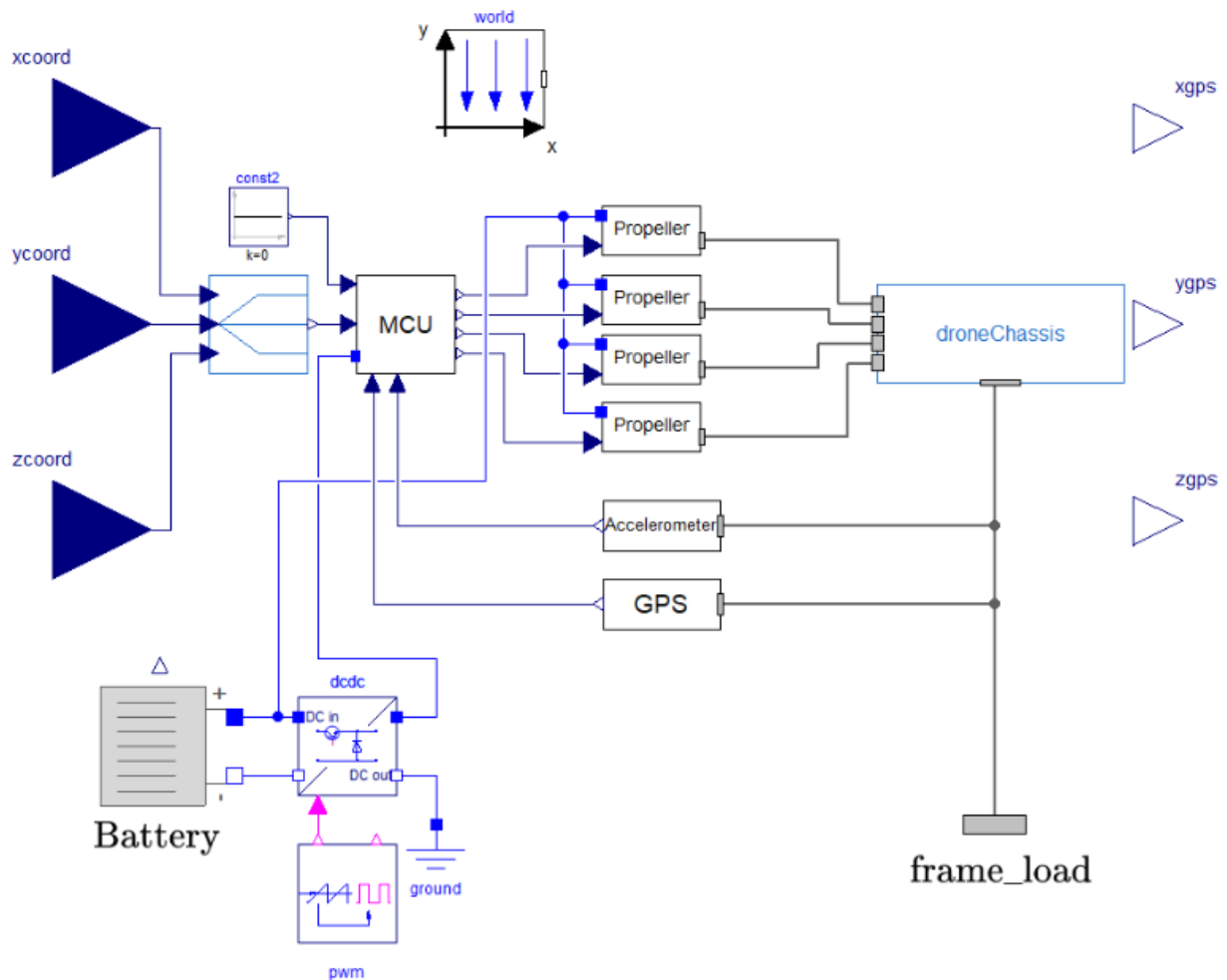


Figure 4.2: Complete drone model consisting of propellers, motor, controller, and chassis with battery power system. Inputs come from x, y, and z coordinate location commanded by the user.

4.2.3.1 Sources

The `Sources` sub-package contains the models for the drone's power system. The example power system presented in this work is parameterized according to the Otus Quadcopter [70] power system; however, these components can be reconfigured to represent any drone power system. The Otus Quadcopter is powered by a 3S LiPo battery and operates at two different voltage levels to satisfy the electrical operational requirements of the various components. The connections between the battery and sensors for the power system of the drone are shown in Figure 4.3. The battery is connected to a DC/DC step down converter to provide 5V connections to power the Raspberry Pi, Pixhawk flight controller, and LCD Display. The motors are directly connected to the battery and operate at 11.1V. The

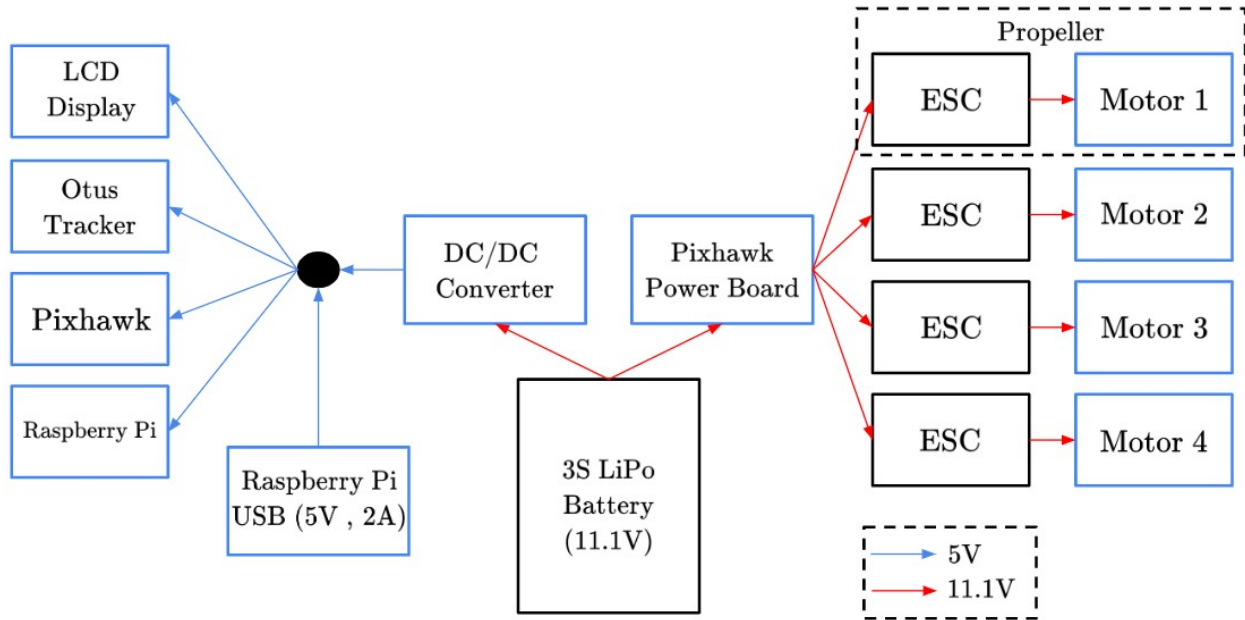


Figure 4.3: Otus Quadcopter power system block diagram.

Otus tracker is represented in the Modelica model as the `GPS` and `Accelerometer` component; however these components do not consider the electrical effects on the sensor accuracy because it is outside the modeling scope.

The electrical architecture of the Otus quadcopter in Figure 4.3 is the same as the Modelica model in Figure 4.2. It consists of a battery that is connected to a DC/DC converter to supply power at a controlled voltage level of 5V to the controller, which is labeled as `MCU` in Figure 4.2. Other auxiliary components are powered at 5V, such as the LCD screen showing the operational status of the drone. The propellers, which contains the speed controlled (`ESC`) and the motor, are connected directly to the battery as shown in both Figures 4.2 and 4.3. These components operate at 11.1V, as they are directly connected to the battery.

The drone's battery model shown in Figure 4.4 is derived from the Modelon Base Library [69]. It contains an internal resistance and stack voltage that discharges according to the extended Shepherd equations for battery pack EMF [71]. The voltage of the cell is defined by Equation 4.1, which use discharge gain K_{bat} and maximum cell voltage $v_{Cell_{max}}$ to determine the cell voltage v_{Cell} as a function of the battery's state of charge SoC . The SoC is calculated using Equation 4.2, which is the ratio of current battery charge to maximum battery charge. The current discharged by the battery is a function of the stored charge Q

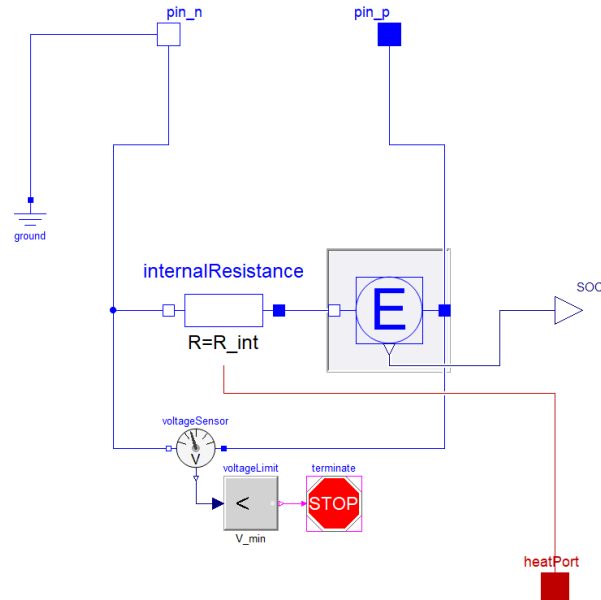


Figure 4.4: Battery from Modelon Library Suite.

as shown in Equation 4.3. The total voltage of the battery is defined in Equation 4.4 by the number of cells in series and voltage per cell, while Equation 4.5 determines the charge capacity of the battery if there are cells placed in parallel. The batteries are assumed to only discharge during flight, so charging dynamics are omitted from the model. In future development of the system, more detailed battery dynamic behavior can be included such as an electro-chemical model.

$$v_{Cell} = v_{Cell_{max}} - \frac{K_{bat}}{SoC} \quad (4.1)$$

$$SoC = \frac{\min(Q, Q_{bat})}{Q_{bat}} \quad (4.2)$$

$$\frac{dQ}{dt} = i \quad (4.3)$$

$$v = v_{Cell} * ns \quad (4.4)$$

$$Q_{bat} = Q_{cell} * np \quad (4.5)$$

The battery used in the presented example is a Li-Ion 18650 with three cells in series, as that is the same battery required to power the Otus Quadcopter. This is modeled such that the maximum, nominal, and minimum voltages of the cell are 4.2 V, 3.7, and 3.0 V respectively. In Equation 4.2, Q_{cell} is 9360 C for a Li-Ion 18650 battery. The internal resistance of the battery shown in Figure 4.4 is 0.1 Ω .

4.2.3.2 Machines

Multiple motor models of varying degrees of complexity are included in the library, expanding upon previous works such as [64]-[66] where only the most simplified motor dynamics are considered. The models offered in the Modelica Drone Library include different types of DC machines along with a simple, ideal motor. The simple motor only utilizes torque τ , linear force f , motor speed ω , and current i to control the motor according to Equations 4.6, 4.7, and 4.8. There are no electrical, thermal, or mechanical losses considered in this model. This model also neglects any electrical dynamics in the system caused by internal inductances.

$$\tau = K_\tau i \quad (4.6)$$

$$J_p \frac{d\omega}{dt} = \tau - b\omega^2 \quad (4.7)$$

$$f = K_f \omega^2 \quad (4.8)$$

Most UAV systems use brushless DC motors for their high efficiency and high power to size ratio, so the most complex DC motor included in the library is a permanent magnet DC machine adapted from the Modelica Standard Library [38]. The model for the permanent magnet DC machine is shown in Figure 4.5, which models the electrical, rotational, and thermal behaviors in the machine. The dark blue lines represent electrical connections in the machine. The gray lines represent rotationally linked components, which covers behavior such as frictional losses due to the air gap in the machine and the rotation of the machine. These domains are connected through the air gap of the motor creating a magnetic field to turn the rotor.

The air gap for this machine has an electrical flux Ψ_e that is linearly dependent on the excitation current I_e , shown in Equation 4.9. The armature voltage V_a , which is the voltage from the **Speed Controller** component in Figure 4.6, relates to the speed of the machine ω using Equation 4.10. The red box in Figure 4.6 contains the components used to calculate the thrust. Equation 4.11 determines the torque τ applied to the propellers. The mechanical model in Figure 4.5 includes the inertia of the stator J_s (which is fixed to the body) and the inertia of the rotor, J_r . This is important, as it allows to specify both stationary and rotational masses that will ultimately impact the drone's closed-loop behavior.

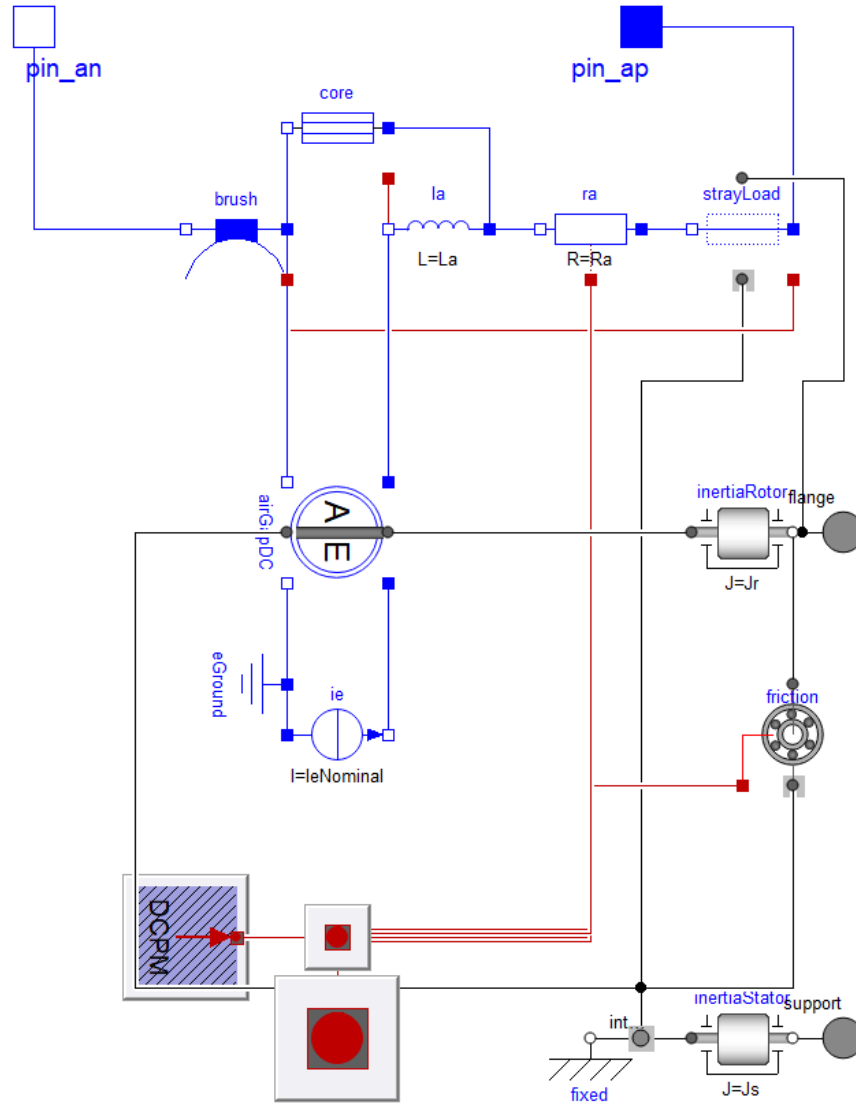


Figure 4.5: Modelica Standard Library permanent magnet DC machine model.

$$\Psi_e = L_e I_e \quad (4.9)$$

$$V_a = n \Psi_e \omega \quad (4.10)$$

$$\tau_e = -\tau = n \Psi_e I_a \quad (4.11)$$

4.2.3.3 Power Electronics

The `Power Electronics` sub-package contains the models for the DC/DC converters and switches used in the drone. This includes the buck DC/DC converter used in the power system, which is shown in Figure 4.7. The buck converter interacts with the electrical and

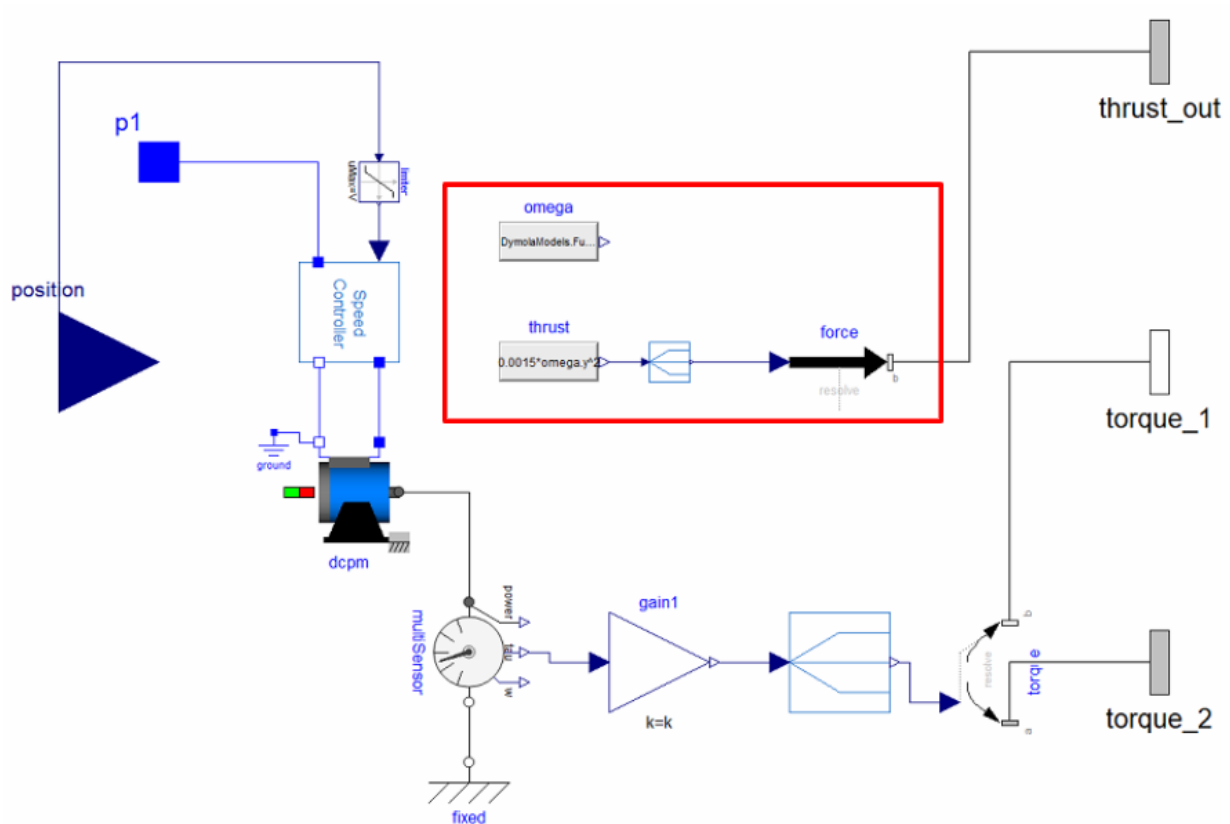


Figure 4.6: Model for the motor in the propeller system. The red box contains the components used to calculate the thrust.

control domain, where the voltage and current are communicated between other models via the blue pin connections `dc_p1`, `dc_p2`, `dc_n1`, and `dc_n2`. The pink lines send boolean signals to control the states of the transistor and the diode, which is referred to as part of the control domain in the rest of the chapter. There is also a `heatPort` component (shown in red) that can communicate heat flow and temperature between other components in the thermal domain, but the thermal domain is omitted from this analysis because it is currently outside of the modeling scope. In future work, the thermal effects can be considered for similar analysis and simulation studies.

Averaged converter model components are also available in this package, but they are currently not used in the studies in this chapter. In previous works focusing on drone modeling, the power electronics have been omitted entirely from the system level model. The power electronics introduce electrical dynamics and losses into the system that can enrich system studies and give insight on how the switching behavior affects other components (which will be discussed in Chapter 5).

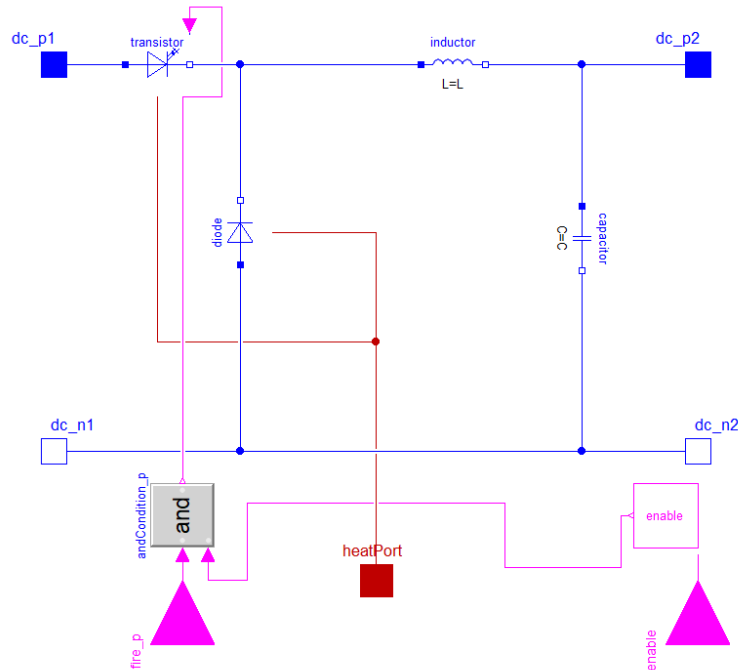


Figure 4.7: Buck converter model in Dymola.

4.2.4 Controllers

The controller for the drone is shown in Figure 4.8. It consists of multiple discrete PID controllers, which are configured using the Modelica Synchronous Library [68] to ensure fast simulation compiling and integration times for models with discrete control components that are being sampled at different rates. The drone library also includes a controller that does not utilize the Modelica Synchronous Library if it is unavailable or more conventional control modeling is desired. By implementing the controller, the system forms a closed loop with tracking of the coordinate position, pitch yaw, and roll of the drone.

In Figure 4.8, the `GPS[]` input translates the XYZ coordinate position of the drone's center of mass into three vectors that provide negative feedback to the position vectors from the user input `position[]`. This ensures that the coordinate position of the drone can follow the user input with a small error. This signal is then used as the input for another PID controller with a reference signal of the relative angles in the X, Y, and Z direction of the drone. This determines the pitch, roll, and lift of the drone. The yaw input of the controller uses a reference yaw signal compared to the gyroscope measurement. In the cases presented in this chapter, the yaw is desired to be 0 to prevent the drone from spinning around the Z axis. Each output of the controller, `y`, `y1`, `y2`, and `y3` takes into account the

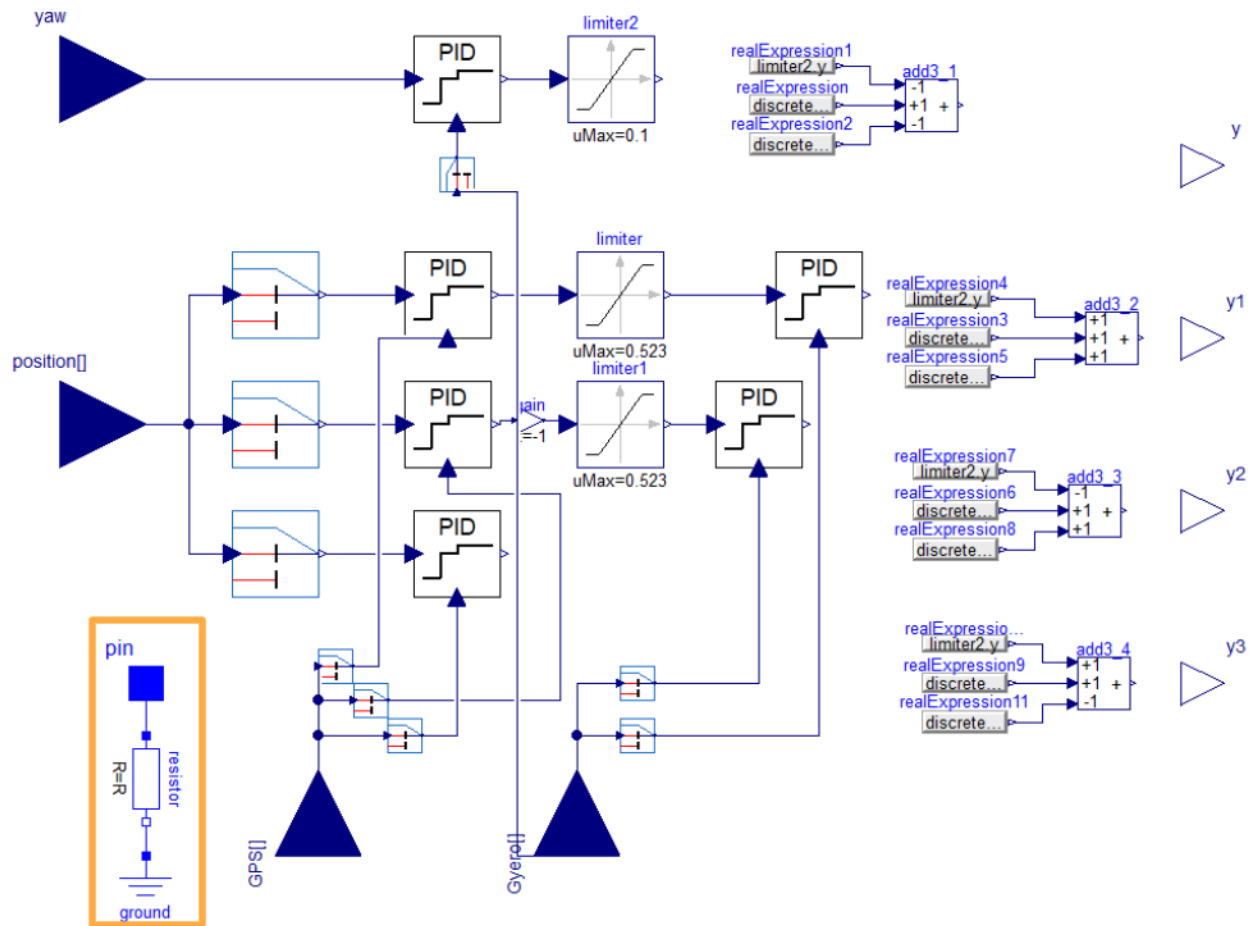


Figure 4.8: Drone controller model in Dymola.

lift and the yaw of the drone; propellers diagonal to each other account for either pitch or roll for balanced operation. The electrical pin, `pin`, represents the electrical losses in the model. The electrical loss model of the controller is denoted by the orange box.

When the power system is accounted for in the model, the power consumption of the controller is modeled as a resistive loss. This is shown as the electrical connection `pin`, 4.2. It operates at 5V and is connected to the output of the buck converter.

The speed controller is also included in the `Controllers` package. It is used in the motor model to adjust the position from the controller by the voltage supplied by the battery. In Figure 4.6, this component is the `Speed Controller` connected to the electrical inputs of the DC permanent magnet machine with external connections to `position` from the controller and `p1` from the battery. The contents of the speed controller is shown in Figure 4.9. The input `position` is the signal from the controller to determine the torque produced by the motor, the input `battery` is an electrical input containing the voltage and current

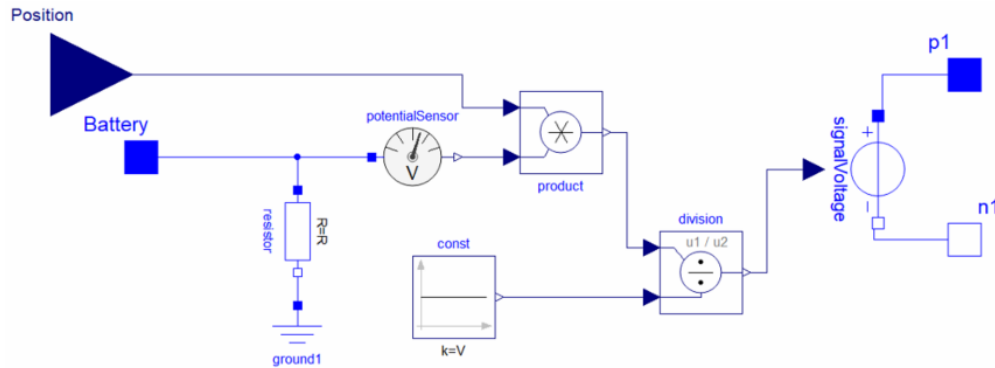


Figure 4.9: Speed controller model in Dymola.

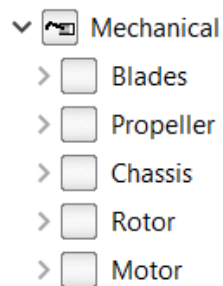


Figure 4.10: Mechanical package setup.

output from the battery. The `const` block is a reference voltage representing the nominal voltage of the battery. As the battery discharges, the potential sensor adjusts the ratio of position. This function assumes that the battery voltage and motor power reduction are linear.

4.2.5 Mechanical

The `Mechanical` package contains the models for the quadcopter propeller, chassis, rotor, and motor. The sub-packages in the `Mechanical` package are shown in Figure 4.10. The components included in this sub-package also are used for the animation and visualization of the drone.

4.2.5.1 Blades

The `Blades` package contains the models of the propeller blades. The propeller blades are modeled as two multi-body masses coupled mechanically to the rotor. These components are from the MSL's Multi-Body Library [72]. Figure 4.11 shows the model used to simulate and animate the blades. In this model, the relationship between angular speed of

the propeller shaft and the thrust is assumed to be linear.

In Figure 4.11, the `fixedShape` component links to a 3D object (.STL) file, which will be used to animate the drone's flight when it is simulated in Dymola. This 3D object file can be changed to represent the blade configuration of any type of drone. The `bodyShape` are single-point mass components that couple to the rest of the system as a function of 3D orientation, cut force, and cut torque.

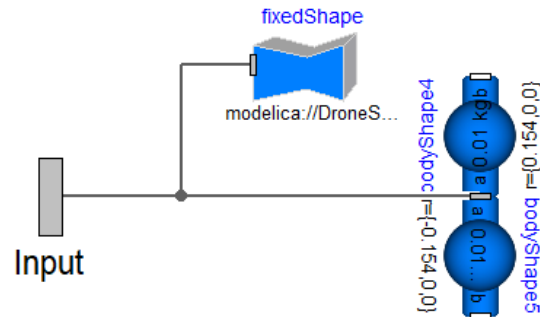


Figure 4.11: Blade model in Dymola.

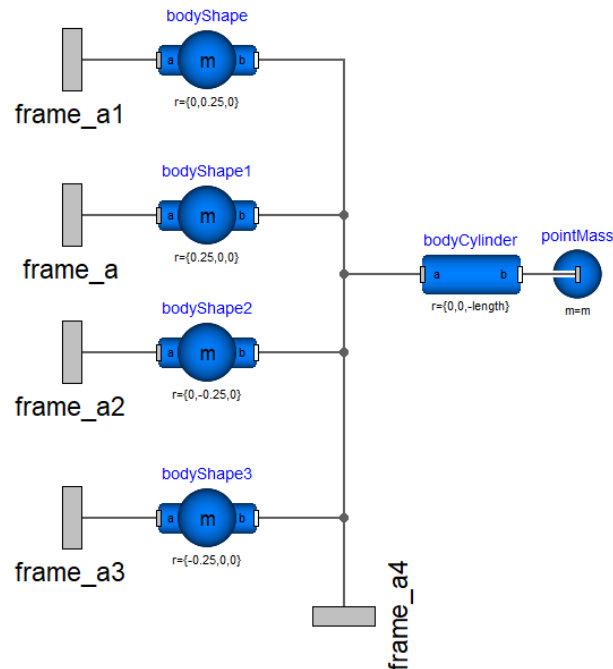


Figure 4.12: Chassis model in Dymola.

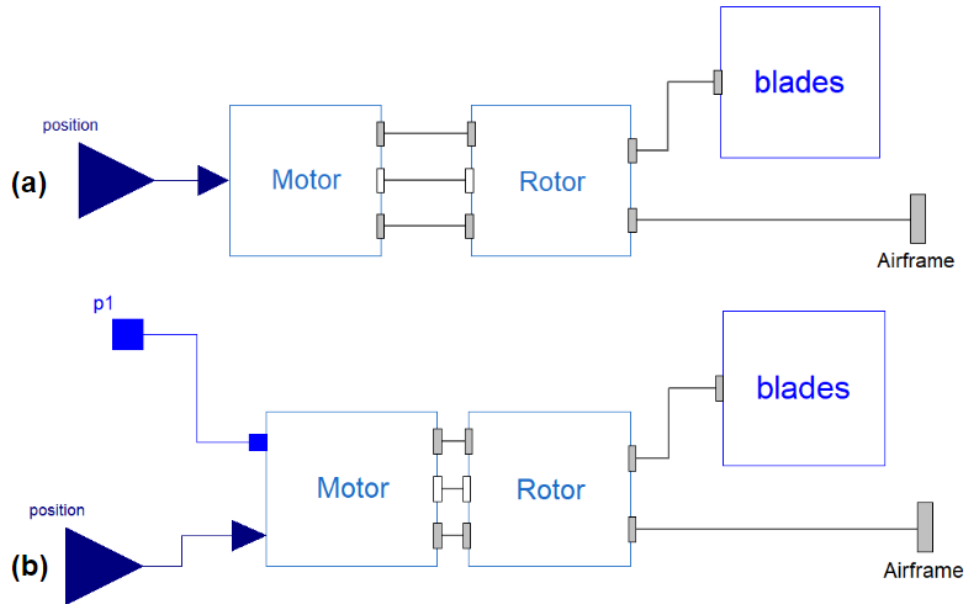


Figure 4.13: Model for the propeller system containing mechanically linked motor, rotor, and blades (a) without; (b) with power connections.

4.2.5.2 Propeller

The `Propeller` models contain the motor and the propeller blades controlled by the relative angular velocity of the blades. The propeller model in Dymola is shown in Figure 4.13. In Figure 4.13, the propeller system is shown to be mechanically linked between the motor, rotor, and propeller, while using a real signal that provides the reference signals used to control the motor. This model can be used to rotate the propeller both clockwise and counterclockwise by adjusting the value of `gain1`. The drone chassis is modeled as a point mass connected to the airframe, which will have the propellers connected at the end. These models are reusable as the weight and size of the chassis can be easily altered to fit the parameters of any quadcopter. Figure 4.13(A) is used when an ideal power source is modeled, while Figure 4.13(B) is used when a non-ideal power system model is included in the system.

Another notable feature seen in the drone model is that multi-domain interfaces can be used. In Figure 4.6, for example, the blue connections represent real signals and the gray connections represent multi-body mechanical variables. This allows for better organization of the models and for different variables to be interfaced between components. For example, in the electrical domain, these interfaces to couple the voltage and current between connected components. When a non-ideal voltage source is used, the propeller will be represented by

Figure 4.6 and p1 must be connected to an external power source.

4.2.5.3 Chassis

The chassis sub-package contains the model of the drone airframe. Similar to the blade models, the chassis is represented by single point masses with a `fixedShape` component to integrate the 3D object file of the drone chassis into the rest of the model. The chassis is mechanically linked to the propellers, as shown in Figure 4.2, where each of the `frame` components are connected to a propeller.

The drone chassis multibody masses in Figure 4.12 follow the mathematical model in Equation 4.12. Each inertia tensor I can be defined individually in this system, which reduces to Equation 4.10.

$$\tau = I_{XYZ} * \alpha = \begin{bmatrix} I_{XX} & 0 & 0 \\ 0 & I_{YY} & 0 \\ 0 & 0 & I_{ZZ} \end{bmatrix} \begin{bmatrix} \dot{\omega}_X \\ \dot{\omega}_Y \\ \dot{\omega}_Z \end{bmatrix} \quad (4.12)$$

4.2.5.4 Rotor

The `Rotor` package contains the rotor models, as shown in Figure 4.14. The rotor is linked mechanically to the motor, airframe, and blades. The multibody connectors labeled `torque_1`, `torque_2`, and `force` are connected to the `torque_1`, `torque_2`, and `thrust_out` connectors respectively on the motor in Figure 4.6. This links the torque from the machine to the revolute. The speed at which the revolute is turning is determined by a scaled measurement of the relative angular velocity between `torque_1` and `torque_2`. The red box in the lower left corner of the model represents the calculations needed to determine aerodynamic forces applied to the rotor.

The aerodynamic forces are applied using the ω^2 model in Equations 4.13 and 4.14. Equation 4.14 is used for the aerodynamic torque is calculated here, and the thrust is calculated in the component `aero_torque`. The thrusts are coupled to the motor component using the multi-body connector `force`. The thrust is calculated in Figure 4.6 using the real

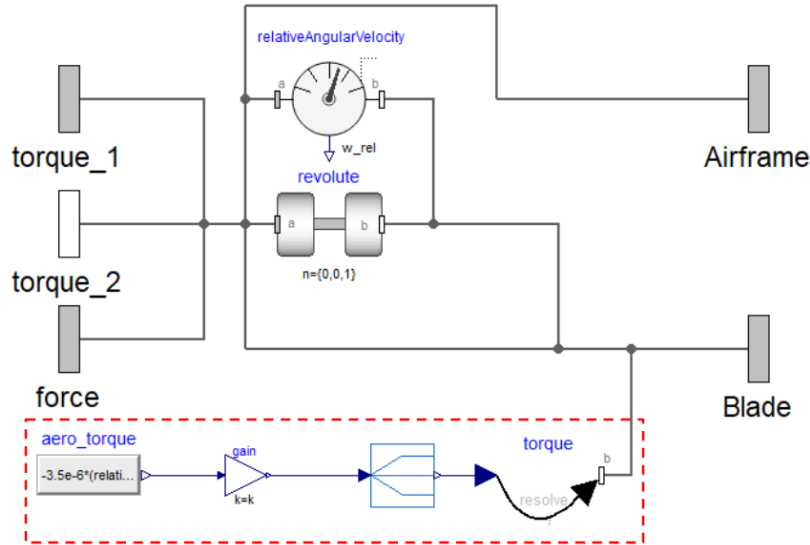


Figure 4.14: Rotor model in Dymola. The aerodynamic forces applied to the rotor are located in the red box.

expression block `thrust`, which uses Equation 4.14 and 4.15

$$\tau_h = 0.0015\omega^2 \quad (4.13)$$

$$\tau_o = (3.5 \times 10^{-6})\omega^2 \quad (4.14)$$

$$P_p = \tau\omega \quad (4.15)$$

4.2.5.5 Motor

The machines included in the `Machines` sub-package are configured to link the machines to the controller and `revolute`. The machine output is controlled by a `real` signal from the controller, as shown in Figure 4.2. In Figure 4.6, the machine output is represented in terms of rotational connections, so the torque sensor, force, and torque components create the multi-body connections necessary to link to the rotor. The `gain1` component in Figure 4.6 adjusts the direction the motor turns, where a gain of “1” turns the motor clockwise and “-1” turns the motor counterclockwise. The motor also contains a speed controller that uses the position signal from the main controller and the battery state of charge. This controls the voltage supplied to the motor and scales it to the available battery voltage, which is connected with electrical pin `p1`.

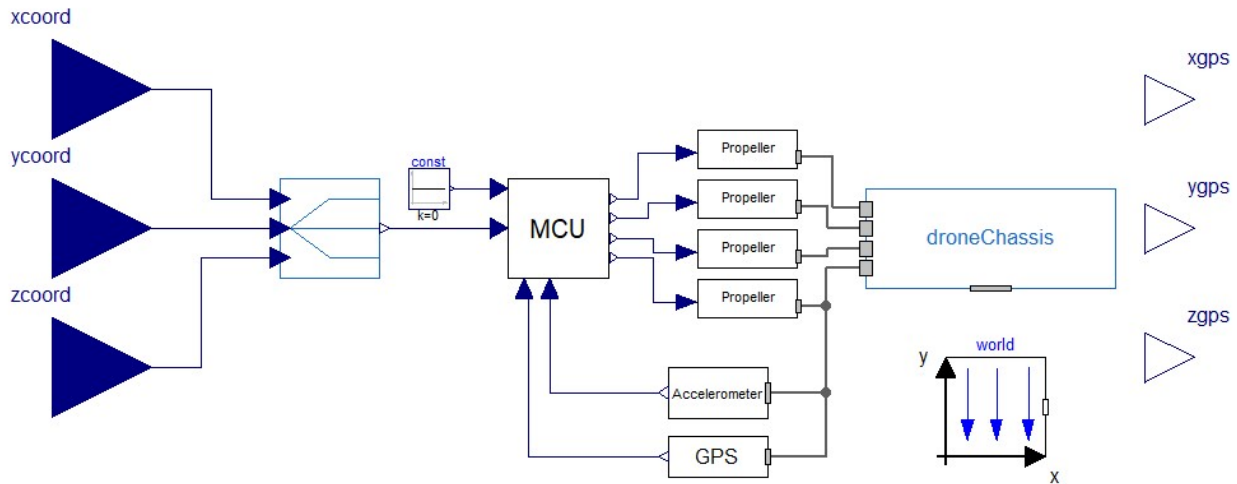


Figure 4.15: Complete drone model consisting of propellers, motor, controller, and chassis with ideal power system.

4.2.6 Examples and Test Systems

All of the components described are configured to create the simple drone model shown in Figures 4.15 and 4.2. Figure 4.15 shows the drone with an ideal power source, while Figure 4.2 shows the drone when a battery is added to the system. The system in Figure 4.2 also has the `frame_a1` connector that can be linked to additional external payloads, such as a camera. The drone is tested in models configured in the `Examples` package. These examples include using different input signals to control the inputs `xcoord`, `ycoord`, and `zcoord`. These input signals can be from the signals provided in the library, signals from the Modelica Standard Library, experimental data, and custom signal functions defined by the user. The inputs for the model can also be left disconnected from any inputs and compiled as a Functional Mock-up Unit (FMU). By selecting this option, the model can be exported to other software tools for analysis and simulation.

The model tests for visualization and VR interaction are saved in the `Tests` package. These models are developed from the same components in the library previously described with the ability to simulate and animate objects from CAD files and other pre-defined shapes using the DLR Visualization library [73]. These conditions are tested using the models saved in the `Examples` package. They are controlled using a ramp signal (shown as `ramp1`) in the Z-direction to linearly move the drone up to a height of 5m while fixing the X- and Y-coordinates to a constant value, which is shown in Figure 4.16.

The `world` component in Figures 4.2 and 4.15 applies the gravity field to every multi-

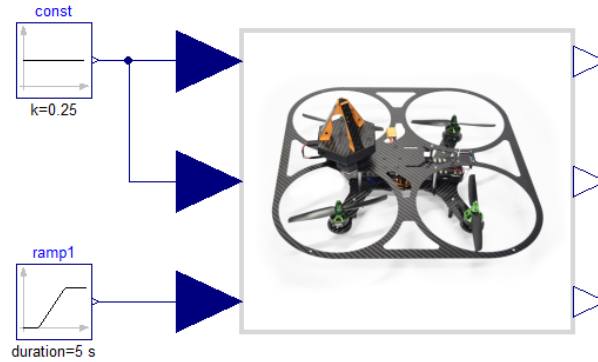


Figure 4.16: Drone model configured for 1 m/s 5 second ramp input in the Z-direction test.

body component in the negative Z-direction. It is not connected to any of the bodies since the MSL multi-body library package has been configured to propagate gravitational parameters into each component.

4.3 Drone Visualization and Animation

When the drone is simulated, the behavior can be observed as an animation. The drone has been configured to use 3D Object (.STL) files to represent the propellers and body of the drone in an animation of the drone, which appears when the drone is simulated. The 3D Object files are defined in the chassis and blade models in Figures 4.11 and 4.12 as `fixedShape` components.

The initial position of the drone is shown in Figure 4.17. The propellers move over time, as shown in Figure 4.18. These snapshots were taken while the drone was hovering a height of 5m, where the drone oscillates slightly in the Z-direction while spinning the propellers. This oscillation is shown in Figure 4.20 occurring between 5 and 10 seconds.

The propellers spinning are also shown in Figure 4.19, where the drone is steadily moving to a height of 5 m over a 5 second period, following the same flight path outlined in Figure 4.16. The trace of the propeller shows that the drone oscillates in the Z-direction due to the dynamic response of the controller, as discussed in a study below.

4.4 Studies

The developed library contains models for varying degrees of complexity for the electric power system. The lowest level of complexity might include the ideal version of the compo-

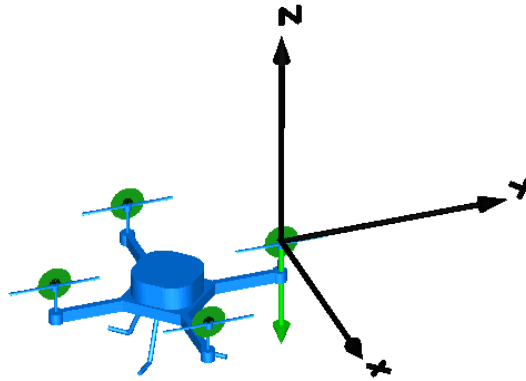


Figure 4.17: Drone animation at time = 0 seconds.

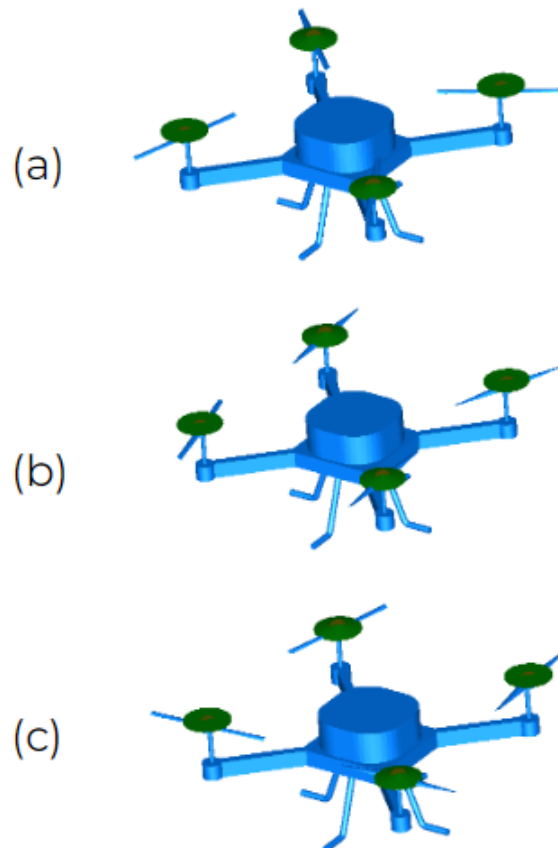


Figure 4.18: Drone animation at time (a) 1 seconds at 1 m (b) 1.5 seconds at 1.5 m (c) 2 seconds at 2 m for an ideal motor and ideal power system.

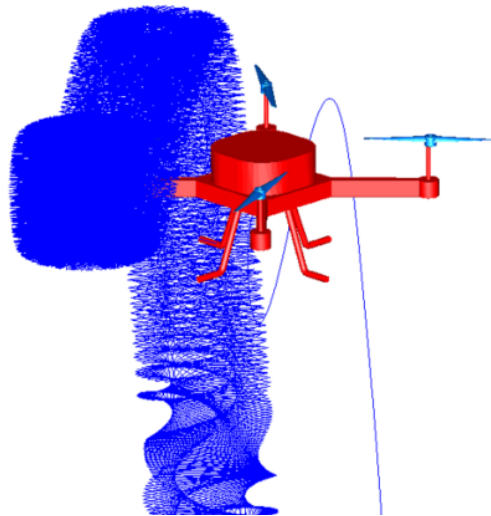


Figure 4.19: Drone animation with the path of the propeller shown as a trace for the flight path in Figure 4.16.

ment, while the most complex models consider losses and non-ideal behavior. In this case, the drone is tested using an ideal power system with a first order motor model, a DC machine with losses and an ideal power system, a battery and DC machine with losses, and the battery with a converter and DC machine with losses to demonstrate the effects of the modeling complexity of each of the components on the drone operation. This helps in determining the electric power requirements that will arise from different operating conditions. In this section, several analysis are made with the drone subject to a flight path with and without a payload applied in different configurations. The system components are parameterized with the values from the Otus quadcopter [70].

4.4.1 Ideal Flight Path Reference Tracking

The system is first studied using an ideal flight path command for four different system configurations: (1) **ideal power system and motor**, (2) **ideal power system with a permanent magnet DC machine with losses**, (3) **non-ideal power System and permanent magnet DC machine with losses**, and (4) **non-ideal power system, permanent magnet DC machine with losses, and DCDC buck converter**. This allows us to compare the drone's dynamic response, power consumption, and losses at various levels of modeling fidelity for the same flight path.

4.4.1.1 *Ideal Power System, Ideal Motor*

The simplest representation of the drone is modeled with an ideal motor and voltage source power system. This assumes that the voltage and current supplied to the system is constant and can consistently meet the needs of the system, so all battery dynamics are neglected. The entire quadcopter system modeled with the ideal components is shown in Figure 4.15.

Figure 4.20 shows this model is simulated under ideal conditions when the Z-position of the controller is subject to a ramp signal from the ground to 5 m. The drone overshoots the position in the Z-direction when the drone reaches its final hovering point by 5.43%. The low damping in the ideal motors also causes the oscillation in the X- and Y-direction. Figure 4.22 shows the effect of the motor damping on the force applied to the propeller blades in the Z-direction. The damping constant in the motor with losses is higher than the ideal case, which is why there is some oscillation at the beginning of the simulation as well as a larger force to stabilize the system during the ramping period. The oscillations in the beginning of the simulation for the DC motor is also due to the charging of the inductances in the motor. The drone is modeled to take the gyroscopic position into account when determining the XYZ-coordinate position of the drone (as shown in the controller in Figure 4.8), so the oscillation causes the change in position in the X- and Y-direction.

4.4.1.2 *Ideal Power System, Permanent Magnet DC Machine with Losses*

The simplified DC machine model described in the previous section is replaced with a permanent magnet DC machine from the Modelica Standard Library [38]. This introduces both resistive losses and dynamics created by the motor inductances to the system. It is assumed that an ideal lossless power supply holds the voltage at a constant value and can provide the necessary current throughout the duration of the test.

When the drone is placed under the same operating conditions as before, it shows better stability in the X- and Y-direction and overshoots less when the drone reaches the hovering height of 5 m. The drone overshoots the hover height by 1.1% for this configuration. The position of the drone over time is shown in Figure 4.21. The DC machine provides more damping to the system than in the case of the ideal motor, so the drone does not overshoot position as much in the Z position when reaching the hovering height and it doesn't cause the drone to move in the X and Y direction; in fact the system is well damped when the

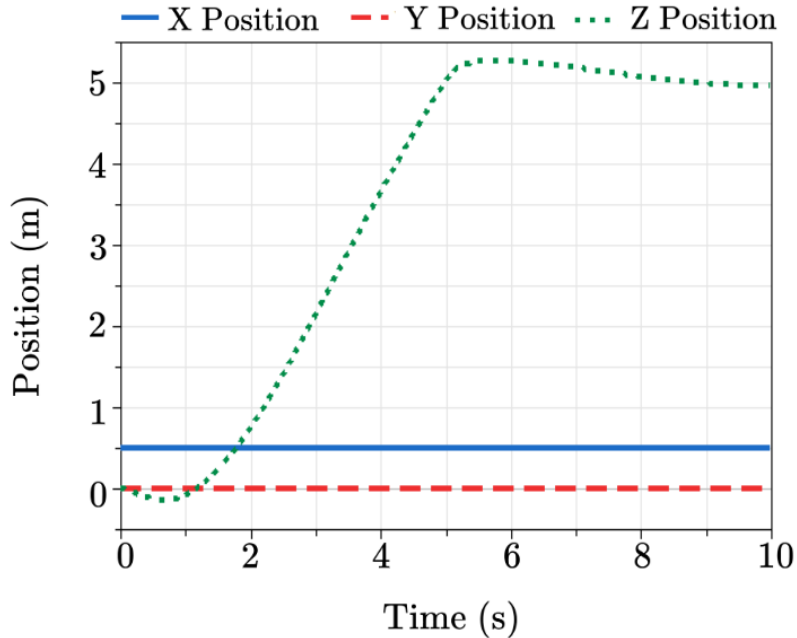


Figure 4.20: Drone with an ideal motor and ideal power system XYZ position under a ramp signal input.

permanent magnet DC motors are used in the system. Figure 4.22 compares the force applied to the blades from the DC and ideal motors. By increasing the model detail of the motor, the force applied to the blades increases due to the increased damping.

4.4.1.3 Non-ideal Power System, Permanent Magnet DC Machine with Losses

The permanent magnet DC machine from the MSL and the battery power system described in the **Sources** section are used to model the drone. The DC machine has a nominal voltage of 12V. The battery starts at a voltage of 9.55V with a state of charge (SoC) of 0.6. When the drone is tested under the same conditions as before, the discharging battery does not affect the behavior, i.e. the system response is the same as before. In this case, the battery assumes a constant power consumption rate, when in reality it discharges at a variable rate depending on the operational state of the drone. The test is only 10 seconds long, so the power consumption will have negligible impact on the battery state of charge for a test occurring over such a short time period. The battery is tested for longer periods and at varying state of charge in the next chapter.

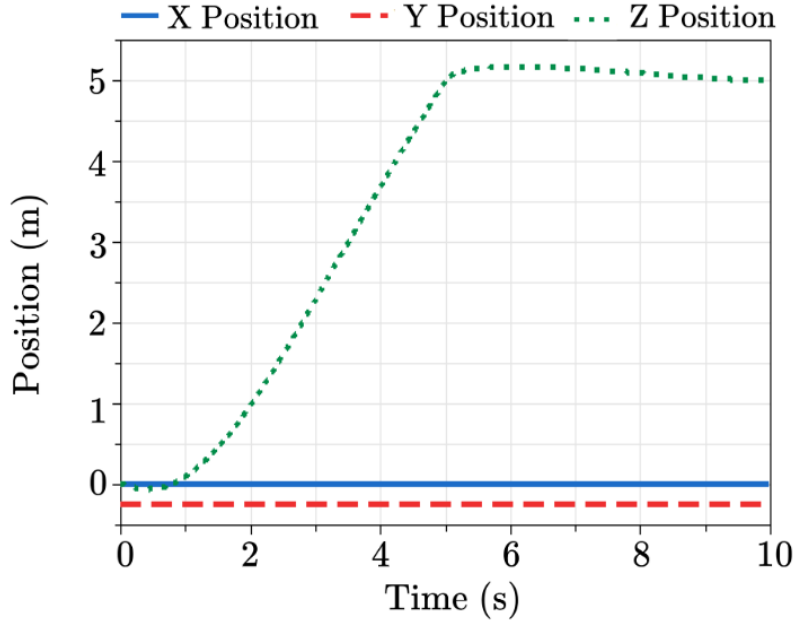


Figure 4.21: Drone with DCPM motor and ideal power system XYZ position under a ramp signal input.

Figure 4.23 shows the flight path of the drone subject to the same operating conditions shown in Figure 4.16. The position of the drone is similar to the response when an ideal power system is used, where the overshoot and steady state error in the Z-direction are 1.36% and 0.13% respectively.

The battery discharges at a constant rate of 0.004 percent per second, which causes the voltage to step down at a rate of $1e-4$ V per second as shown in Figure 4.4. Figure 4.24a shows the battery's state of charge and voltage decreasing over the 10 second simulation period. A 10 second test is not long enough to observe significant changes in battery voltage and the handling of the drone as a result; however, these effects are explored further in the next chapter.

4.4.1.4 Non-ideal Power System, Permanent Magnet DC Machine with Losses, and DC/DC Converter

The controller is now replaced to have an input from a DC to DC step down converter as per the model in Figure 4.2. The system response is shown in Figure 4.25. When the DC/DC buck converter is included in the system, the dynamic response is similar to the other cases where the DC motor was included. The overshoot and steady state error are

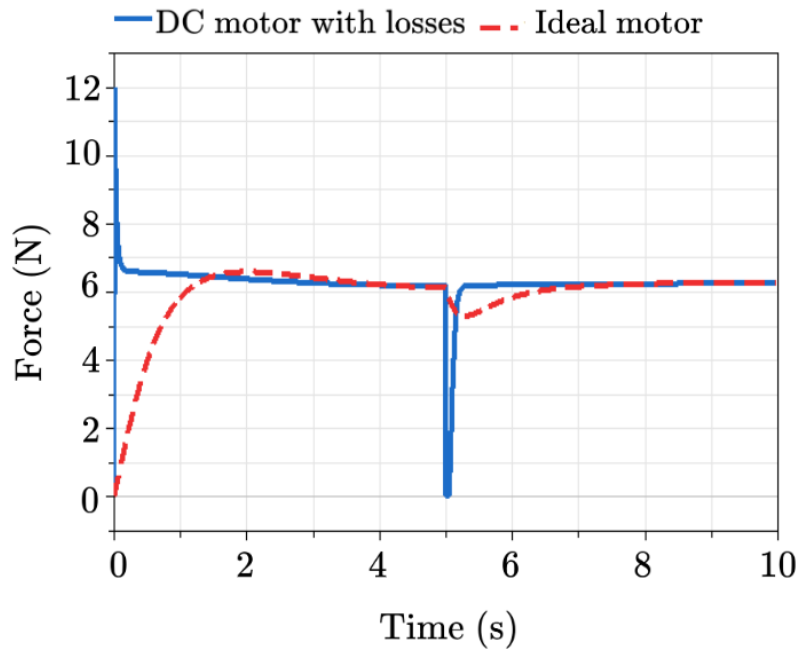


Figure 4.22: Thrust from one motor in the Z direction compared for the ideal motor and DC motor with losses.

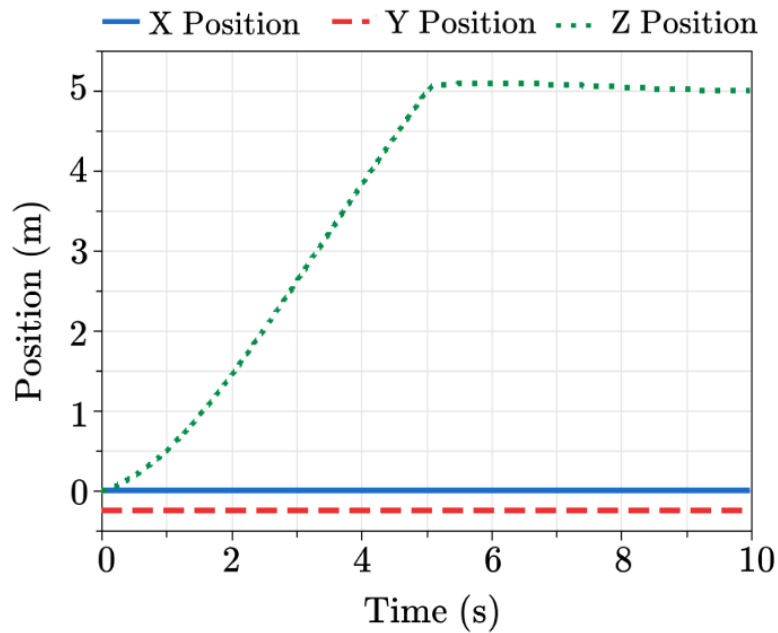
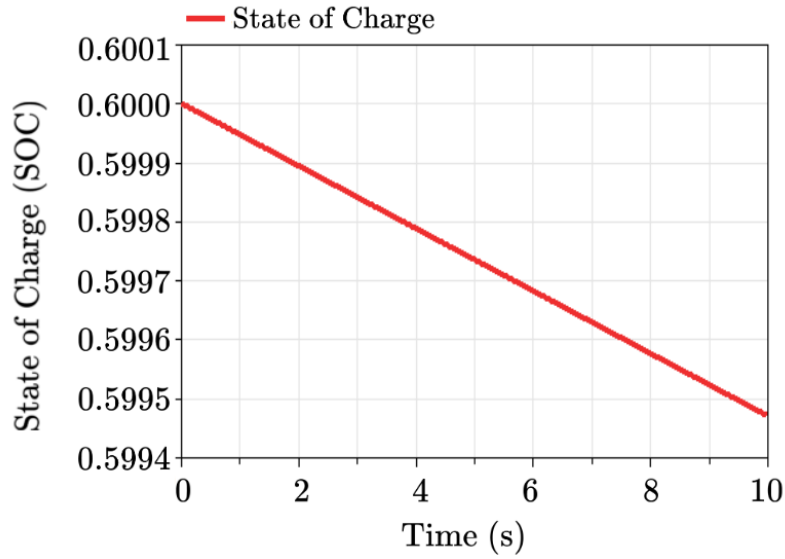
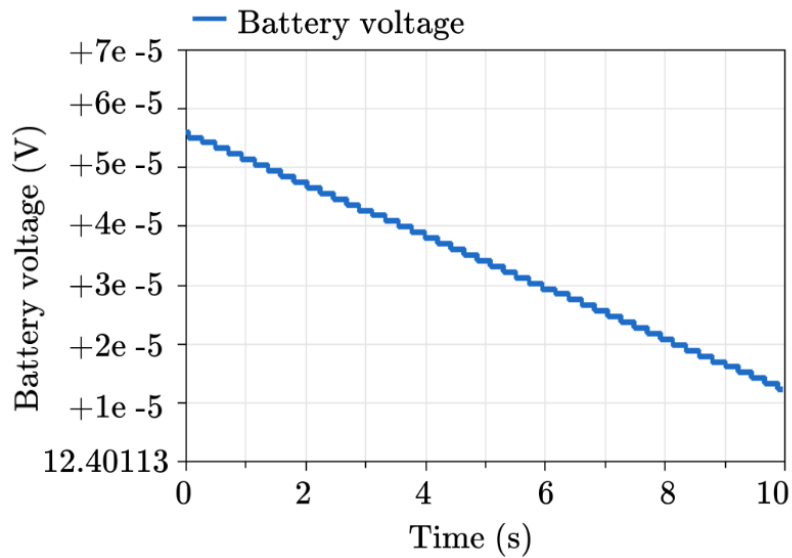


Figure 4.23: Drone with DCPM electrical motor and battery power system XYZ position under a ramp signal input.



(a)



(b)

Figure 4.24: Battery (a) state of charge (b) voltage discharge response under a ramp signal input.

1.04% and -0.072% respectively.

The time domain specifications and energy consumption for the motor and controller are shown in Tables 4.1 and 4.2. While the DC/DC step down converter creates a large voltage ripple, but the system stays stable. This is explained further in the “Power System Impact on Closed Loop Dynamics” section.

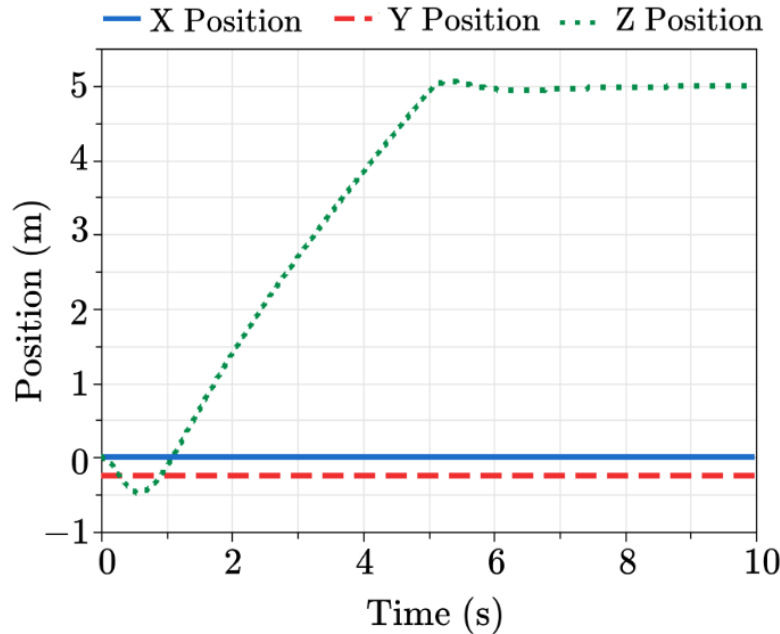


Figure 4.25: Drone with DC permanent magnet electrical motor, battery power system, and DC to DC converter XYZ position under a ramp signal input.

4.4.2 Power System Impact on Closed Loop Dynamics

When the drone model includes a controller that requires a power input, a DC to DC step down converter is required to step down the 12.1 V from the battery to 5V to be used by the controller. The DC to DC controller in Figure 4.7 has transistors and diodes that, depending on how the transistors are modeled, will cause different levels of voltage ripple. This voltage ripple is fed back into the motor voltage input. The power system for the Otus quadcopter in Figure 4.3 does not have a voltage controller for the motors. The voltage profile in Figure 4.26a shows the ripple from the DC/DC converter affecting the battery voltage. As the system stabilizes, the voltage ripple decreases as shown in Figures 4.26b and 4.26c. This voltage ripple propagates through to the scaling of the position signal.

As described in the **Controllers** section, the speed controller uses the battery voltage and current to adjust the position signal from the controller accordingly. Figure 4.27 shows the position input compared to the machine torque output. The solid line in the figure shows the position input to the machine measured in V, which has been scaled by the speed controller to consider the battery voltage. The battery ripple in Figure 4.26a is evident in the input voltage to the machine. The dotted line in Figure 4.27 shows the mechanical

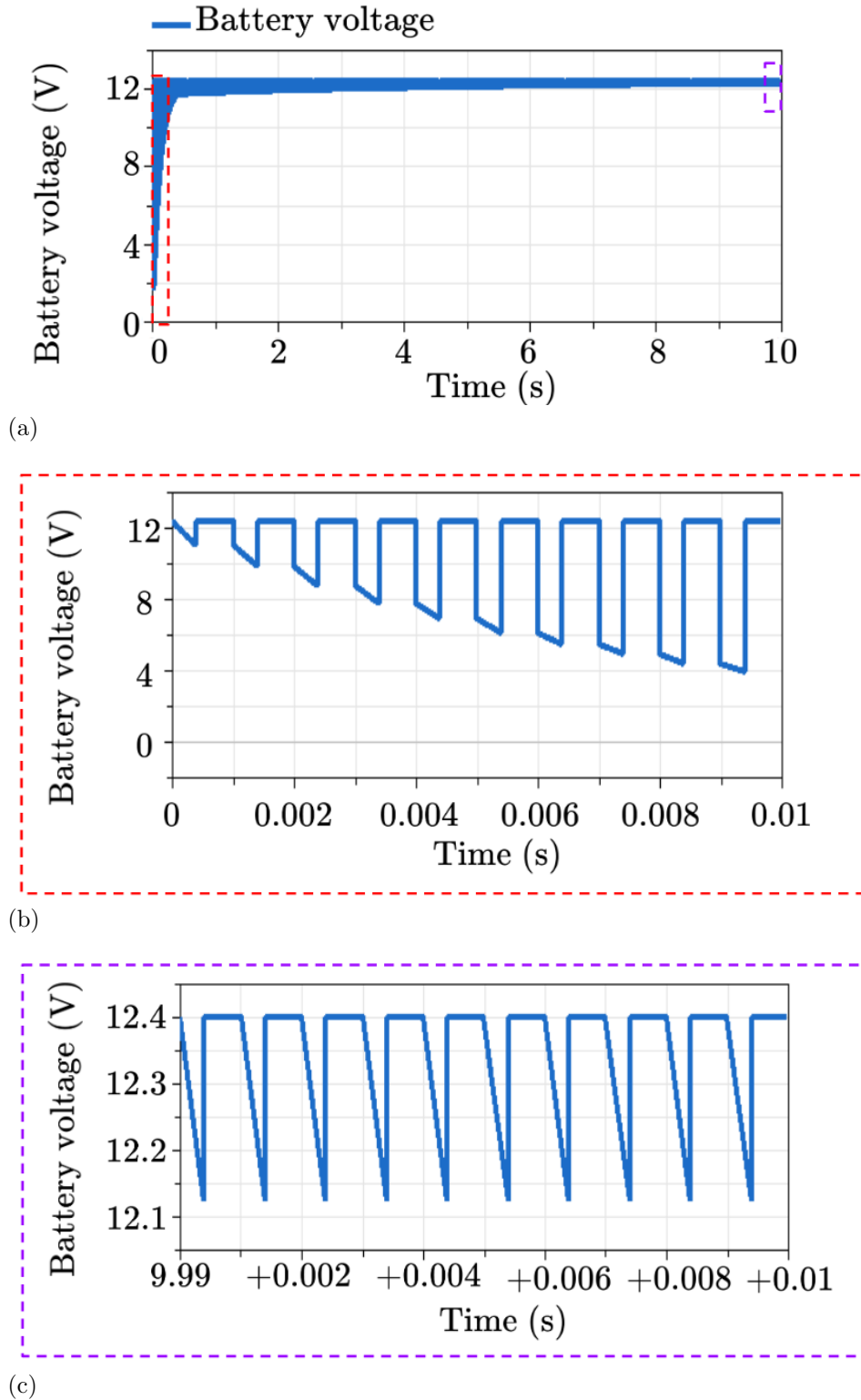


Figure 4.26: Battery voltage with a DC/DC converter included in the power system architecture with (a) Battery voltage over 10 second testing period. (b) Battery voltage inset from 0 seconds to 0.01 seconds. (c) Battery voltage inset from 9.99 seconds to 10 seconds.

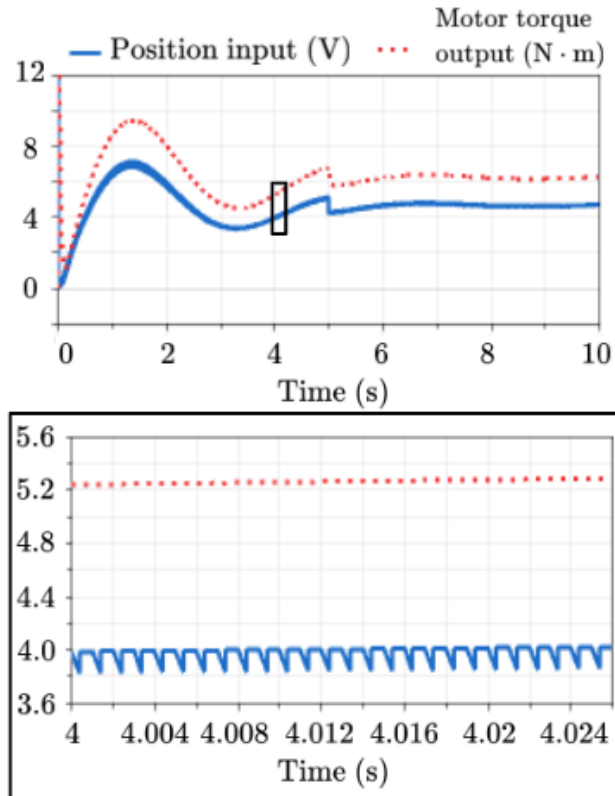


Figure 4.27: Position signal compared to motor output when converter is connected to the power system and supplies voltage ripple.

shaft torque output by the machine. The torque has the similar characteristics as the input voltage, but the output torque does not have the same ripple. The inductances inside of the machine damp the output torque, largely eliminating the ripple in the output.

Another test was run to determine the point at which the battery cannot allow the drone to fly anymore. Using the same simulation set up of ramping the drone to a height of 5m and continuously hovering for 13 minutes. Figure 4.28 shows the discharge of the battery over the discharge period. When the battery discharges to a point of about 8V, the drone falls down to the ground as shown in Figure 4.29. This because batteries have a non-linear voltage when discharging, as shown in the lower plot in Figure 4.28. Once the battery hits a specific state of charge, the voltage will start rapidly decreasing. For the battery considered in this simulation, this occurs when the battery charge reaches 25%, which is reached at approximately at the 13 minute point in the simulation result shown in Figure 4.28. Not only is the drone unable to fly at this point due to low voltage, but the battery is being damaged from over-discharging. This reduces the charge capacity of the battery for future

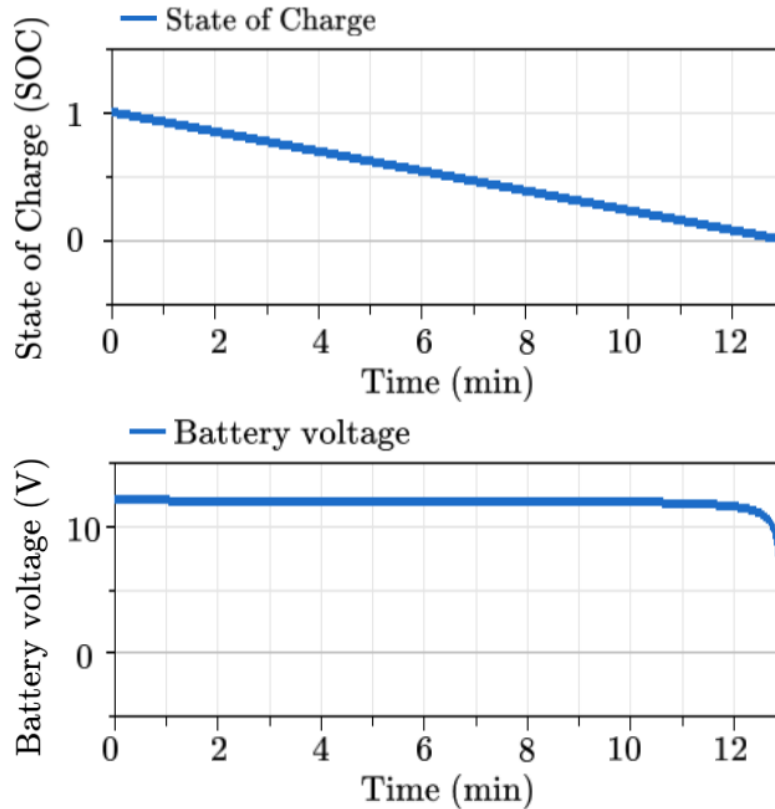


Figure 4.28: Battery voltage and state of charge over 13 minutes at 5m hovering.

charge cycles, or in the case of complete discharge, make the battery completely unusable as it could no longer hold charge.

4.4.3 Payload Variation

One of the attractive uses of UAV is the possibility to carry different payloads. However, these can impact both the system dynamics, the power systems performance, and energy consumption. This section aims to address some of these aspects.

As outlined in Figure 4.2, the drone model has a rotational connection (labeled as `frame_a1`) to connect payloads onto the chassis. In this test, the drone is attached to a 3kg payload in the Z direction, effectively being modeled as a mass attached to the airframe chassis. The ideal flight path used in the reference tracking tests is applied to the drone with the payload. Figure 4.30a shows the drone position with the 3kg payload attached. In this case, the drone is not initialized prior to adding the payload or applying the flight path. The drone overshoots its final hovering height by 1.86%. It also has a steady state error of $-1.64e-4\%$. The thrust per rotor is shown in Figure 4.30b. As outlined in Table 4.1, the

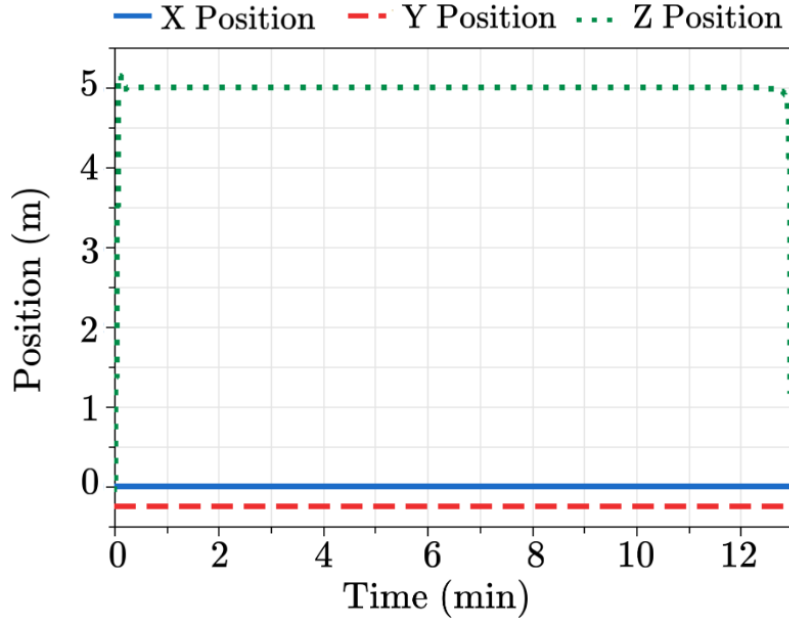


Figure 4.29: Drone XYZ position during test where the battery is discharged and the quadcopter remains in hover at 5m until failure.

motors in the drone consume more power when the payload is attached. Similar to the tests without the payloads, the case of the drone using an ideal power source results in a larger energy consumption by the motors. Similar to the other reference tracking tests outlined in Table 4.1, the power consumption of the motors is large for the ideal case, but as details are added to the model, the power consumption decreases. For brevity, the tracking response plots of all configurations under a payload are not included in this chapter.

4.5 Discussion: Model Variance, Power Consumption, and Dynamic Performance

The power consumption and dynamic performance for each of the model variations discussed in the previous sections are compared in Tables 4.1 and 4.2. When the ideal power source and motor are used in the drone, the power consumption is lower than other configurations (see cases 1-4), as they have no losses considered. The model variants which use the DC permanent magnet machine have more damped dynamic responses than the ideal motor model cases, as shown in Table 4.2. When there is no payload attached to the airframe, all models have comparable steady state error once the drone reaches hover.

The system is also studied for a scenario in which a 3kg payload applied to the chassis to represent a realistic application for the drone. Comparing cases 5, 6, and 7 from Table 4.1,

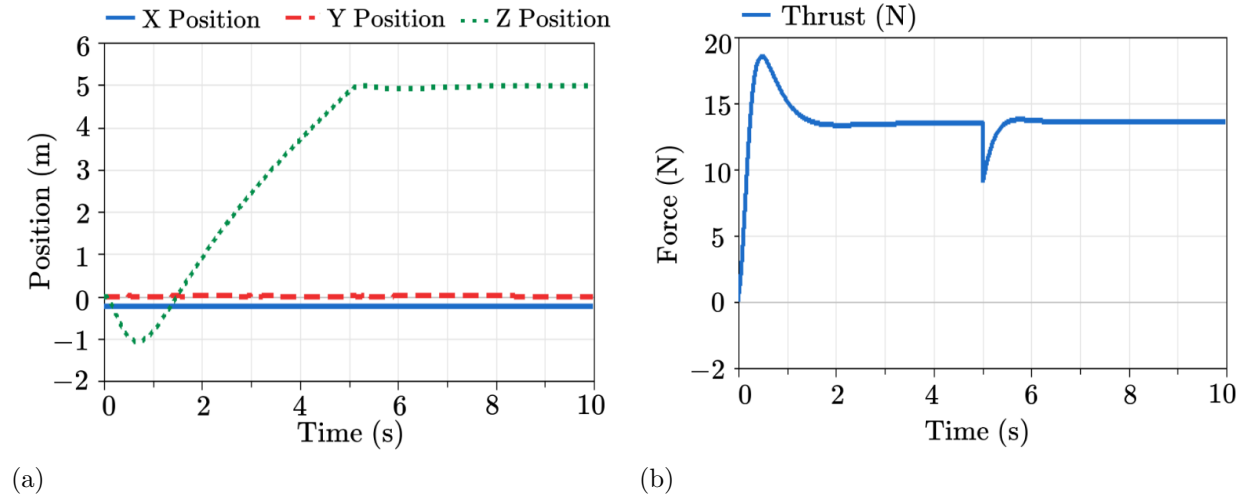


Figure 4.30: Drone position with a payload of 3kg applied to airframe. (a) Drone position. (b) Rotor thrust.

it can be noticed that the addition of the payload leads to a power increase of approximately 2000 W (case 2 vs. case 6, case 3 vs. case 7, case 4 vs. case 8). This will limit the potential flight duration or increase the power requirements from the source, and hence increase the weight. Comparing cases 6 and 7 indicates that substantial power consumption takes place when stabilizing the drone with the additional payload, about 35 W, which is about 80% additional power than the power consumed without the payload. Similarly in configurations, such as comparing cases 2 and 8 from Table 4.1, the 3 kg payload increases power consumption by about 2000 W.¹

¹The energy consumed by the motor controller is a constant 0.25 J.

Table 4.1: Energy metrics for the ideal flight path tests.

#	Test type	Power consumption, total (motor) (W)	Power consumption, during ramp (motor) (W)	Power consumption, during hover (motor) (W)
1	Ideal motor, ideal power system	1075.3	545.7923	529.4588
2	DC motor, ideal power system	1661.5	851.09	810.41
3	DC motor, battery without converter	1661.4	850.9589	810.4825
4	DC motor, battery with converter	1659.5	845.30	814.22
5	Ideal motor, ideal power system, and 3kg payload	3496.1	1766.5	1729.6
6	DC motor, ideal power system, and 3kg payload	3628.1	1830.1	1798
7	DC motor, battery without converter and 3kg payload	3629.1	1832.3	1797.0
8	DC motor, battery with converter and 3kg payload	3614.1	1830.1	1797.1

Table 4.2: Tracking response for the ideal flight path tests.

#	Test type	Overshoot	Steady state error (Z)
1	Ideal motor, ideal power system	5.43%	0.054%
2	DC motor, ideal power system	1.1%	0.021%
3	DC motor, battery without converter	1.36%	0.13%
4	DC motor, battery with converter	1.04%	-0.072%
5	Ideal motor, ideal power system, and 3kg payload	17.6%	-4.48%
6	DC motor, ideal power system, and 3kg payload	1.86%	-1.64e-4%
7	DC motor, battery without converter and 3kg payload	1.04%	0.2%
8	DC motor, battery with converter and 3kg payload	-0.88%	-0.15%

4.6 Conclusions

The drone model presented in this chapter provides a basis for open-source, multi-domain drone modeling at different levels of model complexity. These models are more

complex than previous models developed in the literature, as they feature physics-based models focused on representing the electrical dynamics in the system. In addition, they allow for animation the drone for a given input, which is beneficial for insight, analysis, and communication between domain specialists. This library is designed in a manner that encourages further development to the complexity of the system models, as well as the ability to integrate the system model with other software tools through the FMI Standard [25].

Multiple variations of the drone model were tested and studied to understand how the power consumption and how well the drone followed an input signal command. Based off the results in Table 4.1, it is clear that well-defined power system and motor models are required to conduct component sizing studies and understand new electrical system architectures.

In the next chapter, the drone's drivetrain model is increased in complexity to have a better representation of the aerodynamics. This includes modeling heating losses of the electrical and mechanical components in the system. Thermal behaviors are included as an option to model the losses of the electrical and mechanical components in the system, such as heat dissipation from the resistors and friction, but they currently not used in the drone model and will be included in the next chapter. Averaged power electronic models will illustrate the impact of averaged modeling on the drone and the impact on system dynamics, and the electrical and closed loop response. The speed controller model will also be improved to consider a nonlinear relationship between battery voltage and motor power. These studies are consider longer flight paths than the 10 second command applied in this chapter, allowing for more in depth analysis of the battery discharge dynamics.

CHAPTER 5

MULTI-DOMAIN ELECTRIC DRIVETRAIN MODELING FOR UAM-SCALE eVTOL AIRCRAFT

5.1 Introduction

5.1.1 Motivation

Distributed electric propulsion has enabled a vast array of new concept vehicles, largely centered around NASA’s Advanced Air Mobility (AAM) initiative [10] and Uber Elevate [11]. Most of these concepts take advantage of the ability of electric motors to operate at a relatively wide range of RPM compared to conventional turbine-driven drivetrains, which have a narrow band of efficient operating speeds.

5.1.2 Related Works

Within the VTOL community, substantial attention has been paid to the effectiveness of variable-RPM rotor systems on Urban Air Mobility, a subset of AAM, focused on passenger transport operations. Variable-RPM rotor systems were compared to variable-pitch systems at NASA Ames Research Center [74], [75], and at the Center for Mobility with Vertical Lift (MOVE) [76]. Both of these studies examined variants of the quadcopter concept put forward in [77], finding that variable-RPM systems were not viable unless drivetrain limits were significantly higher than current design trends suggest. In [76], it was found that these same limitations were applicable to variable-pitch systems, due to the large motor torque required to meet yaw handling qualities specifications.

Also at MOVE, recent work [28] explored the impact of motor dynamics on the handling qualities of single-passenger vehicles with different numbers of rotors at a fixed gross weight and disk loading, and related research [29] explored the same on quadcopters at different AAM-relevant scales. Both studies generally found that having smaller rotors, whether by possessing more, smaller rotors or operating at a lower gross weight, reduced the over-sizing necessary for the motors to handle current commands during maneuvers.

All of the above studies utilized an idealized motor model, using simplified DC motor

This chapter previously appeared as: M. Podlaski, R. Niemiec, L. Vanfretti and F. Gandi, “Multi-domain electric drivetrain modeling for UAM-Scale eVTOL aircraft,” in *VFS 77th Annu. Forum & Tech. Disp.*, May 2021, pp. 2566-2579, doi: 10.4050/F-0077-2021-16893.

equations to capture motor dynamics, treating the armature voltage as a command. However, electrical machine dynamics are much more complex than the behavior described by such equations [78], [79]. In addition, the ideal DC motor model neglects the effects of the electronic speed controller [30], which provides the commands to change the voltage and/or current to different parts of the stator (the stationary component of a brushless DC motor), called “phases.” The rapid switching of voltage and/or current required to track a desired speed is carried out by a DC/DC power electronic converter [79]. Such converters have different internal switch configurations (known as topologies, [80] and control modes [30], [81], e.g. armature voltage control or field-oriented control, [82], which result in switching losses at the converter itself. Moreover, the switching also introduces a distortion known as voltage/current ripple to the motor terminals. While filters formed by passive components (capacitors and inductors) can be designed to minimize the ripple, it is impossible to completely remove it [83], [82]. Regardless of its magnitude, the voltage/current ripple will affect the desired performance of the motor and lead to different types of losses in the machine, most of which will ultimately impact the thermal management needs [84] and result in torque ripple that may lead to unacceptable speed ripple, vibration, and acoustic noise [85], all of which reduce the handling qualities and lifetime of the drivetrain. All of these aspects are impossible to capture using the simplified DC motor equations.

Previous studies have also assumed that the battery is a constant voltage source, without regard to aging, or power drain over the course of a flight. Naturally, as batteries discharge over the course of a flight, the pack voltage will drop, increasing the strain on the system (as voltage drops, current has to be increased to deliver the same amount of power), demanding additional effort from the DC/DC converter to deliver the required voltage/current and possibly leading to inadequate handling qualities or even a loss of control.

More sophisticated motor and battery models have been implemented on eVTOLs [86]-[87], though these studies primarily examine performance metrics such as efficiency. However, higher-fidelity drivetrain models are needed for other design aspects such as thermal management [84]-[88], response and mitigation to failures [88]-[89], impact on aircraft handling [85]-[90], etc. For example, the importance of high-fidelity drivetrain modeling can be understood from results in [22], where a switched inverter model is connected to a battery and motor in a quadcopter. Large voltage and current ripples were created by transistor switching in the converter, which impacted system operation depending on the converter

topology [80], control [81], etc. Higher-fidelity models would therefore allow for more realistic analyses, providing a broader insight to the experiments such as those in [86]-[87], and to integrate electrical powertrains with other subsystems that depend on their performance, i.e. aerodynamic and thermal.

5.1.3 Chapter Contributions

The objectives of the study presented in this chapter are:

- Application of multi-engineering domain (mechanical-electrical) models for an electric drivetrain with varying degrees of complexity, including detailed battery, machine, and power electronic converter models.
- Modeling drivetrain response for power source models, including an ideal power source, fully charged battery, and battery at 30% charge.
- Comparing drivetrain response for different machine configurations under various speed commands, namely quadcopters with fully-distributed batteries (where each motor has a dedicated power source) and a fully-centralized battery (where all rotors share a single power source).

5.1.4 Chapter Organization

First, the drivetrain model is introduced and outlined. All of the components and variants of those components are explained.

In the next section, a second order speed command is applied to the drivetrain models to study their aerodynamic response and electrical dynamics.

Next, the brushless averaged DC motor is put into a quadrotor configuration. A heave, pitch, and roll maneuver is applied to the system using an ideal power source, fully charged battery, and battery at 30% charge. This allows us to study the impact of the battery's state of charge on the system performance.

Finally, a comparison of two battery layouts is presented. Specifically, a fully distributed battery system versus a fully-centralized battery on a 300 lb quadcopter (that used in [29]).

Table 5.1: Aircraft parameters.

Vehicle Parameters	
Boom Length (m)	0.905
Gross Weight (kg)	136
I_{xx} (kg m ²)	43
I_{yy} (kg m ²)	51
I_{zz} (kg m ²)	84
Rotor Parameters	
Rotor Radius (m)	0.6096
Rotor Inertia (kg m ²)	0.063
Root Pitch (deg)	21.5
Linear Twist (deg)	-10.4
Solidity	0.09
Taper Ratio	2.5
Motor Parameters	
K_e (Nm/A)	0.1342
R (Ohm)	0.0155
L (μ H)	4
b (Nms/rad)	3.71e-4

5.2 Modeling

5.2.1 Platform Description

The vehicle considered in this study is a 300lb quadcopter used in [29]. The properties of this quadcopter and its rotors are listed in Table 5.1. The rotors are assumed to be linearly twisted and tapered and have a 10% R tip clearance. The motor parameters are based on the Hacker Q150-45-4 [91], and are also included in Table 5.1.

The drivetrain consists of four main components: a controller, pulse width modulation (PWM) of the converter, a DC/DC converter, and a brushless DC machine as shown in Figure 5.1. Starting from the left-hand side of Figure 5.1, a pulse-width modulated signal, which defines the instantaneous desired speed of the motor (based on vehicle-level control needs) is provided to a speed controller, which, among other things, regulates the voltage/current to track the desired speed. The controller feeds a signal to a power converter, which steps-up the voltage and commutates the battery voltage to a suitable waveform for the motor to meet the desired speed. The motor itself converts the electrical current to a mechanical torque, which drives the rotor at Ω_{out} .

Each component of the drivetrain is modeled at multiple levels of fidelity using Dassault

Systemes' Dymola software, which utilizes the equation-based modeling language, Modelica [92], and contains several libraries for drivetrain modeling, including the *Dassault Systems Brushless DC Drive* library [93], and the *Dassault Systems Battery* library [94].

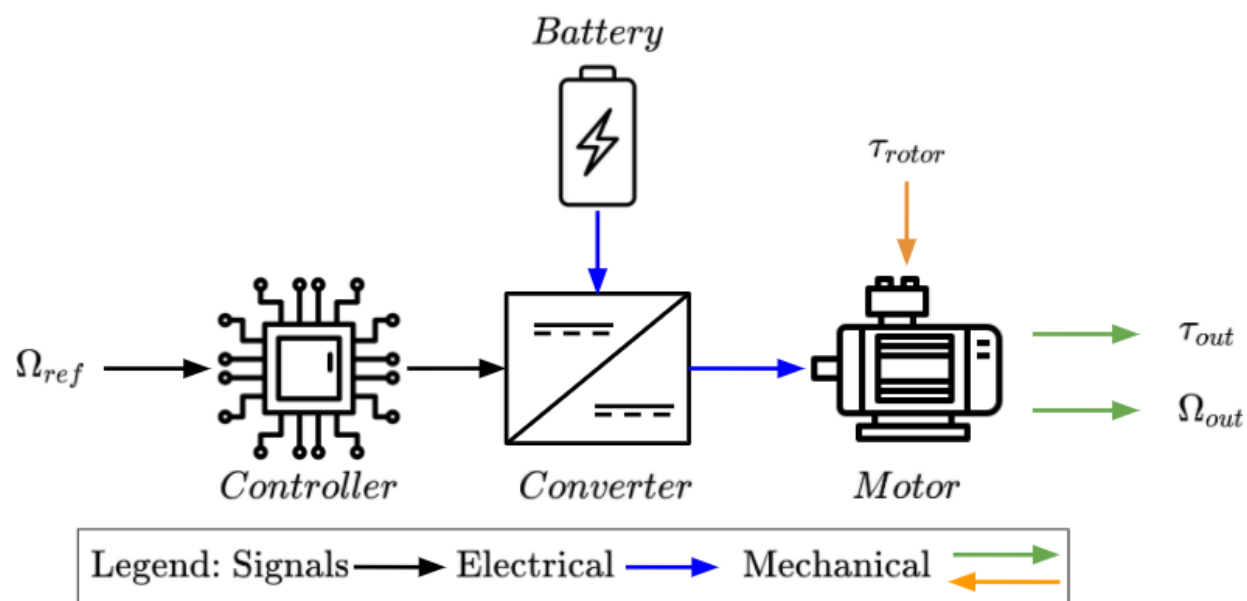


Figure 5.1: Electric powertrain schematic.

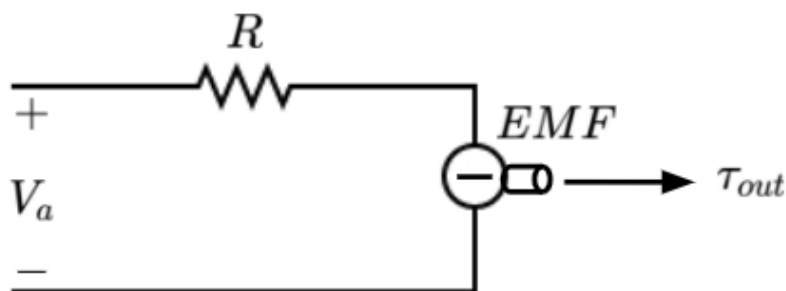


Figure 5.2: Circuit diagram of DC motor without inductance.

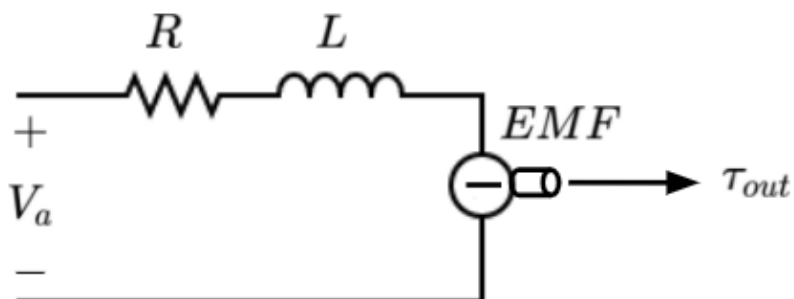


Figure 5.3: Circuit diagram of DC motor with inductance.

5.2.2 Motor Models

In Figure 5.1, the motor can be modeled at multiple levels of fidelity to include different levels of losses. Four different models are used:

1. Simple DC motor without inductance
2. Simple DC motor with inductance
3. Brushless motor with averaged back EMF
4. Brushless motor with trapezoidal back EMF

5.2.2.1 Simple DC Motor without Inductance

The simplest representation of the motor is shown in Figure 5.2. The motor speed is governed by Equation 5.1, where I represents the effective inertia (including the rotor blades), and the right-hand side is the net moment. The motor torque is proportional to the current, and the current is quasi-steady, given by Eq. 5.3.

$$I \frac{d\Omega}{dt} = Q_{\text{motor}} - Q_{\text{aero}} \quad (5.1)$$

$$Q_{\text{motor}} = K_e i \quad (5.2)$$

$$i = \frac{V - K_e \Omega}{R} \quad (5.3)$$

5.2.2.2 Simple DC Motor with Inductance

An inductance is added to the motor model in Figure 5.3. Due to the presence of the machine's inductance, the current no longer evolves instantaneously, but is governed by the dynamic equation, Equation 5.4. Otherwise, this model is identical to the previous.

$$L \frac{di}{dt} = V - Ri - K_e \Omega \quad (5.4)$$

By adding an inductance to the motor, a new time constant (τ_a) is added to the system. This time constant derivation is shown in Equation 5.5, where L is the motor inductance and R is the motor resistance. In many machines, the inductance is so small that the time constant does not have much impact on the system from the mechanical point of view, but whose electrical dynamics cannot be neglected when studying the electrical power train itself. For the Hacker Q150-45 brushless machine used in this study, the motor has a resistance of

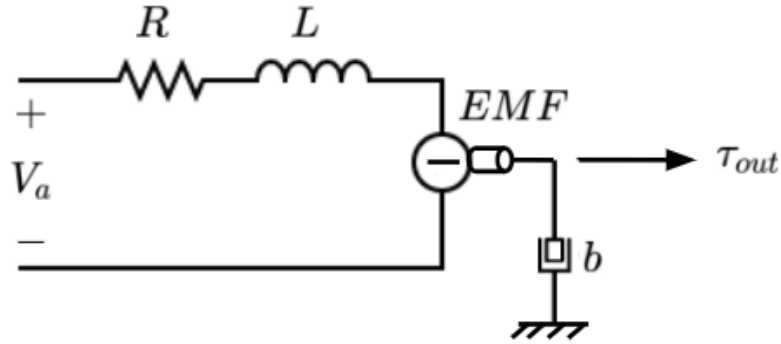


Figure 5.4: Circuit diagram of the averaged brushless motor.

0.0155 Ohm [91] and inductance of $4\mu\text{H}$ (based on regression in [75]). This results in a time constant of $258.06\mu\text{s}$, or a settling time of 1ms. These time constants will interact with the power electronic converter and its controls.

$$\tau_a = \frac{L}{R} \quad (5.5)$$

5.2.2.3 Brushless DC Motor with Averaged EMF

The brushless DC motor with averaged EMF considers builds off the simple motor models to include frictional losses in the machine. The motor model is shown in Figure 5.4. Equation 5.1 is modified to include a viscous torque, resulting in Equation 5.6, where b is the effective damping due to viscosity in the air gap between the stator and rotor. Motor torque and current are governed by Equations 5.2 and 5.4, respectively. For the Hacker Q150-45, $b = 3.71e - 4$.

$$I \frac{d\Omega}{dt} = Q_{\text{motor}} - Q_{\text{aero}} - b\Omega \quad (5.6)$$

5.2.2.4 Brushless DC Motor with Trapezoidal EMF

The brushless DC motor further increases complexity, as the motor's back EMF is component is replaced with a three-phase trapezoidal back EMF. Previously, the back EMF is a function of speed only; in this model, the back-EMF in each phase is also dependent on the motor position, as shown in Figure 5.5. The waveform is trapezoidal, therefore, this motor will be referred to as the "Trapezoidal DC motor" throughout this study. The resistance and inductance in each phase is half that of the whole motor. In a three phase

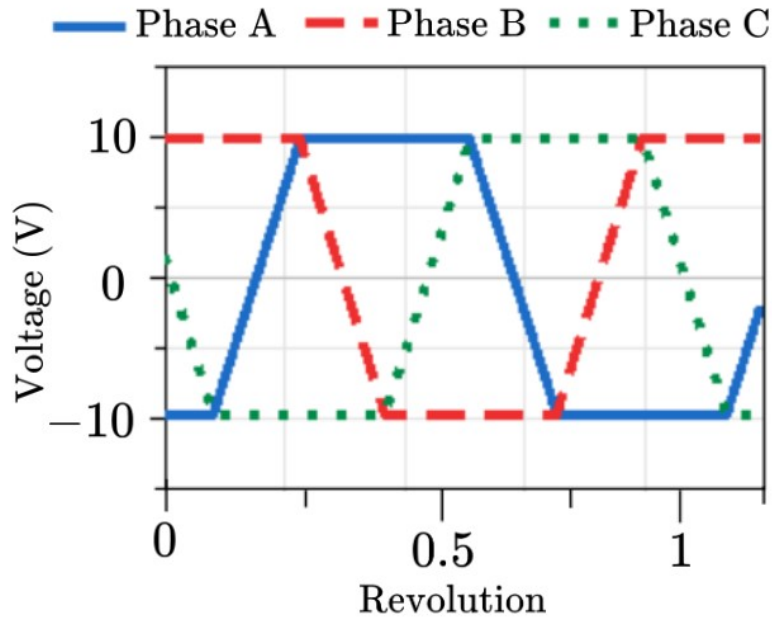


Figure 5.5: Back EMF of trapezoidal brushless machine with a duty cycle of 0.33.

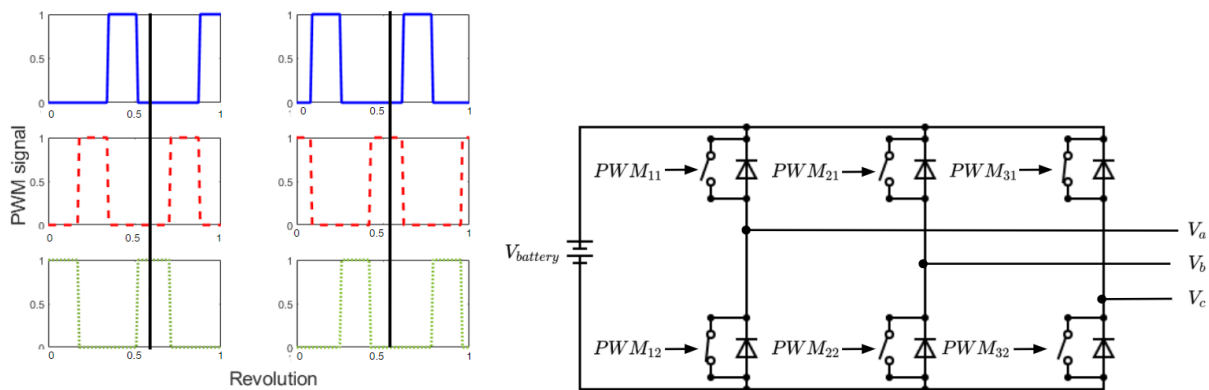


Figure 5.6: Switched three-phase converter with averaged input voltage.

motor, two phases are always conducting in series, so the impedance of each phase is added together as they are electrically in series with each other.

Since the trapezoidal motor configuration operates in three-phases, the converter and controller models include switching instead of the averaged conversion used in the previous models. The converter used with the trapezoidal motor shown in Figure 5.6 is a by a 3-phase full-bridge inverter that of diodes and transistors (represented as switches), that supplies the motor it they can produce the time-varying back EMF. Finally, the battery voltage needs to be stepped up before converted by the full-bridge inverter, this is done using an ideal buck-

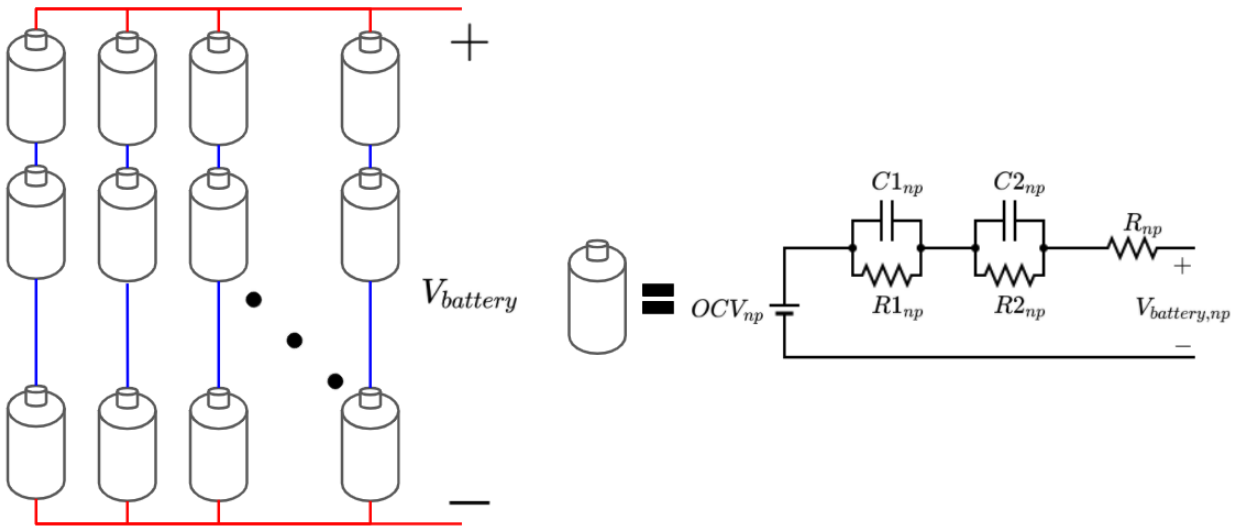


Figure 5.7: Battery schematic.

boost converter. Note that this converter is not shown in Fig. 5.6, but is a very commonly used converter [82].

The PWM signal applied to the motor’s converter is controlled using a six-step controller. Each pulse is separated by 60 degrees electrically to produce three sinusoidal voltages to apply to the machine. In Figure 5.6, the PWM signals are labelled such that there is a signal to control each diode in the converter for each phase, resulting in six signals.

5.2.3 Battery Models

eVTOL systems are commonly modeled with ideal battery sources. Ideal battery sources can deliver any amount of current while maintaining a constant voltage. However, real-world batteries lose voltage when higher current is drawn (resistive losses and changes in battery chemistry), and as charge is depleted. These effects can be modeled using a table-based open circuit voltage (OCV) battery. The OCV battery schematic is shown in Figure 5.7, where each cell of the battery is modeled as an ideal voltage source, plus resistors and capacitors. The values of the capacitances and resistances are functions of the current draw, temperature, and state of charge of the battery, and are based on lookup-tables derived from experimental data on the Sanyo 18650 Li-Ion cylindrical cell [94]. To scale the battery voltage, n cells are wired in series, and to scale the capacity, p sets of n cells are wired in parallel to produce a model for the battery pack.

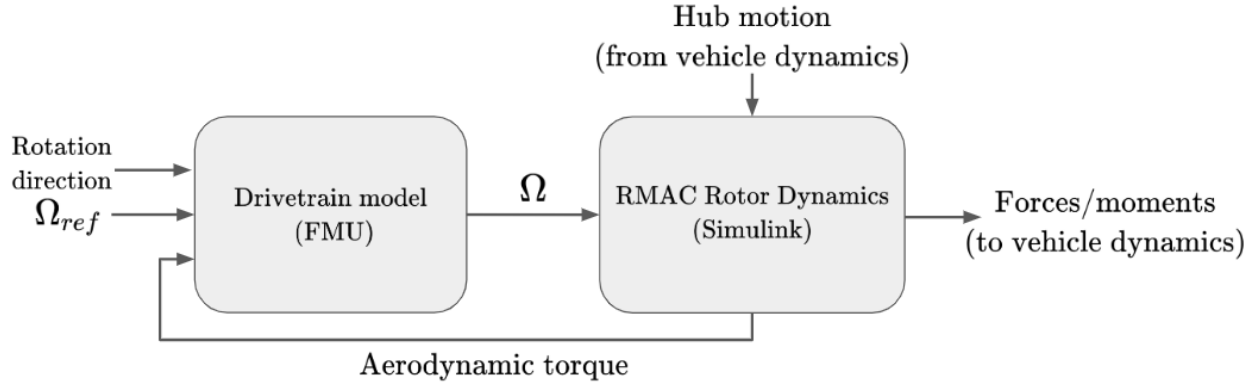


Figure 5.8: Integration of the drivetrain model with RMAC rotor model.

The battery is modeled as matrix of parallel (p) and series (n) cells, as shown in Figure 5.7. Each individual cell produces a voltage using Equation 5.7. The impedance in each cell can be determined using Equation 5.8.

$$V_{battery,ij} = OCV_{ij} - Z_{battery,ij}i_{ij} \quad (5.7)$$

$$Z_{battery,ij} = (R1_{ij}||C1_{ij}) + (R2_{ij}||C2_{ij}) + R_{ij} \quad (5.8)$$

5.3 Multi-Domain Model Coupling in Simulink

The drivetrain is modeled in its entirety using Modelica and is exported to interact with RMAC in MATLAB/Simulink as a Functional Mock-up Unit (FMU). An FMU contains a dynamic model that has been exported according to the Functional Mock-up Interface (FMI) standard, which allows for model export and/or co-simulation in many different simulation tools [25]. The inputs and outputs of the FMU couple to the RMAC rotor model shown in Figure 5.8. The drivetrain model takes inputs for the desired speed (derived from the vehicle attitude/heave control) and rotor torque (taken from the aerodynamic model), and outputs the rotor speed. The actual rotor speed (along with the rotor hub motion) is used to model the aerodynamic forces and moments about the rotor hub, which are passed along to the vehicle dynamics model.

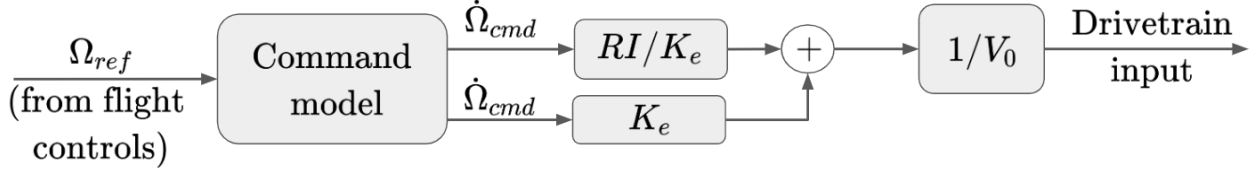


Figure 5.9: Forward path of explicit-model-following controller.

5.3.1 Speed Control Architecture

The controller in Figure 5.1 is divided into two parts, namely a low-frequency feedback controller (for the regulation of speed), and switching controller (to coordinate the switching in the converter). Naturally, the second component is only necessary when switching is actually modeled (only for the trapezoidal motor in this study), but the first component is needed for all machine types. The control architecture chosen for the speed control is explicit-model-following, the forward path of which is shown in Figure 5.9. First, the reference signal is passed through a command model, which can be tuned based on handling qualities requirements [29]-[76]. The command model outputs a commanded speed, Ω_{cmd} , and an acceleration $\dot{\Omega}_{cmd}$. In the forward path, the commanded speed and acceleration are passed through a simplified inverse model, which predicts the required voltage input for the motor. The inverse model is taken from the simple DC motor (neglecting aerodynamic torque), without inductance, and used for all machine types.

$$\hat{G} = \frac{V_0 K_e}{RIs + K_e^2} \quad (5.9)$$

$$u = \frac{1}{K_e V_0} (RI\dot{\Omega}_{cmd} + K_e^2 \Omega_{cmd}) \quad (5.10)$$

To account for deviations from this simplified model (due to inductance, aerodynamic torque, switching, etc.), feedback control is also included. For this application, a PI controller is used, with gains tuned using the simplest DC motor model. To ensure adequate frequency separation from the pitch/roll dynamics of the vehicle (tuned for a crossover frequency of 5 rad/s, [29]), a crossover frequency of 25 rad/s for the rotor speed control loop is chosen. The zero location (the ratio of the integral gain to the proportional gain) is selected to be 1/5 of the crossover frequency [95].

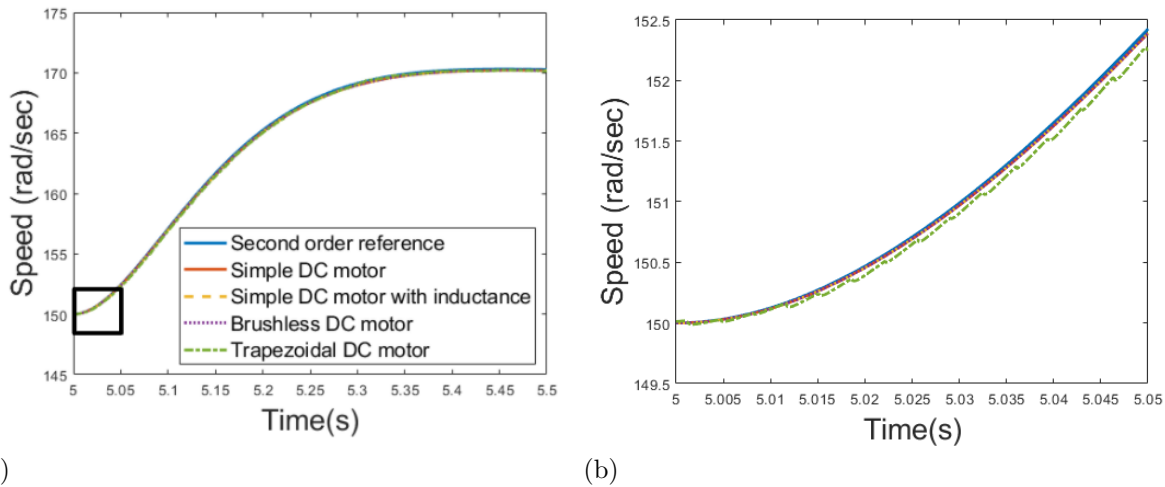


Figure 5.10: Second order speed command response with (a) First 500ms of the response. (b) First 50ms of the response.

5.4 Results

5.4.1 Isolated Rotor

A step command from 150 rad/s to 170 rad/s is commanded to each rotor model. Figures 5.10a and 5.10b show the response for each of the four machine types. Each of the motors have nearly identical speed responses, which is expected due to the small inductance and time constant of the motor. Delays associated with the motor inductance are negligible, as high-frequency commands (where the inductance will cause more phase delay) are filtered out by the command model. There is a small difference visible in the initial response of the trapezoidal motor, with brief lulls in the acceleration due to current/torque ripple as the commutating switches open and close.

While the dynamics of each of the machine configurations are nearly identical, the current draw varies significantly between the motor models, as shown in Figure 5.11a. Of the three non-switching motors, it is clear that the simple DC motor requires the least current, topping out around 72A. The simple DC motor with inductance and the averaged BLDC motor require greater current during the step command, as the inductors become charged, drawing a peak of 78A, but is characteristically similar to the model that neglects inductance. The trapezoidal motor, on the other hand, is characterized by frequent drops to zero current, as the switching between phases occurs. For a brief moment, both of the switches in Figure 5.6 are open, resulting in zero current.

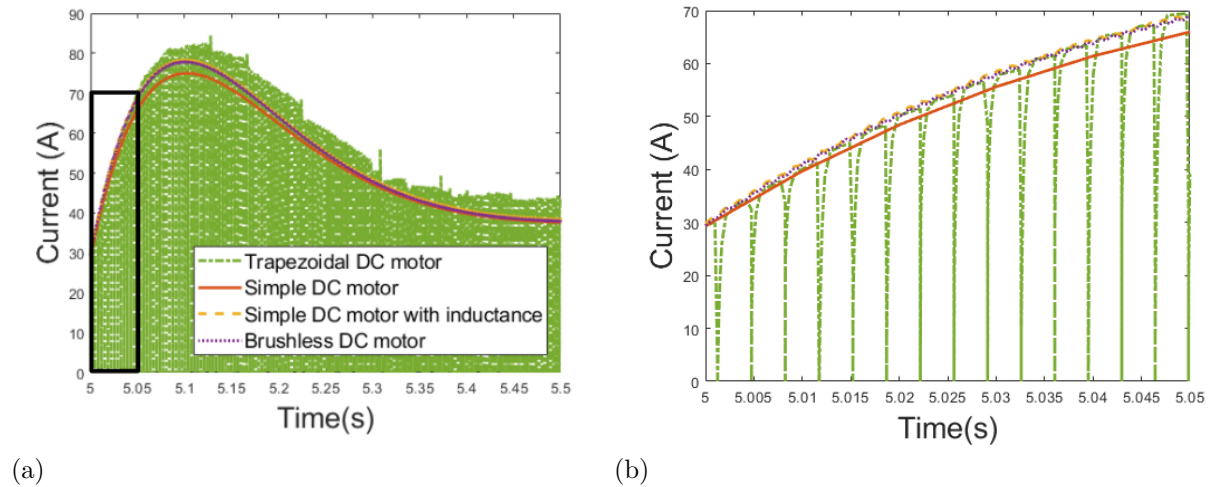


Figure 5.11: Motor current when a second order speed command is applied with (a) First 500ms of the response. (b) First 50ms of the response.

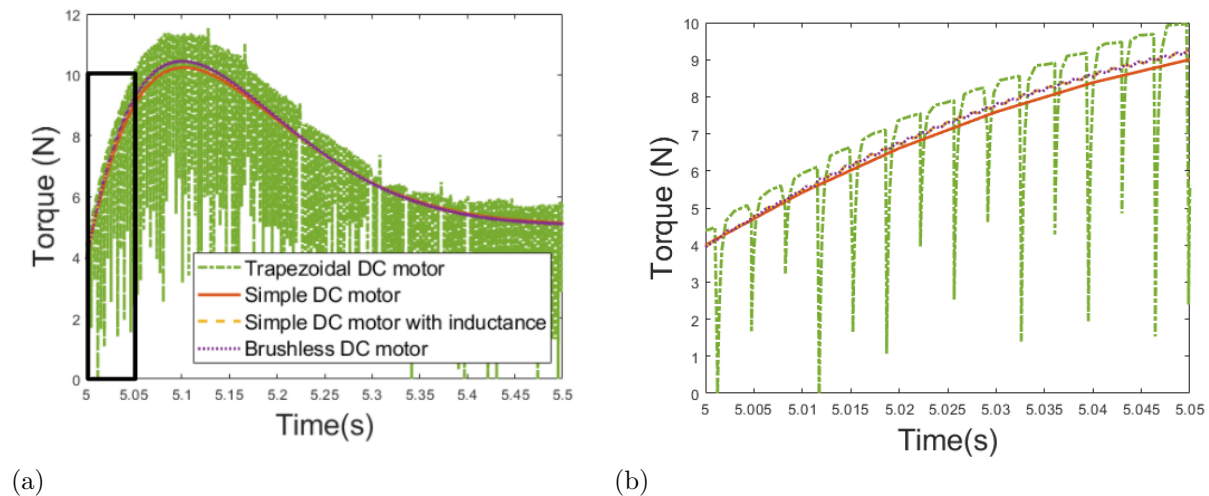


Figure 5.12: Motor torque when a second order speed command is applied with (a) First 500ms of the response. (b) First 50ms of the response.

The level of detail in the machine and converter model also impacts the motor torque. Figure 5.12a shows that the trapezoidal brushless motor model has the same switching behavior seen in the current, again caused by the transistor switching in the converter. Even without the switching, the inductance creates a small ripple torque, as seen in Figure 5.12b, though this is very small in magnitude compared to the switching torque ripple. This type of ripple will cause large periodic loading in the rotor shaft, which may cause fatigue.

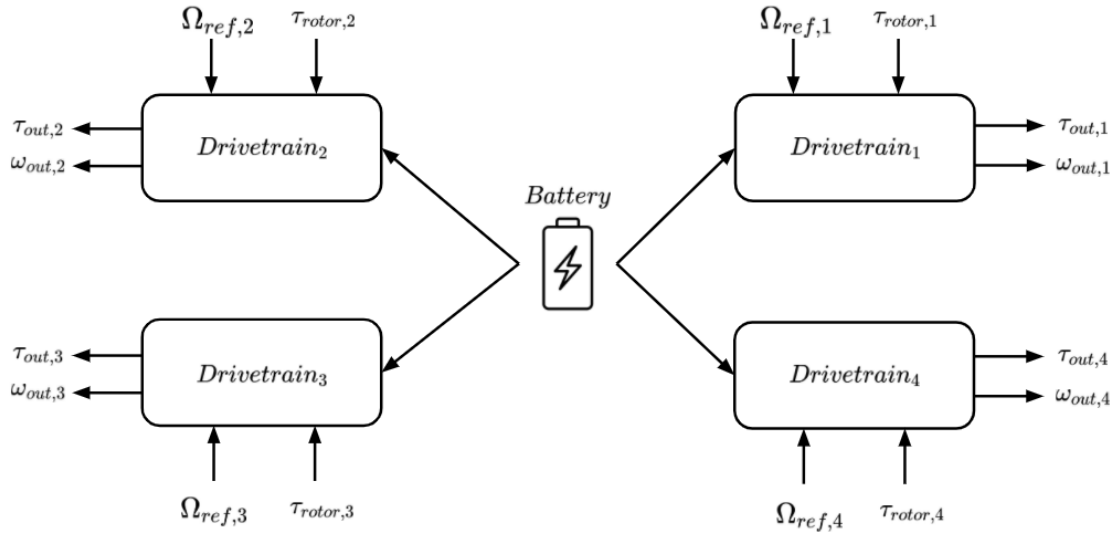


Figure 5.13: Multi-rotor aircraft model with centralized battery.

5.5 Multi-rotor System

5.5.1 Centralized Battery Architecture

To observe the loads of drivetrain architectures during maneuvering flight, the heave and pitch maneuvers are executed. Namely, a 5 m/s climb is commanded for 10 seconds (for a 50m climb) followed by a return to hover, and a 10 degree doublet is executed in pitch. First, a fully centralized battery architecture (Figure 5.13), which provides power for all four motors, and one with a fully distributed battery (so that each motor has an independent power source). Because all of the motors had nearly identical behavior in terms of speed, the averaged BLDC motor is used in all of the simulations. Three power sources are used in this study. To match the conditions in [29], the second-order filter previously used is replaced with a first-order filter, tuned to meet ADS-33 handling qualities standards.

1. An ideal, 60V voltage source
2. A centralized battery at full charge (beginning of a mission)
3. A centralized battery at 30% charge (end of a mission)

Heave Command To examine the closed-loop behavior in heave, a 5 m/s climb rate is commanded to the vehicle and held for 10 seconds, so that the vehicle climbs 50m in total. The unfiltered command, along with the vehicle response is given by Figure 5.14. The

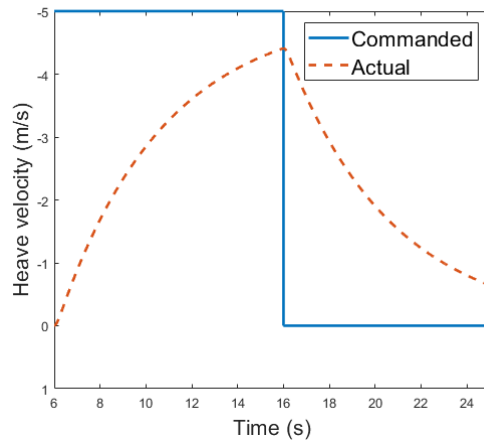


Figure 5.14: Heave command and vehicle response.

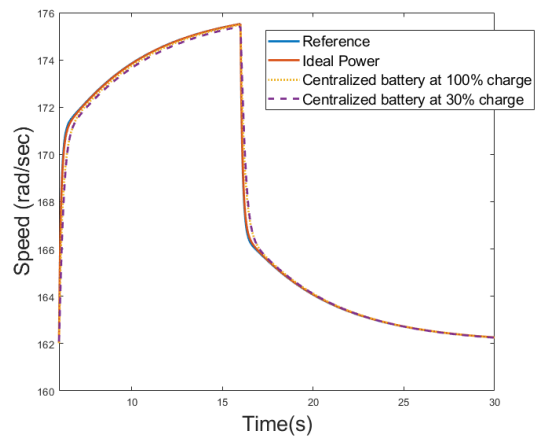


Figure 5.15: Speed response of the multi-rotor system to a heave command.

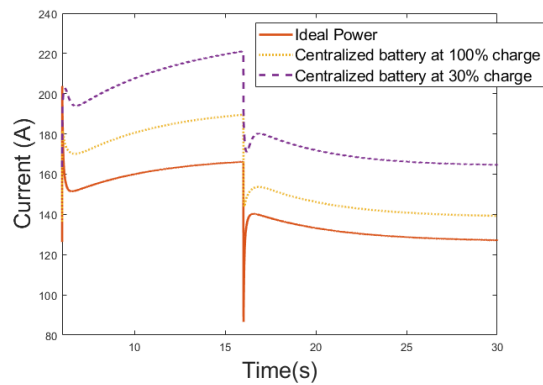


Figure 5.16: Current response of the multi-rotor system to a heave command.

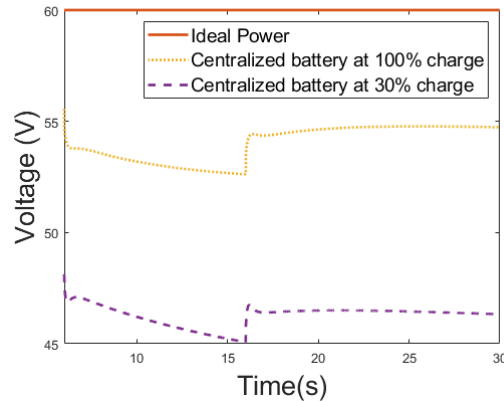


Figure 5.17: Voltage response of the multi-rotor system to a heave command.

difference between the command and response is primarily due to the heave command model, which is first-order ($\tau = 4.6$ sec) by design. Figure 5.15 shows the corresponding rotor speed (all four motors receive identical commands in heave), and the tracking is nearly perfect for all configurations, though there is a very slight lag for both OCV batteries. Figure 5.16 shows the current drawn from the batteries during the heave maneuver, while Figure 5.17 shows the battery voltage during the same. As the initial climb command is issued, the initial need to increase thrust (and thus rotor speed) produces an immediate spike in the current draw. As the vehicle's climb rate increases, the additional down-wash on the rotors increases the torque, leading to a smooth rise in the current drawn. When the climb command is terminated, the rotors slow down, producing a large negative spike in current, and as the aircraft returns to hover, the current and voltage approach their steady-state values. Generally speaking, the ideal voltage source drawn less current than the OCV batteries. This is due to the lower voltage delivered by the OCV batteries (represented by the resistors in Figure 5.7) as current is drawn. The drop in voltage observed for the OCV batteries during the climb are also due to increased current demands; when the climb command is stopped, the voltage mostly recovers to its initial value. Naturally, the 30% charged battery has a lower overall voltage than the fully-charged one, so its current demands are even higher (the same power must be delivered to the motors in all three cases).

Pitch Command To examine the behavior in pitch, a 10 degree pitch doublet is commanded to the quadcopter, as shown in Figure 5.18. The command model for pitch is a second-order transfer function ($\zeta = 0.7$, $\omega_n = 3.46$ rad/s). As discussed in ([29]), the vehicle

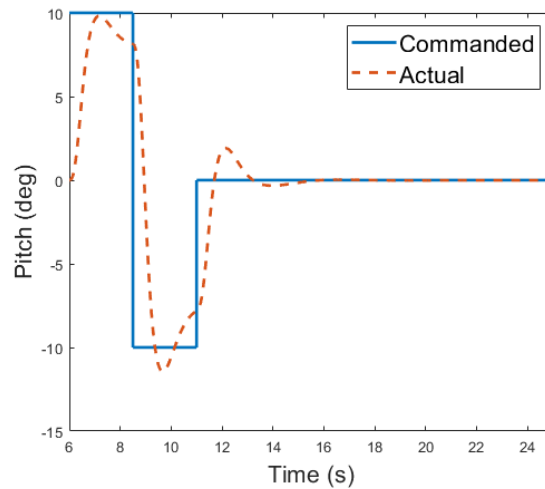


Figure 5.18: Pitch command and vehicle response.

does not track the filtered command well, and the vehicle does not settle to 10 degrees before the doublet ends. The rotor speeds during the pitch doublet are shown in Figure 5.19. The front and rear rotors receive opposite commands, since they are on opposite sides of the pitch axis (Figure 5.20). The current draw from the battery is shown in Figure 5.21. Unlike the heave command, the large spikes as the maneuver begins are not observed in the battery current, despite the large spike in the front rotors' current draw. This is because while the front rotors initially speed up (drawing more current), the rear rotors slow down (drawing less). Thus, the spikes in the battery current draw are small, and the corresponding changes in the voltage (Figure 5.22) are similarly small. This behavior also applies to the roll and yaw axes. Therefore, when a centralized battery architecture is used, heave maneuvers at low charge represent the limiting case for battery current delivery.

5.5.2 Distributed Battery Architecture

The distributed battery architecture is shown in Figure 5.23, where each of the motors in the drivetrain has its own power source. Each of the four batteries is one-fourth the size of the single battery pack that drives the centralized architecture. The same heave and pitch maneuvers used on the centralized battery architecture are applied to examine the demands on the powertrain.

Heave Command The heave command in Figure 5.14 is applied to the multi-rotor system with a distributed battery architecture. The speed response (shown in Figure 5.24) is

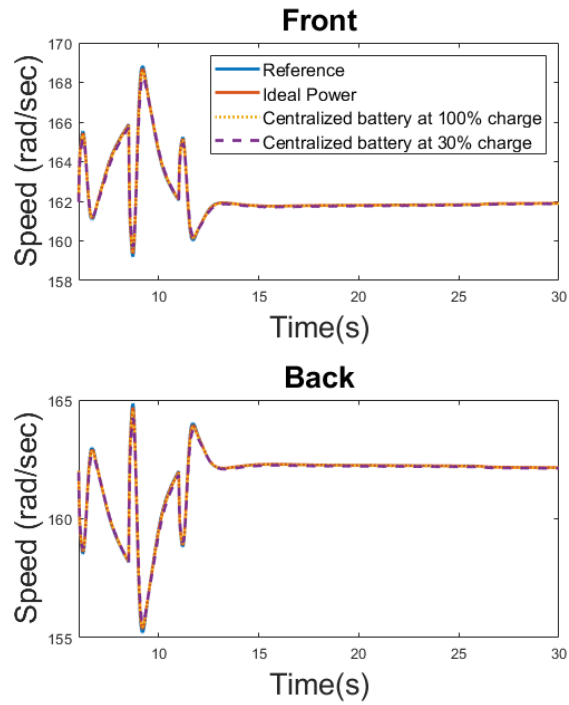


Figure 5.19: Speed response of the multi-rotor system to a pitch command.

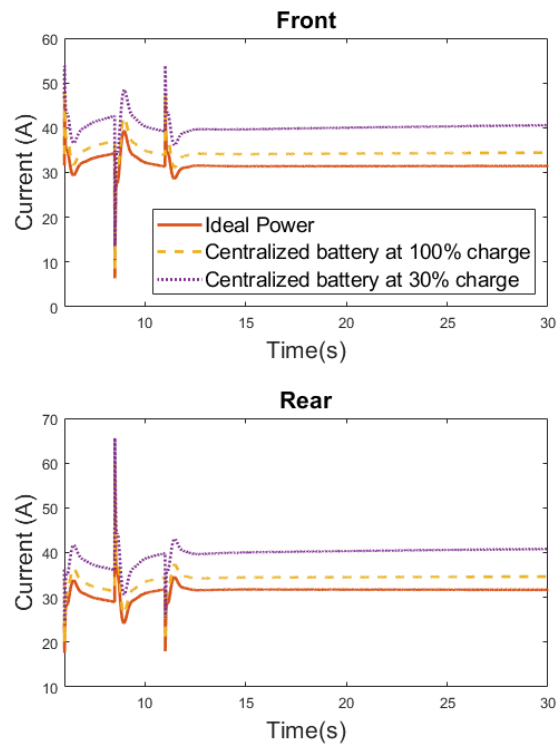


Figure 5.20: Current response of front and rear motors of the multi-rotor system to a pitch command.

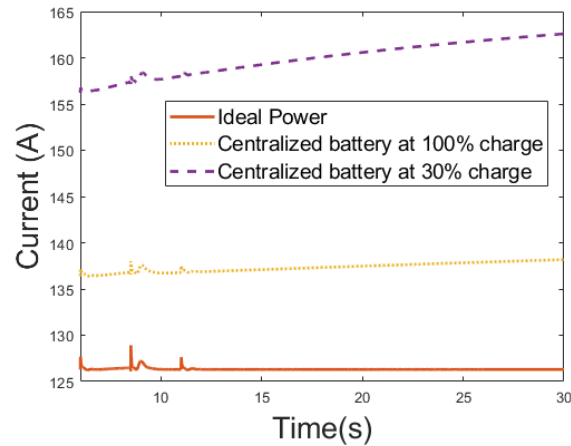


Figure 5.21: Current response of the multi-rotor system battery to a pitch command.

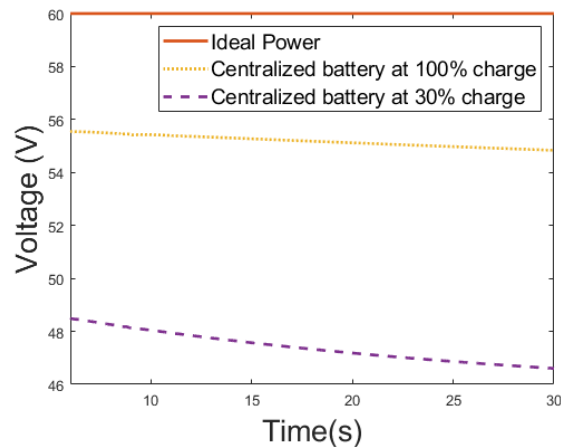


Figure 5.22: Voltage response of the multi-rotor system when pitch command is applied.

identical to that of the centralized battery, as might be expected, considering that heave commands load all four rotors identically. The current draw (Figure 5.25) is exactly one-fourth of the current observed for the centralized battery architecture (compare to Figure 5.16), an intuitive result, since each battery is responsible for one fourth of the powertrain. Since the capacity of each individual battery is also one-fourth that of the centralized battery, the voltage behavior (Figure 5.26) is identical to the centralized battery.

Pitch Command The pitch command and vehicle response are shown in Figure 5.18. The rotor speeds during the pitch doublet are shown in Figure 5.27. The ability to track

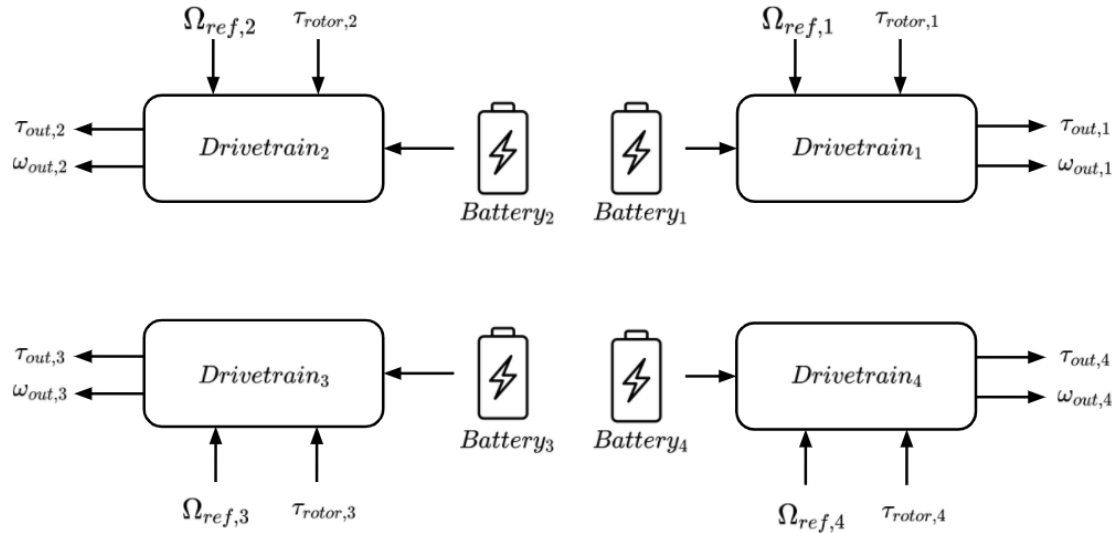


Figure 5.23: Multi-rotor aircraft model with individual batteries connected to each motor, creating a distributed architecture.

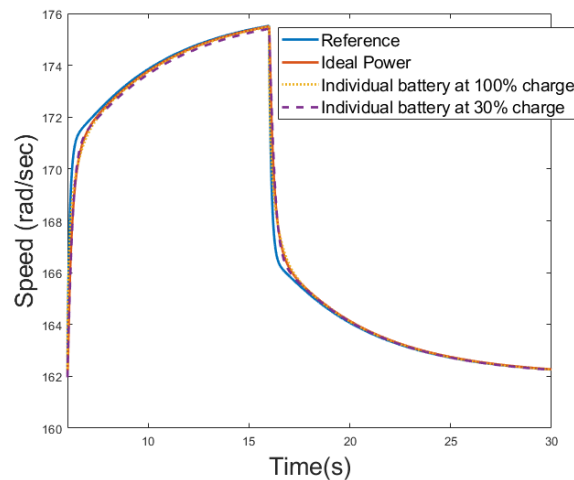


Figure 5.24: Speed response of the multi-rotor system with individual batteries to a heave command.

commanded velocities is identical to the centralized battery architecture (compare to Figure 5.19). However, the current response (Figure 5.28) is characteristically different. Because the front rotors' batteries are not connected to the rear rotors, the additional current drawn during a nose-up is not offset by the reduced current requirement of the rear rotors, and vice-versa. Thus, the current demands during pitch maneuvers will affect the battery sizing and cooling requirements. The batteries' voltage also changes during the doublet (Figure 5.29), though not as dramatically as during the heave maneuver.

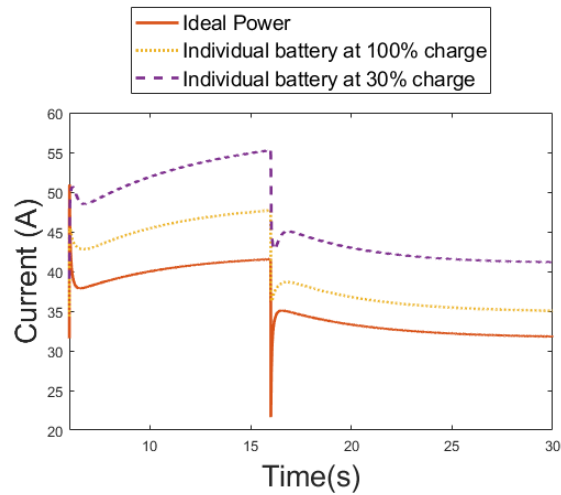


Figure 5.25: Current response of the multi-rotor system with individual batteries to a heave command.

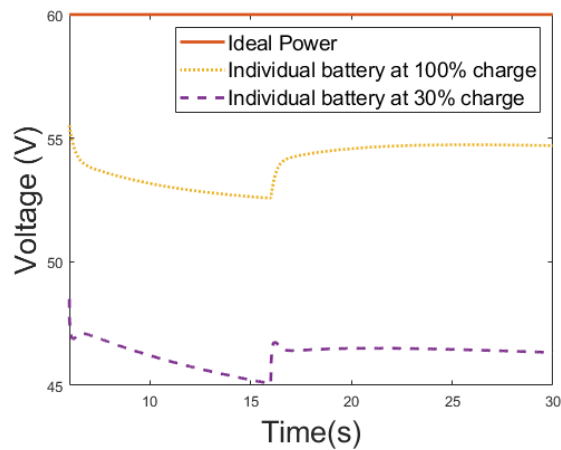


Figure 5.26: Voltage response of multi-rotor system with individual batteries to heave command.

Unbalanced battery charge Because the batteries in the distributed architecture are electrically decoupled from one another, it is plausible that, by the end of a flight, the batteries will have different states of charge. For example, as the rear rotors must spin faster (and consume more power) to maintain a nose-down pitch attitude in cruise, the rear batteries will discharge more than the front ones (assuming that the batteries are evenly divided between the rotors). To determine whether this might affect the tracking of speed commands, the same heave command is issued to a quadcopter whose front batteries are 40% charged and rear rotors are 30% charged.

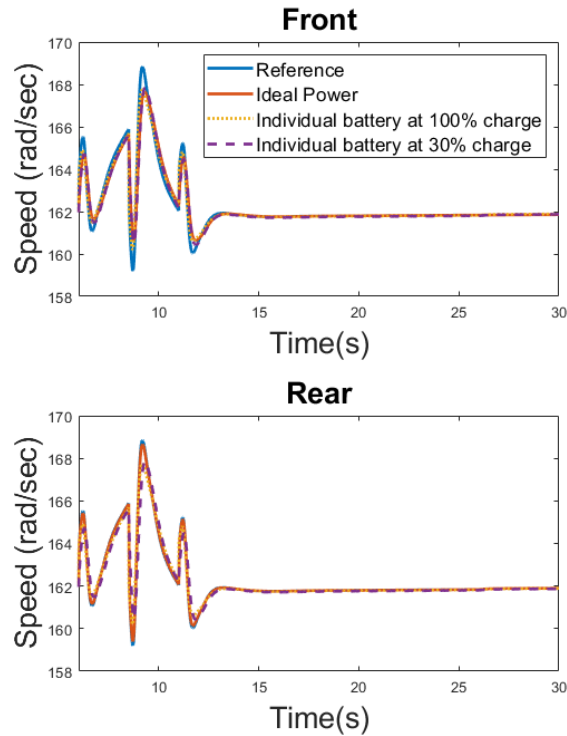


Figure 5.27: Speed response of the multi-rotor system with individual batteries to a pitch command.

The rotor speeds during the 50m climb are plotted in Figure 5.30a. The speed of the front motors very slightly lag the speed of the back motors (Figure 5.30b), though this will not result in any meaningful differences in the vehicle dynamics. Thus, it is clear that power delivery is not a limiting factor for the lithium polymer batteries used in this study, even when the charge is very low.

Figures 5.31 and 5.32 show the current and voltage in the front and back motors in aircraft. The back motors batteries are 6V higher than the front motors. As both of these motors must deliver the same power to the rotors during the climb, the current is greater for the rear batteries than the front.

5.6 Conclusion

Several drivetrain models and configurations were simulated on a 1200lb quadcopter. While the motor model has little effect on the tracking performance to rotor speed commands (and thus little effect on the flight dynamics), the torque ripple present due to the switching

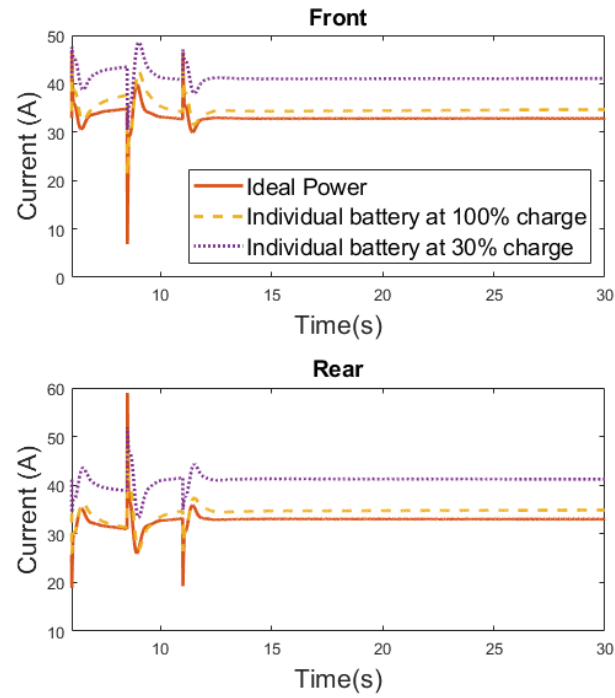


Figure 5.28: Current response of the multi-rotor system with individual batteries to a pitch command.

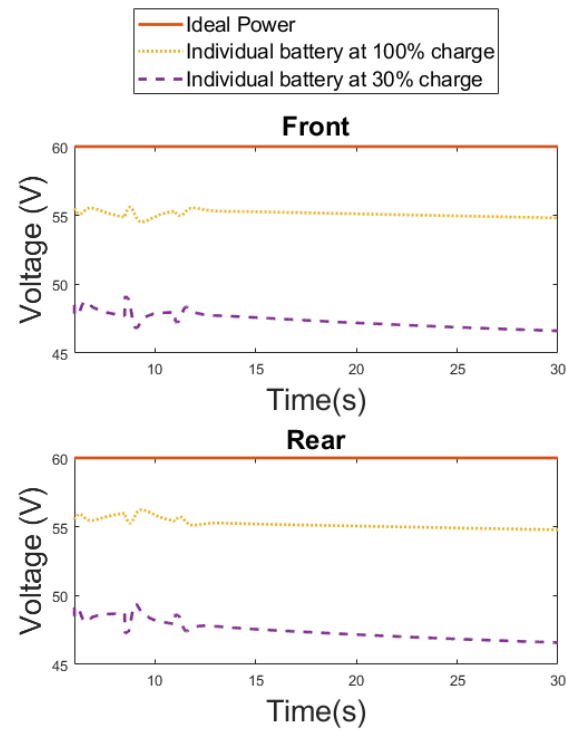


Figure 5.29: Voltage response of the multi-rotor system with individual batteries to a pitch command.

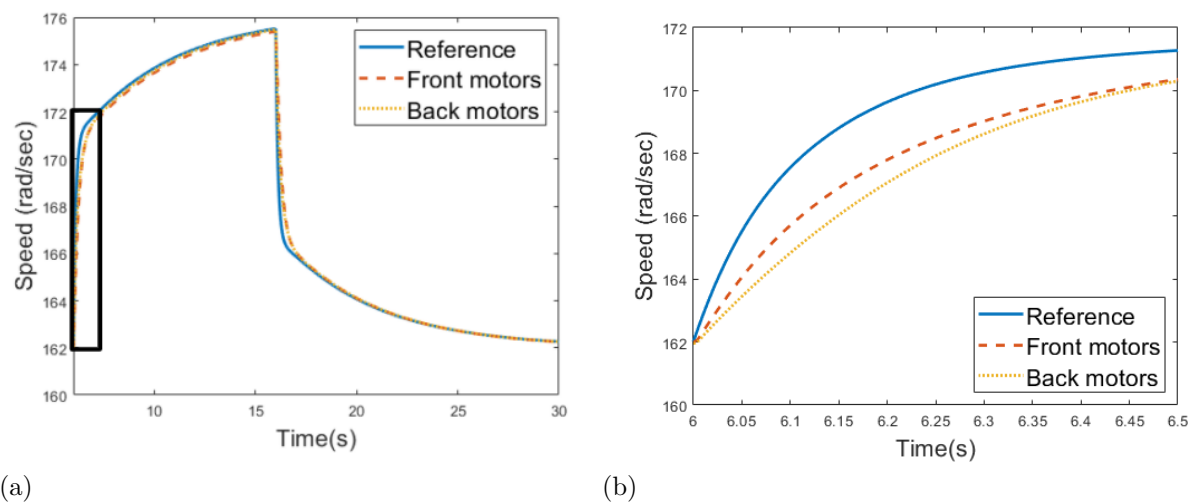


Figure 5.30: Speed response of the multi-rotor system to a heave command with unbalanced batteries with (a) Speed response of the multi-rotor system to a heave command with imbalanced batteries. (b) Inset from 6 to 6.5 seconds.

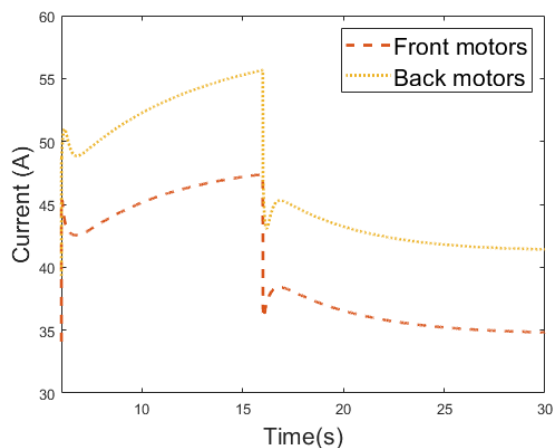


Figure 5.31: Current response of the multi-rotor system to heave command with unbalanced batteries.

behavior can lead to faster degradation of components in the system, and the simplified models commonly used for flight dynamics are not adequate to capture this phenomenon.

The power source model has noticeable impact on the drivetrain performance. Relative to a constant voltage source, the OCV battery model predicts substantial changes in the battery source voltage and current, which is particularly apparent for low states of charge. The additional current drawn from the battery can lead to greater resistance losses and heat

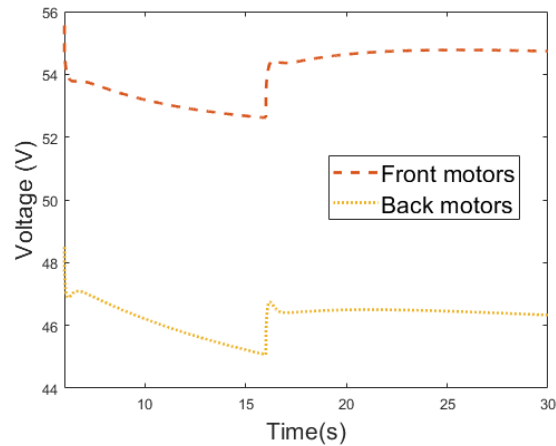


Figure 5.32: Voltage response of the multi-rotor system to heave command with unbalanced batteries.

generation in the powertrain.

Finally, a fully-centralized battery architecture was compared to a fully-distributed architecture. Though both configurations were adequate in terms of rotor speed tracking, the centralized battery experienced very little variation in its load during pitch maneuvers, since accelerating rotors were always offset by decelerating rotors. In the distributed architecture, each battery must be sized based on the maximum current demanded during heave/pitch/roll/yaw maneuvers, while the centralized battery must only be sized for heave maneuvers.

CHAPTER 6

POWER SYSTEM ARCHITECTURE DEVELOPMENT AND MULTI-DOMAIN MODELING FOR FULLY-ELECTRIC AIRCRAFT

6.1 Introduction

6.1.1 Motivation

Emission reductions in transportation require advances in aviation technologies which has led to new research and development efforts in fully electrified propulsion. In the fully-electric aircraft concept currently under development by the Center for High-Efficiency Electrical Technologies for Aircraft (CHEETA), the envisioned power system is cryogenically cooled with liquid hydrogen using many novel components, including high-temperature superconducting (HTS) cables [12].

This research specifically focuses on the application of simulation-based studies for an electrified power system at varying levels of complexity and fidelity, as well as defining the architecture of a complete multi-domain aircraft vehicle. The models have been created using the equation-based, object-oriented modeling language, Modelica [23]. Multi-domain models were created to capture each aspect of the power system, including the mechanical, electrical, and thermal domains. This chapter first introduces the aircraft system architecture, focusing on the electrical and thermal domains. The models and libraries used to create the models, modeling flexibility between different levels of model complexity, and preliminary results of the power system models of the fully-electric aircraft concept currently under development by the Center for High-Efficiency Electrical Technologies for Aircraft (CHEETA) are also described in this chapter.

Portions of this chapter previously appeared in: M. Podlaski, L. Vanfretti, H. Nademi, P. J. Ansell, K. S. Haran, and T. Balachandran, “Initial steps in modeling of CHEETA hybrid propulsion aircraft vehicle power systems using Modelica,” in *AIAA Propulsion and Energy 2020 Forum.*, Aug. 2020, Paper 3580, doi: 10.2514/6.2020-3580.; Reprinted with permission of the American Institute of Aeronautics and Astronautics, Inc.

Portions of this chapter previously appeared in: M. Podlaski, A. Khare, L. Vanfretti, M. D. Sumpston, and P. J. Ansell, “Multi-domain modeling for high temperature superconducting components for the CHEETA hybrid propulsion power system,” in *AIAA Propulsion and Energy 2021 Forum.*, Aug. 2021, Paper 3302, doi: 10.2514/6.2021-3302.; Reprinted with permission of the American Institute of Aeronautics and Astronautics, Inc.

Creating a physical prototype for a cryogenic power system is costly and difficult with limited opportunities for testing, especially because the aircraft is still in a conceptual phase. Well-defined, reliable models are essential for the development, testing, and validation of these novel components. Object-oriented equation-based modeling and simulation technologies allow for the implementation of technologies in the novel CHEETA power system architecture, e.g. HTS models, which in turn allows system responses to be studied under various operating conditions and response times. The models have been created using Modelica, as it offers interoperability and portability for multi-domain modeling. In this chapter, multi-domain models were created for the HTS lines within the power system focusing on the thermal and electrical domains. This chapter introduces the multi-domain modeling and analysis of cryogenically cooled HTS lines. Opportunities for trade-off studies for cooling methods of the HTS cables are also discussed.

6.1.2 Related Works

The power system architecture for the CHEETA aircraft and initial component modeling using the Modelica computer-based modeling language were first introduced in [12], providing a foundation for the development of HTS line model. The power system is cryogenically cooled using liquid hydrogen, which requires mathematical modeling of all components since their losses and operational behavior changes from the conventional behavior in traditional power systems at ambient temperature. As a result, multi-engineering domain models are required to study the system.

Previous electrified and hybrid aircraft designs do not utilize cryogenic cooling and the corresponding components in their power system designs. Electric aircraft configurations modeled in [13],[15],[31] utilize the same first-principles, multi-domain modeling techniques used in modeling the HTS lines and other components in the CHEETA power system. The More Open Electric Technologies (MOET) project explores a more-electric aircraft concept in [13],[15]. This provides a foundation for defining and modeling an aircraft power system covering the electrical, thermal, and mechanical domains. The technologies studied in MOET focus on improving the efficiency and electrification of conventional commercial aircraft components, bridging the gap between conventional aircraft and fully-electric aircraft. Ref. [31] discusses the development of models for the all-electric NASA X-57 aircraft [96]. The NASA X-57 aircraft is powered by batteries with a planned capacity of 47 kW-hr

(usable) or 69.1 kW-hr (total) [96], which is considerably smaller than the planned 20MW electrical system used in the CHEETA aircraft. The models and architecture discussed in [31] provide background for developing multi-domain models for electric aircraft configurations, showing how the mechanical, electrical, and thermal behaviors in the system can be effectively coupled for simulation. Fuel cells have not been extensively studied in electric aircraft using Modelica; the models in [97] can be applied simplified and integrated with the aircraft system-level models.

Cryogenic cooling and subsequent components have not been studied in detail at the multi-domain system level for aircraft applications. For example, HTS components are less studied, and have not been modeled or studied for aircraft applications. Other HTS components have been modeled and experimentally validated, such as in [98], however these studies primarily focus on strict partial differential equation models that only study the HTS material. This chapter focuses on modeling and application for HTS materials in the form of electrical components and the impact of the cooling media for the component with the goal of enabling integrated system analysis of the HTS lines as part of a aircraft power system.

6.1.3 Chapter Contribution

This chapter focuses on the following:

- The multi-domain modeling and development of the components in the CHEETA power system. The thermal and electrical domains are modeled; this allows for trade-off studies for different operating power capacities and cooling mediums.
- The thermal and electrical domains are interfaced at the equation-level, allowing to compute the thermal performance under different electrical configurations and cooling media.

In this work, the term “domain” refers to each engineering problem, e.g. all electrical variables in this model are modeled according to Ohm’s Law, Kirchhoff’s Laws and other electrical principles. The thermal system is modeled such that all variables and equations obey the laws of thermodynamics.

6.1.4 Chapter Organization

Section II introduces the CHEETA power system architecture, the system layout, and cooling system hierarchy to provide background on the application on the individual subsystems. The power system component modeling and development is discussed in Section

III. Preliminary results for simulating the aircraft at the system level and with various subsystems is shown in Section IV.

6.2 CHEETA Electrical System Architecture

6.2.1 Multi-Domain Modeling Approach

The models developed for the CHEETA aircraft are created using the object-oriented, equation-based modeling language, Modelica. Modelica provides flexibility to implement and interface models from different engineering domains by developing physically-meaningful equation-based interfaces between them. In the case of the subsystem components introduced in this chapter, the term ‘domain’ refers to an engineering problem. For example, all electrical variables are modeled according to Ohm’s Law, Kirchhoff’s Laws, and other electrical principles. In the thermal domain, the variables are modeled according to the laws of thermodynamics.

Given the layout of the aircraft in Figure 6.1, it is necessary to create interfaces and models to connect all sub-systems and sub-domains together to study the system. The sub-systems in the aircraft in Figure 6.1 are the cooling lines carrying liquid and gas hydrogen in orange, the fuel cells in green, liquid hydrogen storage tanks shown in blue, and the batteries in purple. The cryogenic environment is contained within the grey dashed lines, and the red dashed lines represent the wing fold lines. The coupling of the domains used to model the subsystems is shown in further detail in Section III.

6.2.2 Power System Architecture Overview

The CHEETA power system consists of a series of liquid hydrogen fuel cells and batteries, power electronics (i.e. inverters), and other components that supply electrical power to motors that drive the fans for aircraft propulsion [12]. The overall CHEETA power system architecture is shown in Figure 6.2. Each group of four fuel cells is connected via HTS transmission line to a distribution bus containing eight machines, inverters, and a battery that provides extra power when necessary. The two fuel cell buses are connected with a tie line for reliability. Each distribution bus bar has a battery directly connected, allowing for better distribution of weight throughout the aircraft as well as added electrical reliability.

The ‘additional loads’ in Figure 6.2 consist of the wing icing protection system, electro-mechanical actuators, environmental control system, and other AC and DC loads. They

all operate at ambient temperature, so they are simplified into one block in the system architecture. Since these ‘additional loads’ have been largely standardized in conventional aircraft, they are not in the scope of the CHEETA aircraft.

All of the bus bars and transmission lines are encapsulated by a cryogenic environment, as designated by the blue portion of the system in Figure 6.2. This schematic focuses on the electrical components; all cooling and thermal components are omitted. The system is modeled to operate at a voltage of 1kV DC with each motor providing 1.6625MW of power for a total of 26.6MW. In traditional power systems, normally the current in a system is minimized to limit the I^2R losses on the line, resulting in an operating voltage that is considerably higher than the current. HTS components provide negligible losses when subject to cryogenic cooling, allowing for a system to operate at a much higher current and lower voltage. The HTS line is cooled separately at a temperature of 20-25 K from the rest of the cryogenic components. The transmission lines and bus bars are the components most vulnerable to failure due to uncontrollable heating, so it is crucial that the temperature is controlled in its own loop.

The cooling architecture for the power system is shown at different levels of fidelity

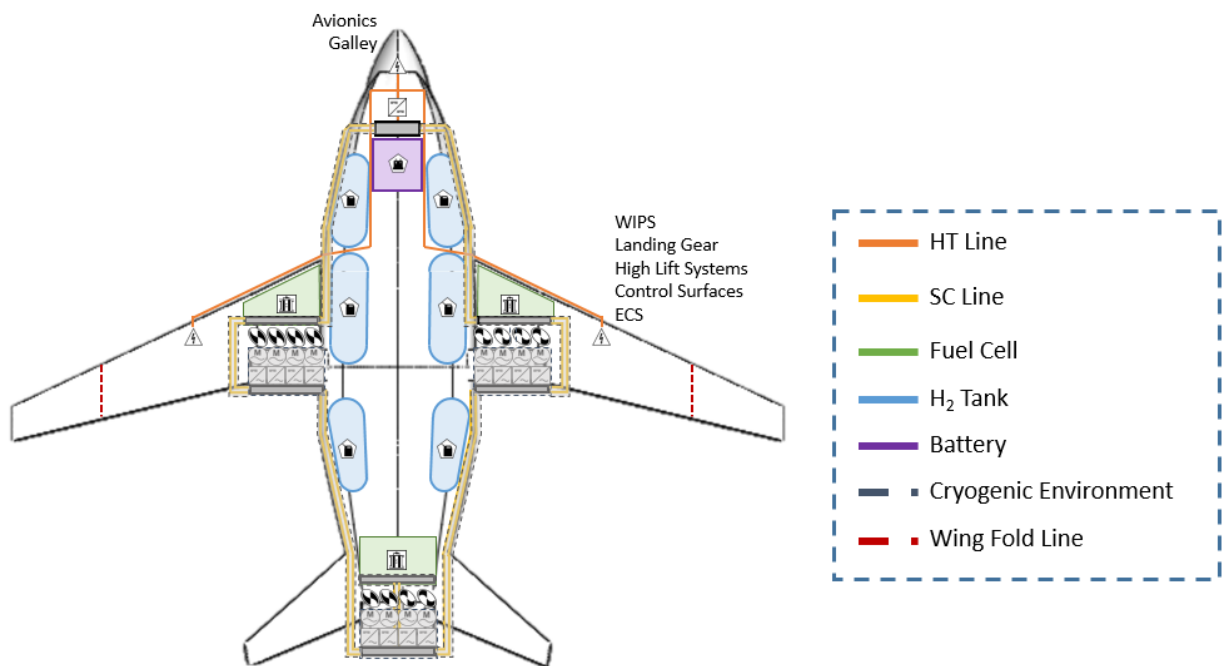


Figure 6.1: Power system architecture layout inside of proposed CHEETA aircraft in terms of sub-systems and sub-domains to demonstrate the physical placement of components.

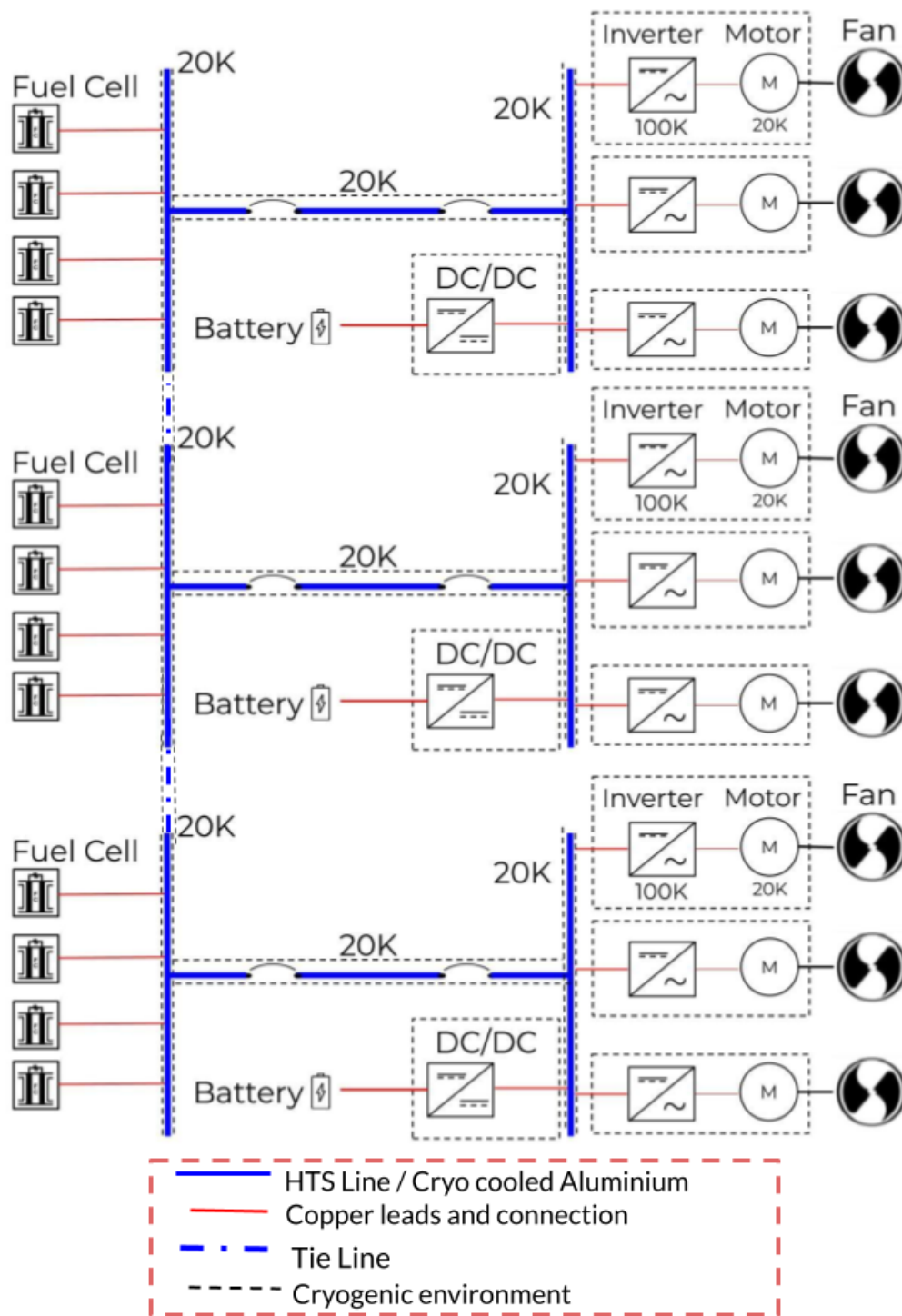


Figure 6.2: The CHEETA electric aircraft architecture configured to show the electrical wiring scheme for the system. This representation only shows the go portion of the circuit, the return lines will also have the same structure.

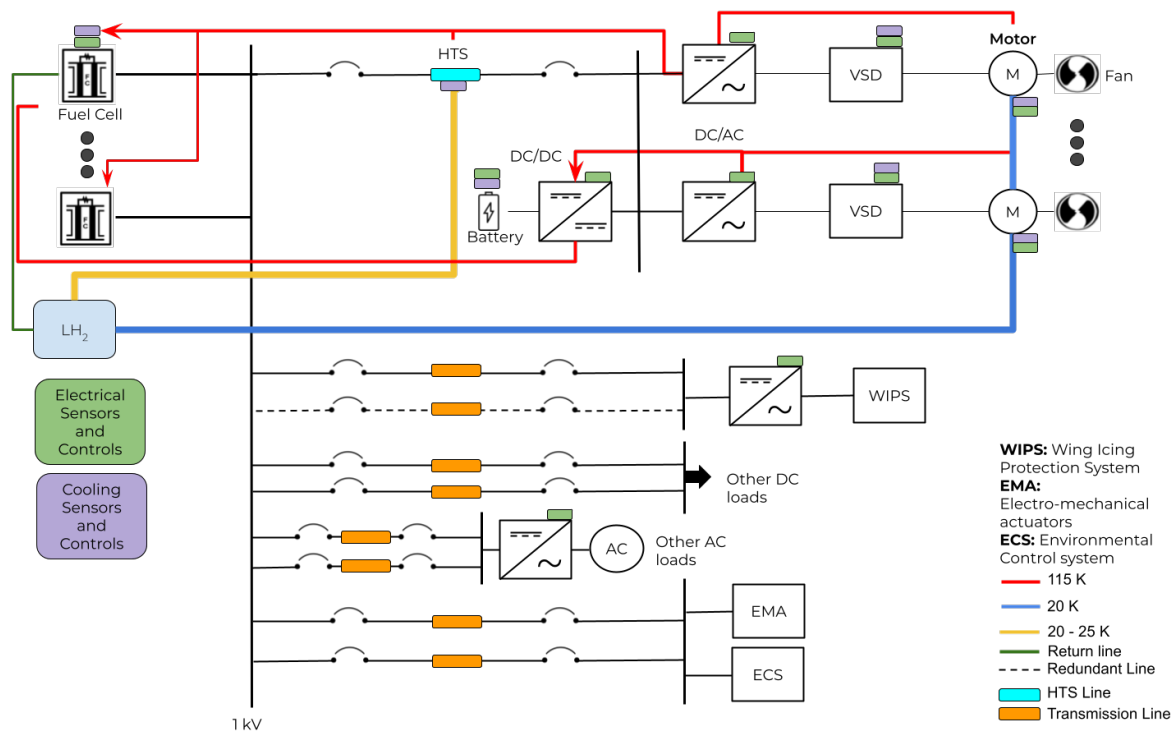


Figure 6.3: Cooling system concept for one branch of the power system.

in Figures 6.3 and 6.2. Figure 6.3 shows a portion of one branch of the fuel cell/drivetrain circuit. It shows the flow of liquid hydrogen and hydrogen gas between components in the electrical system, neglecting the controlled heating components. The HTS transmission lines and bus bars are cooled separately from the drivetrains and other components to ensure stable, constant temperature applied to the cryogenic components. This is necessary because the HTS cable needs to be constantly cooled at 20K to avoid film boiling, which will protect the system in case of a fault as it will have maximum ability to remove heat [99]. These components heat the hydrogen from liquid to gas to be applied to the power electronics, motors, and current leads in the drivetrains. The heated hydrogen gas from the power electronics is then sent to a heater to control the fuel cell cooling temperature. The fuel cell operates at ambient temperature.

The cooling system is further explained by Figure 6.4, which shows the flow of the cryogenic media through the system while generalizing the electrical architecture. The blue lines represent the liquid and gas hydrogen cooling to each component, while the red lines represent the parasitic heat and the heat generated by the component. This diagram also provides preliminary values for the allocation of cooling media to the various components as

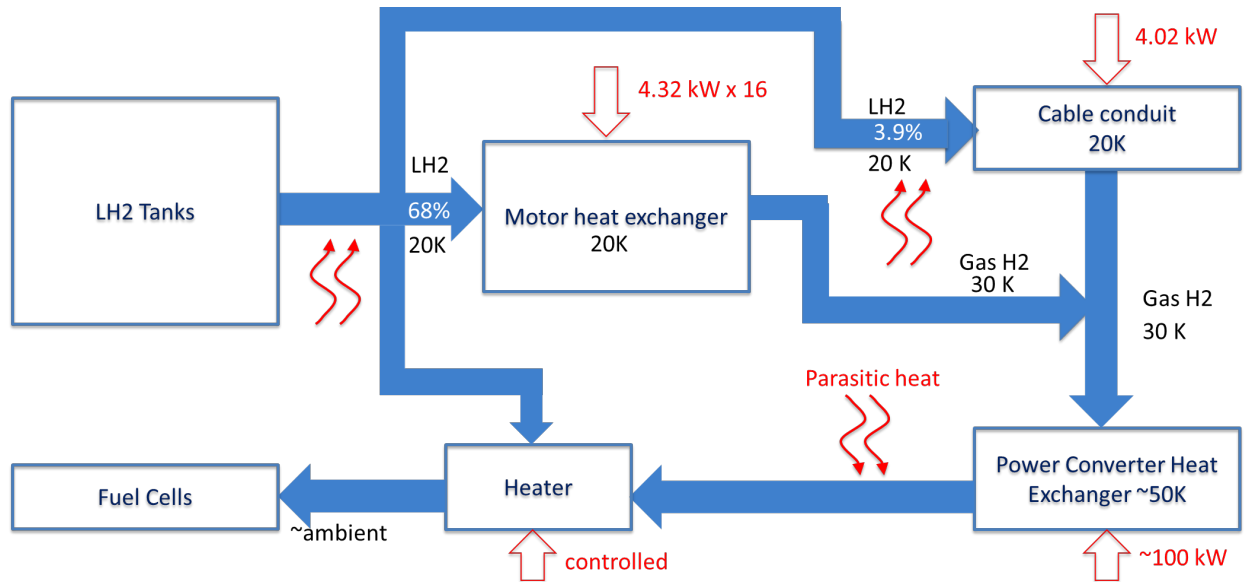


Figure 6.4: Cooling system flow chart for the power system with losses and operating temperatures for each component in the aircraft.

well as the operating temperatures of those components.

6.3 Power System Models

The electrical power system of the aircraft is modeled in terms of domains as shown in Figure 6.5, which shows the relationship between the different sub-systems, domains, and the components in the a simplified representation of the CHEETA power system. The blue lines represent electrical connections between components, the red lines represent thermal connections between components, and the orange and green lines are rotational mechanical connections from the rotor of the machine to drive the fan. As previously stated, these domains follow the principles of their respective engineering problems. The components of the power system in Figure 6.5 are labeled as follows:

- (A) Fuel cell
- (B) Battery
- (C) Drivetrain system
 - (1) Controller
 - (2) Pulse width modulation
 - (3) DC/DC converter
 - (4) Motor
- (D) HTS transmission line
- (E) Propulsion fans
- (F) Liquid hydrogen cooling system
- (G) Main control unit/system controls

6.3.1 Fuel Cell

The system is powered by proton-exchange membrane (PEM) fuel cells, in which a multi-domain model representing the thermal and electrical behaviors of the cell were derived from [100],[101]. Figure 6.6 shows the case of the PEMFC operating with the powertrain, where the fuel cell processing sub-loop is based off of [102]. The block at the bottom of the diagram that expands upon the processes needed to transform the LH₂ to DC power [101],[102].

The electrical schematic of the PEM fuel cell model is shown in Figure 6.7, which consists of a cell voltage denoted as E_{cell} and multiple resistances and capacitors. The value of the activation resistance R_{act} can be determined by Equation 6.1, which is used to determine the voltage drop in the fuel cell due to activation. Equation 6.2 is used to calculate the concentration resistance of the fuel cell. These two resistances can then be used to calculate the voltage drop due to the fuel cell losses according to Figure 6.8. These resistances vary as a function of the operating temperature T_f and current draw I_{FC} of the fuel cell. In Equations 6.1 and 6.2, R is the universal gas constant, α is the electron transfer coefficient, F is the Faraday constant, n_e is the number of electrons, and I_{max} is the

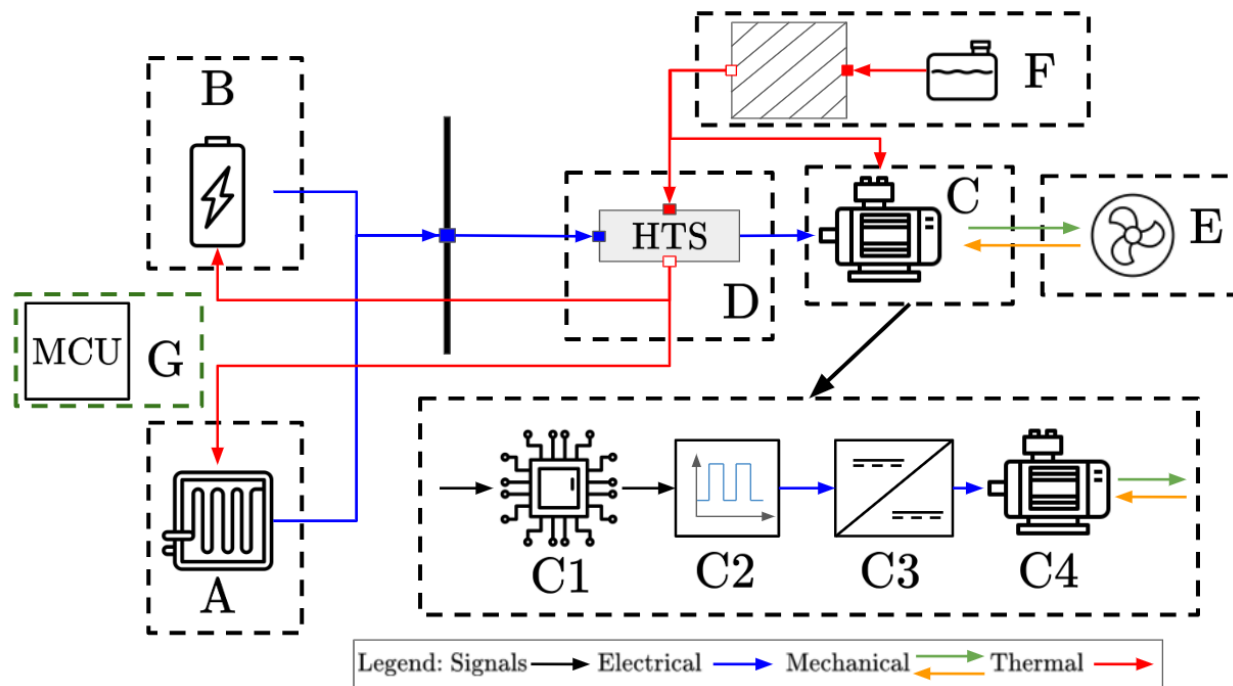


Figure 6.5: Single branch of power system modeled, highlighting the interaction between the domains in the CHEETA power system.

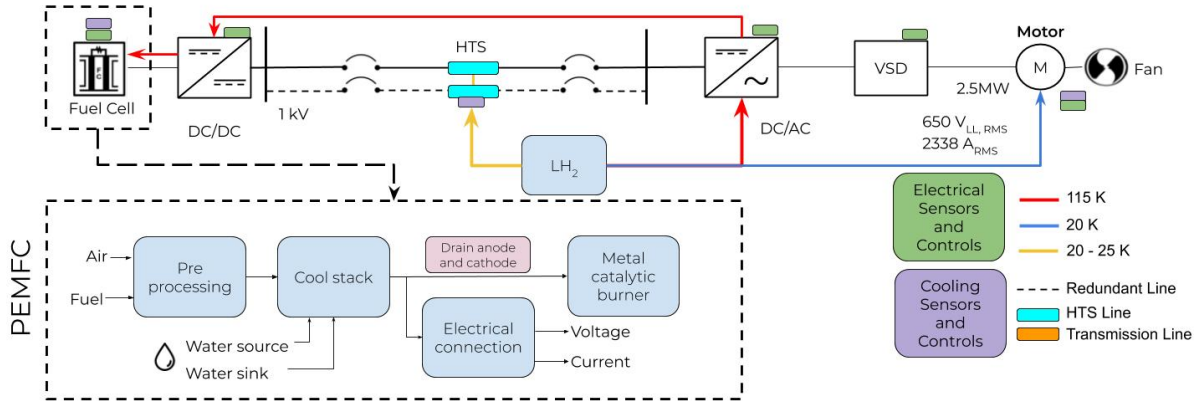


Figure 6.6: Power system with fuel cell operations and functionalities shown in detail.

maximum fuel cell current.

$$R_{act} = -\frac{RT_f \ln(I_{FC})}{\alpha n_e F I_{FC}} = \frac{V_{act,2}}{I_{FC}} \quad (6.1)$$

$$R_{conc} = -\frac{RT_f}{n_e F I_{FC}} \ln\left(\frac{-I_{FC}}{I_{max}}\right) \quad (6.2)$$

The fuel cell is also subject to ohmic losses as denoted in Figures 6.7 and 6.8. In Equation 6.3, R_{ohm0} is the constant portion of R_{ohm} , k_{RI} is an empirical constant for calculating R_{ohm} as a function of current, and k_{RT} is an empirical constant for calculating R_{ohm} as a function of temperature.

$$R_{ohm} = R_{ohm0} + k_{RI} I_{FC} - k_{RT} T_f \quad (6.3)$$

The output voltage of the fuel cell can be determined by Equation 6.4. The activation voltage is described empirically by the Tafel equation in Equation 6.5; this voltage drop is only dependent on the fuel cell's internal temperature. In Equation 6.6, η_0 is the temperature invariant part of the activation voltage, which is measured in Kelvin. The terms a_{FC} and b_{FC} in Equations 6.6 and 6.7 are constant terms used in the Tafel equation. The voltage

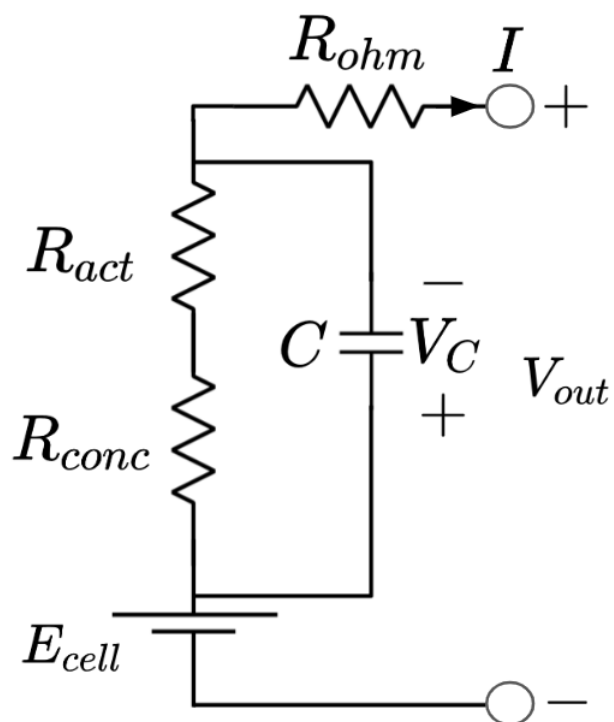


Figure 6.7: Electrical schematic of the PEM fuel cell.

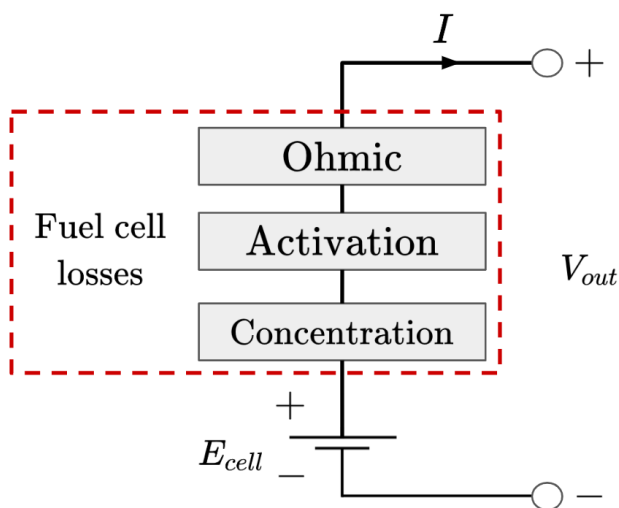


Figure 6.8: Electrical losses in fuel cell.

Table 6.1: Fuel cell parameters.

Parameter	Description	Value
a_{FC}	Constant used in Tafel equation (V/K)	-0.1373
b_{FC}	Constant used in Tafel equation (V/K)	N/A
C	Fuel cell capacitance (F)	10.6
E_{cell}	Total cell voltage (V)	1558.9
F	Faraday constant(sA/mol)	96485.3321
k_{RI}	Empirical constant to calculate R_{ohm} (Ω/A)	1e-9
k_{RT}	Empirical constant to calculate R_{ohm} (Ω/A)	1e-9
I_{max}	Maximum fuel cell current (A)	5000
n_e	Number of electrons (mol)	2
PO_2	Partial pressure of oxygen (unitless)	1.6
PH_2	Partial pressure of hydrogen (unitless)	1.5
R	Universal gas constant ($J/molK$)	8.3145
$R_{ohm,0}$	Constant portion of R_{ohm} (Ω)	0.2793
T_f	Fuel cell temperature (K)	193
α	Electron transfer coefficient (unitless)	0.1373
η_0	Temperature invariant part of V_{act} (V)	20.145

drop across the capacitor in Figure 6.7 can be determined from Equation 6.8.

$$V_{out} = E_{cell} - V_c - V_{ohm} - V_{act1} \quad (6.4)$$

$$V_{act} = \eta_0 + (T_f - 298)a_{FC} + T_f b_{FC} \ln(I_{FC}) \quad (6.5)$$

$$V_{act1} = \eta_0 + (T_f - 298)a_{FC} \quad (6.6)$$

$$V_{act2} = T_f b_{FC} \ln(I_{FC}) \quad (6.7)$$

$$V_C = (I_{FC} - C \frac{dV_C}{dt})(R_{act} + R_{conc}) \quad (6.8)$$

The parameters of the fuel cell in Figure 6.7 are listed in Table 6.1, which were derived from [100],[101] and the system requirements for CHEETA. The fuel cell has a power capacity of 2.5MW, operates at 1000V, and is parameterized with the stack values for the SR-12 stack from [101].

6.3.2 Battery

The multi-domain battery system is shown in Figure 6.9, which consists of a battery, its battery management system, a cold plate, and an inverter. The battery charging, discharging, and idle current is controlled by a bidirectional, averaged DC/DC converter. The

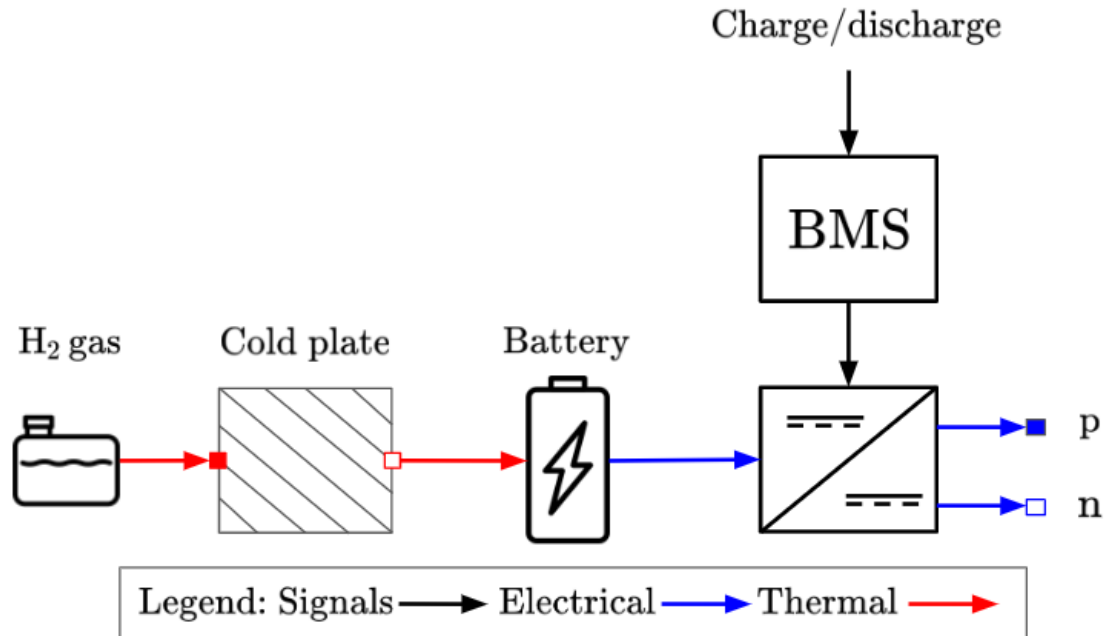


Figure 6.9: Multi-domain schematic for the battery.

state of the converter is determined by the battery management system (BMS), which is coupled to the inverter through the control (signals) domain. The cold plate controls the temperature of the battery cells, which will change electrical properties of the battery such as the internal impedance. In Figure 6.9, the thermal connections between components are shown in red, the electrical connections are shown in blue, and the control signals are shown in black.

The battery system is implemented in Dymola as shown in Figure 6.10. It consists of the bidirectional DC/DC converter, battery, BMS, and simple cold plates to cool the battery. The model considers three domains: electrical (denoted in blue), thermal (denoted in red), and control (denoted in pink and light blue). There are three external connectors to link the model with the rest of the electrical architecture. The pink external connection is a Boolean signal from the main controller unit (MCU) to override the battery system and turn it on if the fuel cell or some connector in the electrical system fails. This functionality improves system reliability and resiliency, as it would ensure safer handling of the aircraft post component failure.

The dark blue lines are electrical signals with `p1` and `n1` as external connectors to the rest of the system. The BMS uses the voltage and current measurements from the positive external electrical connections to determine the operational state of the battery pack and bidirectional converter. The light blue connection between the `batteryPack` and BMS are

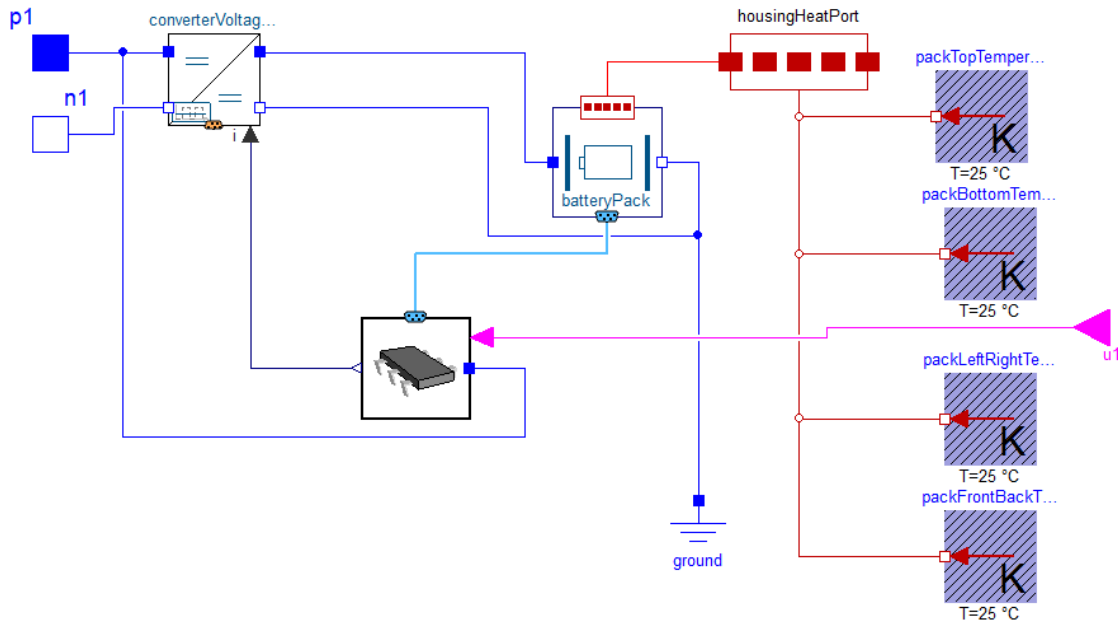


Figure 6.10: Circuit for the battery subsystem in Modelica using Dymola.

used to route the operational measurements from the battery to control the BMS. The red lines are used for the thermal domain to represent the simple cold plate model and interface it with the battery using the `housingHeatPort` component. The battery is thermally coupled to a cold plate that uses hydrogen gas for cooling. The cold plates on the battery are held at a constant temperature, as a dynamic model for the hydrogen cooling is not currently available.

The battery for the power system is modeled using the Dassault Systems Battery Library [94], which was developed using [103],[104]. The library contains models for different cell types. The battery pack currently used in the power system consists of a scaled pack of cylindrical cells with constant temperature applied to each side of the housing to represent the cold plates. Figure 6.11 shows the cylindrical battery pack used in the preliminary power system model. The `cell` block contains the model of the battery cell. It consists of a thermal model, open circuit voltage (OCV) table-based electrical model, and an aging model. The `electricScaling` block is connected to the external electrical connections to the power system and scales the voltage and current through the battery to be calculated per cell. The `housing` and `thermalScaling` blocks that represent the models of the thermal connection to the cold plates. The battery is parameterized according to the Sanyo 18650 Li-Ion battery data as provided by the Dassault Battery Library [94].

The battery parameters are shown in Table 6.2. The housing model parameters are

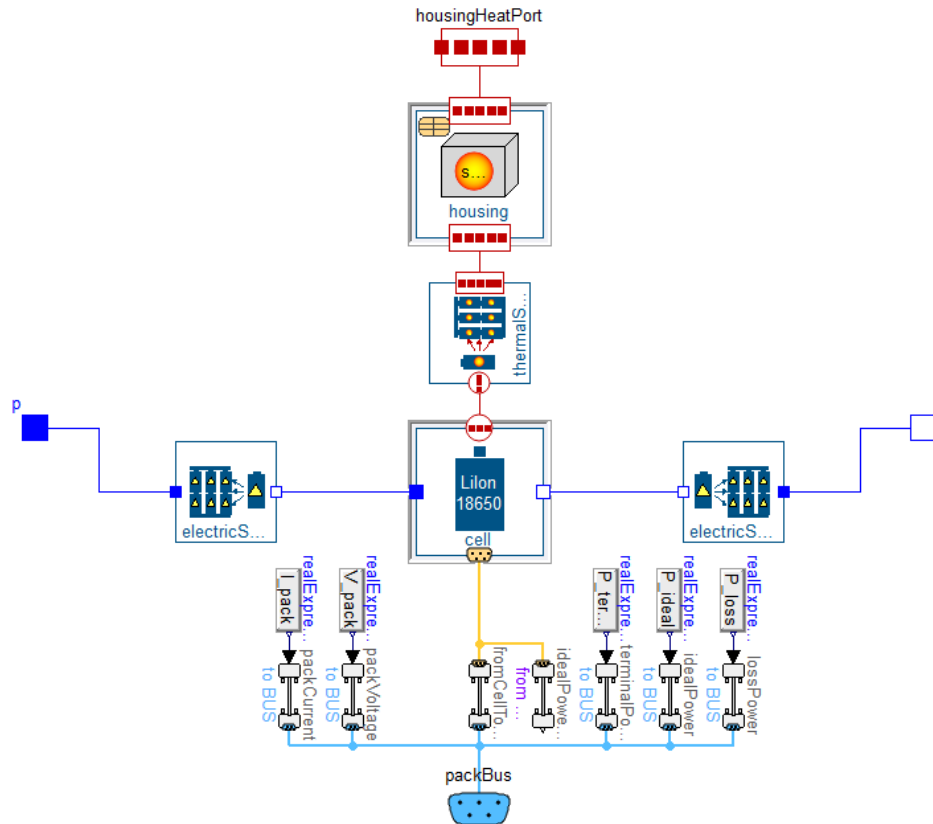


Figure 6.11: Cylindrical scaled battery pack model from Dassault Battery Library.

derived from the examples in the Battery Library [94] and the number of cells in series and parallel were determined from the CHEETA system requirements.

6.3.3 Electrified Drivetrain

The drivetrain is modeled using Dassault System’s Electrified Powertrains Library (EPTL) [33]. The DC drivetrain consists of four parts inside of the expanded block ‘C’: a controller ($C1$), a modulation method ($C2$), an inverter ($C3$), and a motor ($C4$) as shown in Figure 6.5. The models in the drivetrain are replaceable, allowing us to switch between different levels of modeling fidelity for each sub-component (e.g. $C1, C2, C3, C4$) without completely re-configuring the model. This makes the models easy to maintain and re-usable for a variety of simulation studies.

The drivetrain can be configured to use either a torque command or a speed command provided by the energy management system to control the output of the drivetrain, which is denoted by the controller ($C1$) in Figure 6.5. This control signal changes the rate of modulation and duty cycle of the inverter ($C2$). These modulation signals control the switching

Table 6.2: Battery parameters.

Electrical Parameters		
Parameter	Description	Value
C_{nom}	Nominal capacity of the cells based on scaled data (As)	3600
n_p	Number of cells in parallel (unitless)	50
n_s	Number of cells in series (unitless)	125
SOC_{init}	Initial state of charge of the scaled pack (unitless)	1
T_b	Battery operating temperature (C)	20
V	Nominal voltage of battery (V)	500
Housing Model Parameters		
Parameter	Description	Value
D	Cell diameter (m)	0.0181
h	Cell height in z direction (m)	0.0648
$negDiameter$	Negative pin diameter (m)	0.009
$negHeight$	Positive pin height (m)	0.004
$posDiameter$	Positive pin diameter (m)	0.009
$posHeight$	Positive pin height (m)	0.004
t_s	Cell sheet thickness (m)	5e-5
N/A	Pin material	Steel
N/A	Sheet material	Steel
N/A	Core material	Lithium-Ion

of the inverter ($C3$), which will control the speed or torque of the motor ($C4$) via electrical coupling. The motor is a superconducting electrically excited synchronous machine that operates at 20K via liquid hydrogen cooling.

6.3.3.1 Controller

In the current CHEETA configuration, the controller for the electrified drivetrain tracks the desired speed of the motor and line voltage to adjust the operating voltage of the machine. Figure 6.12 shows the PI controller used from the EPTL, which is based off of control Scheme B in [105]. The time constants, limits, and other parameters in the controller are computed from the machine parameters in Table 6.3. The drivetrain controller contains current controllers, a flux controller, a field weakening controller, a controller for maximum torque, and a block for current limitation. Given the current state of system development for the CHEETA aircraft, this controller is adequate as the system is primarily being studied in steady state. When a mission profile for the aircraft becomes available as a result of future development, the controller architecture may change.

The functionalities of the controller in Figure 6.12 are described as follows. The `field weakening control` block sets the reference value for the magnetizing current of the machine based off of the machine's field inductances and nominal flux. The magnetizing current is then used as the input for the `rotor flux estimation` to set the flux producing current. This is calculated by a PI block using the nominal and maximum flux and operating temperature of the machine to determine controller gains. The `current controller` block uses the flux producing current and current from the `speed control` to determine if the machine is operating at maximum voltage. If the machine is not operating at the maximum voltage, the controller will adjust to operating at the nominal flux.

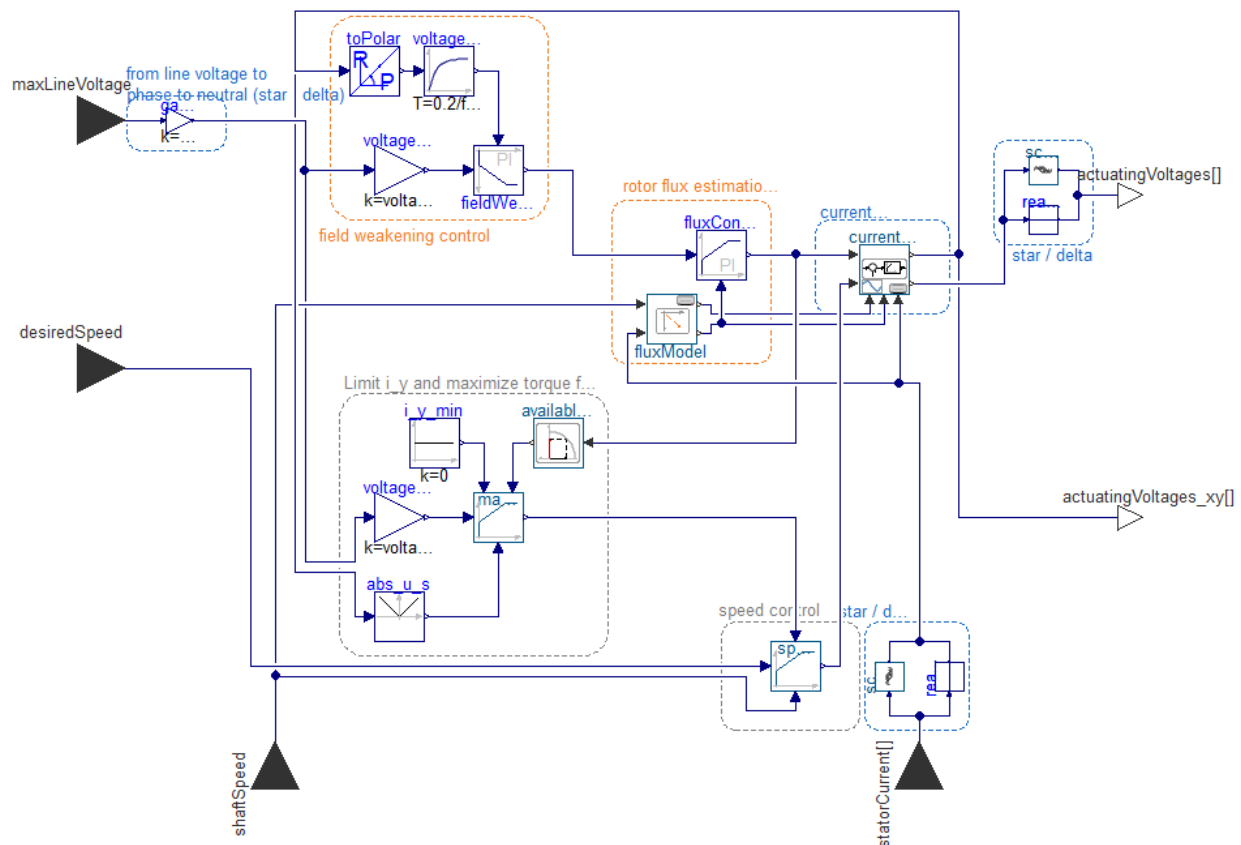


Figure 6.12: PI speed controller used in electric speed drive.

6.3.3.2 Modulation Method for Inverter Control

The functions for modulation of the controller signal to supply an input for the inverter are contained in Block *C2* in Figure 6.5. The EPTL has options to use no modulation, sine triangular modulation, and space vector modulation. Since these models are configured to have a replaceable structure, the modulation method can be easily switched for different cases

without significant reconfiguration of the model. Currently the drivetrain is configured to use no modulation method, which is shown in Figure 6.13. This model takes the phase voltages from the controller and normalizes it to be applied to the inverter with the option to add in a third harmonic distortion. Since the aircraft is in early stages of system development, it is necessary to consider only the simplest model as the modulation requirements have not been defined by the groups researching the power electronic systems.

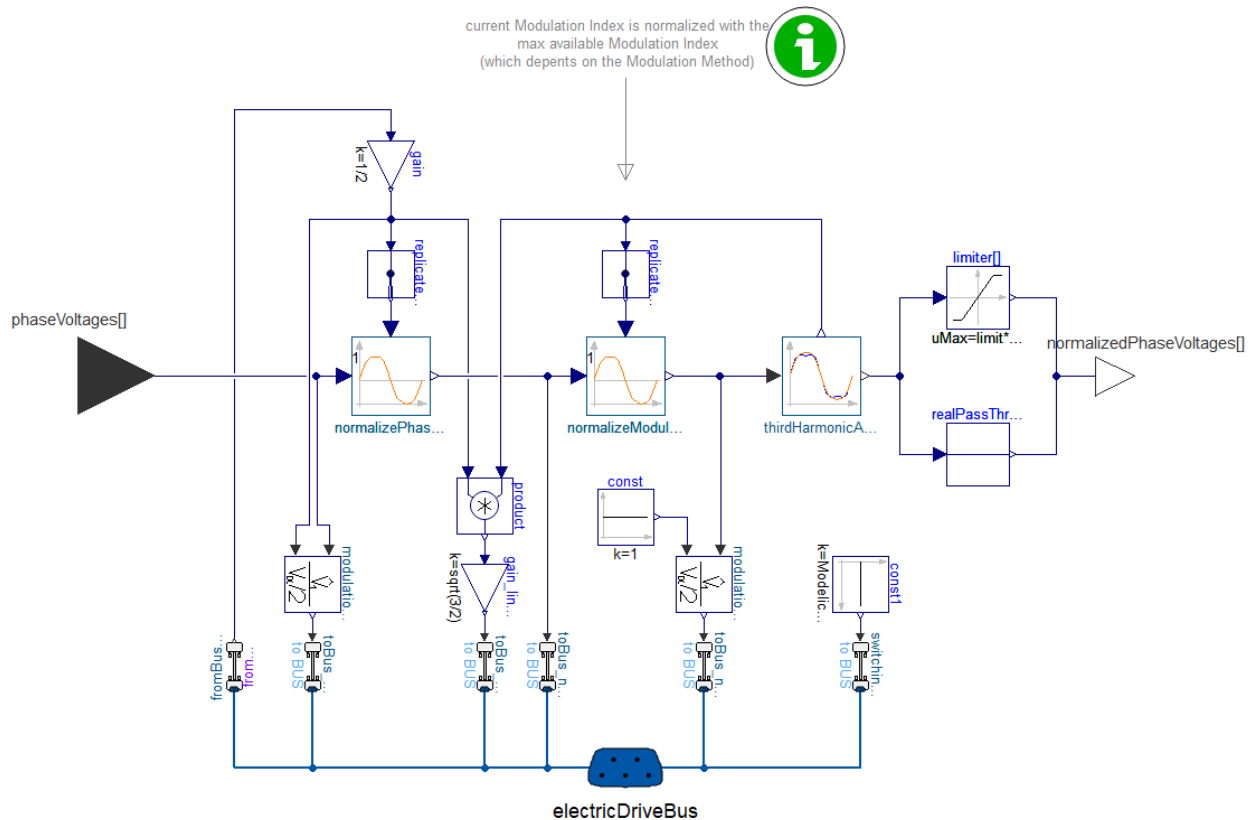


Figure 6.13: No modulation method for electric powertrain controller from EPTL.

6.3.3.3 Inverter

The aircraft power system is driven by DC power sources, so power electronic converters are necessary for maintaining voltage levels and driving the AC machines. Averaged converter models are implemented to eliminate switching functions from the transistors and diodes in the converters to increase simulation speed, however, note that the use of object-oriented features will allow to analyze the impact of both type of converter models within the same architecture. Given the system-level analysis currently being conducted on the system, it is not necessary to include power electronic models with switching functionalities.

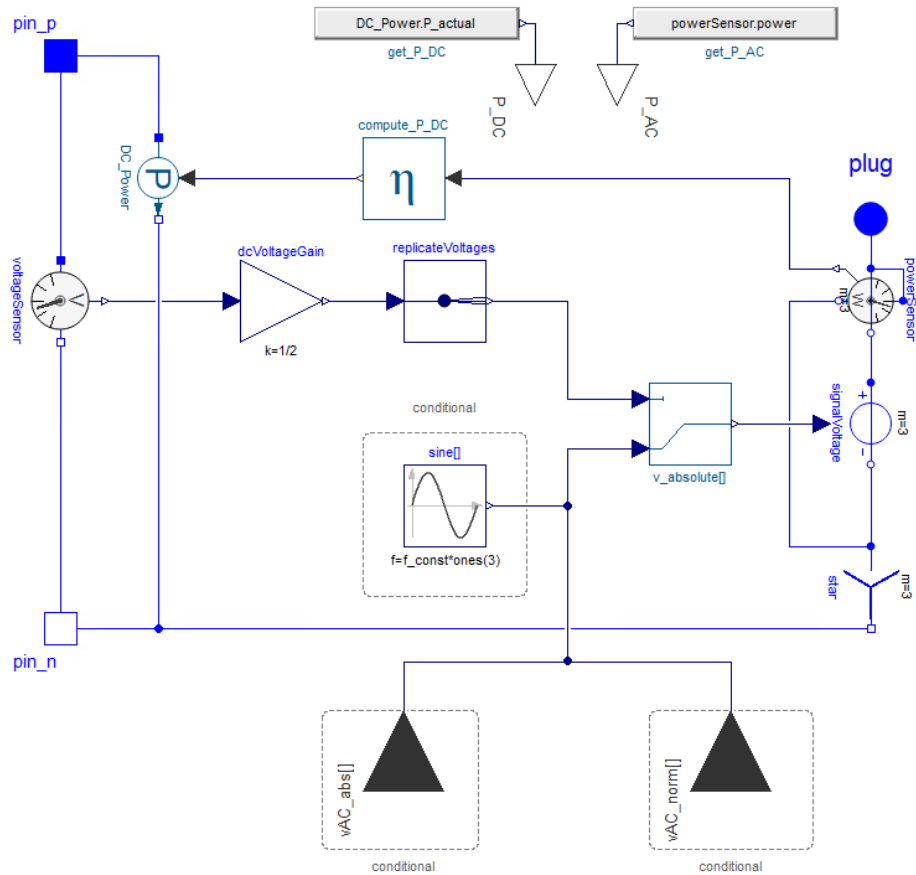


Figure 6.14: Averaged inverter model from EPTL in Dymola.

In the future, switched power electronic models will be used for trade studies focused on inverter behavior and the fast transient dynamics in the system.

The multi-domain model for the averaged inverters are shown in Figure 6.14. The electrical input connections `pin_p` and `pin_n` are connected to the fuel cell/battery input. The signal calculated by Equation 6.9 is used as an input for `signalVoltage` to produce a three phase voltage. The `signalVoltage` is then connected to external multi-phase connector `plug` to drive the machine. The DC voltage from the fuel cell or battery is applied at `pin_p` and `pin_n` and the AC voltage connected to the machine at `plug`. The switching functions from the transistors in a inverter are replaced with the calculations in `dcVoltage`, `replicateVoltage`, and `v_absolute[]` blocks.

$$\begin{bmatrix} V_a \\ V_b \\ V_c \end{bmatrix} = \begin{bmatrix} \frac{V_{dc}}{2} \sqrt{2} V_{rms} \sin(\omega t) \\ \frac{V_{dc}}{2} \sqrt{2} V_{rms} \sin(\omega t - \frac{2\pi}{3}) \\ \frac{V_{dc}}{2} \sqrt{2} V_{rms} \sin(\omega t - \frac{4\pi}{3}) \end{bmatrix} \quad (6.9)$$

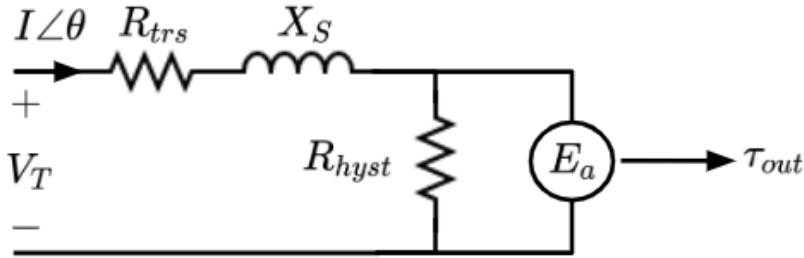


Figure 6.15: Simplified electrical circuit model for the machine.

6.3.3.4 Machine

The final component in the drivetrain is the machine. It can be represented at multiple levels of modeling fidelity, similar to the eVTOL drivetrain study in the previous chapter. The simplest representation of the motor is shown in Figure 6.15, which consists of an inductance and resistive losses for the AC transport and hysteresis. The CHEETA aircraft will use a superconducting motor for propulsion, which may have different behaviors for losses than the conventional machine model. Since the superconducting machine subsystem is currently undergoing development and defining the criteria for the model, the machine is configured for its simplest representations for system-level analysis.

The EMF of the motor in Figure 6.15 is denoted as E_a and can be determined from 6.10. The AC transport loss can then be determined by 6.11 and the hysteresis loss can be determined by 6.12.

$$E_a = V_T - (R_{trs} + jX_s)I \angle \theta \quad (6.10)$$

$$P_{trs,loss} = R_{trs}(I \cos \theta)^2 \quad (6.11)$$

$$P_{hyst,loss} = \frac{E_a^2}{R_{hyst}} \quad (6.12)$$

The Modelica model of the synchronous machine is shown in Figure 6.16, where the electrical, thermal, and mechanical domains are represented. The inverter in Figure 6.14 is electrically connected to the stator plugs `plug_sp` and `plug_sn`. The `spacePhasor` component transforms the AC voltage into phasor form to link to the stator core and inductances. This is then electrically connected to the `airGap` of the machine. The machine model is adapted from the Modelica Standard Library (MSL), which is a library of open-source, standardized models maintained by the Modelica Association [106]. In Figure 6.16, the blue

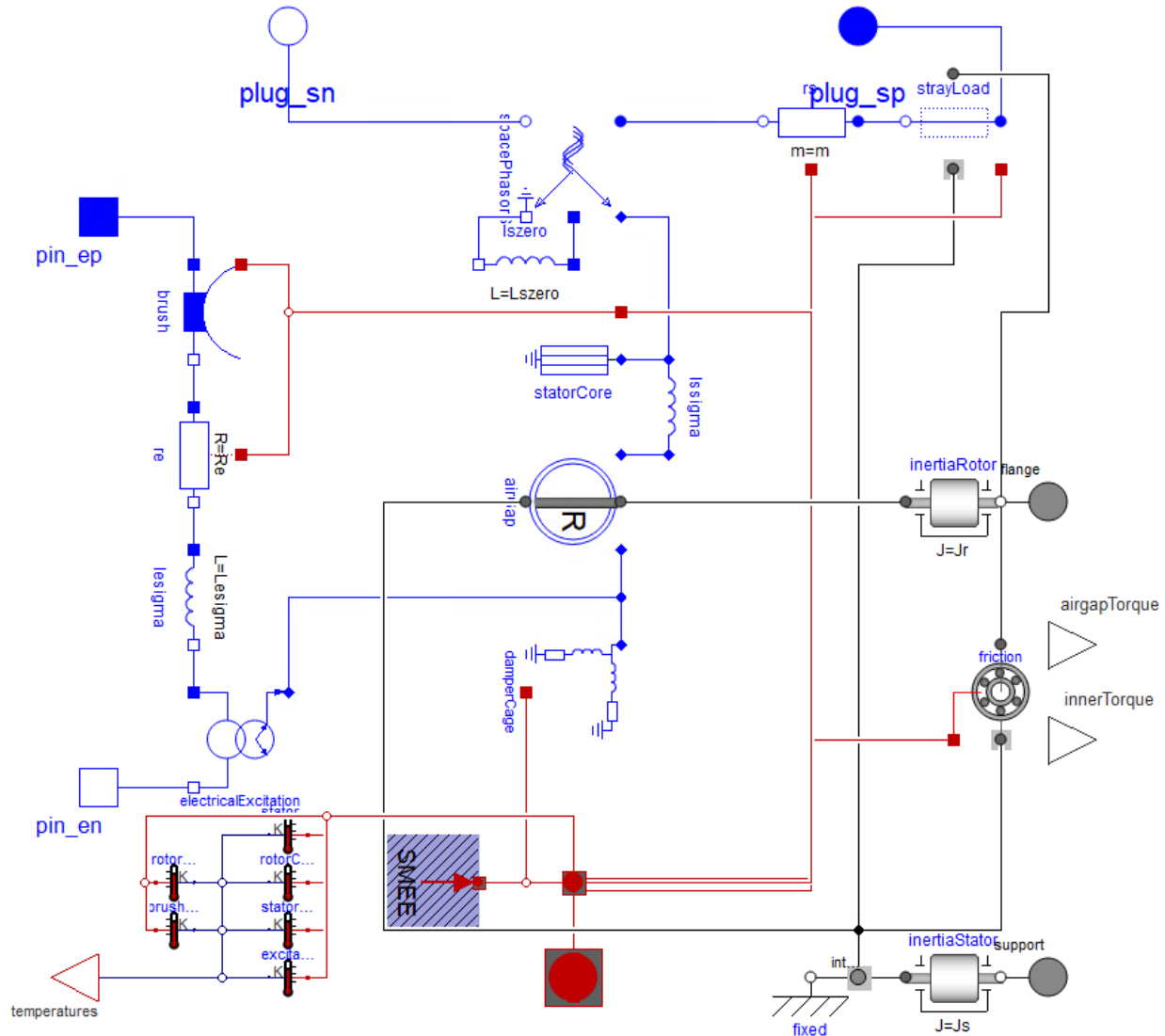


Figure 6.16: Synchronous machine model in Dymola.

lines represent the electrical domain, the red lines represent the thermal domain, and the grey lines represent the mechanical domain. The grey lines and connections coming out of the `airGap` represent the rotational mechanics of the rotor spinning. This also links to the `friction` component to calculate energy losses due to friction from rotation. The output connector `flange` mechanically links to the fan in terms of torque and rotational angle of the component.

The cryogenically cooled motor model is still under development by other groups collaborating on CHEETA, so the standard electrically excited machine is used in our analysis. The behavior of the machine does not significantly change, but the cryogenically cooled

Table 6.3: CHEETA machine parameters.

Electrical Parameters		
Parameter	Description	Value
P	Nominal power per motor (MW)	2.5
ω	Nominal motor speed (RPM)	4500
f	Electrical system frequency (Hz)	300
V_T	Terminal line-to-line voltage (V)	635.62
I	Nominal armature current (A)	2475
p	Pole count (unitless)	8
T_{op}	Operational temperature (K)	20
J_{arm}	Armature current density (A/mm ²)	200
J_{field}	Field current density (A/mm ²)	200
J_{shield}	Shield current density (A/mm ²)	200
pf	Power factor (unitless)	0.9177
X_s	Synchronous reactance (Ω)	0.041
L_{aa}	Armature inductance (μ H)	21.76
L_{ab}	Mutual inductance (μ H)	6.69
L_{ac}	Mutual inductance (μ H)	6.69
R_{hyst}	Effective resistance for hysteresis (Ω)	149
R_{trs}	Effective resistance for transport AC losses ($\mu\Omega$)	1
Motor Geometry Parameters		
Parameter	Description	Value
arm	Armature slots per pole	6
$P_{specific}$	Specific power of the machine (kW/kg)	25
l_{ag}	Air gap length (mm)	5
D_{out}	Outer diameter of the machine (m)	0.5
T_{op}	Operational temperature (K)	20
$Turns_{hand}$	Turns in hand (strands/cable)	27
$Turns$	Turns number (strands/cable)	11

machine has lower AC losses such as those in Equations 6.11 and 6.12.

6.3.4 HTS Transmission Line and Bus Bars

HTS transmission lines can electrically be represented as a pi-line model, similar to a standard co-axial cable model as shown in Figure 6.17. When the line is modeled using Modelica, it is a multi-domain model consisting of thermal (red) and electrical (blue) behavior as all electrical components are temperature dependent. The electrical behaviors of the line are dependent on the temperature of the cooling media surrounding the line, which can affect the lines behavior, and thus, needs to be controlled to a prescribed temperature

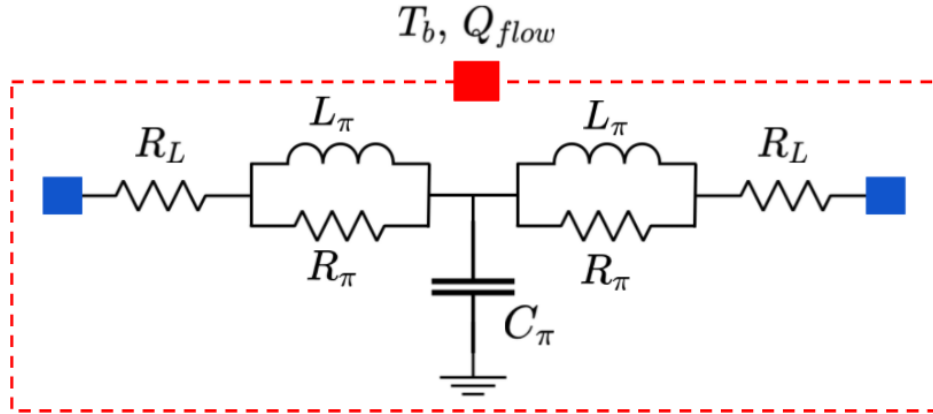


Figure 6.17: HTS pi-line model schematic.

range. In the model, this temperature is held constant by a fixed boundary condition that specifies the ideal temperature that the cooling system should maintain. The blue boxes in Figure 6.17 represent the electrical connections to the rest of the electrical system. In Figure 6.2, this would connect the fuel cells to the motors and batteries. The red box in Figure 6.17 represents the thermal connection to the cryogenic cooling media, where the line is fully submerged in a cooling bath and cooled on all surfaces. The current leads are modeled as R_L in Figure 6.17; currently they are represented by a constant resistance, but in future models they will be modeled as a resistive current lead subject to vapor cooling.

The HTS line is mathematically modeled using the equations outlined in [99],[107] for cold-end cooling. The HTS line's critical current I_c is calculated using Equation 6.13. It is the maximum current rated for the cable, is a function of the temperature of the media that the line is submerged in and a critical temperature T_c . The resistivity of the line is dependent on this critical current, shown in Equation 6.14.

$$I_c = I_{c0} \left(1 - \frac{T_l}{T_c}\right) \quad (6.13)$$

$$\rho = \frac{E * A_{cu}}{I_c} \quad (6.14)$$

$$E = E_0 \left(\frac{I}{I_c}\right)^n \quad (6.15)$$

The line is a pi-line model with resistive, inductive, and capacitive components that vary depending on the line temperature and carrying current. Equations 6.13, 6.15, and 6.14 are then used to calculate the values of the pi-line electrical model. In these equations, μ is the

permeability of free space and ϵ is the permittivity of the dielectric.

$$R_\pi = E_0 * \frac{\left(\frac{I}{I_c}\right)^n}{I} \quad \Omega / \text{m} \quad (6.16)$$

$$L_\pi = \frac{\mu}{2\pi} \log\left(\frac{b}{a}\right) \quad \text{H/m} \quad (6.17)$$

$$C_\pi = \frac{2\pi * \epsilon}{\log\left(\frac{b}{a}\right)} \quad \text{F/m} \quad (6.18)$$

When the HTS line is submerged in a LH₂ cooling bath, so the thermal response of the model is defined by Equations 6.19 and 6.21. These functions are derived from the relationship that the heat transfer coefficient is the result of the heat transfer divided by the change in line temperature, $h = Q/\Delta T_\rho$. In this case, ΔT_ρ is measured at the surface of the HTS line as the difference between the coolant temperature and line surface temperature.

In addition, if the line is cooled by LH₂, the heat transfer coefficient in Equation 6.19 is a piece-wise function based off of the nucleate boiling curve in [108]. The piece-wise function is defined such that the line will remain in the cryogenic cooling region for any change in temperature in the cooling bath less than 3 K, the the line will enter the nucleate boiling region after the change in cooling bath temperature is instantaneously greater than 3 K. Because the line model follows the cold-end cooling outlined in [99], the cold end cooling is modeled using Equation 6.23 as a function of coolant temperature T_b . The heat transfer function for liquid nitrogen in shown in Equation 6.20

$$h = \begin{cases} 100(\Delta T_\rho)^{5.3} & \Delta T_\rho < 3 \\ \frac{10^5}{\Delta T_\rho} & 3 \leq \Delta T_\rho < 100 \\ 1000 & \Delta T_\rho \geq 100 \end{cases} \quad (6.19)$$

$$h = \begin{cases} 1000(0.6953 + 0.001079(\Delta T_\rho^4)) & \Delta T_\rho < 11 \\ 1000 \left(\frac{-5.787 - 0.155\Delta T_\rho}{1 - 0.546\Delta T_\rho} \right) & \Delta T_\rho \geq 11 \end{cases} \quad (6.20)$$

$$\Delta T_\rho = \frac{\left(\frac{\rho I_c^2}{P * A_{cu}} + G_d \right)}{h} \quad (6.21)$$

$$Q_{flow} = h * \Delta T_\rho + Q_{ce} \quad (6.22)$$

$$Q_{ce} = T_b \sqrt{2\kappa * A_{cu} * P * h} \quad (6.23)$$

The HTS line used in the CHEETA system can be parameterized using the values in Table 6.4.

Table 6.4: CHEETA HTS line parameters.

Electrical Parameters		
Parameter	Description	Value
E_0	Reference electric field (V/m)	10e-4
n	Index value of superconductor (unitless)	20
I_{c0}	Critical current at 0K (A)	3700
I_c	Critical current at 20K (A)	2870
R_L	Resistance of the brass connectors (Ω)	1e-3
μ_r	Relative conductivity of wire material (unitless)	1
ϵ_r	Relative permittivity of wire material (unitless)	2.2
Line Geometry Parameters		
Parameter	Description	Value
l	Length of wire (m)	10
A_{cu}	Cross sectional area of copper portion of wire (m^2)	0.1
a	Inner radius of co-axial cable (mm)	0.1
b	Outer radius of co-axial cable (mm)	0.5
P	Circumference of line (m)	1
R_c	Inner radius of cryostat (mm)	3
R_0	Outer radius of cable (mm)	11
Thermal Parameters		
Parameter	Description	Value
C_{pv}	Heat capacity of gas coolant (J/K)	5200
G_d	Energy perturbation causing a fault (W/m^2)	0
T_b	Cooling bath temperature (K)	20
T_c	Critical temperature (K)	92

6.3.4.1 High Temperature Superconductor Component Validation Results

The thermal behavior of the HTS transmission line needed to be validated against the data provided by the experimental work of [99]. To reproduce the laboratory experiments in simulation, the HTS transmission line model is connected to a current source that will ramp up to twice the critical current value, I_c , as shown in Figure 6.18. Since the line is

submerged in LH₂, the material could remain in the nucleate boiling or cryogenic region until approximately the current applied to the line is twice the value of I_c . This is due to the properties of LH₂ [108], as the line is the same temperature at all points on the surface of the line.

The HTS transmission line's thermal behavior was compared against the data in [108] to verify that the same heat transfer curve can be produced as that from experimental data, as shown in Figure 6.19. The thermal behavior was also compared to liquid nitrogen, which is a common coolant for cryogenic applications, in Figure 6.20 to provide a reference when fault and stability studies are conducted on the power system [109],[99]. For both heat transfer curves in Figures 6.19 and 6.20, the models match the expected behavior of LH₂ and LN₂ respectively.

Two different simulation scenarios are configured, one for liquid hydrogen and one for liquid nitrogen cooling according to the circuit in Figure 6.18. The current source is a ramp to make sure the HTS line is simulated in the cryogenic region, nucleate boiling, and film boiling. The same ramp input is applied to each line, which varies the line's current from 0 to 10 kA over a 15 second period. The lines have a critical current I_{c0} of 3.7 kA. In Figure 6.21, the liquid nitrogen cooled line starts entering the nucleate boiling region once the applied current exceeds the critical current I_{c0} at 3.7kA. The liquid hydrogen cooled line stays thermally stable until 8.5 kA is flowing through the line and then it enters the film boiling region. This shows that liquid hydrogen cooling will provide good thermal properties with substantial improvements in current carrying capacity that are critical power system design, as the properties of liquid hydrogen protect the system during faults and current surges without having to scale up the power capacity of the line.

6.3.5 Fan Load

The motors in the entire power system model drive a fan load, which acts as part of the propulsion system of the aircraft. Only the simplest models for a fan load are currently available for analysis in the power system model. This model consists of an inertia and a disk to represent the rotational dynamics and weight of the fan. A propeller model similar to the ones available for the drone in [67] and [22] are also included as simple fan models. These propeller models consist of multi-body masses attached to a rotor shaft. The fan model is

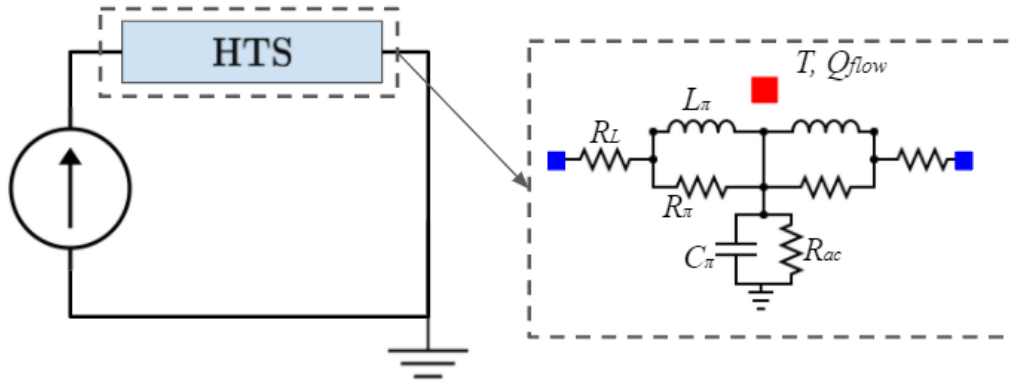


Figure 6.18: Circuit consisting of HTS line and current source.

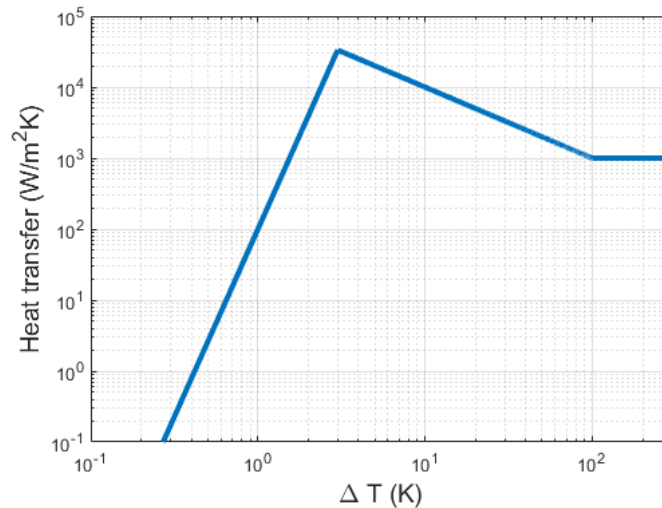


Figure 6.19: Heat transfer characteristics as a function of change in temperature for the line submerged in a liquid hydrogen cooling bath.

shown in Figure 6.22, where the inertia of the fan is converted into a torque that drives a gear that causes two cylinders to rotate. These cylinders are modeled as pipes with a scalar field that changes as a function of time. This assists in the animation and visualization of the fan. The torque from the motor is applied at `flange_a`, which is applied to the cylindrical blades using the `torque1` component. The `pipeWithScalarField` component visualizes the blades of the fan turning. Detailed fan models are not in the scope of the project, as CHEETA focuses on the development of the power system technologies rather than the propulsion system.

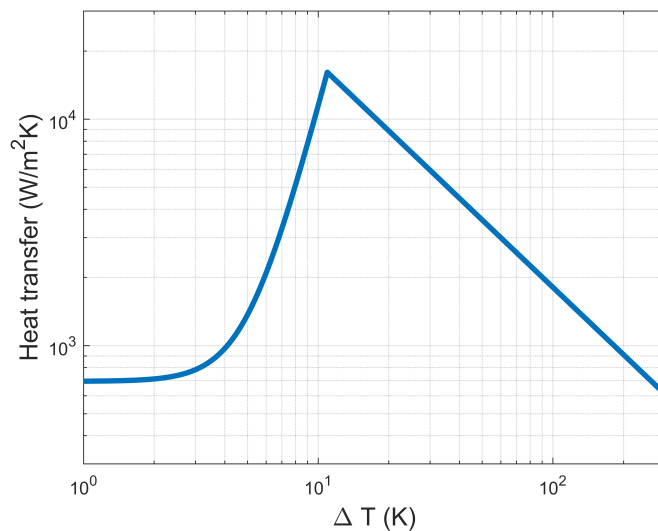


Figure 6.20: Heat transfer characteristics as a function of change in temperature for the line submerged in a liquid nitrogen cooling bath.

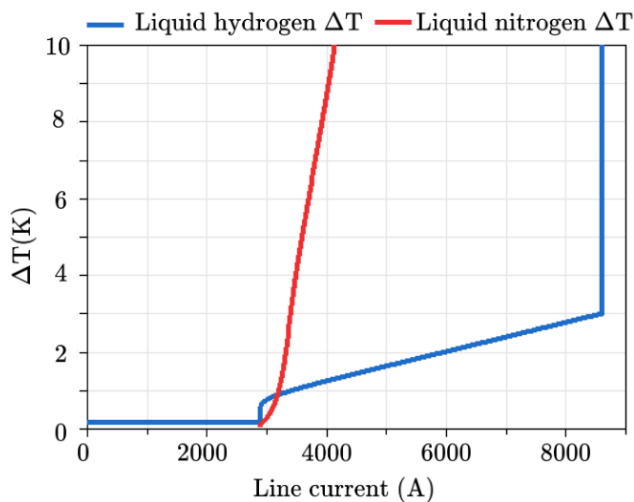


Figure 6.21: Comparison between the difference in temperature of the surface of the transmission line and cooling both media, where liquid hydrogen (blue) and liquid nitrogen (red), as a function of line current.

6.4 Preliminary Results

The system outlined in Figure 6.1 is tested using the CHEETA parameters as a single branch. This single branch consists of a fuel cell (operating as a constant voltage source), the HTS line, the powertrain, and a fan. The aircraft is flown over an hour-long period, where it takes off to a cruising altitude for 2.5 minutes, cruise for 25 minutes, and land for 2.5 minutes. When the aircraft is cruising at a steady altitude, the reference fan speed is 7000 RPM for the 1 MVA machine.

Figure 6.23 shows the voltage and current applied to the DC side at the drive during the hour long flight. While the AC curves are omitted, the RMS voltage through the machine during the steady state flight is 650 V and the RMS current is 850 A. The generator is operating at 1 MVA output. Part 1 is when the aircraft is taking off, it begins to fly at a steady speed during part 2, and is landing during part 3 in Figure 6.23. In the future, a more accurate machine fan load model will be added to the system to better represent the power draw instead of the approximate inertia model shown in Figure 6.22.

Figure 6.24 shows the change in HTS line temperature over the 30 minute flight path. Based off of the mathematical models in [99], the line will be operating safely in the cryogenic region when dT is below 2K. The temperature is maintained by assuming the transmission line is placed in a cooling bath maintained at 20K that can keep the line temperature stable below temperature changes below 2K. The current flowing through the line in Figure 6.23 is far below the critical current, so the line will not heat up uncontrollably and remain in

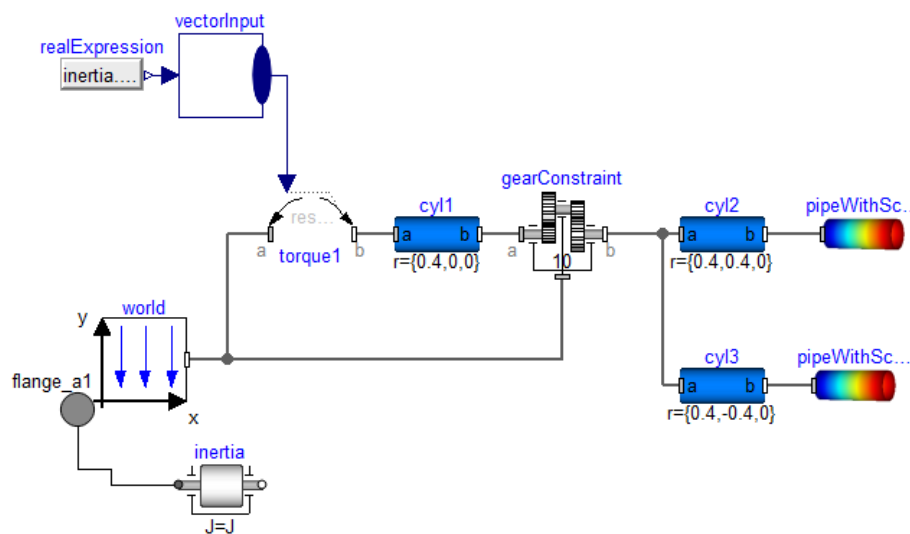


Figure 6.22: The multi-domain fan model in Modelica.

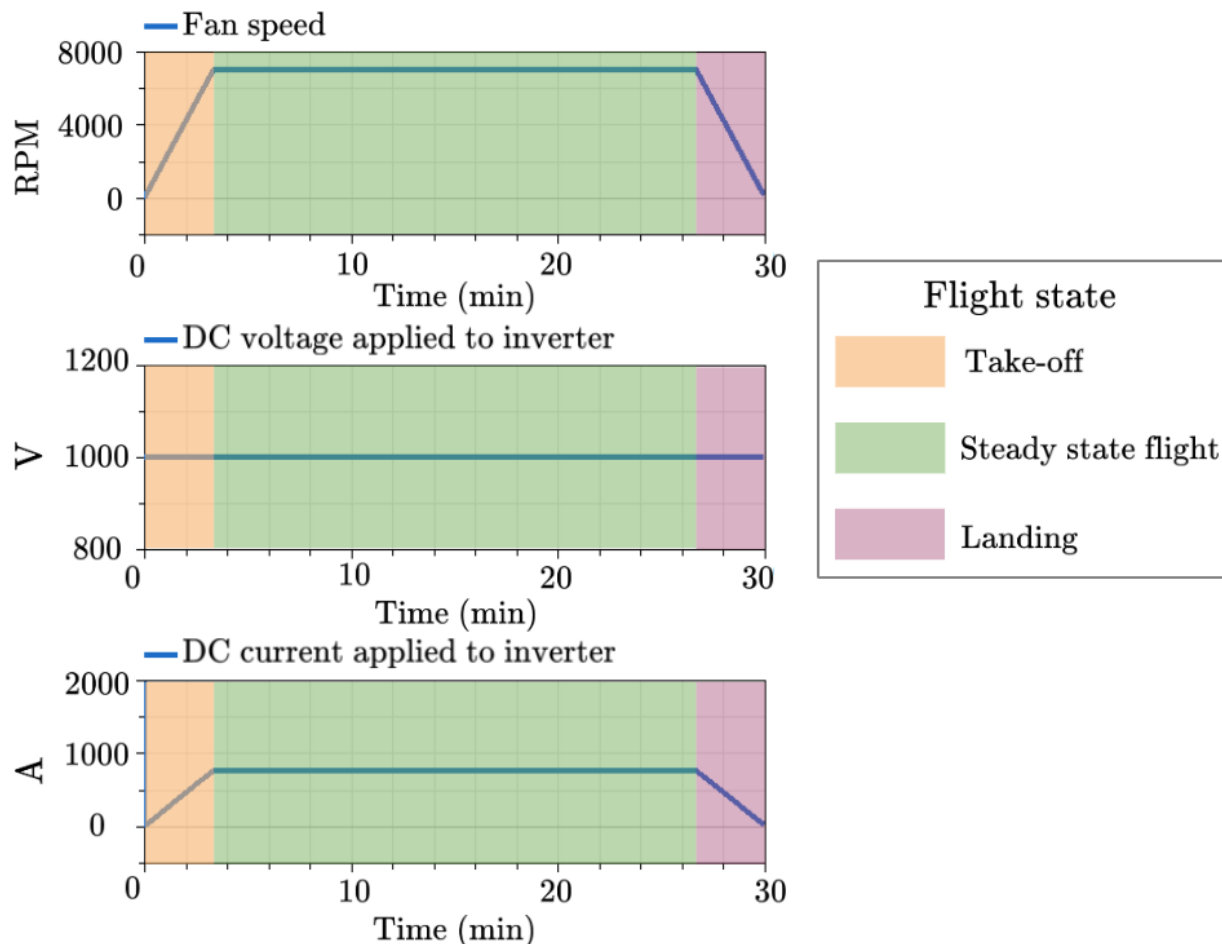


Figure 6.23: Machine during half hour flight path. It is split into three parts: part 1 is when the aircraft is taking off, part 2 is steady state flight, and part 3 is landing.

stable cryogenic operation. In the future, the line will be tested to observe the line behavior when faults are applied and the thermal system fails.

The fan model is a multi-domain model that is coupled to the AC motor, designated as blocks ‘E’ in Figure 6.1. The fan has a multi-body component in it to provide visualization for the fan rotation, which changes the coloring over the time in Figure 6.25. The green arrow in Figure 6.25 represents the changing force applied to the rotor of the propeller/fan system.

6.5 Conclusions

This chapter provides an outline of the novel components and architecture used in the CHEETA power system with replaceable models of varying degrees of fidelity. The electrified

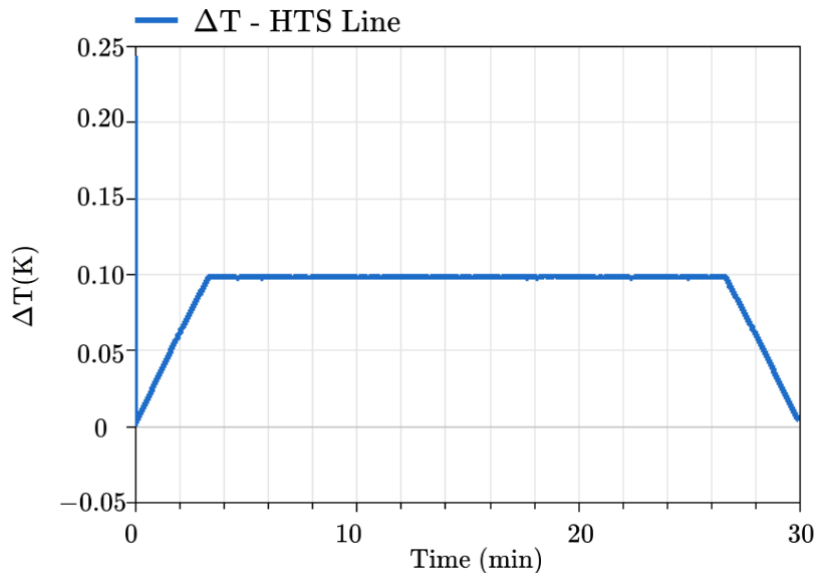


Figure 6.24: Change in HTS line temperature during the 30 minute flight path. Any difference in temperature between the cryogenic media and line less than 2K ensures that the line will operate in the cryogenic region.

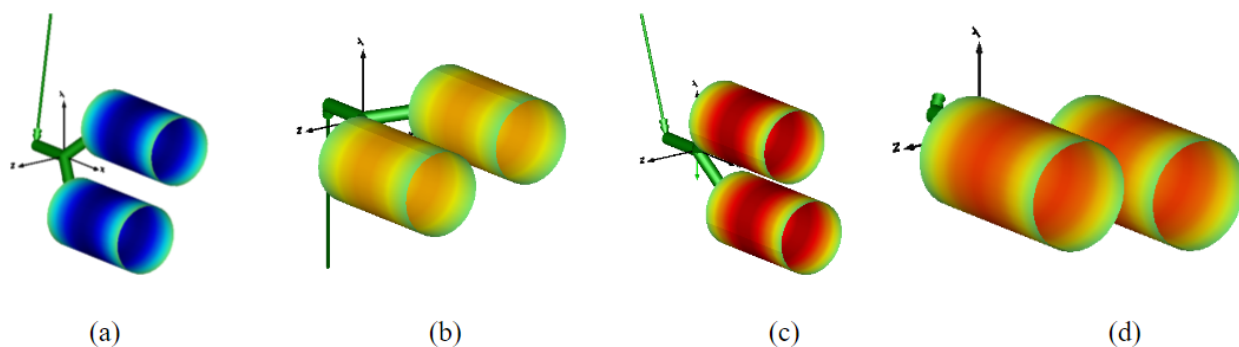


Figure 6.25: Fan model animation at (a) 5 seconds (b) 5.6 seconds (c) 5.8 seconds (d) 5.9 seconds with motor moving at a constant speed of 7000 RPM.

powertain model, for example, can be easily swapped to simulate the power system using different electrical machine models, such as the synchronous and induction motors. The power system has also been tested for a flight path in steady state for proof of concept. In future models, the power system will be tested under fault and component failure conditions to observe reliability of the components and develop more detailed models.

The thermal cooling loop will also be designed and modeled to simulate with the rest of the power system, which will provide useful data on cryogenic cooling of power system

components. These cooling models will help give more detail on the thermal losses in the powertrain and generation components. The BMS and EMS will include control based off of thermal inputs.

CHAPTER 7

MULTI-DOMAIN MODELING AND SIMULATION OF HIGH TEMPERATURE SUPERCONDUCTING TRANSMISSION LINES UNDER SHORT CIRCUIT FAULT CONDITIONS

7.1 Introduction

7.1.1 Motivation

Investment in environmentally-friendly and economical transportation has led to the active exploration of electrified aircraft concepts. Of all of the methods of conventional transportation, however, commercial aircraft features power requirements typically far higher than equivalently-sized ground, marine, and rail systems. To produce electrified propulsion systems capable of meeting these high power requirements in a compact and high-efficiency fashion, we can usefully turn to the use of cryogenically-cooled superconducting materials. However, creating physical prototypes for these kinds of complex systems can be costly and difficult, indicating the important role that modeling and simulation have towards understanding the operation of these new concepts and associated responses to fault modes.

This research specifically focuses on the development of models and their application in simulation-based studies for the design of an electrified aircraft power system enabled by cryogenically cooled high temperature superconducting (HTS) transmission lines. There are two aspects that need to be captured: the electrical behavior and the thermal behavior, so system design, integration, and analysis can be performed for electrical and thermal management. To this end, to perform both the electrical and thermal designs together, we will need to use a technology and modeling methodology that allows us to combine both behaviors in an entire system model. Multi-domain models were created to capture each physical aspect of the power system, specifically the electrical and thermal domains of the HTS line; each component in the power system has an individual, reusable model based on the component's physical equations and behaviors. The models have been created using the object-oriented modeling language, Modelica. This chapter introduces a model of HTS

This chapter previously appeared as: M. Podlaski, A. Khare, L. Vanfretti, M. Sumption, and P. Ansell, "Multi-domain modeling and simulation of high temperature superconducting transmission lines under short circuit fault conditions", *IEEE Trans. Transp. Electrific.*, vol. 8, no. 3, pp. 3859-3869, Sep. 2022, doi: 10.1109/TTE.2021.3131271. Reprinted with permission of IEEE. © 2021 IEEE.

lines configured within a simple yet representative aircraft electrical power system, alongside the modeled response of the system operation to fault conditions. These results inform the design for the fully-electric aircraft concept currently under development by the Center for High-Efficiency Electrical Technologies for Aircraft (CHEETA).

7.1.2 Related Works

Previous works have derived the mathematical models utilized in the current study and conducted experiments using liquid hydrogen (LH₂) to derive thermal response characteristics of the line [108],[109]. The electrical power systems subjected to the fault tests in this study were specified based on the CHEETA electrified aircraft system [12], and earlier models of the HTS lines and their application and integration with the CHEETA power system are described in [110].

HTS lines have been considered in electrified aircraft power system architectures due to the ability to carry high currents with low losses while not adding significant weight to the system. [111] proposes a temperature and time dependent thermo-electric model for an HTS cable according to the E - J power law. The failure modes focus on parameterizing the resistances and inductances of the line to mitigate different effects from the fault. In contrast, the HTS models described in this chapter assume a fixed boundary condition between the thermal port of the cooling media and the cable, allowing for thermal behavior specific to the cooling media used in the model and in-depth system level analysis. Other studies on electric aircraft focus on conducting sensitivity studies adjusting the cable parameters [112] to prevent/observe the time it takes the line to quench. In our study, we focus on how the lumped electrical characteristics of other components in the power system need to be considered to prevent quenching altogether.

In land-based systems, fault studies have been conducted on HTS lines such as the one in [113]. The liquid nitrogen cooled HTS system in [113] is studied under utility fault conditions to analyze the current distribution of the line, where the studies primarily focus on the electrical behavior of the line instead of the thermal behavior with the objective of determining if both layers of the cable would quench under fault conditions. The land-based system in [114] presents a three-phase HTS cable operating at 110kV constructed for grid integration that is subject to various faults. The fault applied vary in severity (e.g. single phase short circuit, electrical insulation breakdown) with the goal of studying current distribution between phases and the shielding and conducting layers of the line. This is

meant to aid in the design of protection systems in the electrical domain only. In contrast, for the CHEETA system fault study, the HTS line needs to be studied from at the system level to determine the effects of other components on the quenching of the line under fault conditions under consideration of both the electrical and thermal domains.

The thermal characteristics of the HTS line models are modeled with the equations in [99], and the treatment of heat transfer for the liquid nitrogen studied is derived from the experiments conducted in [109].

The HTS transmission line simulations of the present study also utilize cold-end cooling models based on studies in [99], which focuses on the detailed analysis of a ReBCO Roebel cable quench and stability. Reference [99] outlined the equations required to model an HTS line cooled in a liquid cooling bath for external and locally applied disturbances.

The heat transfer characteristics for a saturated liquid hydrogen cooling bath are determined from [108]. That chapter studied heat transfer from a horizontal wire immersed in liquid and super-critical hydrogen for a wide range of bath temperatures and pressures.

In this work, the thermo-electrical response of an HTS cable placed within a representative electric aircraft power system is studied during fault conditions. The power system is outlined in [110], which consists of a fuel cell, the HTS line, and the powertrain. The powertrain is divided into three physical components: an inverter, a cryogenically cooled electrically excited synchronous machine, and a speed controller. The electrical dynamic model for the fuel cell is derived from [100], which provides the short circuit characteristics of proton exchange membrane (PEM) fuel cells.

The inverter requires a Thévenin equivalent model to conduct the fault analysis. Reference [115] provides such a model, where the common-mode behavior of the power electronics is provided in terms of a Thévenin common-mode equivalent circuit, which is reliable in predicting the worst-case behavior of the inverter. The Thévenin inverter modeling approach is also tested in [115] in a DC micro-grid system, which proves feasibility for using the equivalent model with the electric aircraft power system.

7.1.3 Chapter Contributions

This chapter contributes the following:

- A multi-engineering domain (thermo-electrical) model for an HTS transmission line that has been corroborated against experimental cryogenic stability studies. The ther-

mal behavior of the HTS line has been studied for liquid and gas hydrogen and liquid nitrogen.

- An inter-operable and open source software implementation of the HTS model, using the open access and standardized Modelica language; facilitating reuse and research reproducibility.
- Fault analysis for a novel electrified aircraft electrical power system architecture that uses the proposed HTS line. The trade-off studies show how the unavoidable impedance of the fuel cell can actually be advantageous to the system design by using it to limit the quench current and temperature rise in the HTS cable to protect the cryogenic system after a short circuit.
- Thermal response analysis under different cooling media. These studies provide a comparison between the use of liquid hydrogen and gas hydrogen as coolant. The results show that liquid cooling offers substantial advantages over gas cooling for the thermo-electrical stability of the HTS line during faults.

7.1.4 Chapter Organization

This chapter is organized as follows. In Section III, the physics- and equation-based models for the HTS line with both liquid and gas cooling are presented. The model is validated against previous experimental studies. In Section IV, the power system used for fault analysis studies is outlined. The model's response is analyzed for different cooling media in Section V. The results from the fault tests are discussed in Section VI.

7.2 HTS Model

7.2.1 Modelica and Multi-Domain Modeling Overview

Models used in the development of the HTS line for the CHEETA aircraft are created using the object-oriented equation-based modeling language, Modelica. The language provides inter-operability and model portability through an open access language specification [92], which is supported by different tools (see [116]). Modelica provides the flexibility to implement and interface models from different engineering domains by developing physically-meaningful equation-based interfaces between them. This means that the equations derived from the principles of physics and engineering are used to connect models together. The term

‘domain’ is used to denote a typical engineering area or discipline. In the case of the HTS component, both electrical and mechanical domains are included in a singular model. All electrical variables are connected and modeled according to Ohm’s Law, Kirchhoff’s Laws, and other electrical principles. Mechanical variables are modeled according to laws of kinematics, and the thermal variables obey the laws of thermodynamics. This approach enables modeling of the HTS line across multiple domains in an equation-based approach instead of having to reduce the model’s Differential and Algebraic Equation System (DAES) into block-diagram oriented representations or declarative programming statements as done in other tools and languages.

Models created using Modelica can also be interchanged (i.e. using the `replaceable` keyword) by exploiting object-oriented programming principles to analyze models at varying levels of complexity, allowing users to analyze how different modeling assumptions affect system or component responses. This means models sharing the same `base class`, or same basic model outline, can be `replaceable` to one another. The HTS lines, for example, share the same `base class` of the electrical characteristics that can be made `replaceable` for different cooling mediums, facilitating model development, maintenance and re-use. This means one base model exists, but each cooling media has a specific heat transfer function. Such functions can be quickly exchanged to represent a cooling media without the need to change the entire model or to create multiple models for each kind of media. No model of the HTS line exists off-the-shelf for system level modeling, so it is necessary to integrate the functionalities for the thermal and electrical system.

The HTS line model described herein is studied under two cooling methods for three different cooling medias. The line is subject to liquid cooling using hydrogen and nitrogen as well as gas cooling using hydrogen gas. The comparison between liquid and gas cooling serves the purpose of showing that different cooling methods impact the sizing and weight of the cable, which is a significant constraint in the aircraft design. System level simulations for liquid nitrogen and liquid hydrogen cooled HTS lines allows for comparison between the sizing of a cable for each type of liquid cooling media.

7.2.2 CHEETA Electrical System One-Line Diagram

The CHEETA electrical power system consists of energy sources (i.e. hydrogen fuel cells and batteries), power electronics (i.e. inverters), and other components that supply electrical power to motors that drive the fans for aircraft propulsion [12]. The CHEETA

power system architecture is shown in Figure 7.1. Each group of fuel cells is connected via HTS transmission line to a distribution bus containing three machines, inverters, and a battery that is sized only to provide power only during transient flight conditions (e.g. fast maneuvers) due to weight/power density constraints. There are three branches for the electrical system, where they are connected at the fuel cell buses with a tie line for reliability.

All of the bus bars and transmission lines are encapsulated by a cryogenic environment, as designated by the blue lines of the system in Figure 7.1. The system is modeled to operate with each motor providing ≈ 1.6 MW of power for a total cruise power of ≈ 14.4 MW, with a rated power of 2.5 MW for high-power flight phases like takeoff and climb. Given the amount of time the aircraft spends in cruise, it is reasonable to suggest that a fault may be more probable under this flight phase. In conventional land-based electric power systems, normally the current in a system is minimized to limit the I^2R losses on the line, resulting in an operating voltage that is considerably higher than the current. In the CHEETA aircraft concept, HTS components provide negligible losses when subject to cryogenic cooling, allowing for a system to operate at a much higher current and lower voltage. The HTS line is cooled separately at a temperature of 20-25 K from the rest of the cryogenic components. The transmission lines and bus bars are the components most vulnerable to failure due to uncontrollable heating, so it is crucial that the temperature is controlled in its own loop.

7.2.3 Model Overview: Liquid Cooled Transmission Line

The HTS line is modeled using a co-axial cable electrical model with a thermal interface to model the cooling bath, which is shown in Figure 7.2. When the line is modeled using Modelica, it is a multi-domain model consisting of thermal and electrical behavior as all electrical components are temperature dependent. The blue blocks in the figure represent the electrical connections to external power system components such as the fuel cell and the inverter. The red box is the thermal connection to the cooling bath, which couples the temperature and heat flow to the thermal behavior of the line. It should be noted that the inductive, capacitive, and most resistive components are time-varying, such that their values can change during a simulation depending on operational conditions as described below. In Figure 7.2, R_L is the current lead resistance. L_π , R_π , and C_π are the pi-line equivalent inductance, resistance, and capacitance, respectively. All variables, units, and definitions are listed in Appendix A.

The transmission line is modeled using the equations outlined in [107],[99]. The critical

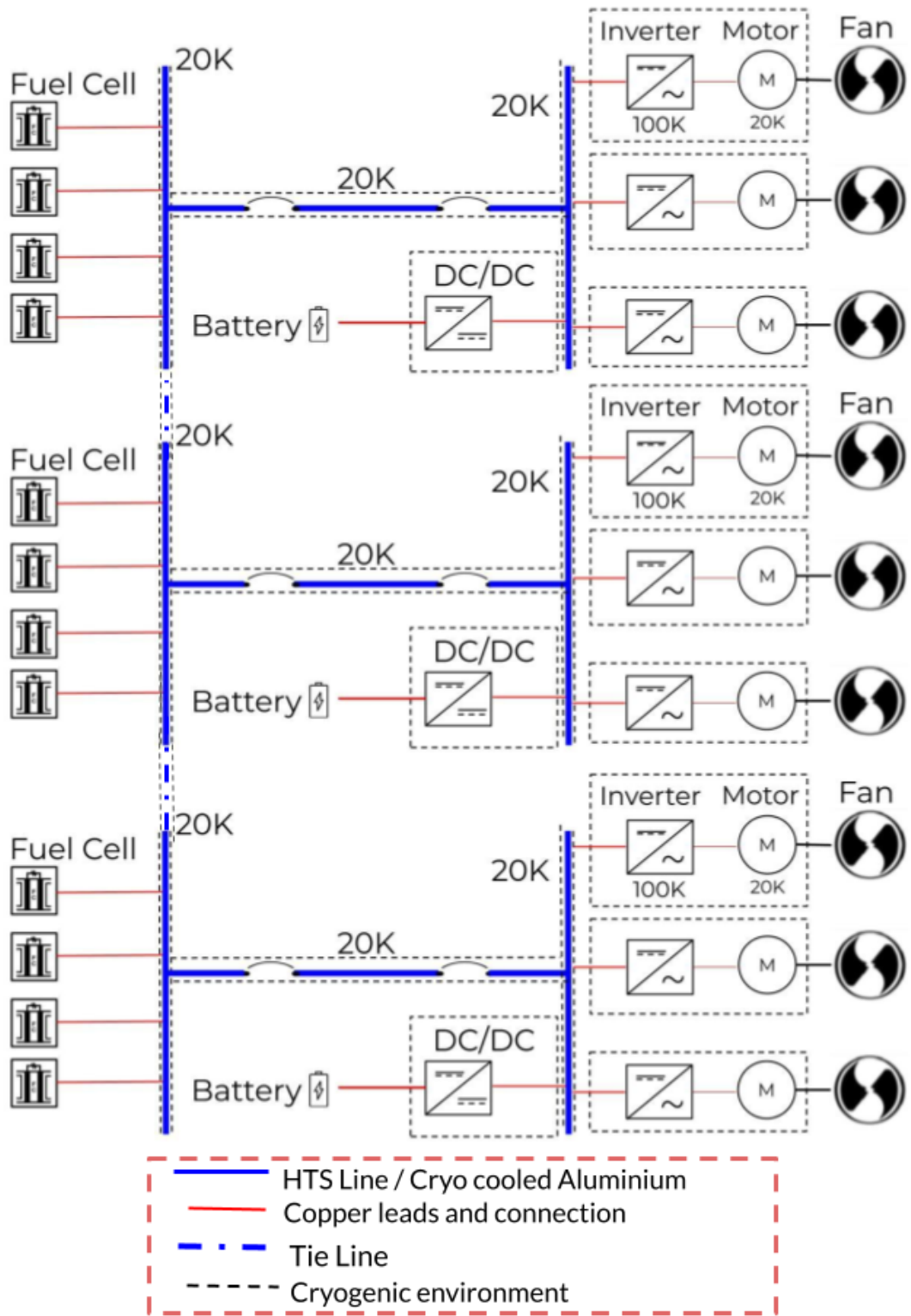


Figure 7.1: The CHEETA electric aircraft architecture configured to show the electrical wiring scheme for the system. This schematic focuses on the electrical components; all cooling and thermal components are omitted. This representation only shows the go portion of the circuit, the return lines will also have the same structure.

current I_c is calculated by Equation 7.1, where it is a function of the temperature at the line surface T and the transition temperature of the superconductor T_c . The electric field is calculated by Equation 7.2 as a function of the current through the transmission line I_{op} , the index value of the line n , the reference electric field E_0 , and the critical current I_c . The resistivity of the line is calculated by Equation 7.3, where A_{cu} is the cross sectional area of the tape in the line as projected onto a surface perpendicular to the line. For this line, the transition temperature (T_c) is 92 K, the reference electric field (E_0) is 1e-6 V/m, and the critical current at 20 K (I_{c0}) is 3700A.

$$I_c = I_{c0} \left(1 - \frac{T}{T_c}\right) \quad (7.1)$$

$$E = E_0 \left(\frac{I_{op}}{I_c}\right)^n \quad (7.2)$$

$$\rho = \frac{E \times A_{cu}}{I_{op}} \quad (7.3)$$

Equations 7.1, 7.2, and 7.3 are then used to calculate the values of the pi-line electrical model. In these equations we assume completely non-magnetic materials, so $\mu = \mu_0$ is the permeability of free space and $\epsilon = \epsilon_0$ is the dielectric permittivity. Equations 7.4, 7.5, and 7.6 determine the resistance, inductance, and capacitance of the line, respectively. In Equations 7.5 and 7.6, the values are dependent on the geometry of the cable, where a is the inner

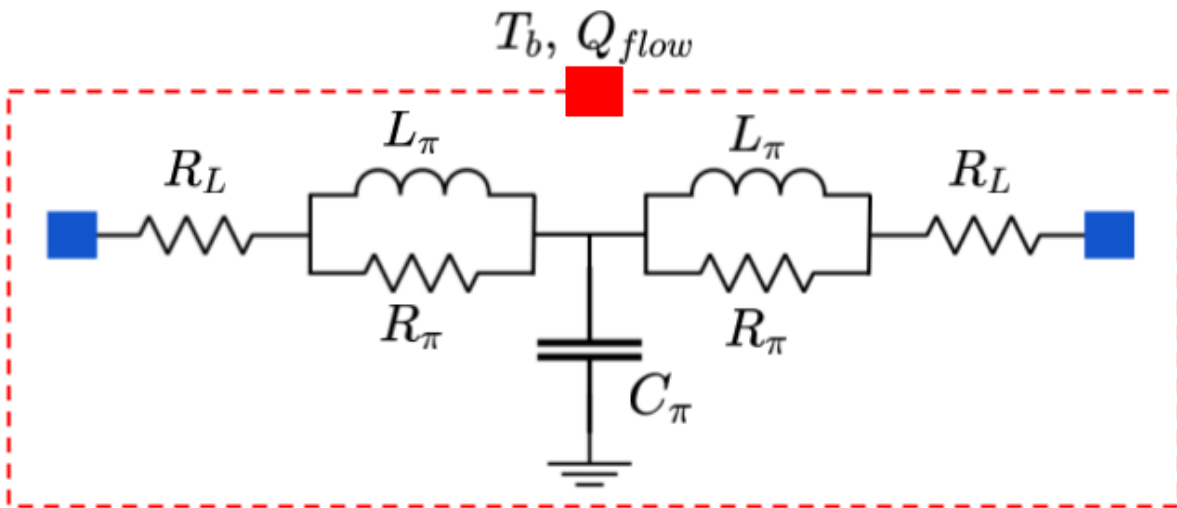


Figure 7.2: HTS pi-line model schematic.

radius of the co-axial cable and b is the outer radius of the co-axial cable.

$$R_{\pi} = E_0 * \frac{\left(\frac{I_{op}}{I_c}\right)^n}{I_{op}} \quad \Omega / \text{m} \quad (7.4)$$

$$L_{\pi} = \frac{\mu}{2\pi} \log\left(\frac{b}{a}\right) \quad \text{H/m} \quad (7.5)$$

$$C_{\pi} = \frac{2\pi * \epsilon}{\log\left(\frac{b}{a}\right)} \quad \text{F/m} \quad (7.6)$$

Equation 7.8 gives the ΔT_{ρ} for a given heat experienced by the cable; here there are two terms: the internally generated ohmic heat present during a quench and a potential perturbation G_d . The heat flow from the transmission line into the cooling bath is calculated by Equation 7.9. It is a function of the heat transfer coefficient (h), change in temperature (ΔT_{ρ}), and cold-end cooling (Q_{ce}). The cold-end cooling excess heat flow is calculated using Equation 7.10. The heat transfer coefficient of liquid hydrogen is defined in Equation 7.7.

$$h = \begin{cases} 100(\Delta T_{\rho})^{5.3} & \Delta T_{\rho} < 3 \\ \frac{10^5}{\Delta T_{\rho}} & 3 \leq \Delta T_{\rho} < 100 \\ 1000 & \Delta T_{\rho} \geq 100 \end{cases} \quad (7.7)$$

$$\Delta T_{\rho} = \frac{\left(\frac{\rho I_c^2}{P \times A_{cu}} + G_d\right)}{h} \quad (7.8)$$

$$Q_{flow} = h \times \Delta T_{\rho} + Q_{ce} \quad (7.9)$$

$$Q_{ce} = T_b \sqrt{2\kappa \times A_{cu} \times P \times h} \quad (7.10)$$

The equations above are necessary in order to study the HTS line under fault and quench conditions. Potential fault conditions can often be the most demanding constraint on the cooling conditions [99].

7.2.4 Model Overview: Gas Cooled Transmission Line

Alternatively, the HTS model can be configured to consider the thermal response for hydrogen gas cooling methods. The electrical analytical expressions for the model under these conditions do not change; they follow Equations 7.1 - 7.6.

When the line is submerged in a liquid hydrogen bath, the difference in temperature

between the cable and the cooling media is consistent for all points on the line. Gas cooling causes the difference between line temperature and the cooling media vary as a function of the distance from the inlet of the transmission line. The change in temperature, ΔT_z , along the line is defined by Equations 7.11 and 7.12. All other equations for calculating the heat transfer remain the same from the liquid cooling case; the h value is vastly different between gas and liquid in functional form. This results in a lower heat transfer value, leading to much higher temperatures in the line. The total change in temperature is represented by ΔT_{total} in Equation 7.13.

$$\langle T(z) \rangle = T_{inlet} + \frac{Q_{flow} \times z}{v \times C_{pv} \times 2 \times \pi \times (R_c - R_0)^2} \quad (7.11)$$

$$\Delta T_z = \langle T(z) \rangle - T_{inlet} \quad (7.12)$$

$$\Delta T_{total} = \Delta T_z + \Delta T_\rho \quad (7.13)$$

7.3 Component Model Analysis

The physics defining the physical behavior of each individual domain used in the proposed HTS model has been corroborated against published results from previous studies such as [108], [109], and [99], where the component has been tested in isolation (i.e. with no other electric power system components) in laboratory experiments. Using the knowledge from these previous studies, i.e. recognizing that the physics and equations for the model fit an experimental real-world system, this work aims to assemble the electrical and thermal equations to implement the HTS model in an aircraft electrical power system with the purpose of design and analysis. Developing such model is valuable, as setting up an experiment of such kind would be costly to do for a system of this size, that does not exist and it is in early development phases. To this end, the work in [99] conducted by one of this chapter's co-authors and the results from [108] were used to corroborate the equations and thermal behavior of the model, as illustrated in the results from this section. This ensures that the responses in the model are consistent with the responses and results in the literature so they can be used in system-level integration and analysis.

The HTS line system in Figure 7.6 is simulated to observe the V-I behavior of the line with the behavior outlined in [107] and [99]. To reproduce the behavior observed from laboratory experiments through the current set of simulations, a small voltage bias is applied

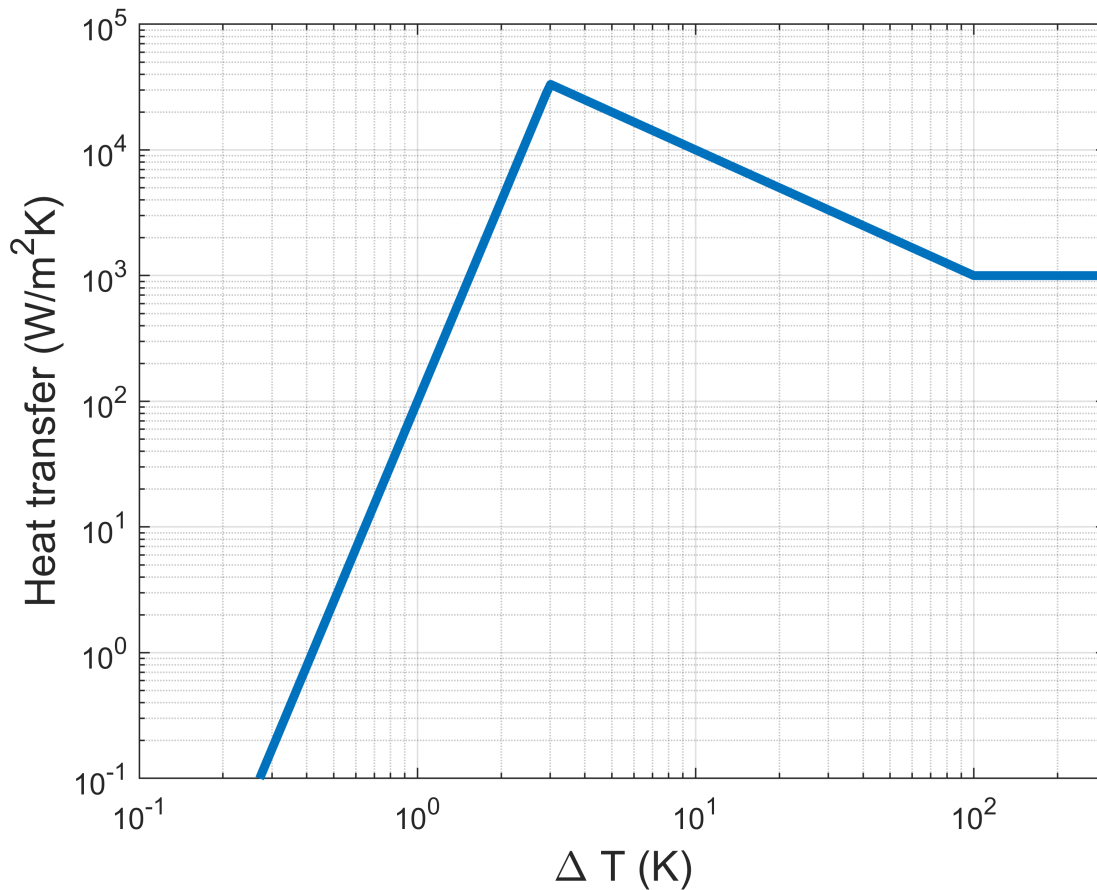


Figure 7.3: Heat transfer characteristics as a function of temperature for the line submerged in a liquid hydrogen cooling bath.

to the line model. This means the voltage drops across the current lead resistance to produce a current in the line such that we can observe the desired V-I behavior. This is done to emulate how the experiment injected a current into the line; given that the present case has a very low load of only the current lead resistance, the associated required voltage is correspondingly low.

The heat transfer behavior of the line submerged in a liquid cooling bath is corroborated against the results from the literature in [108] as shown in Figure 7.3. The nucleate boiling regime occurs at ΔT_ρ below 3 K and the film boiling regime occurs at ΔT_ρ above 3 K. The heat transfer characteristics for nitrogen derived in [109], [99] are shown in Figure 7.4.

The HTS line is configured to be subject to gas cooling as shown in Figure 7.5. In this case, the current is swept from 0 to 4kA, where the I_{c0} of the line is 3.7kA. This is done

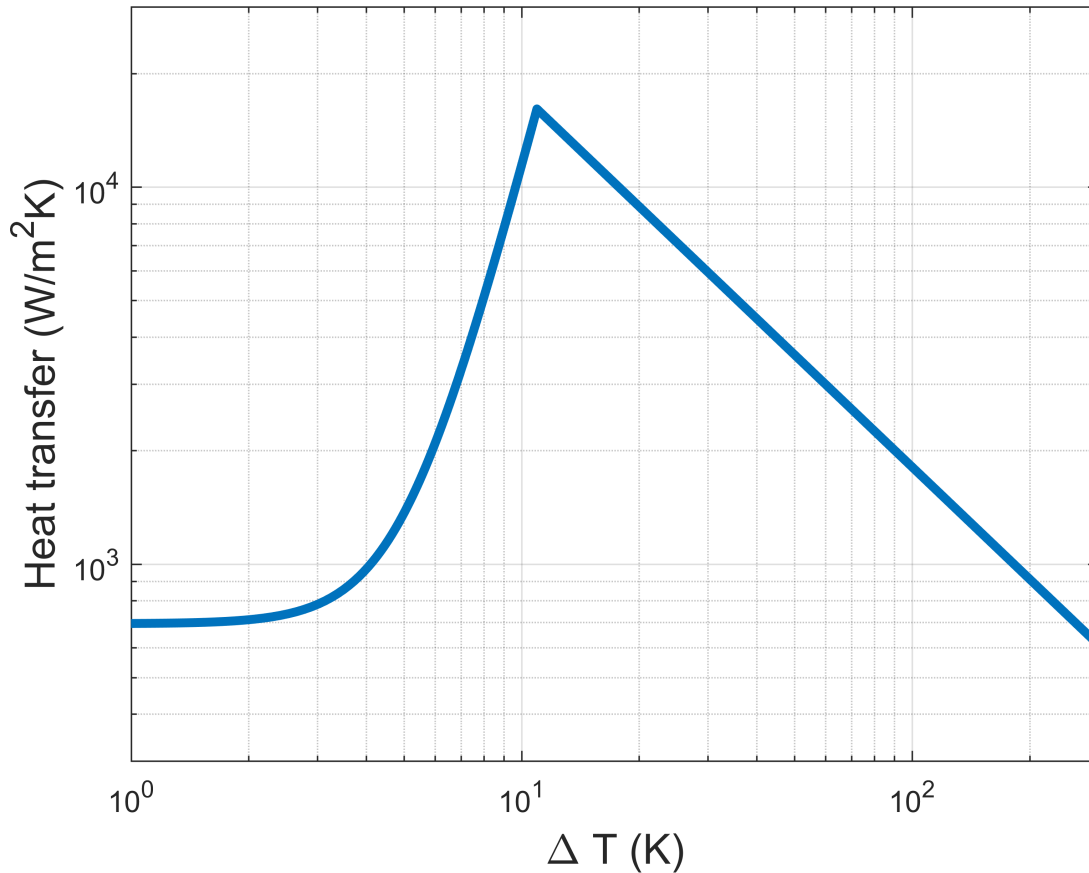


Figure 7.4: Heat transfer characteristics as a function of temperature for the line submerged in a liquid nitrogen cooling bath.

with the goal of injecting a specific current into the line; the only load in the system is the current leads so the required voltage is also low. This shows that the severity of ΔT_z at shorter distances from the gas inlet increases as the current carried by the line approaches I_c . The observed change in ΔT_z drastically increases as compared to liquid hydrogen cooling ΔT_p , especially at the end of the HTS line. This observation suggests that the gas cooling method presents reduced thermal stability and potential drawbacks for integration with the aircraft electrical power system.

7.4 Fault Analysis

7.4.1 Fault Model Overview

To illustrate the application of the HTS line model for aircraft electrical power system analysis, the HTS line model is integrated in a simplified yet representative version of the

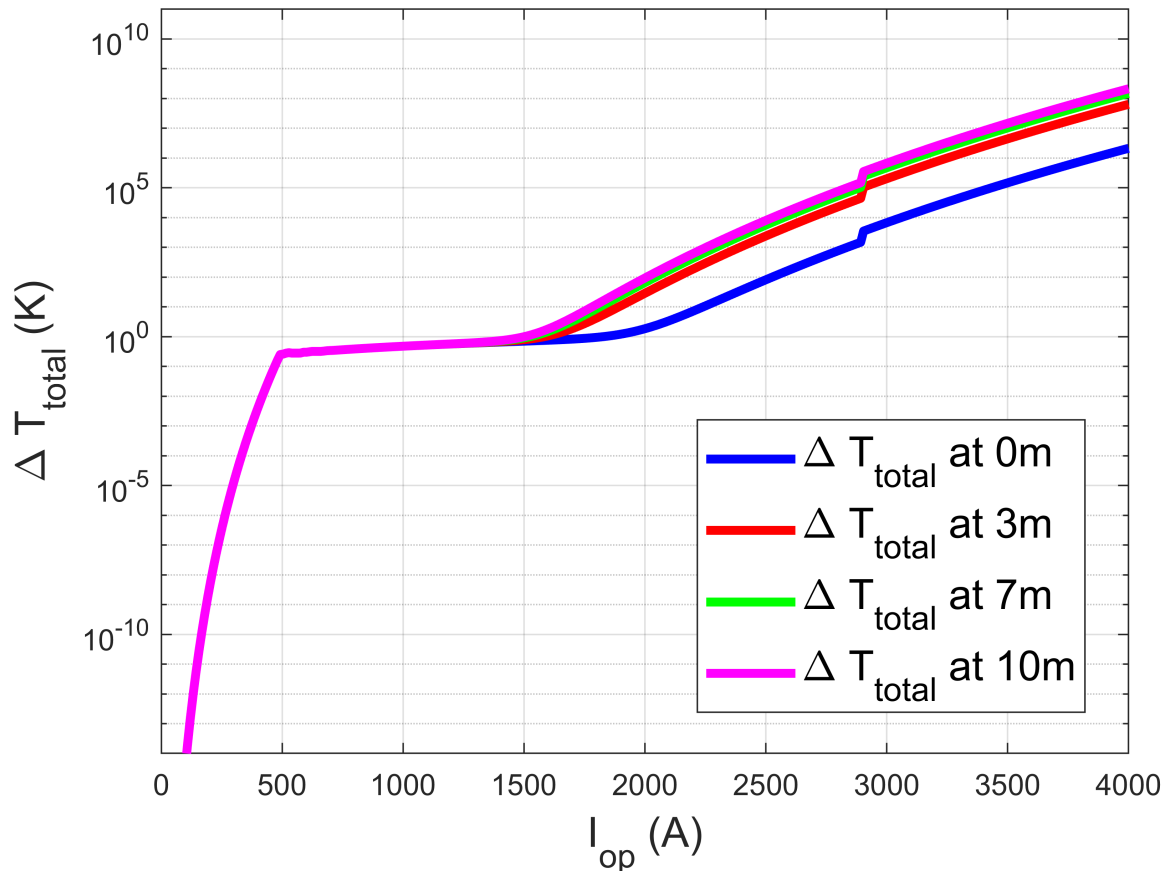


Figure 7.5: Gas cooling ΔT_z vs I_{op} , where ΔT_z is the difference in temperature between the hydrogen gas and the cable at a distance (x) from the gas cooling inlet.

electrified aircraft electrical power system in [12],[110]. The model consists of only one branch of the power system in [12],[110], which is comprised of a fuel cell, an HTS line, an inverter, and an electrical motor operating as a load with a power factor of 0.91 lagging. The multi-domain system is shown in Figure 7.6, with both the HTS line and fuel cell modeled in both electrical and thermal domains. The components in the model are labeled as follows:

- (A) PEM fuel cell (using model in Figure 7.7)
- (B) Boundary conditions set by the cooling system for the fuel cell and HTS line, connected to thermal interface of the HTS line and fuel cell.
- (C) HTS transmission line (using model in Figure 7.2)
- (D) Fault resistance

- (E) Inverter Thévenin equivalent (using model in Figure 7.8) [115]
- (F) Equivalent RL Load model representing the machine operating at a specified power factor

In this configuration, the ground is a reference voltage at 0 V. The schematic in Figure 7.6 only shows the “go” cable for the system; the return is implied. The return line in the system is at 0 V denoted as a common reference voltage. When there is a fault, we assume that the fault occurs between the go cable and the return cable fixed at 0 V.

The thermal interface of the inverter is omitted from the system because the Thévenin equivalent model does not allow for adequate modeling of the thermal behavior of the inverter. To properly model the thermal interface, the thermal impedance of the IGBT under the proposed cryogenic conditions is needed, which is not currently available. In future studies and development when such data becomes available, this behavior will be added as this will have an impact on the cooling media consumption and losses. Similarly, the regenerative capabilities are excluded from the model as the potential for regeneration will be limited by several factors: (a) the superconducting motor design, and (b) the ability to store/utilize re-generated energy.

Finally, the CHEETA system design uses fuel cells as the main energy source for propulsion, the role of the batteries is limited to address transients due to weight constraints. Since the size of the batteries is limited due to their projected weight, which means that the potential for regeneration is trivial compared to the amount of energy used for propulsion [117].

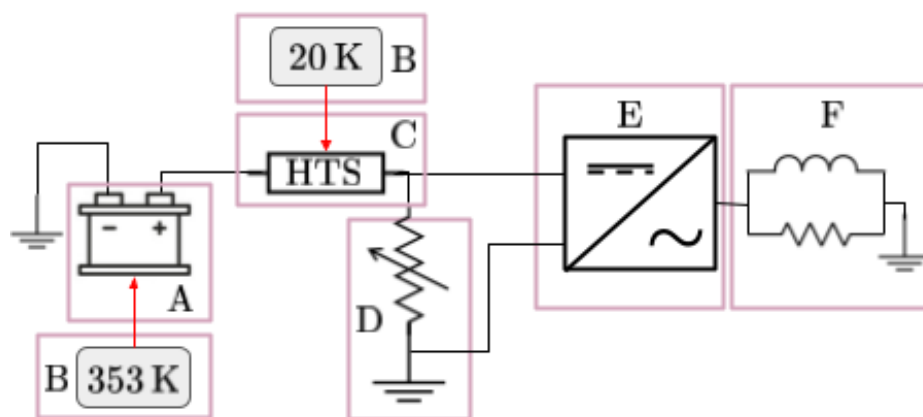


Figure 7.6: Multi-domain aircraft electrical power system modeled using Modelica with each component used labeled.

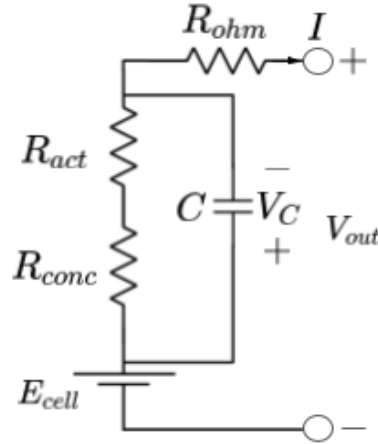


Figure 7.7: PEM fuel cell electrical circuit diagram.

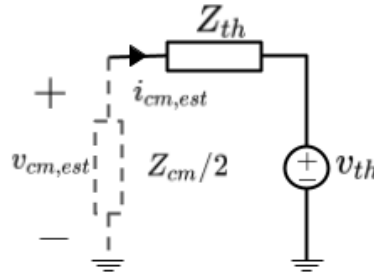


Figure 7.8: The Thévenin equivalent electrical model for common-mode operation of an inverter.

7.4.1.1 PEM Fuel Cell Model

The fuel cell model is derived from the electrical circuit model for a PEM fuel cell in [100],[101] and is implemented using Modelica. The electrical circuit is shown in Figure 7.7. It consists of a cell voltage denoted as E_{cell} , multiple resistances and a capacitor, which values are defined by Equations 7.14, 7.15, and 7.16. Equations 7.14 and 7.15 are both temperature and current dependent components. The activation R_{act} and concentration R_{conc} resistances depend on the current generated by the fuel cell, I_{FC} , which is the operating current of the HTS line (used in Equations 7.2, 7.4) because they are connected in series. In Equations 7.14 and 7.15, which calculates the activation R_{act} and concentration R_{conc} resistances respectively, R is the universal gas constant, T_f is the temperature of the fuel cell, I_{FC} is the fuel cell current, α is the electron transfer coefficient, F is the Faraday constant, n_e is the number of electrons, and I_{max} is the maximum fuel cell current.

$$R_{act} = -\frac{RT_f \ln(I_{FC})}{\alpha n_e F I_{FC}} = \frac{V_{act,2}}{I_{FC}} \quad (7.14)$$

$$R_{conc} = -\frac{RT_f}{n_e F I_{FC}} \ln \left(\frac{-I_{FC}}{I_{max}} \right) \quad (7.15)$$

Equation 7.16 is the resistance of the polymer membrane (R_{ohm}), which consists of the resistance in between the membrane and electrodes, and the resistances of the electrodes [101]. R_{ohm0} is the constant portion of R_{ohm} , k_{RI} is an empirical constant for calculating R_{ohm} as a function of current, and k_{RT} is an empirical constant for calculating R_{ohm} as a function of temperature. This resistance is connected to the activation and concentration resistances in series as shown in Figure 7.7.

$$R_{ohm} = R_{ohm0} + k_{RI} I_{FC} - k_{RT} T_f \quad (7.16)$$

The output voltage of the fuel cell is calculated using Equation 7.17. The activation voltage, which is a voltage drop that is only affected by the fuel cell's internal temperature, is described empirically by the Tafel equation in Equation 7.18. In Equation 7.19, η_0 is the temperature invariant part of the activation voltage, which is measured in K. The terms a_{FC} and b_{FC} in Equations 7.19 and 7.20 is a constant term used in the Tafel equation. The voltage drop across the capacitor in Figure 7.7 can be determined using Equation 7.21.

$$V_{out} = E_{cell} - V_c - V_{ohm} - V_{act1} \quad (7.17)$$

$$V_{act} = \eta_0 + (T_f - 298)a_{FC} + T_f b_{FC} \ln(I_{FC}) \quad (7.18)$$

$$V_{act1} = \eta_0 + (T_f - 298)a_{FC} \quad (7.19)$$

$$V_{act2} = T_f b_{FC} \ln(I_{FC}) \quad (7.20)$$

$$V_C = (I_{FC} - C \frac{dV_C}{dt})(R_{act} + R_C) \quad (7.21)$$

The fuel cell has a power capacity of 2.5MW and is parameterized with the stack values for the SR-12 stack from [101]. It operates at 1000V.

7.4.1.2 Inverter Model

The inverter model used in the fault analysis circuit is an averaged model reduced to a Thévenin equivalent, which is derived from the model outlined in [115]. The purpose for using this model is because the common-mode behavior of the converter must be modeled to analyze the circuit and predict the worst-case common-mode response. Hence, the Thévenin

equivalent model satisfied the needs for the fault analysis studies herein. The electrical model is shown in Figure 7.8.

The Thévenin impedance is calculated using Equation 7.22, which is a function of the common mode resistance, R_{cm} , and diode resistance, R_D . The Thévenin voltage is determined by Equation 7.23, which is a function of the common mode voltage.

$$Z_{th} = \frac{R_D}{3} + R_{cm} \quad (7.22)$$

$$V_{th} = \frac{v_{cm,est}}{2} \quad (7.23)$$

7.4.2 Fault Studies

The fault studies conducted below use the circuit shown in Figure 7.6. To simulate fault conditions, at the beginning of the simulation period, the fault's variable resistor in block D (see Figure 7.6) is set to 1 M Ω to limit current draw, and then drops to $\approx 0\Omega$ when the fault is applied, thereby creating a bolted fault. The line is given a critical current carrying capacity I_{c0} of 3700 A, which translates to critical current I_c of 2870 A at 20 K.

In addition, a trade-off analysis is conducted by performing a parametric sweep total fuel cell impedance in Figure 7.7, allowing the electro-thermal stability boundary of the aggregate source impedance to be determined. For impedance above this threshold the HTS line remains stable after the fault event. However, for impedance values lower than this threshold, the system experiences a quench event, characterized by an uncontrollable heating of the HTS line after a fault occurs.

Finally, the studies analyze different types of cooling media and methods in order to determine which method will offer the best fault performance. The types of media analyzed are hydrogen and nitrogen. For the case of hydrogen, both liquid and gas cooling are analyzed. These results are needed to provide requirements to the cooling system design, which will be addressed in future work.

7.4.2.1 *Liquid Hydrogen Cooling*

The HTS line is cooled with liquid hydrogen for the power system model shown in Figure 7.6. The equivalent resistance of the PEM fuel cell system in Figure 7.7 is swept over 20 values to determine the fuel cell impedance that best serves to protect the HTS system from quenching. The heat transfer of the HTS line follows the behavior in Figure 7.3.

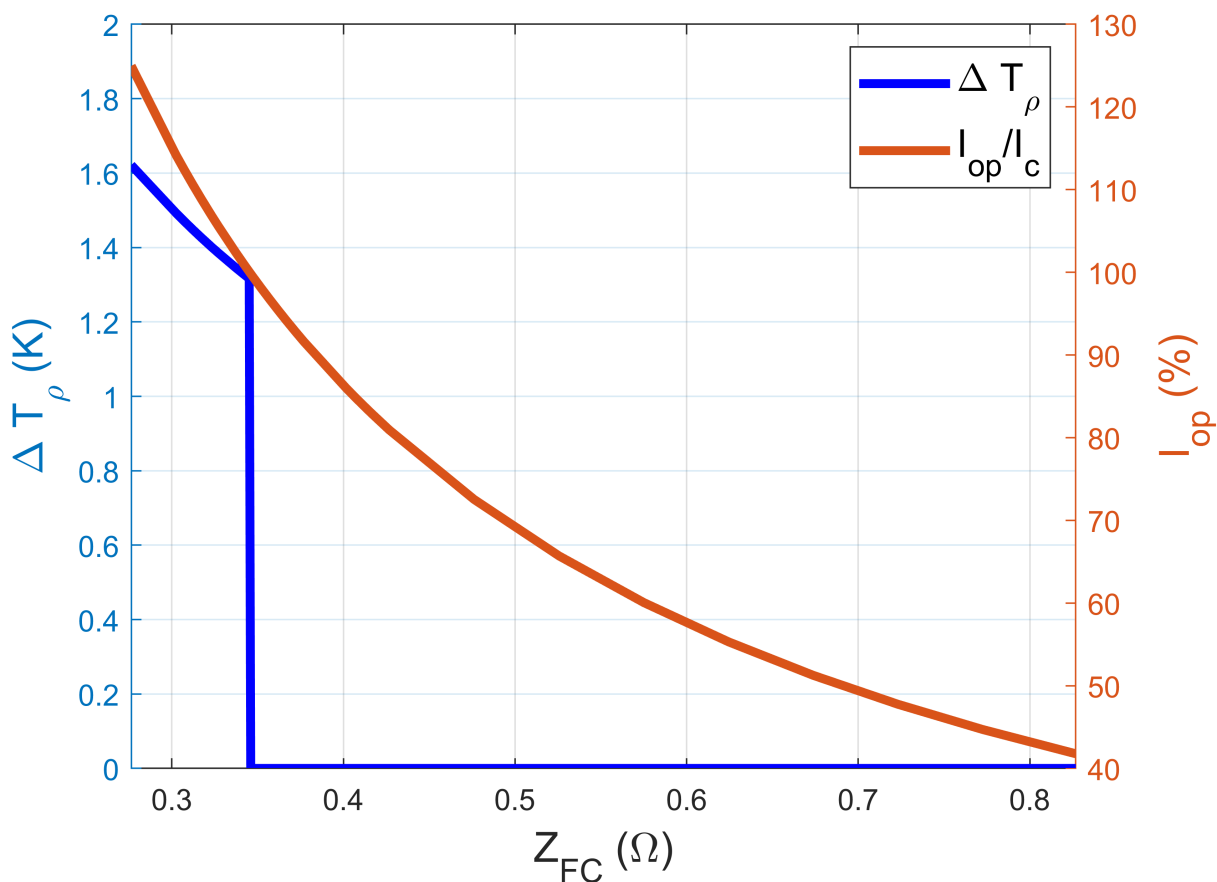


Figure 7.9: Difference between in HTS line and cryogen temperature (ΔT_{ρ}) and fraction of operational current (I_{op}) as a function of fuel cell impedance prior to applying the short circuit fault in liquid hydrogen cooling media.

The change in temperature prior to applying the short circuit as a function of the fuel cell impedance is shown in Figure 7.9. When the resistance of the fuel cell is zero, ΔT_{ρ} is 1.63 K. This ensures that the line will stay below the film boiling region when operating in steady state with the expected load. When the line is cooled with liquid hydrogen, the line can operate at approximately 2.43 times the critical current I_c before entering film boiling. After the short circuit fault is applied, the change in line temperature is modeled to rise to an exceedingly high temperature, indicating a thermal failure of the HTS material. Figure 7.10 shows that the line will rise to an unstable temperature for any fuel cell equivalent resistance value below 0.414 Ω , which for resistance above this, we ensure that the line will remain below film boiling after the short circuit. This trend is observed due to the HTS line quenching whenever the change in temperature (ΔT_{ρ}) is above 3 K, which is based on the

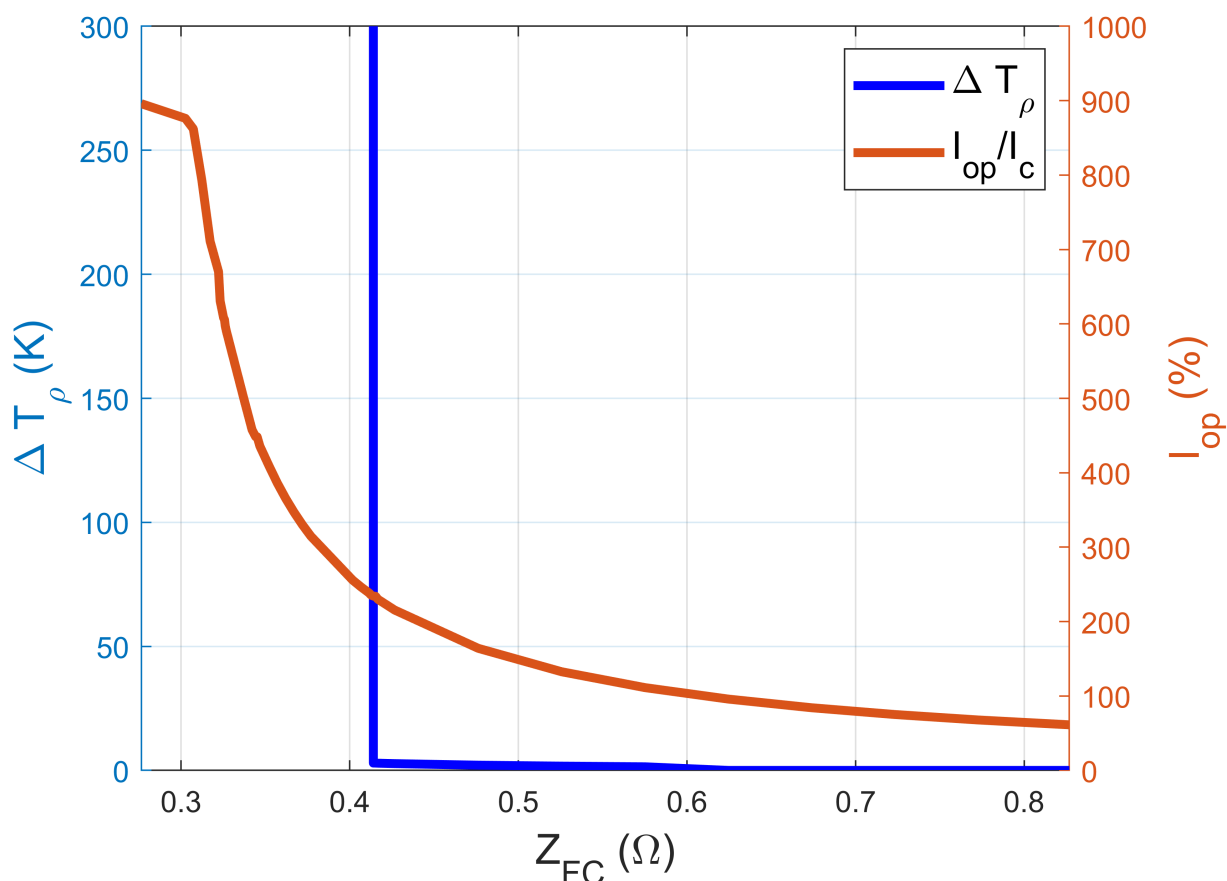


Figure 7.10: Difference between in HTS line and cryogen temperature (ΔT_{ρ}) and fraction of operational current (I_{op}) as a function of fuel cell impedance after to applying the short circuit fault in liquid hydrogen cooling media.

heat transfer characteristics of the line in Figure 7.3.

7.4.2.2 *Liquid Nitrogen Cooling*

A similar study was also conducted with the HTS line thermal behaviors replaced with the liquid nitrogen heat transfer characteristics (shown in Figure 7.4). The nitrogen-cooled line is stable when the change in temperature (ΔT_{ρ}) is below 11 K. The line's thermal behavior and carrying current prior to applying the short circuit fault is shown in Figure 7.11. When the $R_{ohm} \approx 0$, ΔT_{ρ} is exceedingly high, making the line thermally unstable and indicating a failure of the HTS material. The equivalent fuel cell resistance must be at least 0.345Ω for the line to be cryogenically stable in normal operation conditions. In addition, it should be noted that the nitrogen cooled line does not offer the same safety factor as liquid

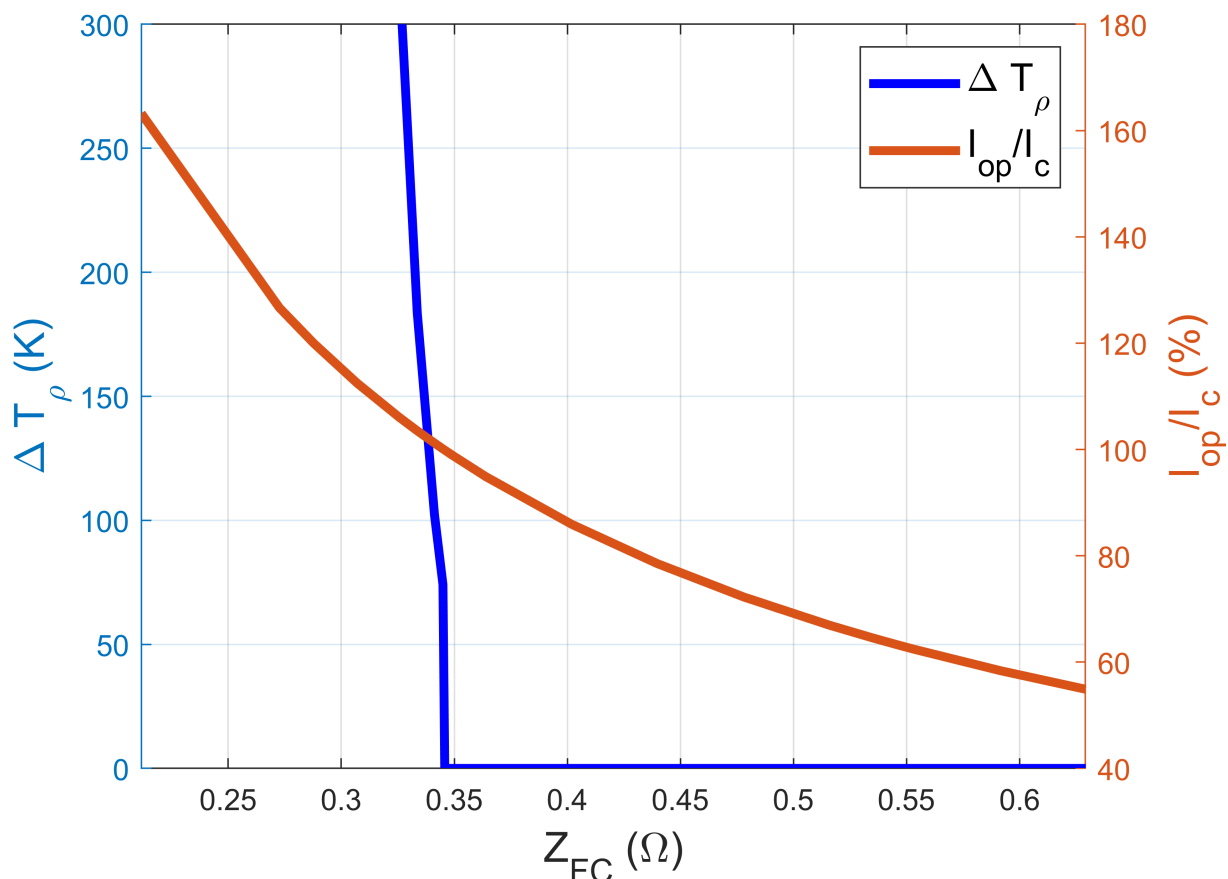


Figure 7.11: Difference between in HTS line and cryogen (ΔT_{ρ}) and fraction of operational current (I_{op}) as a function of fuel cell impedance prior to applying the short circuit fault in liquid nitrogen cooling media.

hydrogen before the cooling media enters the film boiling region. This means that the liquid hydrogen will remain in the cryogenic regime for a carrying current of approximately twice the rated current capacity. In liquid nitrogen cooled cases, the line stays thermally stable only for operational currents less than the rated maximum capacity; the line will not remain in the cryogenic regime if this is exceeded unlike the liquid hydrogen case.

The same sweep of the fuel cell impedance is applied as in the liquid hydrogen case. Figure 7.12 shows that the line is thermally stable for fuel cell impedance larger than 0.548 Ω when a short circuit fault is applied at the inverter terminals.

7.4.2.3 Hydrogen Gas Cooling

Simulations were also conducted with the line's heat transfer characteristics set to represent the behavior of hydrogen gas. Hydrogen gas cooling is stable when the difference

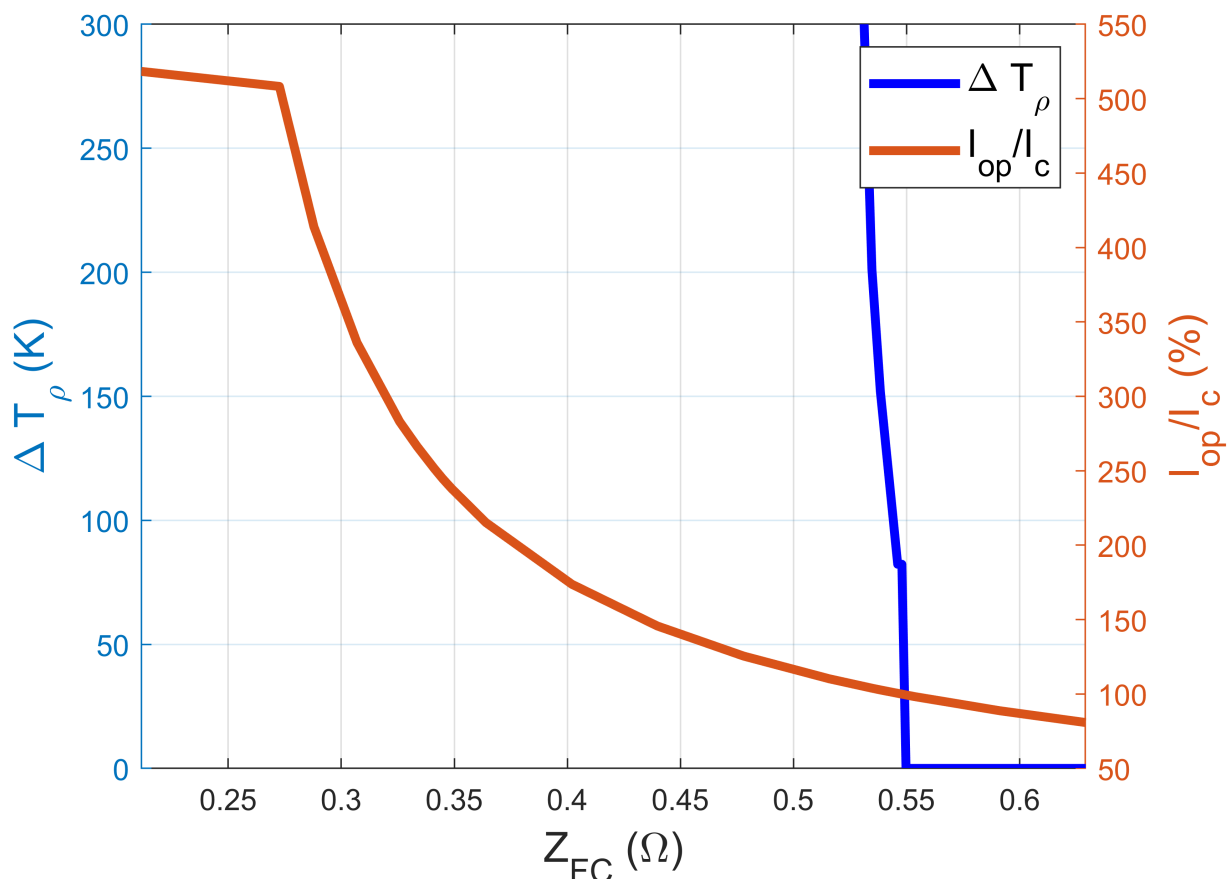


Figure 7.12: Difference between in HTS line and cryogen (ΔT_{ρ}) and fraction of operational current (I_{op}) as a function of fuel cell impedance after applying the short circuit fault in liquid nitrogen cooling media.

between the line temperature and gas is less than 3 K. Because hydrogen gas heats up as a function of the distance from the inlet of the line cooling system, the HTS line's length as a function of the gas inlet's location must be carefully considered.

Figure 7.13 shows the change in line temperature as a function of the distance from the inlet of the hydrogen gas according to Equation 7.11. Hydrogen gas is not as effective at removing heat as liquid nitrogen or hydrogen. When the fuel cell impedance is 0.723Ω , the temperature difference of the hydrogen gas from the inlet to the furthest point on the 10m line stays below the quench temperature prior to the short circuit. The line is operating at 49.6% of the maximum current capability, which limits the robustness of the HTS line and requires a significantly more robust cable design for the same current transfer in the liquid hydrogen and nitrogen cases.

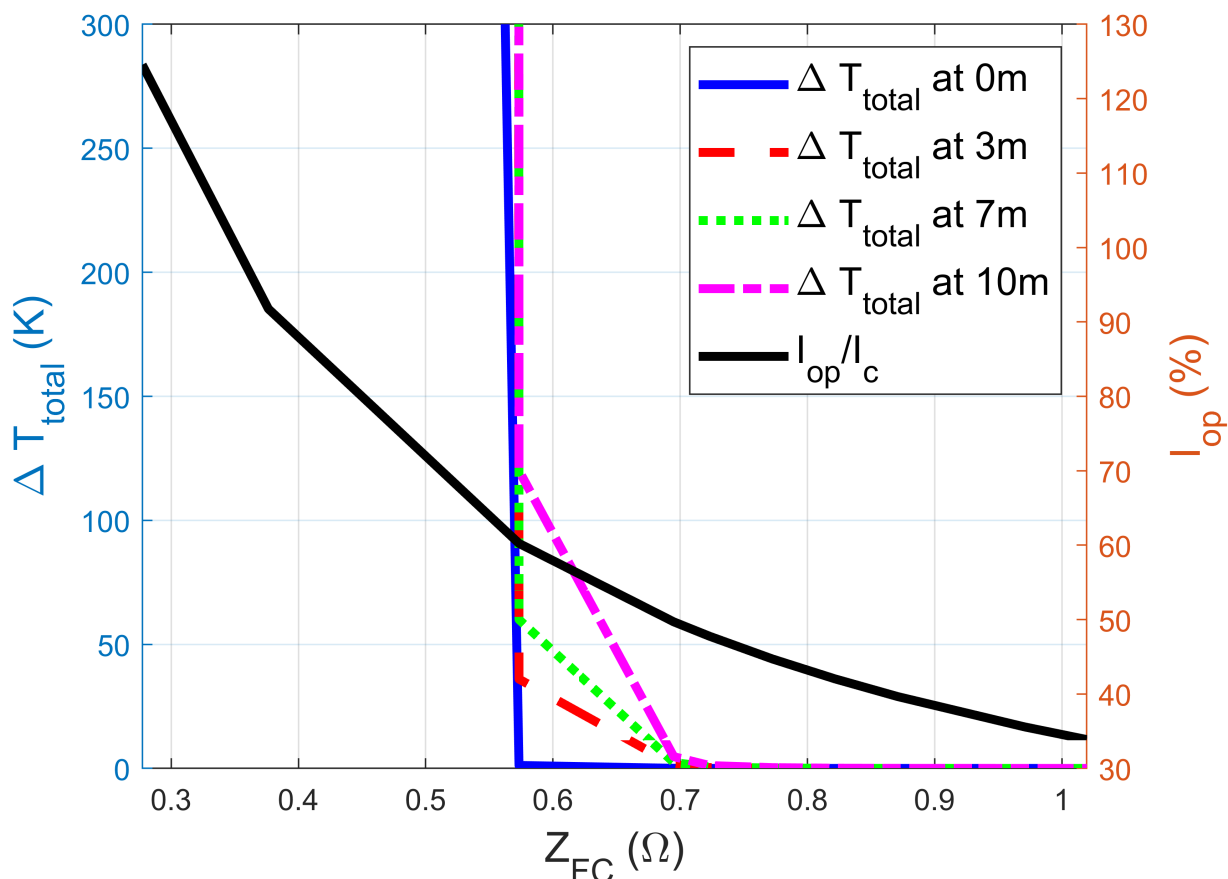


Figure 7.13: Difference between in HTS line and cryogen (ΔT_z) at different locations and fraction of operational current (I_{op}) as a function of fuel cell impedance prior to applying the short circuit fault in hydrogen gas cooling media.

When the short circuit is applied, the line is quenched for any fuel cell impedance below 0.871Ω . This means that difference in temperature ΔT_z of the hydrogen gas from its inlet to the line and the measured temperature at every point in the line is less than 3 K. The line is operating at 56% of the maximum operational current for the line under these conditions. This implies that the line must be designed to have nearly four times the current capacity for the same line used with different cooling media.

7.5 Conclusion

An electric aircraft power system that uses HTS lines with cryogenic cooling has been modeled for fault analysis studies that help inform cooling design by considering different cooling methods and media. Using a multi-domain, thermo-electrical model of the HTS

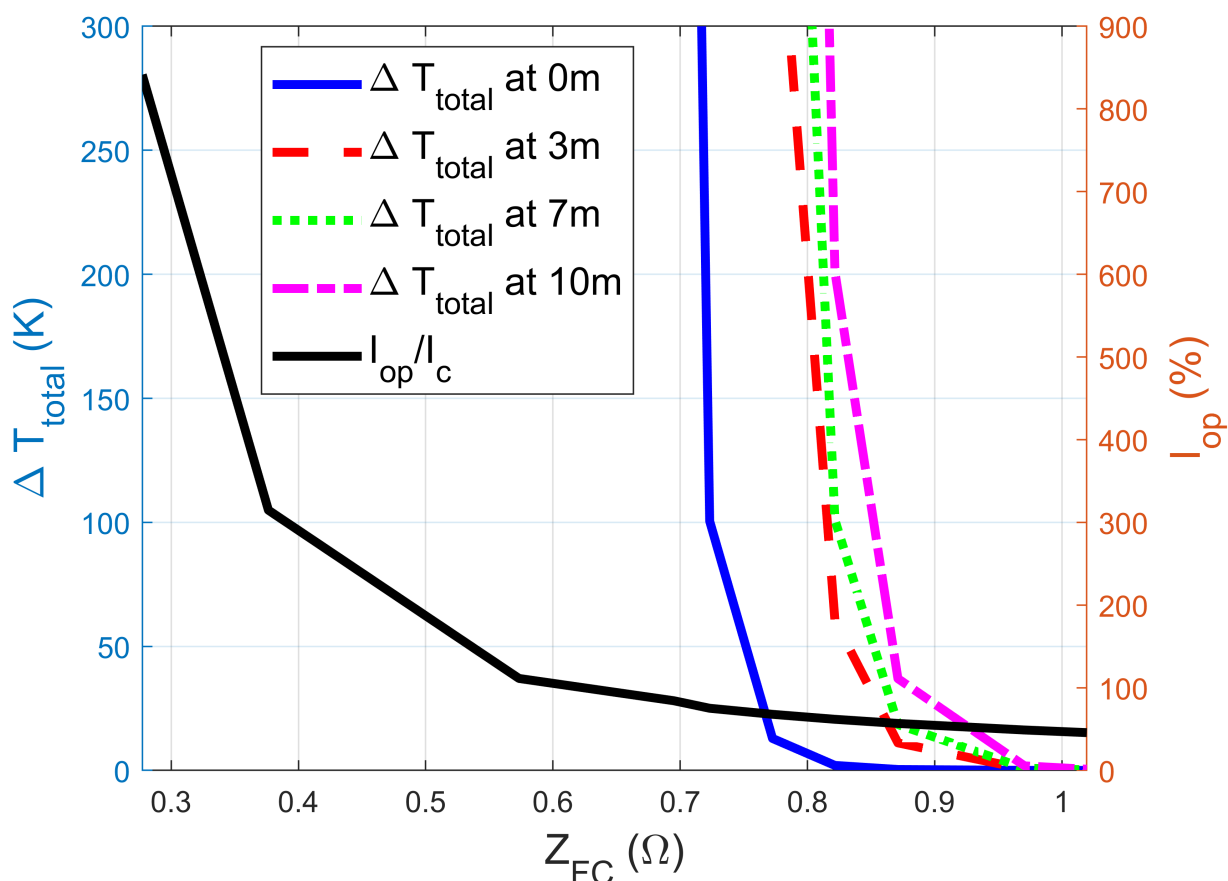


Figure 7.14: Difference between in HTS line and cryogen (ΔT_z) at different locations and fraction of operational current (I_{op}) as a function of fuel cell impedance after applying the short circuit fault in hydrogen gas cooling media.

line within a simple yet representative aircraft system, fault simulations were conducted to inform different trade-offs in the power system electro-thermal design. It was observed that proper sizing of the fuel cell would need to take into account also the characterization of the aggregate equivalent impedance to protect the HTS line when there is a short circuit in the system, alongside observations of the cooling requirements that each media and method should meet to prevent a quench event. While the variable value of the fuel cell impedance itself cannot be controlled, it provides understanding of how the cable can be designed to be protected in both normal and fault conditions. The studies were conducted for three different cooling mediums: liquid hydrogen, liquid nitrogen, and hydrogen gas. When the transmission lines are submerged in liquid hydrogen, the line remains thermally stable for nearly twice the rated current. This behavior shows that liquid hydrogen cooling allows the

system to operate safely and thermally stable under the worst fault conditions considered. This characteristic also provides a buffer to intermittent surge events in the line current, allowing the system to operate safely without having to implement any redundant lines or other protection equipment. This design approach minimizes HTS system size and weight, which is crucial for an aircraft's electrical power system.

Liquid hydrogen cooling provides an operational buffer before quench, where the line can carry currents up to twice the critical current prior to quench. When the lines are subject to cooling with liquid nitrogen and hydrogen gas, the system does not have this buffer and only stays stable when the system remains under the rated current. This gives inherent reliability to and allows for a smaller line to be used in the case of liquid hydrogen cooling, where other cooling methods require adjustment in the line sizing for fault protection. Since this HTS line will be used in an aircraft electrical power system, it is necessary to size the line so that it is as light as possible. The liquid hydrogen cooled HTS line quenches at a lower fuel cell impedance than the liquid nitrogen and hydrogen gas cooled cases, meaning that the line is more flexible for integration with various fuel cell designs and is a good candidate for lower impedance fuel cells. The drawback of gas cooling are that the line does not have the same buffer before quenching as compared to the liquid hydrogen or liquid nitrogen cooling would have for the same cable size. As a result, the gas cooled cable would need to be sized larger or multiple cables would need to be included in the electrical power system design to re-distribute the current. This would add weight to a system where minimizing weight is a priority.

CHAPTER 8

CONCLUSION

This thesis focuses on the modeling, simulation, and identification of three different electrified systems: (1) **hydroelectric power plants**, (2) **eVTOL systems**, and (3) **cryogenically cooled electrified aircraft**. The purpose of studying these three systems is to show how the modeling and analysis approach changes depending on the novelty of the system. hydroelectric power plants have been in operation for decades with plentiful operational data available to define models in a cyber-physical system. Developments in eVTOL systems are more recent, where operational data is limited with few physical prototypes available. The modeling and analysis of these eVTOL systems serve as an example of modeling and analysis for systems that are relatively new and in an intermediate development stage as compared with the hydroelectric power plants, with some design data available but limited operational data for modeling. Fully-electric aircraft systems are still in the conceptual design phase. There is not a complete physical prototype for a cryogenically-cooled electric aircraft to study, so the modeling and development of the complete system is limited to available information on the individual subsystems. This allows us to contrast how to model and simulate: (1) **a system with established models and plentiful measurements from a physical system**, (2) **a system that is undergoing development with limited design data and physical prototypes available**, and (3) **a system at the beginning of the design and development with no established physical system to compare models with**.

8.1 Hydroelectric Power Plants

In the case of hydroelectric power plants discussed in Chapters 2 and 3, the system is physically well-established. The two plants studied have been in operation for decades with well-defined standard models with various types of operational data available, so the validation and calibration process is focused on model maintenance.

Since there is data available from various operational states of the plant, we can study how each operational state affects the validation and calibration of the models. Chapter 2 discusses the calibration of plant parameters for the Itaipú hydroelectric plant using data obtained from faults and disturbances. The PMUs record a few seconds of data while the plant is excited by the disturbance and returns to a stable state. The PMUs only record the

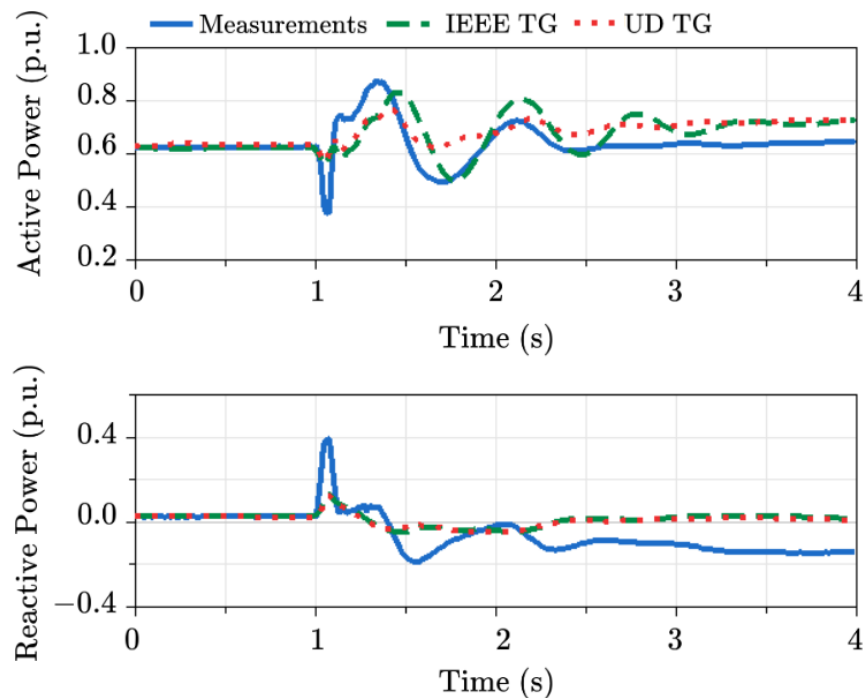


Figure 8.1: Comparison of IEEE standard and user-defined turbine-governor models for the Itaipú plant.

measurements at the terminal bus of the machine, so all plant components must be calibrated in a lumped model. This results in problems with the optimization of the parameters, as it is difficult to find the global minima of the parameters. Both industry standard models and user-defined models were studied to represent the Itaipú plant, which shows the shortcomings of user-defined models. In Figure 8.1 (Figure 2.15 from Chapter 2), both the user-defined models and the generic models are compared for the Itaipú plant. It is evident that the user-defined model is not an accurate representation of the system and has not been maintained over time. These results highlight the importance of using standard models that prioritize easy model maintenance instead of detailed specific models that can be used for only one plant. This lesson can aid in the development in eVTOL and electric aircraft systems, where standard models promote reproducibility of the system.

In Chapter 3, a different hydroelectric plant is studied using commissioning test data. Multiple tests are conducted in the commissioning process, resulting in more data to use to validate the plant. In this case the input is known and repeatable, so these tests can be repeated using a simulator. These tests also have measurements recorded between all of the components, so the generator and controllers of the plant can be validated separately. We

developed a methodology to validate the plant's components individually. The benefit to this validation methodology is that it isolates invalid models, reducing the complexity of the problem and time needed to re-identify the model. This will yield more accurate results, as there will be less parameters to calibrate in contrast to the Itaipú case.

This validation methodology proposed in Chapter 3 highlights the need for sufficiently rich data to observe all parameter changes in the plant. The commissioning test presented in Chapter 3 did not have sufficiently rich data to identify the time constants in the system's power system stabilizer (PSS), as shown in Figures 8.2a and 8.2b (Figures 3.19a and 3.19b in Chapter 3). When the time constant parameters were tested at half and double the nominal value, the model remained validated. After adding a white noise excitation at the input of the PSS, the model was invalid for washout time constant parameter values half and double the nominal value (see Figures 8.3a and 8.3b, which are also Figures 3.20a and 3.20b in Chapter 3).

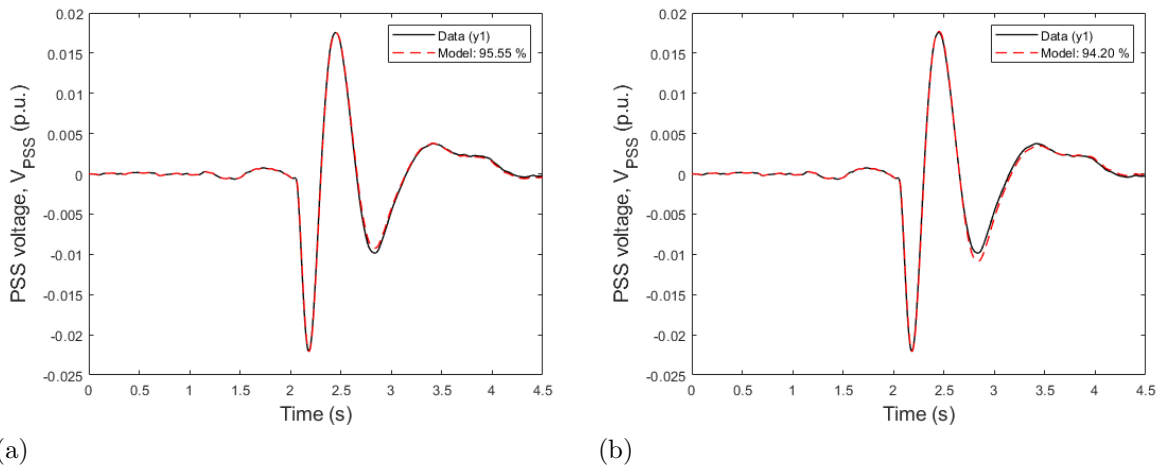


Figure 8.2: PSS validation with only step excitation, where (a) PSS with halved time constants for T_{w1}, T_{w2}, T_6 . (b) PSS with doubled time constants for T_{w1}, T_{w2}, T_6 .

8.2 eVTOL Systems

While eVTOL systems are in the early phases of physical prototype development and testing, simulation studies allow us to understand the interactions between the electrical and mechanical domains in more detail. These models also enable engineers to study different system architectures and designs to understand the potential successes and failures prior to

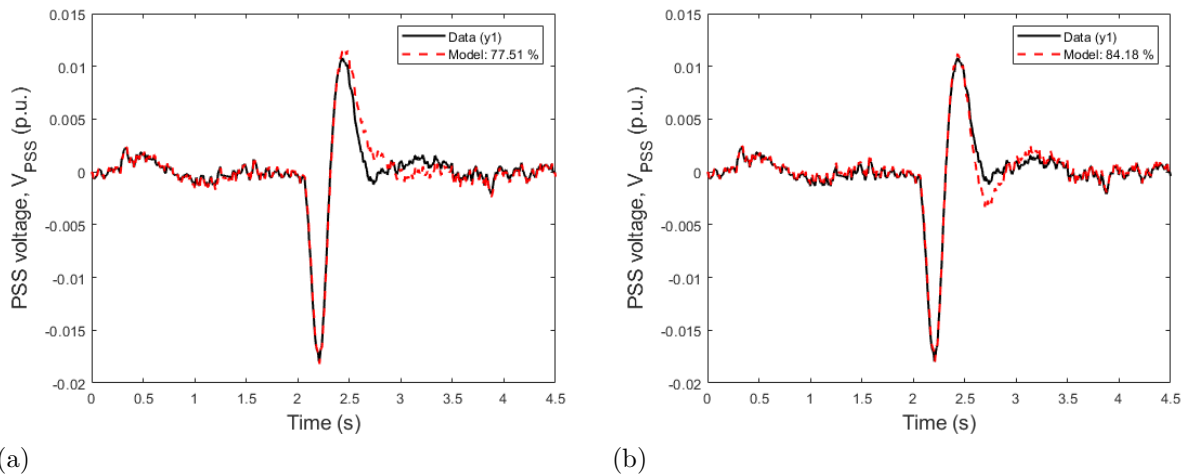


Figure 8.3: PSS validation with both step and white noise excitations, where (a) PSS with halved time constants for T_{w1}, T_{w2}, T_6 . (b) PSS with doubled time constants for T_{w1}, T_{w2}, T_6 .

building a physical prototype. This work shows the modeling and development of a multi-domain quadcopter model in Chapter 4; Chapter 5 demonstrates how these models can be used to conduct trade studies and understand how modeling fidelity affects various aspects of system performance.

Chapter 4 presents a basis for an open-source, multi-domain modeling library to develop quadcopter models. The models included in the library are more complex than the models presented previously in the literature. These models were also configured in a manner such that the drone can be animated for a given input, which is beneficial for insight, analysis, and communication between domain specialists. The animation aspect of the quadcopter model provides a framework in which the models could be used for other interactive animation and simulation by coupling with tools such as the DLR Visualization Library [73].

The open-source nature of the library also promotes further development, where more complex and detailed models can be included in the future. Since these models were developed using Modelica, portions of or the entire quadcopter model can be integrated with other software tools through the FMI Standard. This coupling of the multi-domain quadcopter model with other software tools is discussed in detail in Chapter 5.

While the entire quadcopter is modeled Chapter 4, Chapter 5 focuses on the modeling of an electric drivetrain to study the dynamic response of the system at various levels of modeling fidelity. The relationship between the components of the quadcopter is shown in

Figure 8.4a. The red box in Figure 8.4a highlights the drivetrain component that is studied in detail in Chapter 5. The relationship between the components in the electric drivetrain are shown in Figure 8.4b.

The modeling framework allowed us to study the impact of modeling fidelity on the dynamic response of the system. For example, four different configurations were studied for the drivetrain: (1) a simple DC motor without inductance, (2) a simple DC motor with inductance, (3) a brushless motor with an averaged back EMF, and (4) a brushless motor with a trapezoidal back EMF. While previous handling quality studies explored the impact of the motor dynamics such as in [28, 29], they show that the inductance of the DC motor have minimal impact on the speed response of the drivetrain. Those results are also observed in our drivetrain study; however, the electrical dynamics are modeled in more detail than previous studies, showing the impact of current ripple from the power electronics on the rest of the system. In the drivetrain studied in Chapter 5, two different configurations of the DC/DC converter are considered. First, an averaged DC/DC converter is simulated, where there is no switching behavior observed. When a switched DC/DC converter model is included in the drivetrain model, a ripple current is observed in the electrical domain (see Figure 8.5, which is the trapezoidal current curve in Figure 5.11a of Chapter 5). This ripple behavior is propagated to the mechanical domain, producing a ripple torque seen in Figure 8.6 (trapezoidal current curve from Figure 5.12a in Chapter 5). This observed behavior is notable, as it needs to be taken into consideration in the development of the eVTOL system as the torque ripple will cause large periodic loading in the rotor shaft, which may cause fatigue over time.

The modeling and simulation developments with the eVTOL system shows the value in creating open-source, flexible models. This modeling framework enables collaboration between multiple areas of expertise. The quadcopter models were made in a manner such that they can be reused for other applications such as trade studies and animation. The electric drivetrain shows the value of using these models to collaborate between engineering disciplines. By using the FMI standard to interface the models with other tools and research developments, we are able to conduct better trade studies and understand the system in greater detail.

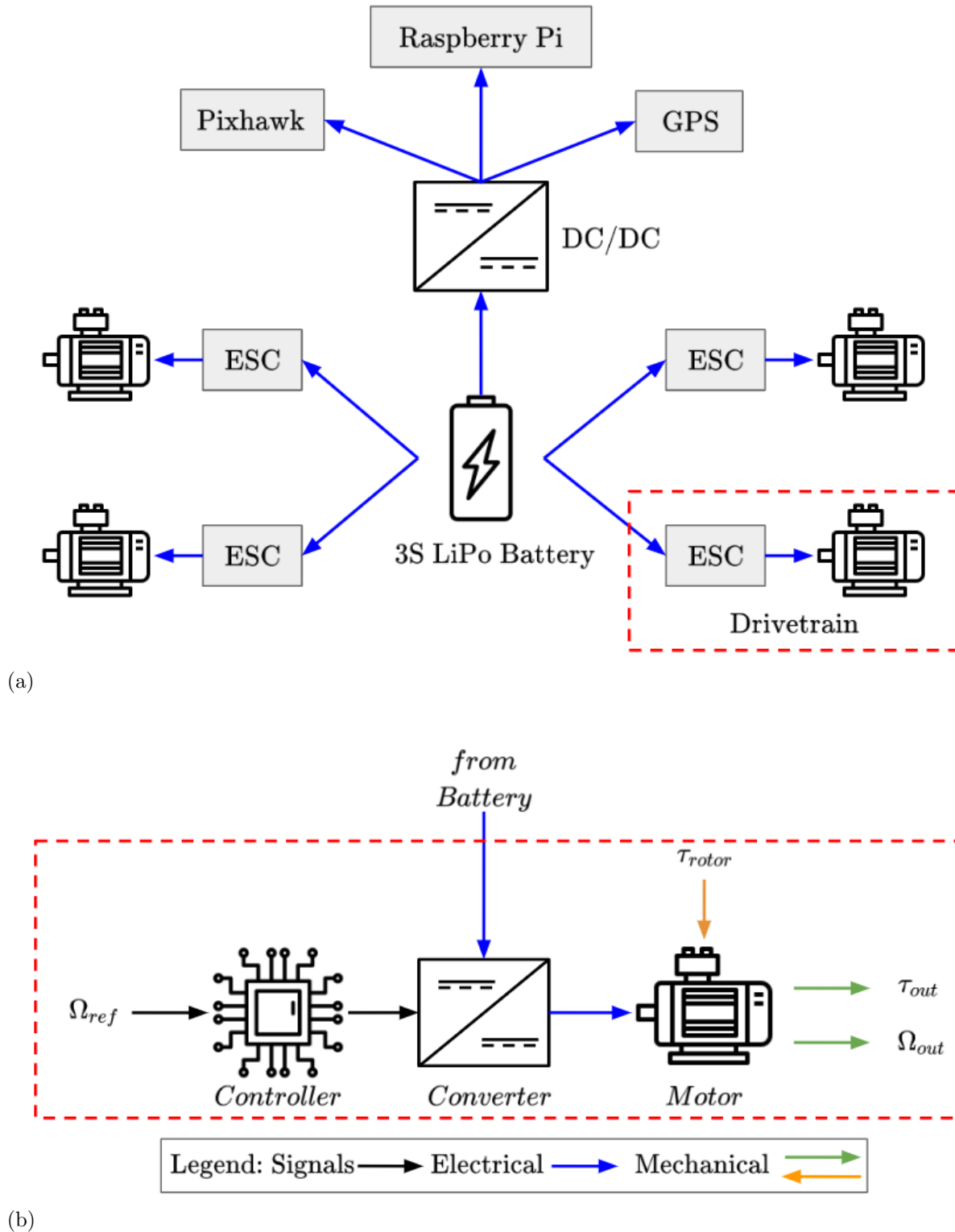
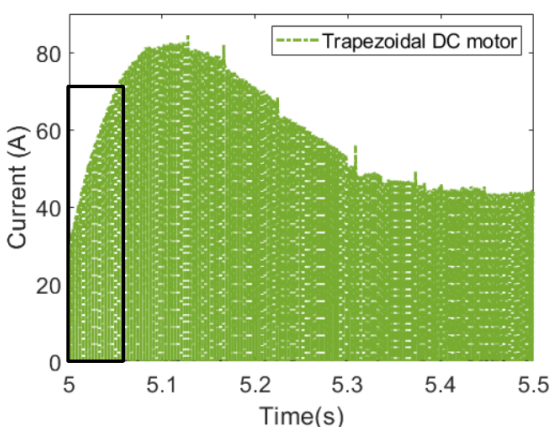
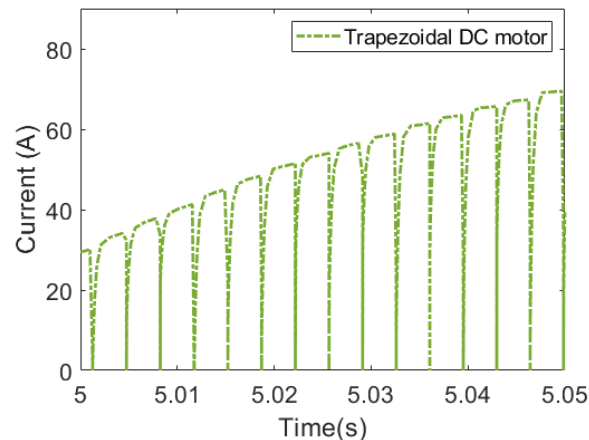


Figure 8.4: Relationship between the quadcopter modeled in Chapter 4 and the drivetrain studied in Chapter 5. (a) Overview of quadcopter model developed in Chapter 4. (b) Overview of electric drivetrain model studied in Chapter 5.

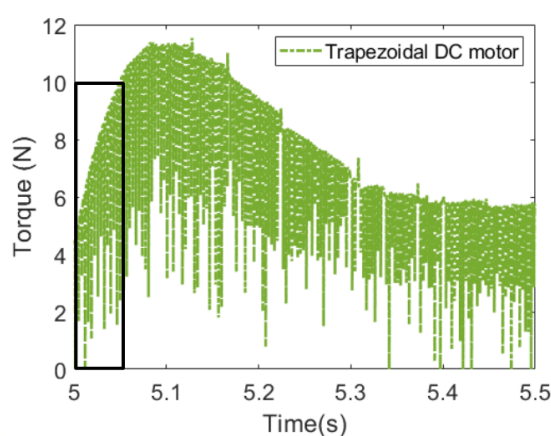


(a)

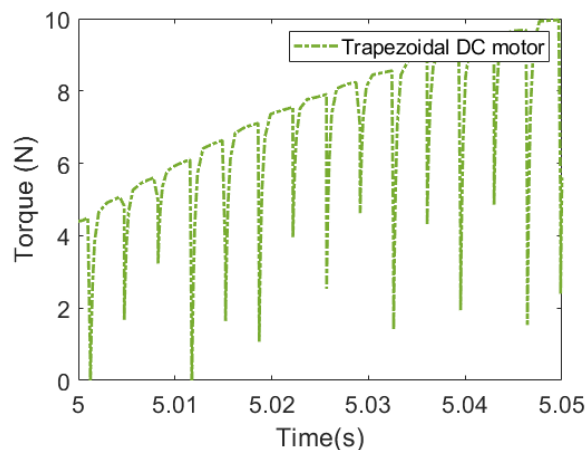


(b)

Figure 8.5: DC motor with trapezoidal back EMF ripple current behavior, where (a) First 500ms of the response. (b) First 50ms of the response.



(a)



(b)

Figure 8.6: DC motor with trapezoidal back EMF ripple torque behavior, where (a) First 500ms of the response. (b) First 50ms of the response.

8.3 Fully-electric Aircraft Systems

Fully-electric aircraft systems are at the beginning of the development phase, making simulation studies necessary to study novel component technologies and system architecture. Physical prototypes and measurements are **not** available for portions of the aircraft's subsystems, and there is no physical representation of the fully-electric aircraft to study yet. Since measurements are available from other experiments and projects, they can be used to

develop and validate models for the individual components used in the aircraft. In Chapters 6 and 7, this modeling approach aided in the design of the aircraft system architecture and the development of models for the novel high temperature superconducting (HTS) transmission lines. The system was then studied for different faults, trade studies, and steady-state simulations.

This work discusses the development of the power system for the CHEETA electric aircraft concept. Chapter 6 introduces the multi-domain models used to model the system. The system went through many iterations of power and cooling system design, which was finalized to have a hybrid centralized-distributed layout. This architecture was selected from factors such as reliability and weight as shown in Figure 8.7 (also Figures 6.2 and 7.1 in Chapters 6 and 7). The power system consists of three generation buses with the fuel cells attached, and each generation bus is linked together via a tie-line to redistribute power in case of failure. The power is sent to the propulsion buses via HTS transmission line, which benefits from near zero losses due to the cryogenic cooling. The propulsion is also divided into three locations: in each of the wings and along the aircraft body. Each of the propulsion bus bars has a battery attached to it to further improve the reliability of the power system. If the link between the fuel cells and propulsion is compromised due to electrical or mechanical failures, the battery would provide additional power for a short period of time to safely land the aircraft. The batteries will be located in the wings to balance the aircraft weight. The cooling system sends liquid hydrogen from the storage tank to cool the motors, inverters, and HTS cables. After cooling those components, the liquid hydrogen is sent to a heat exchanger to transition to hydrogen gas to provide cooling for the fuel cells' cold plates.

After determining the power system architecture, the subsystems could be parameterized. Through collaboration with other research groups within the CHEETA project, multi-models for each of the subsystems were developed according to functional requirements. This first allowed us to study a first-order aircraft power system under simple flight profiles in Chapter 6. The HTS lines were identified as a possible point of failure in the power system, so they were modeled in more detail to study their fault behavior in Chapter 7.

Since the CHEETA system is cryogenically cooled, the HTS lines benefit from low losses since the resistivity of the line is negligible. As a result, the system would suffer from an influx of heat if any portion of the HTS line or the cooling system failed. This would cause

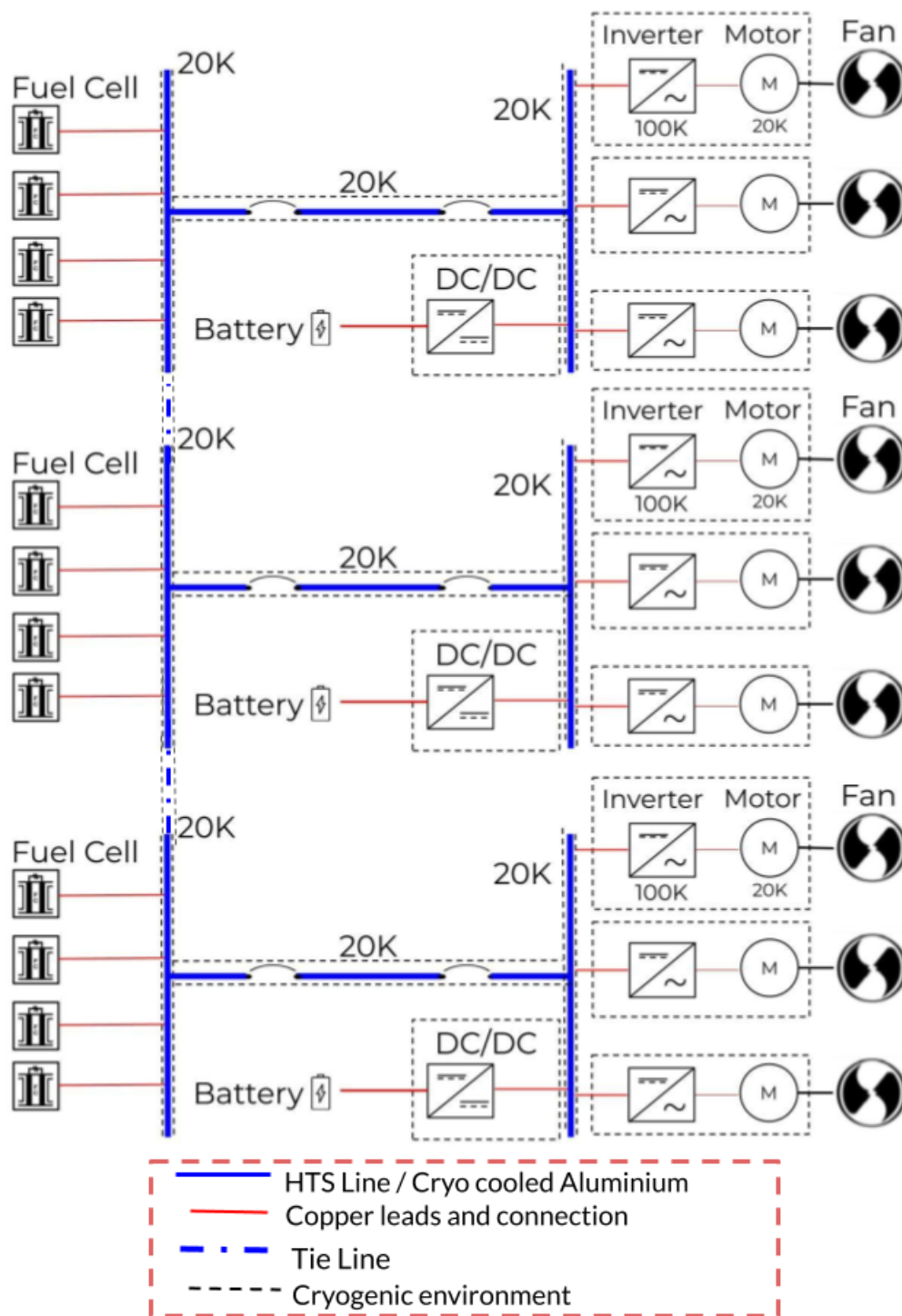


Figure 8.7: The CHEETA electric aircraft architecture configured to show the electrical wiring scheme for the system.

the HTS line to enter a quench period, heat uncontrollably, and cause the transmission line and surrounding components to melt. To prevent this behavior, we studied how we could parameterize the fuel cell to keep the HTS line in a cryogenically stable region when the worst electrical faults were applied to the system. Since a physical prototype does not exist for the HTS system that would be used in the CHEETA aircraft, previous experimental results were used to validate the cooling media models and the HTS line model. This ensured that the models were correct prior to conducting the simulation studies so that the results produced could be trusted for analysis. For example, experiments conducted in studies such as [108] and [109] obtained heating curves for the cooling media that we were able to reproduce using our models. This approach to modeling and simulation studies shows how we can use existing research results to conduct trade studies on systems that do not exist in significant physical capacity yet, showing promise for the development of electrified systems in the future.

REFERENCES

- [1] S. Zanero, “Cyber-physical systems,” *Computer*, vol. 50, no. 4, pp. 14–16, Apr. 2017, doi: 10.1109/MC.2017.105.
- [2] IEEE, “IEEE is fueling the fourth industrial revolution,” <https://innovate.ieee.org/innovation-spotlight-ieee-fueling-fourth-industrial-revolution/> (accessed May 23, 2022).
- [3] U.S. Department of Energy, “Reimagining and rebuilding America’s energy grid,” Jun. 2021, <https://www.energy.gov/articles/reimagining-and-rebuilding-americas-energy-grid> (accessed May 23, 2022).
- [4] U.S. House. 117th Congress, (2021, Nov. 15), *H.R.3684 - Infrastructure Investment and Jobs Act*, [Online] Available: <https://www.congress.gov/bill/117th-congress/house-bill/3684/> (accessed May 25, 2022).
- [5] A. Brown, “Electric cars will challenge state power grids,” PEW Charitable Trusts, Jan. 2020, <https://www.pewtrusts.org/en/research-and-analysis/blogs/stateline/2020/01/09/electric-cars-will-challenge-state-power-grids> (accessed May 23, 2022).
- [6] North American Synchrophasor Initiative, “Model validation using phasor measurement unit data,” Tech. Rep., Mar. 2015, https://www.naspi.org/sites/default/files/reference_documents/19.pdf (accessed May 23, 2022).
- [7] X. Luo, “ISO-NE’s model validation of HVDC and nuclear unit using synchrophasor data,” NASPI, Oct. 2013, https://www.naspi.org/sites/default/files/2016-09/7_model_validation_2013oct_chicago_luo.pdf (accessed May 23, 2022).
- [8] ERCOT, “Review of February 2021 extreme cold weather event – ERCOT presentation,” https://www.ercot.com/files/docs/2021/02/24/2.2_REVISIED_ERCOT_Presentation.pdf, Feb. 2021 (accessed May 23, 2022).
- [9] Air Transport Action Group (ATAG), “Facts and figures,” <https://www.atag.org/facts-figures.html> (accessed May 23, 2022).
- [10] NASA, “AAM overview — NASA,” <https://www.nasa.gov/aeroresearch/aam/description/> (accessed Nov 3, 2020).
- [11] J. Holden and N. Goel, “Fast-forwarding to a future of on-demand urban air transportation,” Uber Elevate, Oct. 2016, https://evtol.news/_media/PDFs/UberElevateWhitePaperOct2016.pdf (accessed May 11, 2022).

- [12] M. Podlaski, L. Vanfretti, H. Nademi, P. J. Ansell, K. S. Haran, and T. Balachandran, “Initial steps in modeling of CHEETA hybrid propulsion aircraft vehicle power systems using Modelica,” in *AIAA Propulsion and Energy 2020 Forum*, Aug. 2020, Paper 3580, doi: 10.2514/6.2020-3580.
- [13] J. Bals, Y. Ji, M. Kuhn, and C. Schallert, “Model based design and integration of more electric aircraft systems using Modelica,” in *MOET Forum at Eur. Power Electron. Conf. and Exhib.*, Sep. 2009, pp. 1–12.
- [14] D. Kramer, “Hydrogen-powered aircraft may be getting a lift,” *Physics Today*, vol. 73, no. 12, p. 27, 2020, doi: 10.1063/PT.3.4632.
- [15] European Commission - CORDIS, “More open electrical technologies,” <https://cordis.europa.eu/project/id/30861>, 2009 (accessed June 14, 2022).
- [16] CFM, “CFM RISE program,” CFM, Cincinnati, OH, USA, 2021, https://www.cfmaeroengines.com/wp-content/uploads/2021/07/CFM_RISE_Whitepaper_Media.pdf (accessed June 14, 2022).
- [17] *IEEE Recommended Practice for Excitation System Models for Power System Stability Studies*, IEEE Std 421.5-2016 (Revision of IEEE Std 421.5-2005), 2016, doi: 10.1109/IEEESTD.2016.7553421.
- [18] Z. Huang, P. Du, D. Kosterev, and S. Yang, “Generator dynamic model validation and parameter calibration using phasor measurements at the point of connection,” *IEEE Trans. Power Syst.*, vol. 28, no. 2, pp. 1939–1949, May 2013, doi: 10.1109/TPWRS.2013.2251482.
- [19] N. Nayak, H. Chen, W. Schmus, and R. Quint, “Generator parameter validation and calibration process based on pmu data,” in *2016 IEEE/PES Transmission and Distribution Conf. and Exp. (T&D)*, May 2016, pp. 1–5.
- [20] D. Kosterev, “Hydro turbine-governor model validation in Pacific northwest,” *IEEE Trans. Power Syst.*, vol. 19, no. 2, pp. 1144–1149, May 2004.
- [21] L. Vanfretti, M. Baudette, A. Amazouz, T. Bogodorova, T. Rabuzin, J. Lavenius, F. Jose Gomez-Lopez, “RaPID: A modular and extensible toolbox for parameter estimation of Modelica and FMI compliant models,” *SoftwareX*, vol. 5, pp. 144–149, 2016, doi: 10.1016/j.softx.2016.07.004.
- [22] M. Podlaski, L. Vanfretti, H. Nademi and H. Chang, “UAV dynamic system modeling and visualization using Modelica and FMI,” in *VFS 76th Annu. Forum & Tech. Display*, Oct. 2020, pp. 1058–1072, doi: doi:10.4050/F-0076-2020-16289.
- [23] P. Fritzson, *Modelica: Equation-Based, Object-Oriented Modelling of Physical Systems*. Cham, Switzerland: Springer International Publishing, 2020, pp. 45–96, doi: 10.1007/978-3-030-43946-0_3.

- [24] X. Ma, Z. Li, and C. Nae, “Multi-domain modeling and simulation of a quad-rotor aircraft based on Modelica,” in *Proc. Intl. Conf. Modeling, Simulation and Visualization Methods (MSV)*, 2016, pp. 120–124.
- [25] Modelica Association, “FMI Standard,” <https://fmi-standard.org/> (accessed May 11, 2022).
- [26] M. Kuric, N. Osmic, and A. Tahirovic, “Multirotor aerial vehicle modeling in Modelica,” in *Proc. 12th Int. Modelica Conf.*, Jul. 2017, pp. 373–380, doi: 10.3384/ecp17132373.
- [27] R. Niemiec and F. Gandhi, “Development and validation of the Rensselaer multicopter analysis code (RMAC): A physics-based comprehensive modeling tool,” in *VFS 75th Annu. Forum & Tech. Display*, Philadelphia, PA, 2019, pp. 1147–1166.
- [28] M. Bahr, M. McKay, R. Niemiec, and F. Gandhi, “Handling qualities assessment of large variable-RPM multi-rotor aircraft for urban air mobility,” in *VFS 76th Annu. Forum & Tech. Display*, Oct. 2020, pp. 945–955.
- [29] A. Walter, M. McKay, R. Niemiec, F. Gandhi, and C. Ivler, “Hover handling qualities of fixed-pitch, variable-RPM quadcopters with increasing rotor diameter,” in *VFS 76th Annu. Forum & Tech. Disp.*, Oct. 2020, pp. 2537–2553.
- [30] P. D. C. Perera, F. Blaabjerg, J. K. Pedersen, and P. Thogersen, “A sensorless, stable V/f control method for permanent-magnet synchronous motor drives,” *IEEE Trans. Ind. Appl.*, vol. 39, no. 3, pp. 783–791, 2003, doi: 10.1109/TIA.2003.810624.
- [31] J. Batteh, J. Gohl, M. Sielemann, P. Sundstrom, I. Torstensson, N. MacRae, and P. Zdunich, “Development and implementation of a flexible model architecture for hybrid-electric aircraft,” in *Proc. 1st Amer. Modelica Conf.* Cambridge, Massachusetts, USA: Modelica Association, Feb. 2019, pp. 37–45, doi: 10.3384/ecp1815437.
- [32] M. Baudette, M. Castro, T. Rabuzin, J. Lavenius, T. Bogodorova, and L. Vanfretti, “Openipsl: Open-instance power system library—update 1.5 to “iTesla power systems library (iPSL): A Modelica library for phasor time-domain simulations”,” *SoftwareX*, vol. 7, pp. 34–36, Jan. 2018, doi: 10.1016/j.softx.2018.01.002.
- [33] Dassault Systems, “CATIA systems engineering: Electrified power trains library,” https://www.3ds.com/fileadmin/PRODUCTS/CATIA/DYMOLA/PDF/3DS_2016_CAT_FLYER_EPTL_A4_WEB.pdf (accessed May 16, 2022).
- [34] L. Vanfretti, W. Li, T. Bogodorova, and P. Panciatici, “Unambiguous power system dynamic modeling and simulation using modelica tools,” in *2013 IEEE Power Energy Soc. General Meeting (PESGM)*, Jul. 2013, pp. 1–5.
- [35] Itaipu Binacional, “Generating units,” <https://www.itaipu.gov.br/en/energy/generating-units> (accessed May 31, 2022).

- [36] J. Chen, P. Shrestha, S. Huang, N. D. R. Sarma, J. Adams, D. Obadina, and J. Ballance, “Use of synchronized phasor measurements for dynamic stability monitoring and model validation in ERCOT,” in *2012 IEEE Power Energy Soc. General Meeting (PESGM)*, Jul. 2012, pp. 1–7, doi: 10.1109/PESGM.2012.6345152.
- [37] S. Andersson and J. Strömner, “Model calibration of a vertical wind power plant using dymola/modelica,” Master’s thesis, Division of Industrial Electrical Engineering and Automation Faculty of Engineering, Lund University, Lund, Sweden, 2013.
- [38] Modelica Association, “Modelica standard library,” <https://github.com/modelica/ModelicaStandardLibrary> (accessed May 11, 2022).
- [39] P. Kundur, “Synchronous machine parameters,” in *Power System Stability and Control*. New York, NY, USA: McGraw Hill, 1994, pp. 139–168.
- [40] J. Weber, “Description of machine models GENROU, GENSAL, GENTPF and GENTPJ,” PowerWorld Corporation, Champaign, IL, USA, Tech. Rep., Dec. 2015, <https://www.powerworld.com/files/GENROU-GENSAL-GENTPF-GENTPJ.pdf> (accessed May 25, 2022).
- [41] Cepel, “CDUEdit - user-defined controller editor,” <http://www.cepel.br/produtos/cduedit/> (accessed May 31, 2022).
- [42] —, “ANATEM - analysis of electromechanical transients,” <http://www.cepel.br/produtos/anatem-2/> (accessed May 31, 2022).
- [43] —, “ANAREDE - analysis of electrical power systems in steady state,” <http://www.cepel.br/produtos/anared-2/> (accessed May 31, 2022).
- [44] Modelon, “FMI toolbox user’s guide 2.6.4,” Modelon AB, Lund, Sweden, Tech. Rep. SE-22370, Jul. 2018, <https://modelon.com/wp-content/uploads/2018/08/UsersGuide-FMI-Toolbox-2.6.4.pdf> (accessed Oct 4, 2022).
- [45] Mathworks, “fmincon interior-point algorithm with analytic hessian,” Mathworks, Natick, MA, USA, Tech. Rep., Jan. 2022, <https://www.mathworks.com/help/optim/ug/fmincon-interior-point-algorithm-with-analytic-hessian.html> (accessed May 31, 2022).
- [46] M. Marenc, D. Milićević, and S. Vučina, “Hydro-power plant Mostarsko blato – a multi-purpose project in karst,” in *Hydro 2003: Int. Conf. and Exhib.*, Jan. 2003, pp. 1–6.
- [47] M. Podlaski, L. Vanfretti, M. de Castro Fernandes, and J. Pesente, “Parameter estimation of user-defined control system models for Itaipú power plant using Modelica and OpenIPSL,” in *2020 Amer. Modelica Conf.*, Sep. 2020, pp. 139–148.
- [48] M. Podlaski, L. Vanfretti, J. Pesente and P. H. Galassi, “Automated parameter identification and calibration for the Itaipú power generation system using Modelica, FMI, and RaPIId,” in *7th Workshop on Model. and Simul. of Cyber-Physical Energy Syst. (MSCPES)*, 2019, pp. 1–6, doi: 10.1109/MSCPES.2019.8738793.

- [49] J. Chow, M. Glinkowski, R. Murphy, T. Cease, and N. Kosaka, "Generator and exciter parameter estimation of Fort Patrick Henry Hydro Unit 1," *IEEE Trans. Energy Convers.*, vol. 14, no. 4, pp. 923–929, Dec. 1999, doi: 10.1109/60.815009.
- [50] P. Pourbeik, C. Pink, and R. Bisbee, "Power plant model validation for achieving reliability standard requirements based on recorded on-line disturbance data," in *2011 IEEE/PES Power Systems Conf. and Exp.*, Mar. 2011, pp. 1–9, doi: 10.1109/PSCE.2011.5772520.
- [51] H. Weber and F. Prillwitz, "Simulation models of the hydro power plants in Macedonia and Yugoslavia," in *2003 IEEE Bologna Power Tech. Conf.*, vol. 3, Jun. 2003, p. 8, doi: 10.1109/PTC.2003.1304511.
- [52] L. Ozkan, X. Bombois, J. Ludlage, C. Rojas, H. Hjalmarsson, P. Modén, M. Lundh, T. Backx, and P. Van den Hof, "Advanced autonomous model-based operation of industrial process systems (Autoprofit): Technological developments and future perspectives," *Annu. Reviews in Control*, vol. 42, pp. 126–142, Nov. 2016, doi: 10.1016/j.arcontrol.2016.09.015.
- [53] K. Schroeder, J. Moyne, and D. M. Tilbury, "A factory health monitor: System identification, process monitoring, and control," in *2008 IEEE Int. Conf. on Automation Science and Engineering*, Aug 2008, pp. 16–22, doi: 10.1109/COASE.2008.4626536.
- [54] M. A. M. Ariff, B. C. Pal, and A. K. Singh, "Estimating dynamic model parameters for adaptive protection and control in power system," *IEEE Trans. Power Syst.*, vol. 30, no. 2, pp. 829–839, Mar. 2015, doi: 10.1109/TPWRS.2014.2331317.
- [55] A. Rouhani and A. Abur, "Constrained iterated unscented Kalman filter for dynamic state and parameter estimation," *IEEE Trans. Power Syst.*, vol. 33, no. 3, pp. 2404–2414, May 2018, doi: 10.1109/TPWRS.2017.2764005.
- [56] R. Huang, R. Diao, Y. Li, J. Sanchez-Gasca, Z. Huang, B. Thomas, P. Etingov, S. Kincic, S. Wang, R. Fan, G. Matthews, D. Kosterev, S. Yang, and J. Zhao, "Calibrating parameters of power system stability models using advanced ensemble kalman filter," *IEEE Trans. Power Syst.*, vol. 33, no. 3, pp. 2895–2905, May 2018, doi: 10.1109/TPWRS.2017.2760163.
- [57] P. Kundur, "Prime mover and energy supply systems," in *Power System Stability and Control*. New York, NY, USA: McGraw Hill, 1994, pp. 377–462.
- [58] NEPLAN AG, "Power system stabilizer models: Standard dynamic power system stabilizers in NEPLAN power system analysis tool," NEPLAN AG, Zürich, Switzerland, Tech. Rep., 2015, https://www.neplan.ch/wp-content/uploads/2015/08/Nep_PSSs.pdf (accessed May 25, 2022).

- [59] J. Culberg, M. Negnevitsky, and K. M. Muttaqi, “Hydro-turbine governor control: theory, techniques and limitations,” in *Australas. Univ. Power Eng. Conf. (AUPEC 2006)*, 2006, pp. 1–7.
- [60] S. H. Jakobsen, X. Bombois, and K. Uhlen, “Non-intrusive identification of hydro power plants’ dynamics using control system measurements,” *Int. J. Elect. Power Energy Syst.*, vol. 122, pp. 1–14, Nov. 2020, doi: 10.1016/j.ijepes.2020.106180.
- [61] M. Podlaski, L. Vanfretti, T. Bogodorova, T. Rabuzin, and M. Baudette, “RaPIId-a parameter estimation toolbox for Modelica/FMI-based models exploiting global optimization methods,” *IFAC-PapersOnLine*, vol. 54, no. 7, pp. 391–396, Jul. 2021, doi: 10.1016/j.ifacol.2021.08.391.
- [62] NEPLAN AG, “Exciter models: Standard dynamic excitation systems in NEPLAN power system analysis tool,” NEPLAN AG, Zürich, Switzerland, Tech. Rep., 2015, https://www.neplan.ch/wp-content/uploads/2015/08/Nep_EXCITERS1.pdf (accessed May 25, 2022).
- [63] *IEEE Guide for Synchronous Generator Modeling Practices and Parameter Verification with Applications in Power System Stability Analyses*, IEEE Std 1110-2019 (Revision of IEEE Std 1110-2002), 2020, doi: 10.1109/IEEESTD.2020.9020274.
- [64] T. Bresciani, “Modelling, identification and control of a quadrotor helicopter,” MSc Thesis, Department of Automatic Control, Lund University, Lund, Sweden, Oct. 2008.
- [65] T. Luukkonen, “Modelling and control of quadcopter,” Independent research project in applied mathematics, School of Science, Aalto University, Espoo, Finland, Aug. 2011.
- [66] R. Mahony, V. Kumar, and P. Corke, “Multirotor aerial vehicles: Modeling, estimation, and control of quadrotor,” *IEEE Robot Autom. Mag.*, vol. 19, no. 3, pp. 20–32, Sep 2012, doi: 10.1109/MRA.2012.2206474.
- [67] ALSETLab, “Modelica drone 3D FMI,” <https://github.com/ALSETLab/Modelica-Drone-3D-FMI/> (accessed May 11, 2022).
- [68] DLR, “Modelica Synchronous Library,” https://github.com/modelica/Modelica_Synchronous (accessed May 11, 2022).
- [69] Modelon, “Modelon library suite,” <https://www.modelon.com/products-services/modelon-library-suite-modelica-libraries/> (accessed May 11, 2022).
- [70] RC Benchmark, “Otus quadcopter manual v1.1,” <https://www.tytorobotics.com/blogs/other/otus-quadcopter-deprecated> (accessed May 11, 2022).

- [71] S. Li and B. Ke, "Study of battery modeling using mathematical and circuit oriented approaches," in *2011 IEEE Power Energy Soc. General Meeting (PESGM)*, Jul 2011, pp. 1–8, doi: 10.1109/PES.2011.6039230.
- [72] M. Otter, H. Elmqvist, and S. E. Mattsson, "The new Modelica multibody library," in *Proc. 3rd Int. Modelica Conf.*, Nov. 2003, pp. 311–330.
- [73] M. Hellerer, T. Bellmann, and F. Schlegel, "The DLR Visualization Library - Recent development and applications," in *Proc. 10th Int. Modelica Conf.*, Mar. 2014, pp. 899–911, doi: 10.3384/ecp14096899.
- [74] C. Malpica and S. Withrow-Maser, "Handling qualities analysis of blade pitch and rotor speed controlled eVTOL quadrotor concepts for urban air mobility," in *VFS Int. Powered Lift Conf.*, Jan. 2020, pp. 118–132.
- [75] S. Withrow-Maser, C. Malpica, and K. Nagami, "Multirotor configuration trades informed by handling qualities for urban air mobility application," in *VFS 76th Annu. Forum & Tech. Display*, Oct 2020, pp. 1861–1875.
- [76] R. Niemiec, F. Gandhi, M. Lopez, and M. Tischler, "System identification and handling qualities predictions of an eVTOL urban air mobility aircraft using modern flight control methods," in *VFS 76th Annu. Forum & Tech. Display*, Oct. 2020, pp. 37–48, doi: 10.4050/F-0076-2020-16384.
- [77] W. Johnson, C. Silva, and E. Solis, "Concept vehicles for VTOL air taxi operations," in *AHS Tech. Conf. on Aeromechanics Des. for Transformative Vertical Flight*, Jan. 2018, pp. 835–858.
- [78] P. Pillay and R. Krishnan, "Modeling, simulation, and analysis of permanent-magnet motor drives. I. The permanent-magnet synchronous motor drive," *IEEE Trans. Ind. Appl.*, vol. 25, no. 2, pp. 265–273, Mar. 1989, doi: 10.1109/28.25541.
- [79] —, "Modeling, simulation, and analysis of permanent-magnet motor drives. II. The brushless DC motor drive," *IEEE Trans. Ind. Appl.*, vol. 25, no. 2, pp. 274–279, Mar. 1989, doi: 10.1109/28.25542.
- [80] R. M. Schupbach and J. C. Balda, "Comparing DC-DC converters for power management in hybrid electric vehicles," in *IEEE Int. Electric Machines and Drives Conf. (IEMDC)*, vol. 3, Jun. 2003, pp. 1369–1374, doi: 10.1109/IEMDC.2003.1210630.
- [81] D. Montesinos, S. Galceran, F. Blaabjerg, A. Sudria, and O. Gomis, "Sensorless control of PM synchronous motors and brushless DC motors - an overview and evaluation," in *European Conf. on Power Electronics and App.*, Sep. 2005, pp. 1–10, doi: 10.1109/EPE.2005.219492.
- [82] J. Hayes and G. A. Goodrazi, *Electric Powertrain: Energy Systems, Power Electronics, and Drives for Hybrid, Electric, and Fuel Cell Vehicles*. Hoboken, NJ, USA: Wiley, 2018, pp. 301–348.

- [83] R. L. Steigerwald and D. C. Hopkins, “Characteristic input harmonics of DC-DC converters and their effect on input filter design,” *IEEE Trans. Ind. Electron.*, vol. 28, no. 2, pp. 73–82, May 1981, doi: 10.1109/TIECI.1981.351029.
- [84] X. Yan, A. Seckold, and D. Patterson, “Development of a zero-voltage-transition bidirectional DC-DC converter for a brushless DC machine EV propulsion system,” in *Proc. IEEE 33rd Annu. Power Electronics Specialists Conf.*, vol. 4, Jun. 2002, pp. 1661–1666, doi: 10.1109/PSEC.2002.1023049.
- [85] Y. Liu, Z. Q. Zhu, and D. Howe, “Commutation-torque-ripple minimization in direct-torque-controlled PM brushless DC drives,” *IEEE Trans. Ind. Appl.*, vol. 43, no. 4, pp. 1012–1021, Jul. 2007, doi: 10.1109/TIA.2007.900474.
- [86] W. Ng, M. Patil, and A. Datta, “Hydrogen fuel cell and battery hybrid architectures for range extension of electric VTOL (eVTOL) aircraft,” in *VFS 75th Annu. Forum & Tech. Display*, May 2019, pp. 435–453.
- [87] M. Ricci, R. Rahn, J. Myers, and B. Paden, “Electric propulsion component sizing for optimal aircraft configuration,” in *VFS 76th Annu. Forum & Tech. Disp.*, Oct. 2020, pp. 3064–3076, doi: 10.4050/F-0076-2020-16413.
- [88] J. O. Estima and A. J. Marques Cardoso, “Performance analysis of a PMSM drive for hybrid electric vehicles,” in *The XIX Int. Conf. on Elect. Machines (ICEM 2010)*, Sep. 2010, pp. 1–6, doi: 10.1109/ICELMACH.2010.5608285.
- [89] R. Speed and A. K. Wallace, “Remedial strategies for brushless DC drive failures,” *IEEE Trans. Ind. Appl.*, vol. 26, no. 2, pp. 259–266, Mar. 1990, doi: 10.1109/28.54251.
- [90] C. Xia, Y. Xiao, W. Chen, and T. Shi, “Torque ripple reduction in brushless DC drives based on reference current optimization using integral variable structure control,” *IEEE Trans. Ind. Electron.*, vol. 61, no. 2, pp. 738–752, Feb. 2014, doi: 10.1109/TIE.2013.2254093.
- [91] Hacker Motor USA, “Hacker Q150-45-4 series datasheet,” <https://hackermotorusa.com/product-category/hacker-brushless-motors/outrunners/q150-series-12000-watt-brushless-motors/> (accessed May 11, 2022).
- [92] Modelica Association, “Modelica Language Specification,” <https://github.com/modelica/ModelicaSpecification> (accessed May 18, 2022), version 3.6-dev.
- [93] Dassault Systemes, “CATIA systems brushless dc drives library,” https://www.3ds.com/fileadmin/PRODUCTS/CATIA/DYMOLA/PDF/3DS_2017_CAT_BrushlessDCDrives_Flyer_A4.pdf (accessed May 12, 2022).
- [94] —, “CATIA systems battery library,” https://www.3ds.com/fileadmin/PRODUCTS/CATIA/DYMOLA/PDF/3DS_2015-CATIA_BTY_Battery_Flyer_A4_WEB.pdf (accessed May 16, 2022).

- [95] M. Tischler, T. Berger, C. Ivler, M. Mansur, K. Cheung, and J. Soong, *Practical Methods for Aircraft and Rotorcraft Flight Control Design: An Optimization-Based Approach*. Reston, VA, USA: AIAA Education Series, 2017.
- [96] NASA, “NASA Armstrong fact sheet: NASA X-57 Maxwell,” <https://www.nasa.gov/centers/armstrong/news/FactSheets/FS-109.html> (accessed August 29, 2022).
- [97] D. Andersson, E. Åberg, J. Eborn, J. Yuan, and B. Sunden, “Dynamic modeling of a solid oxide fuel cell system in Modelica,” in *Proc. 8th Int. Modelica Conf.* Dresden, Germany: Modelica Association, Jun. 2011, pp. 593–602, doi: 10.3384/ecp11063593.
- [98] M. Olm, S. Badia, and A. Martín, “Simulation of high temperature superconductors and experimental validation,” *Comput. Physics Commun.*, vol. 237, pp. 154–167, Apr. 2019, doi: 10.1016/j.cpc.2018.11.021.
- [99] C. Kovacs, M. Majoros, M. Sumption, and E. Collings”, “Quench and stability of Roebel cables at 77 K and self-field: Minimum quench power, cold end cooling, and cable cooling efficiency,” *Cryogenics*, vol. 95, pp. 57–63, Oct. 2018, doi:10.1016/j.cryogenics.2018.07.001.
- [100] F. Grumm, M. Schumann, C. Cosse, M. Plenz, A. Lücken, and D. Schulz, “Short circuit characteristics of PEM fuel cells for grid integration applications,” *Electronics*, vol. 9, p. 602, Apr. 2020, doi: 10.3390/electronics9040602.
- [101] M. H. Nehrir and C. Wang, *Dynamic Modeling and Simulation of PEM Fuel Cells*. Hoboken, NJ, USA: Wiley-IEEE, 2009, pp. 57–84.
- [102] J. Laraminie and A. Dicks, “Proton exchange membrane fuel cells,” in *Fuel Cell Systems Explained*. Hoboken, NJ, USA: Wiley, 2003, pp. 67–119.
- [103] J. Schmalstieg, S. Käbitz, M. Ecker, and D. U. Sauer, “A holistic aging model for Li(NiMnCo)O₂ based 18650 lithium-ion batteries,” *J. of Power Sources*, vol. 257, pp. 325–334, Jul. 2014, doi: 10.1016/j.jpowsour.2014.02.012.
- [104] M. Chen and G. Rincon-Mora, “Accurate electrical battery model capable of predicting runtime and I-V performance,” *IEEE Trans. Energy Convers.*, vol. 21, no. 2, pp. 504–511, Jun. 2006.
- [105] M. Mengoni, L. Zarri, A. Tani, G. Serra, and D. Casadei, “A comparison of four robust control schemes for field-weakening operation of induction motors,” *IEEE Trans. Power Electron.*, vol. 27, no. 1, pp. 307–320, Jan. 2012, doi: 10.1109/TPEL.2011.2156810.
- [106] Modelica Association, “Electrically excited synchronous machine,” https://doc.modelica.org/om/Modelica.Electrical.Machines.BasicMachines.SynchronousInductionMachines.SM_ElectricalExcited.html (accessed May 20, 2022).

- [107] Z.J.J Stekly and J.L. Zar, “Stable superconducting coils,” *IEEE Trans. Nucl. Sci.*, vol. 95, pp. 367–372, Jun. 1965, doi: 10.1109/TNS.1965.4323653.
- [108] H. Tatsumoto, Y. Shirai, M. Shiotsu, Y. Naruo, H. Kobayashi, and Y. Inatani, “Heat transfer characteristics of a horizontal wire in pools of liquid and supercritical hydrogen,” *J. Supercond. Nov. Magn.*, vol. 28, p. 1185–1188, Mar. 2014, doi: 10.1007/s10948-014-2706-x.
- [109] M. Kida, Y. Kikuchci, O. Takahashi, and I. Michiyoshi, “Pool-boiling heat transfer in liquid nitrogen,” *J. Nucl. Sci. Technol.*, vol. 18, no. 7, pp. 501–513, Dec. 1980, doi: 10.1080/18811248.1981.9733284.
- [110] M. Podlaski, A. Khare, L. Vanfretti, M. D. Sumption, and P. J. Ansell, “Multi-domain modeling for high temperature superconducting components for the CHEETA hybrid propulsion power system,” in *AIAA Propulsion and Energy 2021 Forum*, Aug. 2021, p. 3302, doi: 10.2514/6.2021-3302.
- [111] S. S. Fetisov, V. V. Zubko, S. Y. Zanev, A. A. Nosov, V. S. Vysotsky, A. Kario, A. Kling, W. Goldacker, A. Molodyk, A. Mankevich, V. Kalitka, A. Adamenkov, S. Samoilenkov, and D. Melyukov, “Development and characterization of a 2G HTS Roebel cable for aircraft power systems,” *IEEE Trans. Appl. Supercond.*, vol. 26, no. 3, pp. 1–4, Apr. 2016, doi: 10.1109/TASC.2016.2549036.
- [112] K. M. Davies, P. J. Norman, C. E. Jones, S. J. Galloway, and G. M. Burt, “Fault behaviour of a superconducting turboelectric distributed propulsion aircraft network: A comprehensive sensitivity study,” in *2015 Int. Conf. on Elect. Systems for Aircr., Railway, Ship Propulsion and Road Vehicles (ESARS)*, Mar. 2015, pp. 1–6, doi: 10.1109/ESARS.2015.7101487.
- [113] J.-H. Kim, M. Park, J. Cho, K. Sim, S. Kim, and I.-K. Yu, “Current distribution analysis of conducting and shield layers of HTS power cable under utility fault condition,” *IEEE Trans. Appl. Supercond.*, vol. 19, no. 3, pp. 1718–1721, Jun. 2009, doi: 10.1109/TASC.2009.2018450.
- [114] J. Li, Z. Zhao, B. Shu, X. Han, X. Ma, B. Bian, J. Li, and Z. Liang, “Fault analysis for 110 kV HTS power cables,” *IEEE Trans. Appl. Supercond.*, vol. 24, no. 5, pp. 1–5, Oct. 2014, doi: 10.1109/TASC.2014.2347317.
- [115] T. J. Donnelly, S. D. Pekarek, D. R. Fudge, and N. Zarate, “Thévenin equivalent circuits for modeling common-mode behavior in power electronic systems,” *IEEE Open Access J. Power and Energy*, vol. 7, pp. 163–172, May 2020, doi: 10.1109/OAJPE.2020.2996029.
- [116] Modelica Association, “Modelica Tools,” <https://modelica.org/tools> (accessed May 18, 2022).
- [117] E. Waddington, J. M. Merret, and P. J. Ansell, “Impact of LH2 fuel cell-electric propulsion on aircraft configuration and integration,” in *AIAA Aviation 2021 Forum*, Jul. 2021, doi: 10.2514/6.2021-2409.

- [118] NEPLAN AG, “Turbine-governor models: Standard dynamic turbine-governor systems in NEPLAN power system analysis tool,” NEPLAN AG, Zürich, Switzerland, Tech. Rep., 2015, https://www.neplan.ch/wp-content/uploads/2015/08/Nep_TURBINES_GOV.pdf (accessed May 31, 2022).
- [119] P. Pourbeik, G. Chown, J. Feltes, F. Modau, S. Sterpu, R. Boyer, K. Chan, L. Hannett, D. Leonard, L. Lima, W. Hofbauer, L. Gerin-Lajoie, S. Patterson, J. Undrill, and F. Langenbacher, “Dynamic models for turbine-governors in power system studies,” IEEE, Tech. Rep., Jan. 2013, <https://resourcecenter.ieee-pes.org/publications/technical-reports/PESTR1.html> (accessed May 31, 2022).

APPENDIX A

SUPPLEMENTAL FILES

A.1 Permissions for Chapter 2

This file contains the license details and terms and conditions for the reproduction of material used in Chapter 2 of this dissertation.

File name: CopyrightPermissions.pdf

File type: Portable Document Format (PDF)

File size: 534 KB

Required application viewer: Adobe Acrobat or any standard PDF viewer

Special hardware requirements: None

A.2 Permissions for Chapter 6

This file contains the license details and terms and conditions for the reproduction of material used in Chapter 6 of this dissertation.

File name: CopyrightPermissions.pdf

File type: Portable Document Format (PDF)

File size: 534 KB

Required application viewer: Adobe Acrobat or any standard PDF viewer

File name: CopyrightPermissions.pdf

File type: Portable Document Format (PDF)

File size: 534 KB

Required application viewer: Adobe Acrobat or any standard PDF viewer

Special hardware requirements: None

A.3 Permissions for Chapter 7

This file contains the license details and terms and conditions for the reproduction of material used in Chapter 7 of this dissertation.

File name: CopyrightPermissions.pdf

File type: Portable Document Format (PDF)

File size: 534 KB

Required application viewer: Adobe Acrobat or any standard PDF viewer

Special hardware requirements: None

APPENDIX B

PUBLICATIONS

Journal Papers

- [1] M. Podlaski, A. Khare, L. Vanfretti, M. Sumption, and P. Ansell, “Multi-domain modeling and simulation of high temperature superconducting transmission lines under short circuit fault conditions”, *IEEE Trans. Transp. Electrification.*, vol. 8, no. 3, pp. 3859-3869, Sep. 2022, doi: 10.1109/TTE.2021.3131271.
- [2] M. Podlaski, X. Bombois, and L. Vanfretti, “Validation of power plant models using field data with application to the Mostar hydroelectric plant,” *Int. J. Elect. Power Energy Syst.*, vol. 142, no. B, pp. 1-13, Jun. 2022.

Conference Papers

- [1] M. Podlaski, L. Vanfretti, J. Pesente and P. H. Galassi, “Automated parameter identification and calibration for the Itaipú power generation system using modelica, FMI, and RaPIId,” in *7th Work. Modeling and Simulation Cyber-Physical Energy Sys. (MSCPES)*, Apr. 2019, pp. 1–6, doi: 10.1109/MSCPES.2019.8738793.
- [2] M. Podlaski, L. Vanfretti, M. de Castro Fernandes, and J. Pesente, “Parameter estimation of user-defined control system models for Itaipú power plant using modelica and OpenIPSL,” in *Proc. American Modelica Conf.*, Sep. 2020, pp. 139–148, doi: 10.3384/ECP20169139.
- [3] M. Podlaski, L. Vanfretti, H. Nademi and H. Chang, “UAV dynamic system modeling and visualization using modelica and FMI,” in *VFS 76th Annu. Forum & Tech. Display*, Oct. 2020, pp. 1058-1072, doi: 10.4050/F-0076-2020-16289.
- [4] M. Podlaski, L. Vanfretti, H. Nademi, P. J. Ansell, K. S. Haran, and T. Balachandran, “Initial steps in modeling of CHEETA hybrid propulsion aircraft vehicle power systems using modelica,” in *AIAA Propulsion and Energy 2020 Forum.*, Aug. 2020, Paper 3580, doi: 10.2514/6.2020-3580.
- [5] M. Podlaski, A. Khare, L. Vanfretti, M. D. Sumption, and P. J. Ansell, “Multi-domain modeling for high temperature superconducting components for the CHEETA hybrid

- propulsion power system,” in *AIAA Propulsion and Energy 2021 Forum*, Aug. 2021, Paper 3302, doi: 10.2514/6.2021-3302.
- [6] E. Segerstrom, M. Podlaski, A. Khare, and L. Vanfretti, “Parameter estimation and model validation of Quanser AERO using Modelica and RaPIId,” in *AIAA Propulsion and Energy 2021 Forum*, Aug. 2021, Paper 3286, doi: 10.2514/6.2021-3286.
- [7] M. Podlaski, R. Niemiec, L. Vanfretti and F. Gandi, “Multi-domain electric drivetrain modeling for UAM-Scale eVTOL aircraft,” in *VFS 77th Annu. Forum & Tech. Disp.*, May 2021, pp. 2566-2579, doi: 10.4050/F-0077-2021-16893.
- [8] M. Podlaski, L. Vanfretti, T. Bogodorova, T. Rabuzin, and M. Baudette, “RaPIId-A parameter estimation toolbox for Modelica/FMI-based models exploiting global optimization methods,” *19th IFAC Symp. on System Identification*, vol. 54, no. 7, pp. 391–396, Jul. 2021, doi: 10.1016/j.ifacol.2021.08.391.
- [9] C. Canham, M. Podlaski and L. Vanfretti, “Guidance, navigation, and control enabling retrograde landing of a first stage rocket,” in *14th Int. Modelica Conf.*, Sep. 2021, pp. 171-176, doi: 10.3384/ecp21181171.
- [10] M. Podlaski, R. Niemiec, L. Vanfretti, and F. Gandhi, “Extending a multicopter analysis tool using modelica and FMI for integrated eVTOL aerodynamic and electrical drivetrain design,” in *2022 American Modelica Conf.*, Dallas, TX, Oct. 2022.

Presentations

- [1] M. Podlaski, L. Vanfretti, J. Pesente and P. H. Galassi, “Automated parameter identification and calibration for the Itaipu power generation system using Modelica, FMI, and RaPIId,” presented at 2019 NASPI Work Group Meeting, Richmond, VA, USA, Oct. 29-30, 2019.
- [2] M. Podlaski, E. Waddington, “University leadership initiative project 4 - CHEETA - University of Illinois and RPI,” presented at 2021 NASA TACP Showcase, Virtual, Feb. 2-4, 2021.
- [3] A. Khare, M. Podlaski, W. Stautner, J. Feldman, L. Vanfretti, K. Haran, and P. Ansell, “Design and analysis of cryogenic cooling system for superconducting motor,”

presented at joint 23rd Cryogenic Eng. Conf. and Int. Cryogenic Materials Conf., Virtual, Jul. 19-23, 2021, Paper C3Or1B-06.

- [4] M. Podlaski, L. Vanfretti, A. Khare, M. Sumption, P. Ansell, “Electro-thermal modeling of HTS power lines for cryogenically-cooled electric aircraft design,” presented at joint 23rd Cryogenic Eng. Conf. and Int. Cryogenic Materials Conf., Virtual, Jul.19-23, 2021, Paper M5Or2A-01.

APPENDIX C

ITAIPÚ PARAMETER DEFINITIONS AND GENERATOR EQUATIONS

C.1 GENSAE Generator

$$K_{1d} = \frac{(X'_d - X''_d)(X_d - X'_d)}{(X'_d - X_l)^2} \quad (C.1)$$

$$K_{2d} = \frac{(X'_d - X_l) * (X''_d - X_l)}{(X'_d - X''_d)} \quad (C.2)$$

$$K_{3d} = \frac{X''_d - X_l}{X'_d - X_l} \quad (C.3)$$

$$K_{4d} = \frac{X'_d - X''_d}{X'_d - X_l} \quad (C.4)$$

$$\frac{dE_{pq}}{dt} = \frac{1}{T_{pd0}(E_{fd} - X_{ad}I_{fd})} \quad (C.5)$$

$$\frac{d\Psi_{kd}}{dt} = \frac{1}{T''_{d0}(E'_q - \Psi_{kd} - X'_d - X_l) * id} \quad (C.6)$$

$$\frac{d\Psi''_q}{dt} = \frac{1}{T''_{q0}(-\Psi''_q + (X_q - X''_q)) * id} \quad (C.7)$$

$$\Psi_{d'} = E'_q + K_{3d} + \Psi_{kd}K_{4d} \quad (C.8)$$

$$\Psi_d = \Psi''_d - X''_d * i_d \quad (C.9)$$

$$\Psi_q = -\Psi''_q - X''_q * i_q \quad (C.10)$$

$$X_{ad}I_{fd} = K_{1d} * (E'_q - \Psi_{kd} - (X'_d - X_l) * i_d) \quad (C.11)$$

$$+ (X_d - X'_d) * i_d + (SE_{exp} + 1) * E'_q \quad (C.12)$$

$$T_e = \Psi_d * i_q - \Psi_q * i_d \quad (C.13)$$

$$u_d = (-\Psi_q) - R_a * i_d \quad (C.14)$$

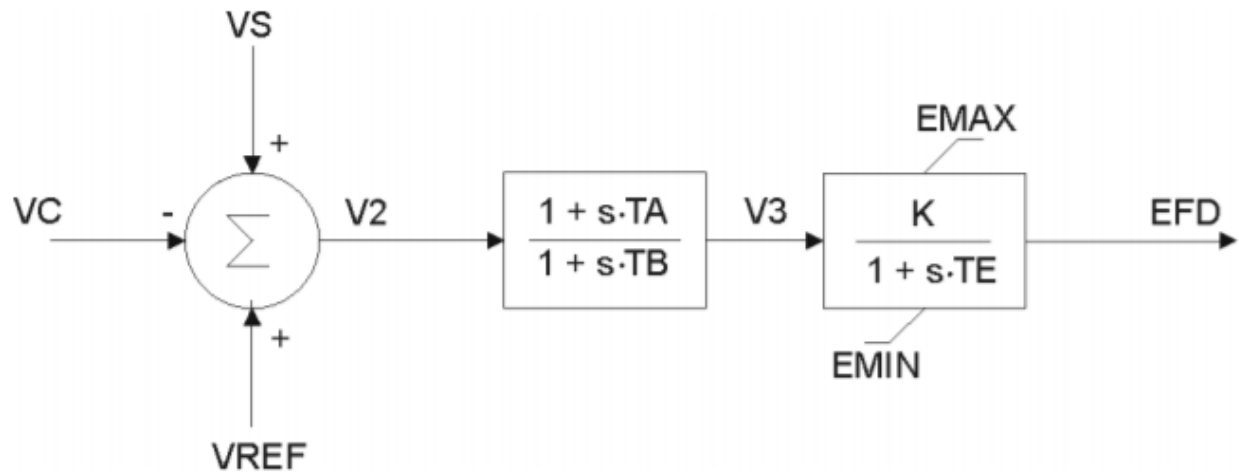
$$u_q = \Psi_d - R_a * i_q \quad (C.15)$$

C.2 SEXS AVR

The simple excitation AVR (SEXS AVR) has a reference voltage that is determined by Equation C.16. The control diagram is shown in Figure C.1 and is derived from [17, 62].

The parameters are listed in Table C.1.

$$V_{REF} = E_{fd0}/K + E_{COMP0} \quad (C.16)$$



$$V_S = V_{PSS} + V_{OEL} + V_{UEL}$$

Figure C.1: Control diagram for SEXS AVR.

Table C.1: SEXS AVR parameters.

AVR - IEEE SEXS	
T_A	Lead/lag time constant
T_B	Lead/lag time constant
K	Gain
T_E	Time constant
E_{MAX}	Limiter
E_{MIN}	Limiter

C.3 STAB3 PSS

The STAB3 PSS model is shown in Figure C.2 and is derived from [17, 58]. The parameters are listed in Table C.2.

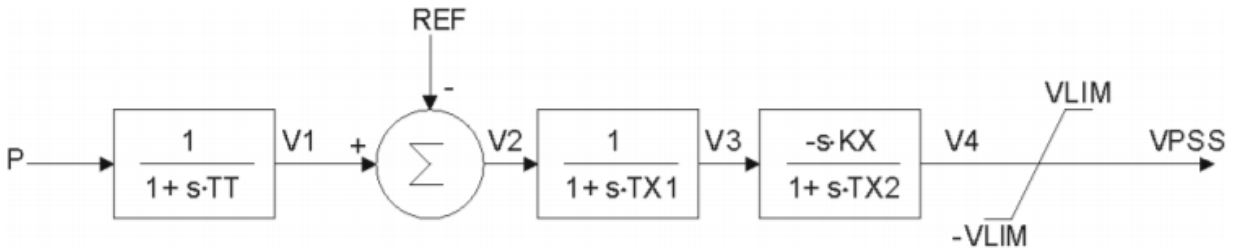


Figure C.2: Control diagram for STAB3 PSS.

Table C.2: STAB3 PSS parameters.

PSS - IEEE STAB3	
T_T	Lead/lag time constant
T_{X1}	Lead/lag time constant
K_X	Gain
T_{X2}	Time constant
V_{LIM}	PSS output limit

C.4 IEEE HYGOV Turbine Governor

The control diagram for the IEEE HYGOV generator is defined in [118, 119]. The parameters are listed in Table C.3.

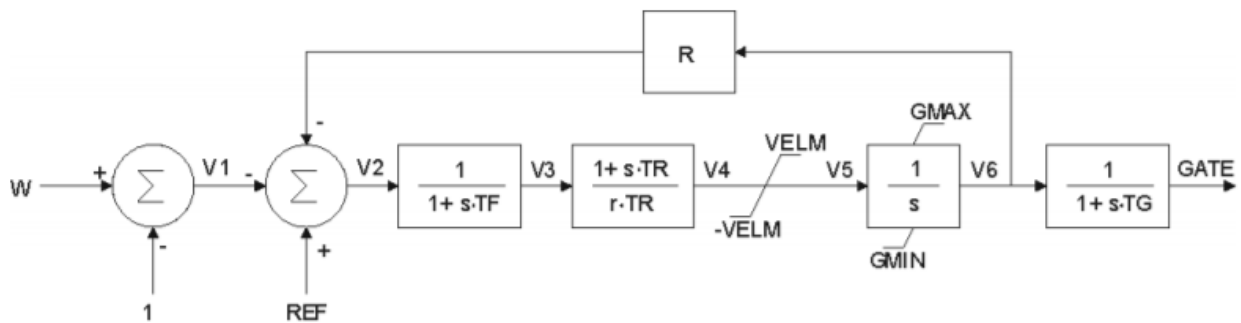


Figure C.3: Control diagram for IEEE HYGOV TG.

Table C.3: HYGOV TG parameters.

TG - IEEE HYGOV	
R_{big}	Permanent droop
R_{small}	Temporary droop
T_R	Governor time constant
T_F	Filter time constant, seconds
T_G	Servo time constant
V_{ELM}	Gate velocity limit
G_{MAX}	Maximum gate limit
G_{MIN}	Minimum gate limit

C.5 Itaipu Component Variables and Parameters

Table C.4: Itaipu component variables and parameters.

Parameter	Details
Generator - IEEE GENSAE Model	
T'_{d0}	d-axis transient open circuit time constant
T''_{d0}	d-axis sub transient open circuit time constant
T''_{q0}	q-axis sub transient open circuit time constant
H	Inertia constant
D	Speed damping
X_d	d-axis reactance
X'_d	d-axis transient reactance
X''_d	d-axis sub transient reactance
X''_q	q-axis sub transient reactance
X_q	q-axis reactance
X_l	leakage reactance
AVR - Itaipu User-Defined Model	
K_v	AVR integrator gain
K_{ei}	AVR gain
K_{min}	Underexcitation limiter gain
K_{point}	AVR gain
T_i	Overexcitation limiter time constant
T_a	Overexcitation limiter time constant
T_b	Overexcitation limiter time constant
T_{ai}	Overexcitation limiter time constant
PSS - Itaipu User-Defined Model	
K_f	
K_{f1}	AVR time constant
T_f	AVR gain
T_p	PSS time constant
K_1	PSS time constant
T_1	PSS time constant
K_2	PSS gain
T_2	PSS gain
TG - Itaipu User-Defined Model	
T_n	Accelerometer time constant
NT_v	Adjustment of accelerometer time constant
T_d	Integrator time constant
T_{f1}	Time of closing distributor fast part
T_{f2}	Time of closing distributor slow part
T_v	Equivalent time of distributor valve
T_w	Water starting time
T_{ya}	Time of opening of the distributor

APPENDIX D
MOSTAR HYDROELECTRIC PLANT PARAMETER
DEFINITIONS AND GENERATOR EQUATIONS

D.1 IEEE Standard Model Equations

GENSAL generator

$$K_{1d} = \frac{(X'_d - X''_d)(X_d - X'_d)}{(X'_d - X_l)^2} \quad (D.1)$$

$$K_{2d} = \frac{(X'_d - X_l) * (X''_d - X_l)}{(X'_d - X''_d)} \quad (D.2)$$

$$K_{3d} = \frac{X''_d - X_l}{X'_d - X_l} \quad (D.3)$$

$$K_{4d} = \frac{X'_d - X''_d}{X'_d - X_l} \quad (D.4)$$

$$\frac{dE'_q}{dt} = \frac{1}{T'_{d0}}(E_{fd} - X_{ad}I_{fd}) \quad (D.5)$$

$$\frac{d\Psi_{kd}}{dt} = \frac{1}{T''_{d0}}(E'_q - \Psi_{kd} - (X'_d - X_l) * I_d) \quad (D.6)$$

$$\frac{d\Psi''_q}{dt} = \frac{1}{T''_{q0}}(-\Psi''_q + (X_q - X''_q) * I_d) \quad (D.7)$$

$$\Psi_{x'} = E'_q + K_{3d} + \Psi_{kd}K_{4d} \quad (D.8)$$

$$\Psi_d = \Psi''_d - X''_d * I_d \quad (D.9)$$

$$\Psi_q = -\Psi''_q - X''_q * I_q \quad (D.10)$$

$$X_{ad}I_{fd} = K_{1d} * (E'_q - \Psi_{kd} - (X'_d - X_l) * I_d) \quad (D.11)$$

$$+ (X_d - X'_d) * I_d + (SE_{linear} + 1) * E'_q \quad (D.12)$$

$$T_e = \Psi_d * I_q - \Psi_q * I_d \quad (D.13)$$

$$u_d = (-\Psi_q) - R_a * I_d \quad (D.14)$$

$$u_q = \Psi_d - R_a * I_q \quad (D.15)$$

Table D.1: GENSAL generator parameter definitions.

Generator variables	
K_{1d}	Generator constant 1
K_{2d}	Generator constant 2
K_{3d}	Generator constant 3
K_{4d}	Generator constant 4
E'_q	q-axis voltage behind transient reactance
Ψ_{kd}	d-axis rotor flux linkage
Ψ''_d	d-axis subtransient flux linkage
Ψ''_q	q-axis subtransient flux linkage
Ψ_d	d-axis flux linkage
Ψ_q	q-axis flux linkage
I_d	d-axis armature current (p.u.)
I_q	q-axis armature current (p.u.)
SE_{linear}	linear saturation function
T_e	Electrical torque (p.u.)
u_d	d-axis terminal voltage (p.u.)
u_q	q-axis terminal voltage (p.u.)

Table D.2: Generator variables used in estimation - IEEE GENSAL Model.

Generator parameter defintions	
T'_{d0}	d-axis transient open circuit time constant
T''_{d0}	d-axis sub transient open circuit time constant
T''_{q0}	q-axis sub transient open circuit time constant
H	Inertia constant
D	Speed damping
X_d	d-axis reactance
X'_d	d-axis transient reactance
X''_d	d-axis sub-transient reactance
X''_q	q-axis sub-transient reactance
X_q	q-axis reactance
X_l	leakage reactance

IEEE ST5B AVR

The ST5B AVR model is shown in Figure D.1 and is derived from [17, 62]. The parameters are labeled in Table D.3.

Table D.4: PSS2A PSS parameters.

PSS - IEEE PSS2A	
T_{w1}	First washout time on signal 1
T_{w2}	Second washout on signal 1
T_{w3}	First washout on signal 2
T_{w4}	Second washout on signal 2
T_{w6}	Time constant on signal 1
T_{w7}	Time constant on signal 2
T_1	Lead/lag time constant
T_2	Lead/lag time constant
T_3	Lead/lag time constant
T_4	Lead/lag time constant
T_8	Lead of ramp tracking filter
T_9	Lag of ramp tracking filter
T_{10}	Lead/lag time constant
T_{11}	Lead/lag time constant
K_{S1}	PSS gain
K_{S2}	Gain on signal 2
K_{S3}	Gain on signal 2 input
$V_{ST,max}$	PSS output max limit
$V_{ST,min}$	PSS output min limit
$V_{SI1,max}$	Input signal 1 max limit
$V_{SI1,min}$	Input signal 1 min limit
$V_{SI2,max}$	Input signal 2 max limit
$V_{SI2,min}$	Input signal 2 min limit
M	Denominator order of ramp tracking filter
N	Order of ramp tracking filter

APPENDIX E

CHEETA SUBSYSTEM PARAMETER DEFINITIONS

Table E.1: HTS line parameters.

Parameter	Description	Unit
HTS - Electrical Parameters		
C_π	Pi-Line Capacitance per unit length	F/m
E_0	Reference electric field	V/m
E	Electric field	V/m
f	Frequency of AC system	Hz
L_π	Pi-Line Inductance per unit length	H/m
n	Index value of superconductor	N/A
I_{op}	Current into the HTS line	A
I_{c0}	Critical current at 0 °K	A
I_c	Critical current at 20 °K	A
R_{AC}	Pi-Line AC Resistance	Ω
R_L	Resistance of the brass connectors	Ω
R_π	Pi-Line Resistance per unit length	Ω/m
ω	Frequency of AC system	rad/sec
$\tan \delta$	Phase angle lag in AC operation	N/A
μ_r	Relative conductivity of wire material	N/A
ϵ_r	Relative permittivity of wire material	N/A
ρ	Resistivity of HTS tape	Ωm
HTS - Thermal Parameters		
C_{pv}	Heat capacity of gas coolant	J/K
G_d	Energy perturbation causing a fault	W/m^2
h	Heat transfer coefficient	W/m^2K
Q_{ce}	Cold-end cooling of the line	W
Q_{flow}	Heat flow out of the line	W
T_b	Cooling bath temperature	°K
T_c	Critical temperature	°K
T_{inlet}	Inlet temperature for gas cooling	°K
$T(z)$	Temperature of gas coolant as a function of linear distance	°K
v	Velocity of gas coolant	m/s
z	Distance from gas coolant inlet	m
ΔT_ρ	Temperature jump at interface between cryogen and HTS surface	°K
ΔT_{total}	Total temperature jump at interface between cryogen and HTS surface in gas cooling	°K

ΔT_z	Temperature jump at interface between cryogen and HTS surface at a distance (z) from inlet of gas cooling	$^{\circ}\text{K}$
κ	Cable thermal conductivity	W/mK
HTS - Geometrical Parameters		
A_{cu}	Cross sectional area of copper portion of wire	m^2
a	Inner radius of co-axial cable	mm
b	Outer radius of co-axial cable	mm
P	Circumference of line	m
R_c	Inner radius of cryostat	m
R_0	Outer radius of cable	m
Fuel Cell Parameters		
a_{FC}	Constant term in Tafel equation to calculate activation voltage	V/K
b_{FC}	Constant term in Tafel equation to calculate activation voltage	V/K
I_{FC}	Fuel cell current	A
I_{max}	Fuel cell maximum current	A
E_{cell}	Fuel cell internal voltage	V
F	Faraday Constant	A/mol
k_E	Empirical constant to calculate E_{cell}	V/K
k_{RI}	Empirical constant to calculate R_{ohm}	Ω/A
k_{RT}	Empirical constant to calculate R_{ohm}	Ω/K
n_e	Number of electrons	N/A
R	Universal gas constant	J/mol
R_{act}	Activation resistance	Ω
R_{conc}	Concentration resistance	Ω
R_{ohm}	Ohmic loss resistance	Ω
R_{ohm0}	Reference term used in ohmic loss resistance calculation	Ω
T_f	Temperature of fuel cell	$^{\circ}\text{K}$
V_{out}	Output voltage of fuel cell	V
V_c	Voltage drop from internal capacitance	V
V_{ohm}	Voltage drop from ohmic loss, R_{ohm}	V
V_{act}	Total voltage drop from activation loss from R_{act} , $V_{act1} + V_{act2}$	V
V_{act1}	Voltage drop due to activation loss from R_{act} only dependent on fuel cell internal temperature	V
V_{act2}	Voltage drop due to activation loss from R_{act} dependent on fuel cell internal temperature and current	V
α	Electron transfer coefficient	N/A
η_0	Temperature invariant part of V_{act}	V
Inverter Parameters		
R_{cm}	Common-mode resistance	Ω
R_D	Diode resistance	Ω
$V_{cm,est}$	Common-mode voltage	V
V_{th}	Thevenin voltage	V
Z_{th}	Thevenin impedance	Ω

Motor - Electrical Parameters		
P	Nominal power per motor	MW
ω	Nominal motor speed	RPM
f	Electrical system frequency	Hz
V_T	Terminal line-to-line voltage	V
I	Nominal armature current	2475
p	Pole count	N/A
T_{op}	Operational temperature	K
J_{arm}	Armature current density	A/mm ²
J_{field}	Field current density	A/mm ²
J_{shield}	Shield current density	A/mm ²
pf	Power factor	N/A
X_s	Synchronous reactance	Ω
L_{aa}	Armature inductance	μH
L_{ab}	Mutual inductance	μH
L_{ac}	Mutual inductance	μH
R_{hyst}	Effective resistance for hysteresis	Ω
R_{trs}	Effective resistance for transport AC losses	$\mu\Omega$
Motor - Geometry Parameters		
arm	Armature slots per pole	N/A
$P_{specific}$	Specific power of the machine	kW/kg
l_{ag}	Air gap length	mm
D_{out}	Outer diameter of the machine	m
T_{op}	Operational temperature	K
$Turns_{hand}$	Turns in hand	strands/cable
$Turns$	Turns number	strands/cable